UAB
Universitat Autònoma de Barcelona

UAB
Universitat Autònoma de Barcelona

SIZE CONTROL OF MAGNETIC IRON OXIDE NANOPARTICLES IN WATER: THE ROLE OF LANTHANIDES

Memòria presentada per optar al grau de Doctor per la
UNIVERSITAT AUTONOMA DE BARCELONA
Doctorat en Química

KAREN MEJÍA CARMONA

Supervisores
Prof. Víctor F. Puntes
Dra. Neus G. Bastús

Tutor
Prof. Víctor F. Puntes

Barcelona, Septiembre 2024

ICN2ᴿ
Institut Català de Nanociència i Nanotecnologia

"Si en algo nos parecíamos tú y yo, era en el hecho de que aborrecíamos esas profesiones diseñadas sólo para llenarse los bolsillos de plata. Sospechábamos desde muy jóvenes que la vida, por fortuna, era mucho más que dinero".

–Mario Mendoza, Buda Blues.

"Look deep into nature, and then you will understand everything better".

–Albert Einstein.

ACKNOWLEDGMENTS

I would like to express my sincere thanks and gratitude to all the people who have been present throughout this time of my doctoral studies:

To my supervisors Professor Dr. Víctor F. Puntes and Dra. Neus G. Bastús for conducting my doctoral work and welcoming me in the Inorganic Nanoparticles Group at ICN2. For their guidance, discussions, advice and learning opportunities during this stage. Thank you Neus for your involvement and commitment to my work, it would not have been possible without your help.

To the Catalan Institute of Nanoscience and Nanotechnology - ICN2, and the Autonomous University of Barcelona (UAB) for the opportunity to pursue this PhD.

To all my former colleagues in the Inorganic Nanoparticles Group for sharing their knowledge, but more importantly their friendship: Steve, Carmen, Jana, Oscar and Cristiane, I wish you always the best, the world is full of opportunities. To my colleagues of the Vall d'Hebron Hospital group, with special mention to Vivian and Muriel, thanks for the company, support and "coffee" in my last year of PhD, to Joan, thanks for his kindness and help, and to Ramon, Lena and Joana for the time shared.

To my collaborator Pablo Guardia for his contribution to this thesis and sharing his knowledge.

To the ICN2 staff, Jessica and Marcos for their kind help and technical support. To the people I met by chance in the ICN2 halls, and we shared a cup of coffee and friendship: Enric, Omar, Martino, Lingxin, Noelia, Gloria, Despina and Roque, thanks.

The most special and important thanks go to my family: to my mom Leyla Carmona, my father Fernando Mejía, and my sister Caroll for their unconditional support from the distance but always so close to me. For their efforts in the past, which have given me the courage to come here and pursue my dreams. A mi familia… gracias por todo!

Finally, I want to thank the circumstances of life, and myself, for being brave during the difficult moments, to keep trying without giving up in every aspect of my life, I am surely better today. Even when you don't know how, just trust...vai dar tudo certo!

Table of Contents

Table of Figures

List of Abbreviations

AMF	Alternating Magnetic Field
ANOVA	Analysis of Variance
AOP	Advanced Oxidation Process
BF TEM	Bright field Transmission Electron Microscopy
CAT	Catalase
Ce@IONPs	Cerium coated Iron Oxide Nanoparticles
CDT	Chemo-dynamic therapy
CN	Coordination Number
D_c	Critical Diameter
D_{spm}	SPM Critical Diameter
D_{TEM}	NP diameter determined by TEM
D_{XRD}	NP diameter determined by TEM
f	Frequency
F	Fast base addition
Fe_3O_4	Magnetite
$\gamma\text{-}Fe_2O_3$	Maghemite
FM	Ferrimagnetic
G	Graphene
GO	Graphene oxide
H	Magnetic field amplitude
H_c	Coercivity
HO·	Hydroxyl radical
HRP	Horseradish Peroxidase Enzyme
HRTEM	High-Resolution Transmission Electron Microscopy
HAADF-STEM	High-Angle Annular Dark Field Scanning TEM
HSP	Heat Shock Protein
IEP	Isoelectric Point
IONP	Iron Oxide Nanoparticles (magnetite/ maghemite)
Km	Michaelis-Menten Constant
Ln	Lanthanides

LS	Leaching Solution
MF	Magnetic Field
MH	Magnetic Hyperthermia
MHT	Magnetic Hyperthermia
M-M	Michaelis-Menten Kinetic model
MNP	Magnetic Nanoparticles
MRI	Magnetic Resonance Image
M_s	Saturation Magnetization
NC	Nanocrystal
NP	Nanoparticle
oct	Octahedral
POD	Peroxidase
RE	Rare earth elements
ROS	Reactive Oxygen Species
RT	Room temperature
S	Slow Base Addition
SAR	Specific Absorption Rate
SC	Sodium Citrate
SC-IONPs	Sodium Citrate coated Iron Oxide Nanoparticles
SD	Single Domain
SLP	Specific Loss Power
SPM	Superparamagnetic
t_B	Brownian relaxation time
td	Tetrahedral
TMA^+	Tetramethyl ammonium cation
TMAOH	Tetramethyl ammonium hydroxide
TMB	3,3´,5,5´-tetramethylbenzydine
t_N	Neel relaxation time
VS	Very slow base addition
XRD	X-ray Diffraction
ZFC/FC	Zero-field cooling / field-cooling

Chapter 1

General Introduction

1.1 Nanoscience and Nanotechnology

Today, nanoscience and nanotechnology are two keywords that represent an intensifying area of research, involving a variety of structures, materials, devices, and systems at the atomic and molecular level, typically –but not limited– in the range of 1–100 nm. At the nanoscale, materials behave differently and that is why we have taken advantage of them over the years.

Nanomaterials are not a new discovery; however, the latest instrumental techniques allow us today to observe and control them better. The development of nanomaterials dates to ancient times, as evidenced by the famous 4th century Lycurgus cup, which illustrates the optical effects of light absorption and transmission produced by Au and Ag nanoparticles in the glassy matrix of the cup. Similarly, ancient glassmakers from the 13-18th centuries decorated medieval churches and European cathedrals by staining their windows with colloidal Au and Ag (Figure 1-1).[1]

While the first documented preparation and study of colloidal Au was performed by Michel Faraday around 1857, a century later, the use of citrate seems relevant as a reducing and stabilizing agent to produce size-controlled Au NPs by the Turkevitch method, a

technique later applied in the preparation of Ag, Pd, and Pt NPs.[2] On the other hand, magnetic liquids or ferrofluids were also relevant in the history of nanotechnology. The first ferrofluid was synthesized by Elmore in 1938, and around 1960 Papell patented an oil-
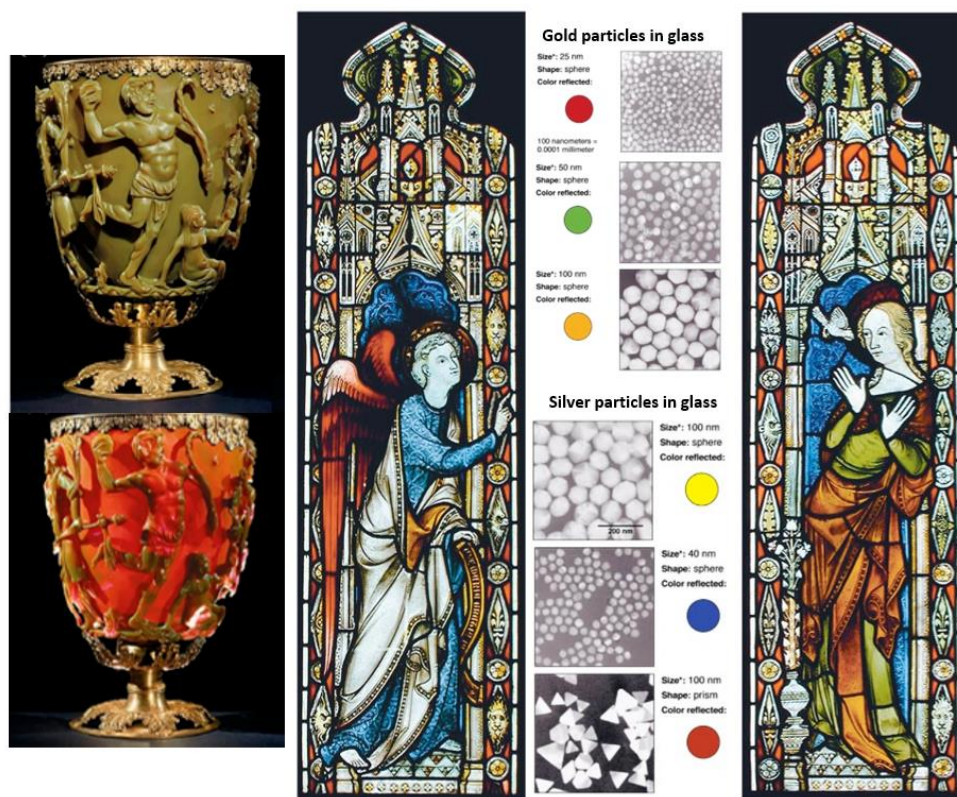
Figure 1-1. The Lycurgus cup (green in reflected light and red in transmitted light), and the annunciation to the Virgen medieval window. Adapted from [1,3].

based ferrofluid.[4,5] René Massart carried out extensive research on aqueous magnetic liquids, and again the use of citrate appears to be relevant for the production of fine magnetic particles.[5,6]

Remarkable advances in nanotechnology have been made since the Feynman gave his famous lecture "There's Plenty of Room at the Bottom" in 1959, and Taniguchi first introduced the term "nanotechnology" in 1974, spreading interest in the field and envisioned the direct manipulation of atoms, opening the doors to modern nanotechnology.[1] It is noteworthy that, in just few decades, nanoscience and nanotechnology have progressed simultaneously in different fields, such as materials synthesis, instrumental techniques, informatics, and industrial and medical fields. Current trends include nanorobotics, smart materials, nanoelectronics and biomedical applications.[7–12]

However, fundamental research on chemical knowledge was highlighted last year, the 2023 Nobel Prize in Chemistry was awarded to Moungi Bawendi, Louis Brus, and Alexei Ekimov for "the discovery and synthesis of quantum dots".[13] This award highlights the

significance of fundamental science at the nanoscale, through fine control of particle size, understand size-dependent properties, and employ of wet-chemistry methods for the sake of technological applications. The ongoing research on the synthesis of other nanomaterials, such as metals, oxides, perovskites, and more, remains an important research area for emerging applications. We now have a versatile library of nanoparticles (NPs) and the capacity to manipulate and control their synthesis, predict their properties through modeling and simulation, and characterize them at the nanoscale using advanced instrumental tools, is a significant achievement. We are moving towards high-performance materials, 3D structures, self-assembling materials and hybrids NPs, all while adopting more environmentally friendly and sustainable methodologies that utilize bioavailable elements, reduce waste, and minimize exposure to toxic substances.

While the potential benefits of nanotechnology are vast, it is essential to investigate the associated risks, such as higher reactivity and interaction with biological systems, and how they can be merged with societal needs and emerging technologies. Establishing regulations that ensure the secure and sustainable development of nanotechnology is crucial.[14] The potential for innovation in nanotechnology is immense and vast across multiple disciplines, including physics, chemistry, biology, and engineering.[15]

1.2   Nanomaterials

The study of nanomaterials involves the manipulation and creation of matter at the nanometric scale. Nanomaterials are in the range between 1–100 nm in size, in at least one of their dimensions. These materials exhibit quantum mechanical effects that significantly impact their optical, electrical, and magnetic properties.

Nanoparticles (NPs) are considered a zero-dimension (0D) nanomaterial with a well-defined arrangement of atoms, usually in spherical form. NPs can be made from a variety of materials, and their small size and large surface area provides them unique properties that make them incredibly useful in numerous applications. For instance, their increased reactivity is well-suited for catalytic reactions, or their enhanced mechanical properties when compared to their bulk counterparts. NPs come in a variety of shapes, sizes, and compositions, each with specific properties and uses. Some common types include i) Inorganic NPs, divided into metal and metal oxide NPs (i.e., Au, Ag, Pt, TiO_2, and Fe_3O_4 NPs), known for their quantum effects on their electrical, optical, thermal, catalytic, and

3

magnetic properties; ii) Carbon-based NPs (i.e., fullerenes, carbon nanotubes, and graphene), valued for their strength and electrical conductivity; and iii) Organic NPs (i.e., polymers, micelles, and liposomes) used in drug delivery and biomedical applications due to their biocompatibility.[16]

The synthesis of nanomaterials can be generally categorized into two main approaches: top-down and bottom-up, which can be considered as physical and chemical methods, respectively.[17] The main aim of nanomaterial synthesis is to produce materials with controlled size, shape, composition and stability by controlling nucleation and growth steps. Recently, many efforts have been focused on green synthesis procedures and the transition to use more bioavailable, renewal, and non-toxic sources are greatly encouraging.

This thesis is specifically focused on the synthesis of metal oxides, particularly magnetic iron oxides (magnetite/maghemite). The use of iron compounds continues to be a significant area of exploration due to their abundance, biocompatibility, and low toxicity. Their widespread use and replacement of other materials in the nanotechnology field, as well as their magnetic properties, make them useful. Their properties, synthesis methods, and applications will be discussed in greater detail below.

1.3   Magnetic Nanoparticles

Magnetic nanoparticles (MNPs) constitute a class of materials whose size influences their intrinsic magnetic properties and set them apart from bulk materials. At nanoscale, MNPs exhibit remarkable magnetic behaviors, dominated by finite size-effects such as superparamagnetism.[18] The magnetic properties of the materials and magnetism at nanoscale are detailed in Appendix A. Briefly, their size, shape, composition and surface chemistry are critical in determining their magnetic properties and their functionality and efficiency across different applications.[19] Stability and biocompatibility of MNPs in various environments, including aqueous solutions and biological systems, are fundamental for medical applications. The ongoing research into MNPs continues to reveal new and exciting possibilities, with advancements in synthesis and application fields. In synthesis, ensuring consistent quality and modulated magnetic properties remains a significant research focus.

Magnetism at Nanoscale

Magnetism is a physical phenomenon produced from the spin electrons and their orbital motion around the nucleus.[20] At the nanoscale, the reduction in NP size and their magnetic properties are mainly influenced by two key features, finite-size effects and surface/interface effects.[21] The most relevant finite-size effects are the single magnetic domain (SD) and superparamagnetism (SPM) detailed in the following Figure 1-2.[22]

MNPs are typically divided into magnetic domains, which are regions of uniform magnetization. Large MNPs are multidomain structures, separated by domain-walls. As the particle size decreases, finite-size effects become significant, and below a certain critical diameter (D_C), NPs exist in a single-domain (SD) state, where the magnetic dipoles are

Figure 1-2. Schematic variation of the coercivity with the particle diameter, from magnetic single domain to multi-domain..[23]

uniformly aligned in the same direction, and the coercivity (H_C) reaches their maximum.[24]

As the particle size continues to decrease reaches another critical diameter (D_{SP}), where the H_C becomes zero, and the superparamagnetic state emerge, where thermal fluctuations can randomize the direction of magnetization. In the Figure 1-2 curved arrows represent random spin fluctuations, while straight arrows indicate the blocked state.[25] NPs sizes which exhibited a strong magnetic response under an applied magnetic field (MF), and a magnetic moment equal to zero in absence of MF are called superparamagnetic NPs.[19,21] For several MNPs the D_c is typically around 100 nm and the $D_{sp} \ll D_c$, which vary with the NPs composition, size and shape.[21]

Another crucial aspect at the nanoscale are the surface/interface effects. As NPs size decreases, a significant percentage of atoms are surface atoms. The surface effects arise from the lack of transitional symmetry at the particle boundary, leading to surface spin disorder or misalignment respect to the core spins.[18,21] Consequently, the surface spins can greatly influence the magnetization of the NPs, remarkably in smaller particles. Surface spin disorder can lead to a decrease of the saturation magnetization (M_s), associated with the existence of a magnetically dead layer on the particle surface.[18,21]

Among MNPs, magnetic iron oxide nanoparticles (IONPs), specifically magnetite (Fe_3O_4) and maghemite (γ-Fe_2O_3), have been intensively studied because their high magnetism, high stability, low toxicity.[19] These feature make IONPs ideal for several applications, comprising magnetic resonance image (MRI),[26] sensing,[27] data storage,[24] batteries,[28] catalysis[29] and environmental remediation.[17] Furthermore, both nanomaterials are very relevant for biotechnology and biomedicine[20,30–32]

1.3.1 Iron Oxides

Iron oxides are abundant compounds widely prevalent on the Earth, being an important part of natural environments, soils, and living organisms. Nowadays, they can also be synthetically produced as needed. There are sixteen distinct types of iron oxides, which include oxides, hydroxides, and oxyhydroxides, differing in their Fe, O^{2-} and OH^- structural arrangement. Most of these compounds contain iron in a trivalent state (Fe^{3+}), except for $Fe(OH)_2$, magnetite (Fe_3O_4), and wüstite (FeO), which have it in a divalent state (Fe^{2+}).[33]

Iron oxides can be interconverted between them under specific conditions to form a more thermodynamically stable phase, which is a useful process for several industries. The transformations typically proceed via dehydroxylation, dehydration, reduction, oxidation, and dissolution-reprecipitation process.[33] The versatility of iron oxides offers numerous interdisciplinary applications, such as pigments, sorbents, catalysts, rocks, nutrients, oxidants, magnetic fluids, and biomedical materials.[33] Iin this thesis we will focus on the synthesis of magnetic iron oxides, specifically magnetite (Fe_3O_4) and maghemite (γ-Fe_2O_3), hereinafter referred to as IONPs.

1.3.1.1 Magnetite and Maghemite

Magnetite (Fe_3O_4) and maghemite (γ-Fe_2O_3) are ferrimagnetic materials. Both are isostructural materials, with lattice parameters of a=0.839 nm and a=0.834 nm, respectively. Magnetite contains both Fe^{2+} and Fe^{3+} ions in a 1:2 stoichiometry and crystallizes in an inverse spinel crystal structure $(B^{III})_{td}(A^{II}B^{III})_{oct}O_4$ (Figure 1-3). Its unit cell, face-centered cubic (FCC), Fd3m space group, is closed packed with 32 O_2^- ions, 8 Fe^{2+} ions are occupying the octahedral (*oct*) sites, and 16 Fe^{3+} ions are distributed in the *oct* and tetrahedral (*td*) sites, resulting in the formula $[Fe^{3+}_8]_{td}[Fe^{2+}_8Fe^{3+}_8]_{oct}O_{32}$,

simplified as Fe_3O_4.[33] Magnetite frequently presents an Fe^{3+} cation-deficient sublattice, which is known as non-stoichiometric magnetite ($Fe_{3-X}O_4$).[33]

For maghemite (γ-Fe_2O_3), in its unit cell most of the Fe ions are in the highest oxidized state (Fe^{3+}).[34] Maghemite crystalizes in a cubic structure, its unit cell is packed with 32 O_2^- ions, $21\frac{1}{3}$ Fe^{3+} and $2\frac{1}{3}$ oxygen vacancies, where 8 Fe^{3+} ions are occupying the *td* sites and the rest are distributed in the *oct* sites together with the oxygen vacancies, balancing for the oxidation of Fe^{2+}.[33]
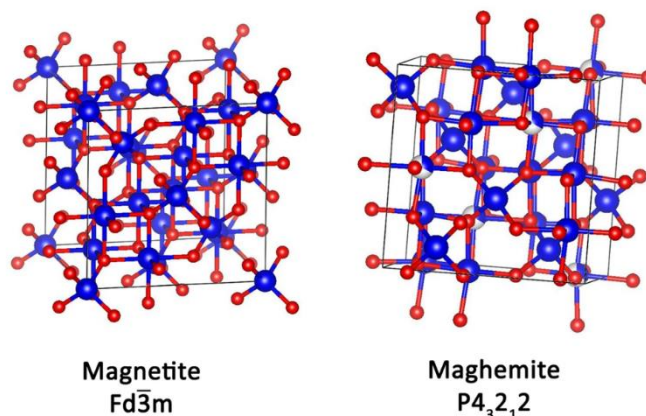
Figure 1-3. Crystal structure of magnetite and maghemite. Reproduced from 35.

Under oxidizing conditions magnetite (Fe_3O_4) becomes maghemite (γ-Fe_2O_3), and usually synthetic magnetite crystals with a size below 200 nm tend to oxidize to form a magnetite/maghemite solid solution ($Fe_{3-x}O_4$), with a unit cell which ranges from 0.8389 to 0.8338 nm.[33,36] It also reported that small crystal of maghemite (<100 nm) exhibited the same diffraction of the Fd3m space group, being difficult to differentiate them by XRD. [33]

1.3.2 Synthesis of magnetite NPs

Given the significant dependency of IONPs magnetic performance on their NP design, research is focused on optimizing their response to an external magnetic field by adjusting their physicochemical properties.[19]

The synthesis of magnetic IONPs can be generally categorized into two main approaches: "top-down" and "bottom-up", and three main categories: physical methods, chemical methods, and biological methods.[17] The physical methods follow a top-down approach, which starting from bulk material and depleting it to generate NPs (i.e., mechanical milling and laser ablation). On the contrary, the chemical methods employ a bottom-up approach, assembling atoms or molecules to form NPs. Techniques such as co-precipitation, thermal decomposition, microemulsion synthesis, hydrothermal synthesis,

sol-gel method, belong to this category. Whereas, biological methods also follow a bottom-up approach, by using biological organisms or molecules to synthesize NPs (i.e., microbes, membranes). They are often referred to as green synthesis methods and are gaining popularity due to their environmentally friendly approach.[17]

Among the various methods, some of the most popular used for synthesizing IONPs are thermal decomposition, solvothermal and microemulsions synthesis, which are the most preferred for the precise morphological control to produce high-quality IONPs. The use of organic precursors and solvents allowed unprecedented control over the synthesis of IONPs, shape and size, which is often difficult to replicate in aqueous media[22,31] However, they present drawbacks as high consuming energy, use of solvents and are non-ecofriendly approaches. These methods are far from the aim of this thesis and are thus not presented. Instead, we will emphasize on the synthesis of magnetite NPs in aqueous media at room temperature.

The complexity by using water as a solvent, include the aqueous solubility of iron ions, high solution supersaturations, high pH conditions, and the formation of several iron oxides and hydroxides phases in aqueous media, that complicated and limited the synthesis of magnetite.[33] In other words, water is a complex synthesis player!.

Speciation and Pourbaix diagrams offer relevant insights into the behavior of iron in aqueous systems and serve as guides for aqueous synthesis protocols. Since the proposed syntheses of IONPs in this thesis we employed Fe and Ce ions in aqueous medium both diagrams will be briefly explained in Appendix B.

Briefly, a speciation diagram provides an indication of the species around and their relative concentrations formed during the hydration process of the soluble and precipitated species.[37] Pourbaix diagrams indicates the thermodynamic stability of various soluble, hydrated or solid species as function of pH and their redox potential. For instance, in the Fe-H$_2$O system, 32 species have been identified, from which only 17 are considered relevant for Pourbaix diagram calculations.[38] It is important to note that these diagrams only indicates the thermodynamic data under equilibrium conditions, and do not illustrate the kinetics governing the processes.

Despite the challenges that come from the synthesis in aqueous media for adjusting the size and produce high-quality IONPs, it has become increasingly attractive approach for their green and scalable production at room temperature and low energy conpsumption.[39] One of the primary advantages of using aqueous media is the inherent stability of these particles in water, which enhances their biocompatibility compared to

those synthesized in organic solvents, avoiding the phase transfer step[39,40] This stability makes aqueous synthesis particularly appealing for biomedical applications, where biocompatibility is crucial.

In recent decades, substantial research has been dedicated to the aqueous synthesis of magnetic IONPs, to improved their properties by achieving shape-control, monodisperse NPs, and high-stability by using simple and reproducible methodologies.[21]

Particularly through co-precipitation and bioinspired methods, such as transformation of oxyhydroxides and partial oxidation. The formation of magnetite by these methods can be achieved by two main mechanism: i) direct co-precipitation from solutions which contain Fe^{2+} and or Fe^{3+}, and ii) via solid state transformation of a Fe oxide precursor, or by dissolution–reprecipitation process.[33] Figure 1-4 summarize these three synthesis pathways explained below.
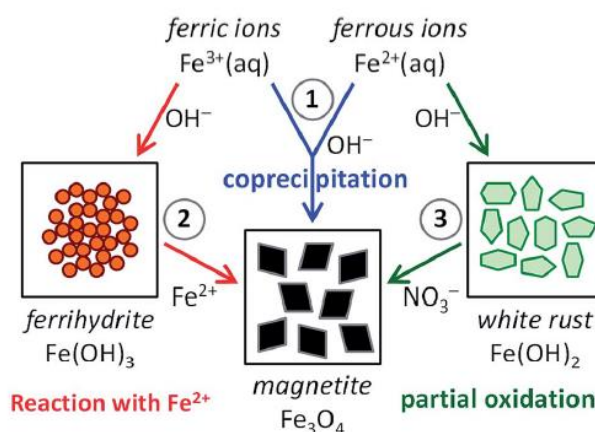
Figure 1-4. Scheme of the three main synthesis routes to magnetite (Fe_3O_4) in aqueous medium: A) by coprecipitation from Fe^{3+}: Fe^{2+} ions, B) through a solid ferrihydrite ($Fe(OH)_3$) precursor and Fe^{2+} ions, and C) by partial oxidation through a solid white rust ($Fe(OH)_2$) and Fe^{2+} ions. Reproduced from [40].

1.3.2.1 Aqueous Synthesis Routes of magnetite NPs

1.3.2.1.1 Co-precipitation

The co-precipitation method is the most common, easiest and low-cost method to produce magnetic IONPs (Fe_3O_4 or γ-Fe_2O_3) in aqueous media and large quantities.[21] This method was first described by Lefort et al., in 1852 and popularized by Massart.[5,6] The synthesis consists on the co-precipitation of a mixture of Fe^{2+} and Fe^{3+} salts in a 1:2 molar ratio, into a free-oxygen aqueous alkaline media under inert atmosphere (N_2 or Ar) according to the following reaction (Eq. 1):

$$Fe^{2+} + 2Fe^{3+} + 8OH^- \rightarrow Fe_3O_{4(s)} + 4H_2O \qquad (1)$$
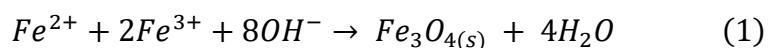
According to the iron Pourbaix diagram (Appendix B), complete precipitation should occur between pH 8 and 14, and inert conditions are necessary to prevent the easy Fe^{2+} oxidation. This procedure typically produces small spherical superparamagnetic magnetite NPs <20 nm, and can be performed at room or high temperatures (~70–90 °C).[20] As mentioned before, magnetite NPs are not thermodynamically stable, and they gradually oxidize into maghemite. To obtain maghemite NPs, the procedure is the same but without extreme inert conditions or by subjecting the obtained magnetite NPs to a controlled oxidation process in an acidic medium. The magnetization saturation of magnetic IONPs is generally in the range 30–50 emu/g.[20]

During the synthesis, NPs size, shape, and composition can be influenced by varying the nature of iron precursor (i.e., chlorides, sulfates, nitrates) and type of base (i.e., NH_3, NaOH, KOH, $(C_2H_5)_4NOH$, etc.) used, iron Fe^{2+}/Fe^{3+} ratio, reagents concentration and rate addition, pH, ionic strength, and reaction temperature. [41–43] In general, size decreases as the pH and ionic strength of the medium increases, and size increases as the reagent rate addition decreases.[44] Nevertheless, magnetic IONPs production is easily reproducible once the reaction conditions are fixed.[20]

Despite the simplicity of the method, its main drawback is the broad particle size distribution and limited control over the shape and crystallinity.[45] This is mostly due to the fact that nucleation and crystal growth during co-precipitation occur simultaneously during the reaction.[20] The rapid crystallization of magnetite, which can occur in just seconds to a few minutes (depending on the pH), and their extremely low solubility ($Kps= 6.3\times10^{-109}$) inhibits further crystal growth often before the reactants are fully mixed. Consequently, controlling the particle size and morphology via this method is challenging.[46] Conversely, this brings the advantage that compared with other synthesis methods, the co-precipitation is the fastest method.

1.3.2.1.2   Bioinspired Aqueous Route - Ferrihydrite transformation

For scientists, nature has been an invaluable source of inspiration for emulating mineralization and biomineralization processes. Inspired by the examples found in nature, such as rocks, soils transformations and biomineralization by living organisms over magnetite formation, the essential aspects of solid precursor-based mineralization processes have been mimicked to achieve control over the magnetite properties.[33] Iron oxides found in living organisms include magnetite, ferrihydrite, lepidocrocite, and goethite oxides. The most representative example is the formation of magnetite within the

cells of magnetotactic bacteria, where magnetite crystals are well developed and shaped into a magnetosome in single domain (SD) state and self-assemble in chains, serving as a navigation tool allowing the bacteria motility in the geomagnetic field. These crystals are particularly interesting because they are single crystals, exhibited a high saturation magnetization (M_S) and excellent crystallinity (Figure 1-5).[33]
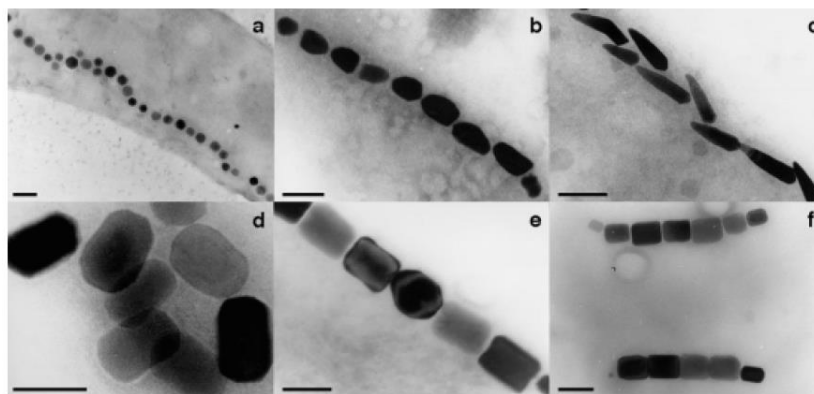
Figure 1-5.Magnetite shapes and intracellular chain arrangements in different magnetotactic bacteria (scale bar: 100 nm). [33]

Recent studies inspired by the biosynthesis of magnetite, relies on precise control over reaction kinetics, nucleation and growth steps. They are based on the use of a primary metastable phase as precursor to form a thermodynamically stable magnetite phase.

Magnetite synthesis can be achieved through the use of ferrihydrite as a co-precipitation precursor via solution transformation.[33] Ferrihydrite precursor is a metastable iron-oxyhydroxide denoted by simplicity as $Fe(OH)_3$, which includes $Fe_2O_3 \cdot 3H_2O$, $2Fe_2O_3 \cdot H_2O$, and $5Fe_2O_3 \cdot 9H_2O$ forms. The precursor is poorly nanocrystalline and is classified as 2-line to 6-line based on the broadened peaks observed by XRD.[47] Ferrihydrite transformation is widely studied, especially in geochemistry, biomineralization and engineer NPs, cause its transformation usually yield SD magnetite <100 nm.[48–51]

Ferrihydrite is also a common and reactive precursor to produce other Fe oxides as goethite, hematite, lepidocrocite, and green rust, which are determined by reaction conditions and kinetics. From that the importance of carefully controlling the experimental factors.[33]

Ferrihydrite precursor in presence of high levels of Fe^{2+} (as an additive), and high pH > 7 yields magnetite NPs, being this the same route of magnetite formation in the magnetotactic bacteria.[33] Similar to the coprecipitation method both inert conditions and molar ratio of 1:2 (Fe^{2+}: $Fe(OH)_3$) should be kept, according to the following reactions:

$$Fe^{3+} + 3OH^- \rightarrow Fe(OH)_{3\ (s)} \qquad (1)$$

$$2Fe(OH)_{3\ (s)} + Fe^{2+} + 2OH^- \rightarrow Fe_3O_{4(s)} + 4H_2O \qquad (2)$$
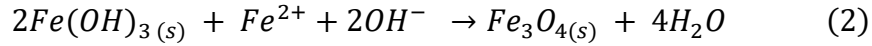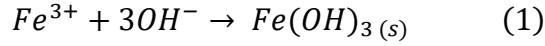
Experimentally, Baumgartner et al.,[52] through the very slow addition of iron precursors to an alkaline solution at a constant pH, demonstrated that magnetite coprecipitation is formed through a primary-particle aggregation mechanism. The process involved the formation of an unstable ferrihydrite-like hydrogel precursor phase, that by interaction with Fe^{2+} ions lead to the formation of amorphous primary particles (~2 nm). Then these primary particles aggregated to form a denser spheroidal NPs (~5–15 nm), that by coalescence fused to form bigger crystalline magnetite.

The mechanisms involved redissolution, recrystallization, coalescence and dehydration mechanisms, making it possible to obtain magnetite single crystals up to 60 nm. Nevertheless, the obtained product often results polydisperse due to the inability to limit the nucleation of new NPs at different stages.[34]

To reduced polydispersity, the employ of different macromolecular additives such as magnetosomes proteins (i.e., Mms6, MamC, MmsF),[53–55] polyarginine,[48] polypeptides that containing negatively charged molecules, as aspartic and glutamic acid,[56] polycations,[57] lysine,[58] and templates (i.e., gels, membranes), has been shown to decrease the NP size and distribution, as well as modify their magnetic properties.[33,40,52,59]

1.3.2.1.3 Partial Oxidation - White Rust Transformation

The partial oxidation method was described for first time by Sugimoto and Matijevic in 1979, for the obtention of SD magnetite from 20–200 nm.[60] In this procedure, a ferrous (Fe^{2+}) precursor is precipitated in an strong alkaline media to form ferrous hydroxide $Fe(OH)_2$ or white-rust precursor in a molar ratio Fe^{2+}:OH ≈ 1:2. This procedure is carried out in the presence of a mild oxidizing agent, typically NO_3^- or O_2 flow to promote the slow and partial oxidation of Fe^{2+}, as denoted by the following equations:

$$Fe^{2+} + 2OH^- \rightarrow Fe(OH)_{2\ (S)} \qquad (1)$$

$$3Fe(OH)_{2\ (S)} + NO_3^- \rightarrow Fe_3O_{4(s)} + NO_2^- + 3H_2O \qquad (2)$$
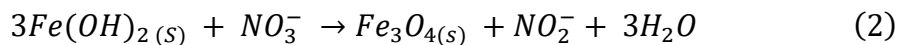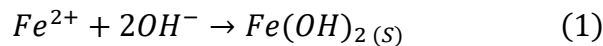
Similarly, this mechanism involved a low soluble intermediate precursor, the white rust ($Kps = 7.1 \times 10^{-16}$).[61] High temperatures (~90°C) favored the redissolution or release of Fe^{2+} to the media that is slowly oxidized to Fe^{3+}, which promotes the reprecipitation and

recrystallization with the remaining Fe^{2+} precursor, yielding magnetite NPs with adjustable morphology and magnetic properties.[60,62,63]

Similar to the ferrihydrite, this mechanism involved a redissolution/reprecipitation process, but here the intermediate phase is the same Fe^{3+} source. In this case thoroughly adjustment of reactant concentrations (oxidant concentration or flow) and synthesis conditions (time, temperature and undisturbed systems) are necessary to control reaction kinetics and achieve the desired NP size.[62,64] Mirabello et al.,[58] demonstrated that crystallization of primary (~2 nm) particles assembled colloidally, that growth via the oriented attachment of crystalline building blocks to form higher magnetite crystals. This study showed a merge between the colloidal and crystallization theory in magnetite formation.

1.4 Applications of magnetic IONPs

Magnetic IONPs have held significant importance in the progression of nanotechnology, covering a wide range of applications, making them useful across multiple fields including catalysis, analytical chemistry, biosensing, nanomedicine, energy, engineering, data storage, and environmental remediation.[45]

The design of these particles, –particularly with respect to their size, shape, composition, and core-shell structure– plays a crucial role in optimizing their physico-chemical properties and application into an specific field.[19] Size is the most critical factor for bare IONPs, because their magnetic properties depend on their size, as well as the superparamagnetic (SPM) or ferrimagnetic (FM) behavior exhibited by IONPs, are particularly notable.[19] SPM IONPs are often favored for biomedical and biological applications owing their versatility, high biocompatibility and low toxicity.[20] These nanoparticles are typically coated with inorganic or organic molecules to enhance biocompatibility and stability in physiological fluids, or to provide a modified surface for further functionalization or coupling. However, the choice of the coating can influence the magnetic properties of the NP core. For instance, non-magnetic coatings can create a surface-disordered spin layer which reduces the saturation magnetization (M_S) of IONPs.[19]

Applications of IONPs are widespread, but mainly focus on two fields: industrial applications as catalysts,[29,31,65] and clinical applications.[20,32,66] For instance, IONPs effectively remove contaminants from water, contributing to cleaner water sources;[17,67,68]

They are also employed in cleaning up oil spills and removal of environmental pollutants; they act as catalysts in chemical reactions, speeding up processes and enhancing efficiency.[69] On the other hand, can be applied to enhance MRI scan contrast helping in more accurate medical diagnoses; delivering medication precisely to target specific cells; and to heat and destroy cancer cells selectively, providing targeted treatment options.[20,70] This section provides a brief overview of two relevant applications where the synthesized magnetic IONPs were applied.

1.4.1 Catalytic Applications

Catalysts are crucial in industry, enabling efficient chemical processes. A catalyst, by definition, is a substance that accelerates a chemical reaction without being consumed in the process, a property known as catalytic activity.[71] In reactions yielding multiple products, a catalyst can direct the reaction towards producing a specific product, demonstrating catalytic selectivity. Nanocatalysts, are a form of heterogeneous catalysts, that significantly facilitate reactions at their extensive surface and active sites.[71] Size effects also govern their catalytic activity, and as the nanocatalysts particle size is reduced they exhibit a higher specific surface area maximizing the number of active sites and minimizing the "unused core" in a bulk catalyst (Figure 1-6).[72] Additionally, this size reduction is often accompanied by an increase in surface defects (i.e., crystal edges, boundaries, and faces) that further enhancing catalytic efficiency. [73]
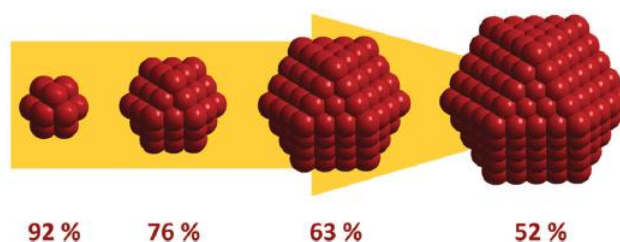
Figure 1-6. Scheme of the decrease of surface-to-volume ratio and percentage of atoms at the NP surface. Reproduced from [72].

Nanocatalysts are in the boundary between homogeneous and heterogeneous catalysts, offering advantages from both categories, in terms of activity, stability, and reusability.[74] In addition, they offer effects from structural and quantum size and electronic properties owing to nanoscale confinement, which enhances their performance and versatility in various chemical reactions.[73] Advances in the development of new nanocatalysts consist of the employ of abundant and inexpensive materials (i.e., iron), and the optimization of

proven existing catalysts. Research relies on surface techniques at the atomic scale, aiming to produce more stable surface active sites, by controlling the size, shape, chemical composition of nanocatalysts or by combining different properties in a controlled manner.[71] [73] The efficacy of a catalyst is heavily influenced by the availability and arrangement of its active sites on the surface. Additionally, nanocatalysts must exhibit high stability across various conditions, such as temperature, pH, and solvent environment. Moreover, nanocatalysts can become less effective due to different mechanisms, such as surface aggregation, sintering, phase transformations, and leaching ions.[73]

Magnetic IONPs exhibit a wide variety of morphologies, including nanospheres, nanoclusters, and nanofibers.[69,75,76] In terms of composition, they can be hybrid NPs, composites, or alloys, among others, and most of them are considered eco-friendly and easy to prepared.[73,77,78] IONPs catalyst have been used for the degradation of organic compounds as dyes, pesticides, and pharmaceutical products that often possess a complex aromatic structure hardly biodegradable causing adverse health effects.[78] Regarding its mechanisms IONPs participated in catalytic oxidation, photocatalysis, CO_2 conversion, water splitting, hydrogenation/dehydrogenation reactions, Fenton and photo-Fenton reaction, electrocatalysis, and organic reactions as epoxidation, C-C bonding, etherification, and alkylation.[78]

Magnetic IONPs serve as a dispersible magnetic catalyst, as well as platform to anchor other catalytic nanostructures, which is easy recyclable due its magnetism. As a platform, it is usually covering with SiO_2 shell to protect it to oxidation.[31] As catalyst, can be assembled to carbon nanostructures as graphene (G) o graphene oxide (GO), to further increase their catalytic surface area and as a platform to retain the contaminant by hydrophobic or hydrophilic interactions, while the magnetic part catalyzes their oxidation.[79]

1.4.1.1   Environmental remediation – Fenton reaction

Nowadays, the presence of chemical pollutants in water sources are one of the major society concerns.[17] Fenton reaction is a most used oxidation process that involves the intermediation of highly reactive species in the wastewater treatment. Reactive oxygen species (ROS) are molecules that contain an unpaired electron, make them highly reactive such as hydroxyl (HO·), superoxide (O_2^-·), and hydroperoxyl (HO_2·) radicals. Hydroxyl radicals are the second most powerful oxidizing species (E° 2.8V) after fluorine (E° 3.03V)

in aqueous medium, and it can degrade or mineralize most organic substrates in advanced oxidation processes (AOP). [80]

Original Fenton reaction is a homogeneous catalytic process which employs iron (Fe^{2+}/Fe^{3+}) and H_2O_2 (mixture called as Fenton reagent) to form ROS species, as denoted by the following reactions:

$$Fe^{2+} + H_2O_2 + H^+ \rightarrow Fe^{3+} + HO \cdot + H_2O \qquad k = 76 \ M^{-1}s^{-1} \ (Eq.1)$$

$$Fe^{3+} + H_2O_2 \rightarrow Fe^{2+} + HO_2 \cdot + H^+ \qquad k = 0.02 \ M^{-1}s^{-1} \ (Eq.2)$$

$$Fe^{2+} + HO_2 \cdot \rightarrow Fe^{3+} + HO_2^- \cdot \qquad k = 1.3 \times 10^6 \ M^{-1}s^{-1} \ (Eq.3)$$

$$Fe^{3+} + HO_2 \cdot \rightarrow Fe^{2+} + O_2 + H^+ \qquad k = 1.2 \times 10^6 \ M^{-1}s^{-1} \ (Eq.4)$$

$$H_2O_2 + HO \cdot \rightarrow HO_2 \cdot + H_2O \qquad k = 2.7x10^7 \ M^{-1}s^{-1} \ (Eq.5)$$
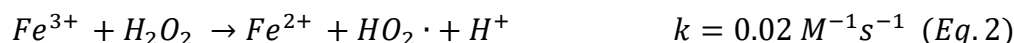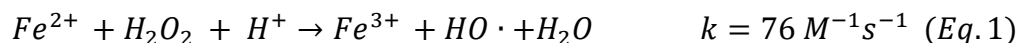
In the Fenton reaction Fe is considered as a catalyst. The reaction starts with the Fe^{2+} is oxidized to ferric ion Fe^{3+} to form $HO\cdot$. Both Fe^{2+} and Fe^{3+} are catalytic and during the process the Fe^{3+} is reduced back to Fe^{2+}, and vice-versa. Their success lies in their efficient redox cycling, environmentally friendly approach without producing toxic products, low-cost-reagent, and RT reaction conditions. However, the Fenton reaction presents some drawbacks when implementing in water treatment. First, the reaction works at acidic conditions, with maximum efficiency at pH 2.8–3.0. At pH higher than 4.0, the reaction terminates due to the Fe^{3+} precipitation. Second, generally high amount of Fenton reagent is required, and working as homogeneous catalyst require further treatment by precipitation to be recovery from the sludge.[74] To overcome that, the use heterogeneous Fenton catalyst can improve the reaction efficiency by increasing $HO\cdot$ generation and Fe redox recycling.

The use of magnetic IONPs as Fenton heterogeneous catalysts has proven effective for various inorganic and organic pollutants.[67,68] This process benefits from the high-surface to volume ratio, which greatly promote $HO\cdot$ generation to degrade these compounds, with the advantages to have excellent sorption capacity, ease magnetic separation, and be an environmentally friendly and cost-effective nanomaterial.[26,32] Magnetite NPs are ideal for these application since they have Fe^{2+} ions in its surface. IONPs can further modifying its catalytic properties by use of a light source, known as photo Fenton reaction, or by their modification with other materials, such as porous materials as SiO_2 to extend it life, or with other catalytic elements like cerium, due to their ease of redox cycle Ce^{3+}/Ce^{4+}.

Some studies have reported the absorption and catalysts of organic pollutants by cerium-modified IONPs, displaying advantages such as enhanced catalytic activity.

Aashima et al., employed Ce-doped Fe_3O_4 NPs for the degradation of 30 ppm of Reactive Black 5 (RB5) azo dye with an efficiency of 87 %, at pH 3 in 90 min. Additionally, the material demonstrated multianalyte capability to remove other azo dyes (methylene orange (MO), alizarin red 5, phenol red, and orange G).[81] Qi et al.[82] utilized Ce-doped Fe_3O_4 NPs for antimony (Sb^{3+} and Sb^{5+}) removal from water at neutral pH. In this study, the Ce-doped IONPs doubled the absorption capacity compared with the non-doped NPs. In another study, Xu et al.,[83] synthesized a Fe_3O_4/CeO_2 composite as a Fenton heterogeneous catalyst for the degradation of 4-chlorophenol, demonstrating high potential for the degradation of organic pollutants with an efficiency of 79.2% at pH 3 and six reusable cycles.

1.4.1.2   Bio-catalysis applications

Currently, the application of IONPs in cancer treatment is very promising. IONPs can be delivered into the tumor to promote in situ apoptosis by increasing ROS in the tumor microenvironment via Fenton like reactions.[78] In addition, Fe_3O_4 NPs possess intrinsic enzyme-mimetic activities such as peroxidase (POD), and catalase (CAT) enzymes, indicating their potential for biomedical treatment.[84,85] To date, iron oxide nanozymes are the most stablished due to their stability, low toxicity, adjustable catalytic activity and excellent cost-effectiveness.[86] Cancer treatment strategies are based on the combination of synergistic effects by employing bimodal particles, or by enhanced Fenton reaction with magnetothermal or photothermal therapies. Some examples will be briefly described below and the characteristics of the nanozymes will be described in more detail in Chapter 4.

Bimodal NPs are also promised in cancer treatment. For instance, a composite of Fe_3O_4 core and Au NPs embedded in mesoporous silicon can specifically target receptors using hyaluronic acid to specific tumor cells. In this study, Au NPs catalyzed the production of H_2O_2 by glucose, which was then catalyzed by Fe_3O_4 NPs to produce HO· in the tumor microenvironment (Figure 1-7). This composite uses a nanozyme treatment strategy, self-activating cascade ROS reactions, leading to apoptosis in 53% of cancer cells without affecting healthy cells.[87]

Multifunctional platforms combined Fe_3O_4 NPs Fenton catalysts with polypyrrole (PPy) photothermal therapy as therapeutic cancer treatments.[88] The multifunctional nanomaterial reaches the tumor using an external magnetic field. Thereafter, near-infrared light was irradiated and absorbed by the PPy coating to ablate the tumor cells and promote

the release of Fe^{2+}/Fe^{3+} from the NPs to enhance the Fenton reaction, thereby inducing apoptosis of the tumor cells.
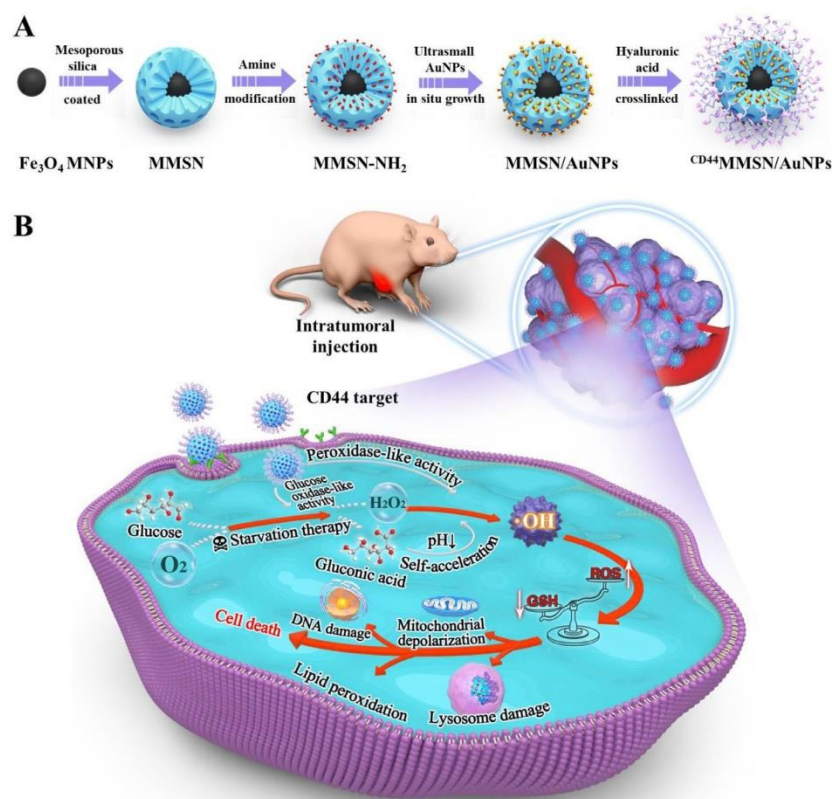
Figure 1-7. A) Schematic illustration of synthetic process for CD44 MMSN/AuNPs nanozymes, and (B) the serial therapeutic mechanism of NPs with •OH generation for hepatocellular carcinoma therapy. Reprinted from [87].

Ce-doped IONPs have been also tested mimicking enzymatic activity, combined with the thermally enhanced Fenton rection, and magnetic recovery of IONPs, leading to their application for non-invasive cancer treatments,[78] magnetic hyperthermia,[89] glucose detection,[90] peroxidase activity,[91] and ROS scanvenging.[92]

For instance, CeO_2 decorated γ-Fe_2O_3 NPs were tested for ROS scavenging using a DPPH (2,2-diphenyl-1-picrylhydrazyl) assay and the antioxidant activity increased from 13% to 78% in comparison with bare γ-Fe_2O_3 NPs. Moreover, the NPs were tested in-vivo in rats with hereditary hypertriglyceridemia (HHTg), which effectively scavenged radicals and decreased oxidative stress.[93] Other study employed Fe_3O_4/CeO_2 core-shell NPs as a contrast agent for MRI and ROS scavenging. The in vitro tests exhibited high cell uptake, low toxicity, strong MRI response, and ROS-scavenging ability, which are useful for monitoring and treating inflammatory diseases.[94]

1.4.2 Magnetic Hyperthermia

Hyperthermia has emerged as an alternative for cancer treatment, either independently or in combination with conventional treatments such as chemotherapy and radiotherapy. Hyperthermia refers to a state in which body temperature exceeds the typical range of 37.5–38.3°C, as a natural defense mechanism for fighting infections. Hyperthermia treatment consists of elevating the temperature to the range of 41–46°C, which effectively helps to destroy or induce harmful effects on cancer cells at the cellular and tissue levels. Above 46–56°C, this causes thermoablation.[70]

Magnetic hyperthermia (MH) employs magnetic nanoparticles (MNPs) to generate localized heat as accurately as possible to the tumor tissue/cell, to reduce negative side effects and make the tumor cells more vulnerable to specific treatments.[70] The magnetic material, dissipates heat by applying an external alternating current (AC) magnetic field (AMF).

To date, IONPs have been the most studied and used NPs in biomedical applications, being some approved by the Food and Drug Agency (FDA) as contrast agents and for magnetic hyperthermia.[95] Magnetic IONPs are particularly beneficial for hyperthermia, owing to their biocompatibility and good magnetic properties. They offer several benefits on their nanoscale size, allowing for intravenous injection via the bloodstream to the target tissues. Furthermore, targeted therapy can be achieved through the surface modification of IONPs with recognition molecules or drugs. In addition, their tunable magnetic responses allow them to be controlled by external magnetic fields, integrating functionalities such as heating, imaging, guiding, and drug delivery within the same IONPs.[70]

The amount of heat produced by the MNPs or thermal losses is approximately equal to the hysteresis loop area during each AMF cycle.[96] The magnetic heating efficiency is assessed through calorimetric measurements, which determine the specific absorption rate (SAR) or specific loss power (SLP).[70] The SAR value indicates the rate at which energy is absorbed per unit mass of NP when exposed to an oscillating magnetic field, given by:[70]

$$SAR\ (W/g)\ =\ \frac{C_d m_d}{m_{Fe}} \cdot \frac{dT}{dt}$$

Where, C_d is the specific heat capacity of the dispersion medium per unit volume ($Cd_{water} = 4.2/g\ °C$ at 25°C), m_{Fe} is the mass concentration of the magnetic metal in the solution (Fe amount in g/L), and dT/dt is the initial slope of the temperature change versus

time.[97] Thus, temperature versus time curves of a solution containing magnetic NPs exposed to an AMF (at a given amplitude (H) and frequency (f)) provides the SAR value.

The heating efficiency of magnetic hyperthermia depends on the size, shape, and surface properties of the IONPs.[19] In this application, NP size is a crucial parameter because the generation and absorption of heat arises from NP relaxation effects by Neel or Brownian relaxation processes or by hysteresis losses.[96] Single domain NPs, either ferromagnetic or superparamagnetic NPs, within the AMF their magnetic moments or the NP itself rotate, and when they relax they return to their original magnetic moment orientation (known as Neel relaxation time (t_N), and Brownian relaxation time (t_B)) dissipating heat (Figure 1-8).[19]
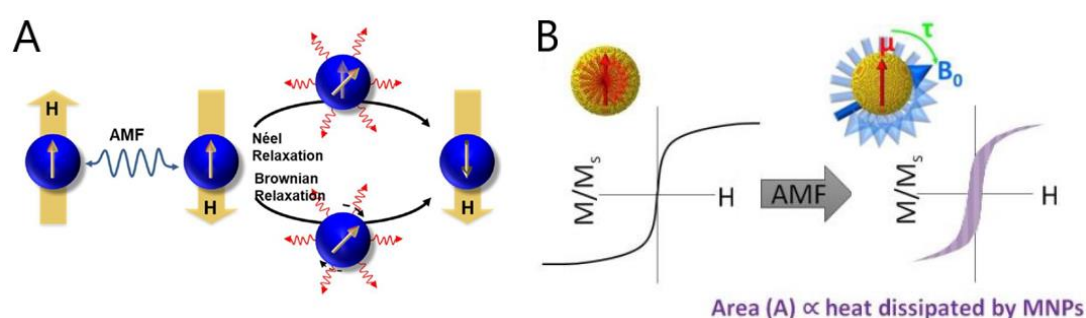
Figure 1-8. Representation of the (A) Néel and Brownian relaxation mechanisms and (B) heat release by SPM NPs under of an alternating magnetic field (AMF) showing the hysteresis losses, where the larger the area of the hysteresis loop, the higher the heat dissipated. Reproduced from (A) [96] and (B) [98].

For safe biomedical application of magnetic hyperthermia the $H \times f$ product for AMF should be below $< 5 \times 10^9$ A/m·s.[99] Regarding the NPs, the SAR value increases as the size increases, reaching a maximum value at a specific size.[96] Moreover, the SAR value is proportional to M_s and the magnetocrystalline anisotropy constant (K) but inversely proportional to the NPs size distribution. Therefore, monodisperse magnetic NPs with high M_s values are preferred for effective magnetic losses.[96] In a study, Hergt et al.,[99] indicate that higher SAR values of magnetic IONPs might be achieved in the transition size range from the SPM to FM state, approximately ~20 nm.

On the other hand, SAR values also depend on the AMF parameters, amplitude (H) and frequency (f), applied during the measurement. Although, superparamagnetic NPs are approved for medical trials, their SAR value usually are low, and usually higher NPs amount and increasing H and f are necessary to increase SAR value, that sometimes surpasses the safety threshold.[70] Therefore, synthesizing magnetic IONPs with optimal size and magnetic properties, sharp size distribution, and stability in aqueous solutions remains

a significant challenge to develop the most effective NPs hold the promise of making magnetic hyperthermia even more effective and safer.

Alternatively, magnetic hyperthermia (MH) can be promisingly combined with other cancer treatments as radiotherapy, chemotherapy (known as a thermo-chemo-sensitization), photothermal therapy, and immunotherapy, which improves the cancer treatment and reduce the side effects. In addition, it was demonstrated that intracellular ROS production increases during hyperthermia treatment,[100] and combination with photodynamic therapy could increase the ROS production, reducing the concentration of both photosensitizer and IONPs to be used.[98] For instance, hollow magnetite monocrystals were applied MH to produce heat in the tumor tissue. This study exhibited excellent magnetothermal conversion efficiency with a SAR value of 722 W/g, attributed to the high-quality crystals and high mimicking peroxidase-like activity for the production of HO· via Fenton reaction, inducing cell apoptosis and reducing the expression of heat shock protein (HSP). Thus, *in-situ* rising temperature resulted from MH facilitates the chemo-dynamic therapy (CDT) achieving a synergistic effect.[100]

1.5   Thesis Aims and Outline

The aim of this doctoral thesis is to provide a framework for the design, synthesis, size control, and characterization of magnetic iron oxide nanoparticles (IONPs) produced in aqueous media.

- Within this framework, the main objective is to develop a synthetic protocol to produce size controlled and low polydispersity IONPs, by aqueous co-precipitation. For this purpose, the addition of ions and molecules will be used to achieve kinetic control over the reaction.

- To achieve the complete characterization of the physicochemical properties of all the synthesized materials.

- To investigate the role and possible mechanism of the introduction of lanthanides cations and molecules in the synthesis method, and to extend this protocol to other nanoparticle syntheses.

- To define the possible applicability of the most interesting synthesized nanomaterials, and to study their structure-activity relationships, such as catalytic activity and magnetic hyperthermia, to be used for these potential biomedical applications.

This thesis is divided in six chapters and their contents are summarized below:

- **Chapter 1** presents a brief introduction to nanomaterials and aspects related to their synthesis, physicochemical properties and applications. The aim of this chapter is to provide an overview of current synthesis directions and challenges.

- **Chapter 2** presents the Massart´s co-precipitation method and the effect of base addition and its rate, as well as the effect of the presence of trisodium citrate ions in the synthesis. The main objective is to investigate and correlate the influence of the mentioned parameters on the size, shape and physicochemical properties of the obtained magnetic iron oxide NPs.

- **Chapter 3** presents the synthesis of size-controlled magnetic iron oxide NPs in the presence of cerium cations and citrate ions by the co-precipitation method. It presents the experimental conditions, and complete characterization of the resulting NPs. This chapter is also addressed to present the effects of cerium and sodium citrate ions on the size and properties of the IONPs, and a possible reaction

mechanism, deducted in parallel, by the use of other lanthanide and metal cations, and phase transformation experiments.

- **Chapter 4** presents the application of the synthesized NPs in two potential biomedical applications areas. This chapter provides a study of the structure-activity relationships by comparing the peroxidase-mimicking activity of the synthesized IONPs, and by evaluating their performance in magnetic hyperthermia experiments.

- **Chapter 5** presents a summary of the main conclusions and experimental achievements of this work. Based on this work some perspectives are also presented.

- Finaly in **Chapter 6** is found the characterization techniques and experimental setup for the experiments. **Appendix A and B** highlight the theoretical and fundamental aspects about the magnetic properties at the nanoscale, iron speciation in water, and Pourbaix diagrams.

1.6 References

(1) Bayda, S.; Adeel, M.; Tuccinardi, T.; Cordani, M.; Rizzolio, F. The History of Nanoscience and Nanotechnology: From Chemical-Physical Applications to Nanomedicine. *Molecules* **2020**, *25* (1), 1–15. https://doi.org/10.3390/molecules25010112.

(2) Turkevich, J.; Kim, G. Palladium: Preparation and Catalytic Properties of Particles of Uniform Size. *Science (80-.).* **1970**, *169* (3948), 873–879. https://doi.org/10.1126/science.169.3948.873.

(3) Times, N. Y. *The Firts Nanoctechnologists*. Feb 21, 2005. https://archive.nytimes.com/www.nytimes.com/imagepages/2005/02/21/science/20050222 _NANO1_GRAPHIC.html.

(4) Papell, S. . Low Viscosity Magnetic Fluid Obtained by the Colloidal Suspension of Magentic Particles. 3215572A.

(5) Massart, R. Preparation of Aqueous Magnetic Liquids in Alkaline and Acidic Media. *IEEE Trans. Magn.* **1981**, *17* (2), 1247–1248. https://doi.org/10.1109/TMAG.1981.1061188.

(6) Bee, A.; Massart, R.; Neveu, S. Synthesis of Very Fine Maghemite Particles. *J. Magn. Magn. Mater.* **1995**, *149* (1–2), 6–9. https://doi.org/10.1016/0304-8853(95)00317-7.

(7) Urso, M.; Ussia, M.; Pumera, M. Smart Micro- and Nanorobots for Water Purification. *Nat. Rev. Bioeng.* **2023**, *1* (4), 236–251. https://doi.org/10.1038/s44222-023-00025-9.

(8) Giri, G.; Maddahi, Y.; Zareinia, K. A Brief Review on Challenges in Design and Development of Nanorobots for Medical Applications. *Appl. Sci.* **2021**, *11* (21). https://doi.org/10.3390/app112110385.

(9) Zhou, H.; Mayorga-Martinez, C. C.; Pané, S.; Zhang, L.; Pumera, M. Magnetically Driven Micro and Nanorobots. *Chem. Rev.* **2021**, *121* (8), 4999–5041. https://doi.org/10.1021/acs.chemrev.0c01234.

(10) Sun, L.; Liu, H.; Ye, Y.; Lei, Y.; Islam, R.; Tan, S.; Tong, R.; Miao, Y. B.; Cai, L. Smart Nanoparticles for Cancer Therapy. *Signal Transduct. Target. Ther.* **2023**, *8* (1). https://doi.org/10.1038/s41392-023-01642-x.

(11) Cohen-Karni, T.; Langer, R.; Kohane, D. S. The Smartest Materials: The Future of Nanoelectronics in Medicine. *ACS Nano* **2012**, *6* (8), 6541–6545. https://doi.org/10.1021/nn302915s.

(12) Rahimi-Iman, A. Advances in Functional Nanomaterials Science. *Ann. Phys.* **2020**, *532* (9), 1–23. https://doi.org/10.1002/andp.202000015.

(13) The Nobel Prize. *No Title*. https://www.nobelprize.org/prizes/chemistry/.

(14) Pokrajac, L.; Abbas, A.; Chrzanowski, W.; Dias, G. M.; Eggleton, B. J.; Maguire, S.; Maine, E.; Malloy, T.; Nathwani, J.; Nazar, L.; Sips, A.; Sone, J.; van den Berg, A.; Weiss, P. S.; Mitra, S. Nanotechnology for a Sustainable Future: Addressing Global Challenges with the International Network4Sustainable Nanotechnology. *ACS Nano* **2021**, *15* (12), 18608–18623. https://doi.org/10.1021/acsnano.1c10919.

(15) Altammar, K. A. A Review on Nanoparticles: Characteristics, Synthesis, Applications, and Challenges. *Front. Microbiol.* **2023**, *14* (April), 1–20. https://doi.org/10.3389/fmicb.2023.1155622.

(16) Khan, Y.; Sadia, H.; Ali Shah, S. Z.; Khan, M. N.; Shah, A. A.; Ullah, N.; Ullah, M. F.; Bibi, H.; Bafakeeh, O. T.; Khedher, N. Ben; Eldin, S. M.; Fadhl, B. M.; Khan, M. I. Classification, Synthetic, and Characterization Approaches to Nanoparticles, and Their Applications in Various Fields of Nanotechnology: A Review. *Catalysts* **2022**, *12* (11). https://doi.org/10.3390/catal12111386.

(17) Shukla, S.; Khan, R.; Daverey, A. Synthesis and Characterization of Magnetic Nanoparticles, and Their Applications in Wastewater Treatment: A Review. *Environ. Technol. Innov.* **2021**, *24*, 101924. https://doi.org/10.1016/j.eti.2021.101924.

(18) Batlle, X.; Labarta, A. Finite-Size Effects in Fine Particles: Magnetic and Transport Properties. *J. Phys. D. Appl. Phys.* **2002**, *35* (6). https://doi.org/10.1088/0022-3727/35/6/201.

(19)   Kolhatkar, A. G.; Jamison, A. C.; Litvinov, D.; Willson, R. C.; Lee, T. R. *Tuning the Magnetic Properties of Nanoparticles*; 2013; Vol. 14. https://doi.org/10.3390/ijms140815977.

(20)   Nguyen T. K. Thanh. *Magnetic Nanoparticles: From Fabrication to Clinical Applications*; 2012.

(21)   Lu, A. H.; Salabas, E. L.; Schüth, F. Magnetic Nanoparticles: Synthesis, Protection, Functionalization, and Application. *Angew. Chemie - Int. Ed.* **2007**, *46* (8), 1222–1244. https://doi.org/10.1002/anie.200602866.

(22)   Muro-Cruces, J.; Roca, A. G.; López-Ortega, A.; Fantechi, E.; Del-Pozo-Bueno, D.; Estradé, S.; Peiró, F.; Sepúlveda, B.; Pineider, F.; Sangregorio, C.; Nogues, J. Precise Size Control of the Growth of Fe3O4 Nanocubes over a Wide Size Range Using a Rationally Designed One-Pot Synthesis. *ACS Nano* **2019**. https://doi.org/10.1021/acsnano.9b01281.

(23)   Mohapatra, J.; Liu, J. P. *Rare-Earth-Free Permanent Magnets: The Past and Future*, 1st ed.; Elsevier B.V., 2018; Vol. 27. https://doi.org/10.1016/bs.hmm.2018.08.001.

(24)   Singamaneni, S.; Bliznyuk, V. N.; Binek, C.; Tsymbal, E. Y. Magnetic Nanoparticles: Recent Advances in Synthesis, Self-Assembly and Applications. *J. Mater. Chem.* **2011**, *21* (42), 16819. https://doi.org/10.1039/c1jm11845e.

(25)   Cullity, B. D.; Graham, C. D. *Introduction to Magnetic Materials*; Wiley, 2008; Vol. 11. https://doi.org/10.1002/9780470386323.

(26)   Kudr, J.; Haddad, Y.; Richtera, L.; Heger, Z.; Cernak, M.; Adam, V.; Zitka, O. Magnetic Nanoparticles: From Design and Synthesis to Real World Applications. *Nanomaterials* **2017**, *7* (9). https://doi.org/10.3390/nano7090243.

(27)   Gloag, L.; Mehdipour, M.; Chen, D.; Tilley, R. D.; Gooding, J. J. Advances in the Application of Magnetic Nanoparticles for Sensing. *Adv. Mater.* **2019**, *31* (48), 1–26. https://doi.org/10.1002/adma.201904385.

(28)   Wu, Q.; Jiang, R.; Mu, L.; Xu, S. Fe3O4 Anodes for Lithium Batteries: Production Techniques and General Applications. *Comptes Rendus. Chim.* **2018**, *22* (1), 96–102. https://doi.org/10.1016/j.crci.2018.09.016.

(29)   Hudson, R.; Feng, Y.; Varma, R. S.; Moores, A. Bare Magnetic Nanoparticles: Sustainable Synthesis and Applications in Catalytic Organic Transformations. *Green Chem.* **2014**, *16* (10), 4493–4505. https://doi.org/10.1039/C4GC00418C.

(30)   Du, K.; Zhu, Y.; Xu, H.; Yang, X. Multifunctional Magnetic Nanoparticles: Synthesis Modification and Biomedical Applications. *Prog. Chem.* **2011**, *23* (11), 2287–2298.

(31)   Wu, L.; Mendoza-Garcia, A.; Li, Q.; Sun, S. Organic Phase Syntheses of Magnetic Nanoparticles and Their Applications. *Chem. Rev.* **2016**, *116* (18), 10473–10512. https://doi.org/10.1021/acs.chemrev.5b00687.

(32)   Mohammed, L.; Gomaa, H. G.; Ragab, D.; Zhu, J. Magnetic Nanoparticles for Environmental and Biomedical Applications: A Review. *Particuology* **2017**, *30*, 1–14. https://doi.org/10.1016/j.partic.2016.06.001.

(33)   Cornell, R. M.; U. Schwertmann. *The Iron Oxides: Structure, Properties, Reactions, Occurences and Uses*, Second.; Wiley VCH, Ed.; Weinheim, 2003; Vol. 664.

(34)   Mirabello, G.; Lenders, J. J. M.; Sommerdijk, N. A. J. M. Bioinspired Synthesis of Magnetite Nanoparticles. *Chem. Soc. Rev.* **2016**, *45* (18), 5085–5106. https://doi.org/10.1039/c6cs00432f.

(35)   Wareppam, B.; Kuzmann, E.; Garg, V. K.; Singh, L. H. Mössbauer Spectroscopic Investigations on Iron Oxides and Modified Nanostructures: A Review. *J. Mater. Res.* **2023**, *38* (4), 937–957. https://doi.org/10.1557/s43578-022-00665-4.

(36)   Goss, C. J. Saturation Magnetisation, Coercivity and Lattice Parameter Changes in the System Fe3O4-ΓFe2O3, and Their Relationship to Structure. *Phys. Chem. Miner.* **1988**, *16* (2), 164–171. https://doi.org/10.1007/BF00203200.

(37)   Channei, D.; Phanichphant, S.; Nakaruk, A.; Mofarah, S.; Koshy, P.; Sorrell, C. Aqueous and Surface Chemistries of Photocatalytic Fe-Doped CeO2 Nanoparticles. *Catalysts* **2017**, *7* (12), 45. https://doi.org/10.3390/catal7020045.

(38)   Beverskog, B. Revised Diagrams for Iron At 25-300 ° C. *Science (80-.).* **1996**, *38* (12), 2121–2135.

(39)   Marciello, M.; Connord, V.; Veintemillas-Verdaguer, S.; Vergés, M. A.; Carrey, J.; Respaud, M.; Serna, C. J.; Morales, M. P. Large Scale Production of Biocompatible Magnetite Nanocrystals with High Saturation Magnetization Values through Green Aqueous Synthesis. *J. Mater. Chem. B* **2013**, *1* (43), 5995–6004. https://doi.org/10.1039/c3tb20949k.

(40)   Lenders, J. J. M.; Mirabello, G.; Sommerdijk, N. A. J. M. Bioinspired Magnetite Synthesis via Solid Precursor Phases. *Chem. Sci.* **2016**, *7* (9), 5624–5634. https://doi.org/10.1039/C6SC00523C.

(41)   Iwasaki, T.; Mizutani, N.; Watano, S.; Yanagida, T.; Kawai, T. Size Control of Magnetite Nanoparticles by Organic Solvent-Free Chemical Coprecipitation at Room Temperature. *J. Exp. Nanosci.* **2010**, *5* (3), 251–262. https://doi.org/10.1080/17458080903490731.

(42)   Martínez-Mera, I.; Espinosa-Pesqueira, M. E.; Pérez-Hernández, R.; Arenas-Alatorre, J. Synthesis of Magnetite (Fe3O4) Nanoparticles without Surfactants at Room Temperature. *Mater. Lett.* **2007**, *61* (23–24), 4447–4451. https://doi.org/10.1016/j.matlet.2007.02.018.

(43)   Faiyas, A. P. A.; Vinod, E. M.; Joseph, J.; Ganesan, R.; Pandey, R. K. Dependence of PH and Surfactant Effect in the Synthesis of Magnetite (Fe3O4) Nanoparticles and Its Properties. *J. Magn. Magn. Mater.* **2010**, *322* (4), 400–404. https://doi.org/10.1016/j.jmmm.2009.09.064.

(44)   Mascolo, M. C.; Pei, Y.; Ring, T. A. Room Temperature Co-Precipitation Synthesis of Magnetite Nanoparticles in a Large Ph Window with Different Bases. *Materials (Basel).* **2013**, *6* (12), 5549–5567. https://doi.org/10.3390/ma6125549.

(45)   Ali, A.; Shah, T.; Ullah, R.; Zhou, P.; Guo, M.; Ovais, M.; Tan, Z.; Rui, Y. K. Review on Recent Progress in Magnetic Nanoparticles: Synthesis, Characterization, and Diverse Applications. *Front. Chem.* **2021**, *9* (July), 1–25. https://doi.org/10.3389/fchem.2021.629054.

(46)   Wu, J.; Shi, M.; Feng, F.; Hao, J.; Zhao, D.; Wang, X.; Li, J.; Zhang, W.; Wang, Q.; Ke, Y.; Yan, X.; Lin, Z.; Chai, L. Recent Advances in Magnetite Crystallization: Pathway, Modulation, and Characterization. *Cryst. Growth Des.* **2023**, *23* (8), 6201–6218. https://doi.org/10.1021/acs.cgd.3c00530.

(47)   Michel, F. M.; Ehm, L.; Antao, S. M.; Lee, P. L.; Chupas, P. J.; Liu, G.; Strongin, D. R.; Schoonen, M. A. A.; Phillips, B. L.; Parise, J. B. The Structure of Ferrihydrite, a Nanocrystalline Material. *Science (80-.).* **2007**, *316* (5832), 1726–1729. https://doi.org/10.1126/science.1142525.

(48)   Kuhrts, L.; Macías-Sánchez, E.; Tarakina, N. V.; Hirt, A. M.; Faivre, D. Shaping Magnetite with Poly-l-Arginine and PH: From Small Single Crystals to Large Mesocrystals. *J. Phys. Chem. Lett.* **2019**, *10* (18), 5514–5518. https://doi.org/10.1021/acs.jpclett.9b01771.

(49)   Aeppli, M.; Kaegi, R.; Kretzschmar, R.; Voegelin, A.; Hofstetter, T. B.; Sander, M. Electrochemical Analysis of Changes in Iron Oxide Reducibility during Abiotic Ferrihydrite Transformation into Goethite and Magnetite. *Environ. Sci. Technol.* **2019**, *53* (7), 3568–3578. https://doi.org/10.1021/acs.est.8b07190.

(50)   Kuhrts, L.; Prévost, S.; Chevrier, D. M.; Pekker, P.; Spaeker, O.; Egglseder, M.; Baumgartner, J.; Pósfai, M.; Faivre, D. Wettability of Magnetite Nanoparticles Guides Growth from Stabilized Amorphous Ferrihydrite. *J. Am. Chem. Soc.* **2021**, *143* (29), 10963–10969. https://doi.org/10.1021/jacs.1c02687.

(51)   Raghav, M.; Sáez, A. E.; Ela, W. P. Understanding Abiotic Ferrihydrite Re-Mineralization by Ferrous Ions. *Int. J. Environ. Sci. Technol.* **2015**, *12* (6), 1945–1956. https://doi.org/10.1007/s13762-014-0599-7.

(52)   Baumgartner, J.; Dey, A.; Bomans, P. H. H.; Le Coadou, C.; Fratzl, P.; Sommerdijk, N. A. J. M.; Faivre, D. Nucleation and Growth of Magnetite from Solution. *Nat. Mater.* **2013**, *12* (4), 310–314. https://doi.org/10.1038/nmat3558.

(53)   Prozorov, T.; Mallapragada, S. K.; Narasimhan, B.; Wang, L.; Palo, P.; Nilsen-Hamilton, M.; Williams, T. J.; Bazylinski, D. A.; Prozorov, R.; Canfield, P. C. Protein-Mediated Synthesis of Uniform Superparamagnetic Magnetite Nanocrystals. *Adv. Funct. Mater.* **2007**, *17* (6), 951–957. https://doi.org/10.1002/adfm.200600448.

(54)   Valverde-Tercedor, C.; Montalbán-López, M.; Perez-Gonzalez, T.; Sanchez-Quesada, M.

S.; Prozorov, T.; Pineda-Molina, E.; Fernandez-Vivas, M. A.; Rodriguez-Navarro, A. B.; Trubitsyn, D.; Bazylinski, D. A.; Jimenez-Lopez, C. Size Control of in Vitro Synthesized Magnetite Crystals by the MamC Protein of Magnetococcus Marinus Strain MC-1. *Appl. Microbiol. Biotechnol.* **2015**, *99* (12), 5109–5121. https://doi.org/10.1007/s00253-014-6326-y.

(55)   Baumgartner, J.; Antonietta Carillo, M.; Eckes, K. M.; Werner, P.; Faivre, D. Biomimetic Magnetite Formation: From Biocombinatorial Approaches to Mineralization Effects. *Langmuir* **2014**, *30* (8), 2129–2136. https://doi.org/10.1021/la404290c.

(56)   Lenders, J. J. M.; Zope, H. R.; Yamagishi, A.; Bomans, P. H. H.; Arakaki, A.; Kros, A.; De With, G.; Sommerdijk, N. A. J. M. Bioinspired Magnetite Crystallization Directed by Random Copolypeptides. *Adv. Funct. Mater.* **2015**, *25* (5), 711–719. https://doi.org/10.1002/adfm.201403585.

(57)   Kuhrts, L.; Prévost, S.; Scoppola, E.; Hirt, A. M.; Faivre, D. Biomimetic Approach for Sustainable Magnetite Nanoparticle Synthesis Using Polycations. *Adv. Funct. Mater.* **2024**, *34* (16), 1–9. https://doi.org/10.1002/adfm.202311856.

(58)   Mirabello, G.; Ianiro, A.; Bomans, P. H. H.; Yoda, T.; Arakaki, A.; Friedrich, H.; de With, G.; Sommerdijk, N. A. J. M. Crystallization by Particle Attachment Is a Colloidal Assembly Process. *Nat. Mater.* **2020**, *19* (4), 391–396. https://doi.org/10.1038/s41563-019-0511-4.

(59)   Lenders, J. J. M.; Altan, C. L.; Bomans, P. H. H.; Arakaki, A.; Bucak, S.; De With, G.; Sommerdijk, N. A. J. M. A Bioinspired Coprecipitation Method for the Controlled Synthesis of Magnetite Nanoparticles. *Cryst. Growth Des.* **2014**, *14* (11), 5561–5568. https://doi.org/10.1021/cg500816z.

(60)   Sugimoto, T.; Matijević, E. Formation of Uniform Spherical Magnetite Particles by Crystallization from Ferrous Hydroxide Gels. *J. Colloid Interface Sci.* **1980**, *74* (1), 227–243. https://doi.org/10.1016/0021-9797(80)90187-3.

(61)   Altan, C. L.; Lenders, J. J. M.; Bomans, P. H. H.; de With, G.; Friedrich, H.; Bucak, S.; Sommerdijk, N. A. J. M. Partial Oxidation as a Rational Approach to Kinetic Control in Bioinspired Magnetite Synthesis. *Chem. – A Eur. J.* **2015**, *21* (16), 6150–6156. https://doi.org/10.1002/chem.201405973.

(62)   Vergés, M. A.; Costo, R.; Roca, A. G.; Marco, J. F.; Goya, G. F.; Serna, C. J.; Morales, M. P. Uniform and Water Stable Magnetite Nanoparticles with Diameters around the Monodomain-Multidomain Limit. *J. Phys. D. Appl. Phys.* **2008**, *41* (13). https://doi.org/10.1088/0022-3727/41/13/134003.

(63)   Luengo, Y.; Morales, M. P.; Gutiérrez, L.; Veintemillas-Verdaguer, S. Counterion and Solvent Effects on the Size of Magnetite Nanocrystals Obtained by Oxidative Precipitation. *J. Mater. Chem. C* **2016**, *4* (40), 9482–9488. https://doi.org/10.1039/c6tc03567a.

(64)   Vereda, F.; de Vicente, J.; Hidalgo-Alvarez, R. Oxidation of Ferrous Hydroxides with Nitrate: A Versatile Method for the Preparation of Magnetic Colloidal Particles. *J. Colloid Interface Sci.* **2013**, *392* (1), 50–56. https://doi.org/10.1016/j.jcis.2012.09.064.

(65)   Munoz, M.; de Pedro, Z. M.; Casas, J. A.; Rodriguez, J. J. Preparation of Magnetite-Based Catalysts and Their Application in Heterogeneous Fenton Oxidation - A Review. *Appl. Catal. B Environ.* **2015**, *176–177*, 249–265. https://doi.org/10.1016/j.apcatb.2015.04.003.

(66)   Pankhurst, Q. A.; Connolly, J.; Jones, S. K.; Dobson, J. Applications of Magnetic Nanoparticles in Biomedicine. *J. Phys. D. Appl. Phys.* **2003**, *36* (13), R167–R181. https://doi.org/10.1088/0022-3727/36/13/201.

(67)   Su, C. Environmental Implications and Applications of Engineered Nanoscale Magnetite and Its Hybrid Nanocomposites: A Review of Recent Literature. *J. Hazard. Mater.* **2017**, *322*, 48–84. https://doi.org/10.1016/j.jhazmat.2016.06.060.

(68)   Panda, S. K.; Aggarwal, I.; Kumar, H.; Prasad, L.; Kumar, A.; Sharma, A.; Vo, D. V. N.; Van Thuan, D.; Mishra, V. *Magnetite Nanoparticles as Sorbents for Dye Removal: A Review*; Springer International Publishing, 2021; Vol. 19. https://doi.org/10.1007/s10311-020-01173-9.

(69)   Ashraf, M.; Khan, I.; Usman, M.; Khan, A.; Shah, S. S.; Khan, A. Z.; Saeed, K.; Yaseen, M.; Ehsan, M. F.; Tahir, M. N.; Ullah, N. Hematite and Magnetite Nanostructures for Green and Sustainable Energy Harnessing and Environmental Pollution Control: A Review. *Chem.*

Res. Toxicol. **2020**, *33* (6), 1292–1311. https://doi.org/10.1021/acs.chemrestox.9b00308.

(70) Guardia, P.; Riedinger, A.; Kakwere, H.; Gazeau, F.; Pellegrino, T. Magnetic Nanoparticles for Magnetic Hyperthermia and Controlled Drug Delivery. *Bio- Bioinspired Nanomater.* **2014**, *9783527335*, 139–172. https://doi.org/10.1002/9783527675821.ch06.

(71) Li, Y.; Somorjai, G. A. Nanoscale Advances in Catalysis and Energy Applications. *Nano Lett.* **2010**, *10* (7), 2289–2295. https://doi.org/10.1021/nl101807g.

(72) Sonström, P.; Bäumer, M. Supported Colloidal Nanoparticles in Heterogeneous Gas Phase Catalysis: On the Way to Tailored Catalysts. *Phys. Chem. Chem. Phys.* **2011**, *13* (43), 19270–19284. https://doi.org/10.1039/c1cp22048a.

(73) Prinsen, P.; Luque, R. *Chapter 1: Introduction to Nanocatalysts*; 2019; Vol. 2019-Janua. https://doi.org/10.1039/9781788016292-00001.

(74) Wang, C.; Liu, H.; Sun, Z. Heterogeneous Photo-Fenton Reaction Catalyzed by Nanosized Iron Oxides for Water Treatment. *Int. J. Photoenergy* **2012**, *2012* (1). https://doi.org/10.1155/2012/801694.

(75) Gao, M. R.; Zhang, S. R.; Jiang, J.; Zheng, Y. R.; Tao, D. Q.; Yu, S. H. One-Pot Synthesis of Hierarchical Magnetite Nanochain Assemblies with Complex Building Units and Their Application for Water Treatment. *J. Mater. Chem.* **2011**, *21* (42), 16888–16892. https://doi.org/10.1039/c1jm13517a.

(76) Behera, M.; Kumari, N.; Raza, K.; Singh, R. Fabrication of Glutathione Functionalized Self-Assembled Magnetite Nanochains for Effective Removal of Crystal Violet and Phenol Red Dye from Aqueous Matrix. *Environ. Sci. Pollut. Res.* **2022**, *29* (48), 72260–72278. https://doi.org/10.1007/s11356-022-19520-4.

(77) Escoda-Torroella, M.; Moya, C.; Rodríguez, A. F.; Batlle, X.; Labarta, A. Selective Control over the Morphology and the Oxidation State of Iron Oxide Nanoparticles. *Langmuir* **2021**, *37* (1), 35–45. https://doi.org/10.1021/acs.langmuir.0c02221.

(78) Liu, M.; Ye, Y.; Ye, J.; Gao, T.; Wang, D.; Chen, G.; Song, Z. Recent Advances of Magnetite (Fe3O4)-Based Magnetic Materials in Catalytic Applications. *Magnetochemistry* **2023**, *9* (4). https://doi.org/10.3390/magnetochemistry9040110.

(79) Singh, P.; Sharma, K.; Hasija, V.; Sharma, V.; Sharma, S.; Raizada, P.; Singh, M.; Saini, A. K.; Hosseini-Bandegharaei, A.; Thakur, V. K. Systematic Review on Applicability of Magnetic Iron Oxides–Integrated Photocatalysts for Degradation of Organic Pollutants in Water. *Mater. Today Chem.* **2019**, *14*, 100186. https://doi.org/10.1016/j.mtchem.2019.08.005.

(80) Miklos, D. B.; Remy, C.; Jekel, M.; Linden, K. G.; Drewes, J. E.; Hübner, U. Evaluation of Advanced Oxidation Processes for Water and Wastewater Treatment – A Critical Review. *Water Res.* **2018**, *139*, 118–131. https://doi.org/10.1016/j.watres.2018.03.042.

(81) Aashima; Uppal, S.; Arora, A.; Gautam, S.; Singh, S.; Choudhary, R. J.; Mehta, S. K. Magnetically Retrievable Ce-Doped Fe3O4 Nanoparticles as Scaffolds for the Removal of Azo Dyes. *RSC Adv.* **2019**, *9* (40), 23129–23141. https://doi.org/10.1039/c9ra03252e.

(82) Qi, Z.; Joshi, T. P.; Liu, R.; Liu, H.; Qu, J. Synthesis of Ce(III)-Doped Fe3O4 Magnetic Particles for Efficient Removal of Antimony from Aqueous Solution. *J. Hazard. Mater.* **2017**, *329*, 193–204. https://doi.org/10.1016/j.jhazmat.2017.01.007.

(83) Xu, L.; Wang, J. Magnetic Nanoscaled Fe3O4/CeO2 Composite as an Efficient Fenton-like Heterogeneous Catalyst for Degradation of 4-Chlorophenol. *Environ. Sci. Technol.* **2012**, *46* (18), 10145–10153. https://doi.org/10.1021/es300303f.

(84) Gao, L.; Zhuang, J.; Nie, L.; Zhang, J.; Zhang, Y.; Gu, N.; Wang, T.; Feng, J.; Yang, D.; Perrett, S.; Yan, X. Intrinsic Peroxidase-like Activity of Ferromagnetic Nanoparticles. *Nat. Nanotechnol.* **2007**, *2* (9), 577–583. https://doi.org/10.1038/nnano.2007.260.

(85) Zhang, S.; Ruan, H.; Xin, Q.; Mu, X.; Wang, H.; Zhang, X. D. Modulation of the Biocatalytic Activity and Selectivity of CeO2 Nanozymes via Atomic Doping Engineering. *Nanoscale* **2023**, *15* (9), 4408–4419. https://doi.org/10.1039/d2nr05742e.

(86) Gao, L.; Fan, K.; Yan, X. Iron Oxide Nanozyme: A Multifunctional Enzyme Mimetic for Biomedical Applications. *Theranostics* **2017**, *7* (13), 3207–3227. https://doi.org/10.7150/thno.19738.

(87) Wang, X.; Xiong, T.; Cui, M.; Guan, X.; Yuan, J.; Wang, Z.; Li, R.; Zhang, H.; Duan, S.;

Wei, F. Targeted Self-Activating Au-Fe3O4 Composite Nanocatalyst for Enhanced Precise Hepatocellular Carcinoma Therapy via Dual Nanozyme-Catalyzed Cascade Reactions. *Appl. Mater. Today* **2020**, *21*, 100827. https://doi.org/10.1016/j.apmt.2020.100827.

(88) Wu, H.; Cheng, K.; He, Y.; Li, Z.; Su, H.; Zhang, X.; Sun, Y.; Shi, W.; Ge, D. Fe 3 O 4 - Based Multifunctional Nanospheres for Amplified Magnetic Targeting Photothermal Therapy and Fenton Reaction. *ACS Biomater. Sci. Eng.* **2019**, *5* (2), 1045–1056. https://doi.org/10.1021/acsbiomaterials.8b00468.

(89) Yadel, C.; Michel, A.; Casale, S.; Fresnais, J. Hyperthermia Efficiency of Magnetic Nanoparticles in Dense Aggregates of Cerium Oxide/Iron Oxide Nanoparticles. *Appl. Sci.* **2018**, *8* (8). https://doi.org/10.3390/app8081241.

(90) Huang, F.; Wang, J.; Chen, W.; Wan, Y.; Wang, X.; Cai, N.; Liu, J.; Yu, F. Synergistic Peroxidase-like Activity of CeO2-Coated Hollow Fe3O4 Nanocomposites as an Enzymatic Mimic for Low Detection Limit of Glucose. *J. Taiwan Inst. Chem. Eng.* **2018**, *83*, 40–49. https://doi.org/10.1016/j.jtice.2017.12.011.

(91) Honarasa, F.; Keshtkar, S.; Eskandari, N.; Eghbal, M. Catalytic and Electrocatalytic Activities of Fe3O4/CeO2/C-Dot Nanocomposite. *Chem. Pap.* **2021**, *75* (6), 2371–2378. https://doi.org/10.1007/s11696-020-01443-4.

(92) Sun, Y.; Xu, L.; Liu, X.; Shen, Y.; Zhang, Y.; Gu, N.; Xiong, F. Coronal Relay Reactor Fe3O4@CeO2 for Accelerating ROS Axial Conversion through Enhanced Enzyme-like Effect and Relay Effect. *Chem. Eng. J.* **2022**, *429* (March 2021). https://doi.org/10.1016/j.cej.2021.132303.

(93) Moskvin, M.; Marková, I.; Malínská, H.; Miklánková, D.; Hüttl, M.; Oliyarnyk, O.; Pop-Georgievski, O.; Zhigunov, A.; Petrovský, E.; Horák, D. Cerium Oxide-Decorated γ-Fe2 O3 Nanoparticles: Design, Synthesis and in Vivo Effects on Parameters of Oxidative Stress. *Front. Chem.* **2020**, *8* (August), 1–13. https://doi.org/10.3389/fchem.2020.00682.

(94) Wu, Y.; Yang, Y.; Zhao, W.; Xu, Z. P.; Little, P. J.; Whittaker, A. K.; Zhang, R.; Ta, H. T. Novel Iron Oxide-Cerium Oxide Core-Shell Nanoparticles as a Potential Theranostic Material for ROS Related Inflammatory Diseases. *J. Mater. Chem. B* **2018**, *6* (30), 4937–4951. https://doi.org/10.1039/c8tb00022k.

(95) Kallumadil, M.; Tada, M.; Nakagawa, T.; Abe, M.; Southern, P.; Pankhurst, Q. A. Suitability of Commercial Colloids for Magnetic Hyperthermia. *J. Magn. Magn. Mater.* **2009**, *321* (10), 1509–1513. https://doi.org/10.1016/j.jmmm.2009.02.075.

(96) Liu, X.; Zhang, Y.; Wang, Y.; Zhu, W.; Li, G.; Ma, X.; Zhang, Y.; Chen, S.; Tiwari, S.; Shi, K.; Zhang, S.; Fan, H. M.; Zhao, Y. X.; Liang, X. J. Comprehensive Understanding of Magnetic Hyperthermia for Improving Antitumor Therapeutic Efficacy. *Theranostics* **2020**, *10* (8), 3793–3815. https://doi.org/10.7150/thno.40805.

(97) Sojková, T.; Rizzo, G. M. R.; Di Girolamo, A.; Avugadda, S. K.; Soni, N.; Milbrandt, N. B.; Tsai, Y. H.; Kuběna, I.; Sojka, M.; Silvestri, N.; Samia, A. C.; Gröger, R.; Pellegrino, T. From Core-Shell FeO/Fe3O4 to Magnetite Nanocubes: Enhancing Magnetic Hyperthermia and Imaging Performance by Thermal Annealing. *Chem. Mater.* **2023**, *35* (16), 6201–6219. https://doi.org/10.1021/acs.chemmater.3c00432.

(98) Gavilán, H.; Avugadda, S. K.; Fernández-Cabada, T.; Soni, N.; Cassani, M.; Mai, B. T.; Chantrell, R.; Pellegrino, T. Magnetic Nanoparticles and Clusters for Magnetic Hyperthermia: Optimizing Their Heat Performance and Developing Combinatorial Therapies to Tackle Cancer. *Chem. Soc. Rev.* **2021**, *50* (20), 11614–11667. https://doi.org/10.1039/d1cs00427a.

(99) Hergt, R.; Dutz, S.; Müller, R.; Zeisberger, M. Magnetic Particle Hyperthermia: Nanoparticle Magnetism and Materials Development for Cancer Therapy. *J. Phys. Condens. Matter* **2006**, *18* (38). https://doi.org/10.1088/0953-8984/18/38/S26.

(100) Flanagan, S. W.; Moseley, P. L.; Buettner, G. R. Increased Flux of Free Radicals in Cells Subjected to Hyperthermia: Detection by Electron Paramagnetic Resonance Spin Trapping. *FEBS Lett.* **1998**, *431* (2), 285–286. https://doi.org/10.1016/S0014-5793(98)00779-0.

Chapter 2

Magnetic Iron Oxide Nanoparticles: Exploring the Synthetic Parameters

2.1 Introduction

Magnetic NPs have emerged as a captivating subject of study. Preceding the age of nanotechnology, these particles, once referred to as fine magnetic particles,[1,2] continue to hold significant scientific and technological interests.[3–6] The attention in MNPs derives from their distinct magnetic behavior at the nanoscale, influenced by two key factors: finite-size effects and surface/interface effects.[7]

Superparamagnetic NPs are especially important; Their unique properties, including strong response to an external magnetic field and the absence of residual magnetization upon removal of the field prevents their undesired aggregation, make them ideal in applications such as drug delivery systems and MRI contrast imaging.[8]

Among superparamagnetic (SPM) NPs, magnetic Iron Oxide NPs (IONPs), such as magnetite (Fe_3O_4) and maghemite (γ-Fe_2O_3), have been intensively studied because of their good magnetic properties as well as their low cost, biocompatibility, biodegradability and easy funtionalization.[9,10] At room temperature, for magnetite the SPM behavior is typically below 20 nm size.[7]

Co-precipitation is the most widely applied synthesis method for producing superparamagnetic IONPs (Fe_3O_4 or γ-Fe_2O_3) in aqueous media at room temperature. This method is based on the co-precipitation of a mixture of Fe^{2+} and Fe^{3+} salts into a free-oxygen strongly alkaline aqueous solution. The size, shape, and composition of magnetic IONPs may vary depending on the type of iron precursor used (e.g., chlorides, sulfates, nitrates), type of base (e.g., NaOH, KOH, $(C_2H_5)_4NOH$, etc.), rate addition, iron ratio (Fe^{2+}/Fe^{3+}), pH, ionic strength of the media, reaction temperature, and presence of surfactants or organic agents.[11–16] This procedure is relatively simple and leads to high yields, with the advantage that once the reaction conditions are fixed, the IONPs production is easily reproducible.[7] However, the main drawbacks are the limited control over the particle size and size distribution, as well as the produced IONPs exhibited low defined morphology, poor crystallinity, and modest magnetic properties[17]

The addition of organic molecules and surfactants into co-precipitation synthesis has emerged as a tool for facilitating size tuning and subsequent nanoparticle stabilization and manipulation. The effect of organic additives on magnetite co-precipitation has been reported for several organic compounds as a key for using functionalized IONPs across numerous applications.[2,14–16,18] However, it deserves special mention the use of citrate ions for obtaining very fine magnetite NPs (4–10 nm).[2,19–22] The effects of carboxylate and hydroxy carboxylate ions on the formation of magnetic iron oxides have been extensively studied.[23–25] Citrate ions are attached to iron ions on the NPs surface through coordination bonds formed by one or two carboxylate groups.[24] The negatively charge COO^- interacts strongly on the NPs surface retarding the crystallization of the iron oxides and provides electrostatic stability at pH above 4 at least at low ionic strength.[25,26] In addition, the surface citrate coating is important in biomedical applications to stabilize and prevent the aggregation of IONPs at physiological pH, improving their biocompatibility and further functionalization.

In this chapter, we will focus on the effect of the base and its rate addition, and the effect of trisodium citrate ions on the synthesis of magnetic iron oxide (magnetite/maghemite) nanoparticles (IONPs) by the co-precipitation method at room temperature. The main goal of this study was to investigate and correlate the influence of above-mentioned parameters on the size, shape, and chemical characteristics of the obtained IONPs as a preliminary study for the samples described in the second chapter.

2.2 Experimental

2.2.1 Chemicals

Iron (II) chloride tetrahydrate (FeCl$_2$·4H$_2$O, >99%), Iron (III) chloride anhydrous (FeCl$_3$, >99%), tetramethylammonium hydroxide (TMAOH, 1.0 M in H$_2$O), trisodium citrate (Na$_3$C$_6$H$_5$O$_7$, >99%). All reagents were purchased from Sigma-Aldrich and used as received without further purification. Milli-Q water (18 MΩ cm^{-1}) was used in all the experiments. All glassware was first cleaned with aqua regia and washed with Milli-Q water prior to the experiments.

2.2.2 Synthesis of magnetic Iron Oxide Nanoparticles (IONPs)

Magnetic IONPs were prepared by co-precipitation method at room temperature as described below. All the aqueous solutions in Milli-Q-water were first degassed by sonication (10 min) and then purged with N$_2$ at least 30 min before use.

In a typical reaction, in a glass vessel sealed with a rubber septum, a 92 mL aqueous solution was magnetic stirring and constant N$_2$ bubbling for 30 min. After, freshly prepared solutions of iron (II) chloride (2 mL, 100 mM) and iron (III) chloride (2 mL, 200 mM) (Fe^{2+}: Fe^{3+} (1:2 ratio)) were then added to the previously deoxygenated aqueous solution under vigorous magnetic stirring (800 rpm) and constant N$_2$ bubbling. After, a TMAOH aqueous solution (4 mL, 1 M) at different addition rates (fast addition, and slow addition at: 800 µL/min and 80 µL/min) were added to the reactant mixture. This caused the precipitation of magnetic IONPs, as indicated by a gradual color change of the solution from yellow to black. The resulting mixture was aged for 2 h while stirring under N$_2$ to prevent oxidation.

Thereafter, the magnetic IONPs were collected by centrifugation or magnetic decantation and washed at least three times with deoxygenated water to remove the excess of ions in solution and further redispersed in a TMAOH (10 mM) oxygen-free aqueous solution or in milli-Q-water before sample characterization.

2.2.3 Synthesis of citrate-coated IONPs (SC-IONPs)

SC-IONPs were synthesized following the above-described protocol in the presence of trisodium citrate. Briefly, 92 mL aqueous solution was prepared containing different concentrations of trisodium citrate (SC) (final concentration from 0.5–20 mM) before the addition of the Fe^{2+}/Fe^{3+} aqueous mixture and the TMAOH (4 mL, 1 M) solution, under magnetic stirring and constant N_2 bubbling.

All the samples were synthesized under the same synthetic conditions: room temperature, alkaline titration rate at 800 µL/min, unless otherwise state. After 2 h of reaction, colloidally stabilized magnetic SC-IONPs were magnetically collected and washed a minimum of three times (which was increased to 8 washes as SC concentration increased), before characterization.

2.3   Results and Discussion

2.3.1 Synthesis of Magnetic IONPs

Magnetite synthesis by co-precipitation method has been comprehensively studied for a long time and stands as one of the simplest and most convenient aqueous synthetic routes for the preparation of magnetite at mild reaction conditions (temperature and pressure).[17] Mechanisms of direct and indirect coprecipitation are used in literature. The direct co-precipitation of Fe^{2+} and Fe^{3+} mixed solution in a 1:2 ratio (consistent with magnetite stoichiometry) into strong alkaline media and inert conditions can be described by:

$$Fe^{2+} + 2Fe^{3+} + 8OH^- \rightarrow Fe_3O_{4(s)} + 4H_2O \qquad (Eq.\,1)$$
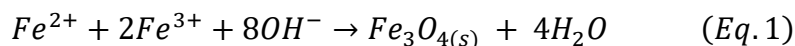
In the direct iron co-precipitation (Eq. 1), the fast formation of iron hexacoordinated aquohydroxo complexes $[Fe(OH)_x(OH_2)_{6-x}]^{(z-x)+}$ into aqueous media, almost instantaneously dehydrated, and simultaneous olation and oxolation process happens leading to magnetite NPs formation without intermediate solid phases.[27,28] Olation refers to the condensation of aquohydroxo complexes, by elimination of a H_2O molecule to form hydroxy bridges. While oxolation refers for oxohydroxo complexes ($[Fe(O)_x(OH)_y]^{(z-2x-y)+}$), where a two-condensation steps lead to H_2O formation as leaving group to form oxo bridges as shown in Figure 2-1.
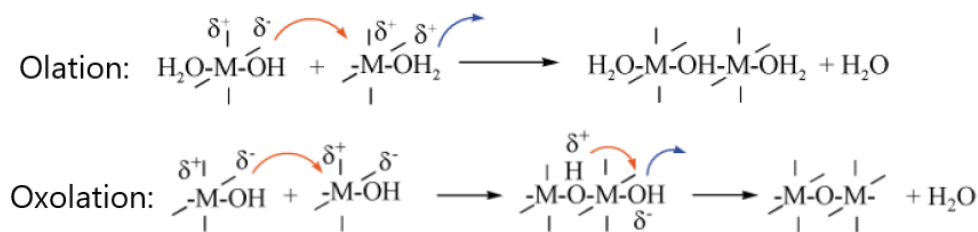
Figure 2-1. Schem of the hydroxylated complexes condensed by olation and oxolation mechanisms. Adapted from[27].

In contrast, indirect co-precipitation, that is the inverse process, in which the base is added to the mixed valent iron, can be described by the following reactions:

$$Fe^{3+} + 3OH^- \rightarrow Fe(OH)_{3\,(s)} \rightarrow FeO(OH)_{(s)} + H_2O \qquad (Eq.\,2)$$

$$Fe^{2+} + 2OH^- \rightarrow Fe(OH)_{2\,(s)} \qquad (Eq.\,3)$$

$$2FeO(OH)_{(s)} + Fe(OH)_{2\,(s)} \rightarrow Fe_3O_{4(s)} + 2H_2O \qquad (Eq.\,4)$$
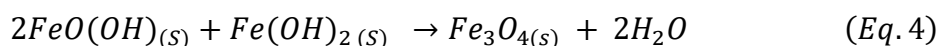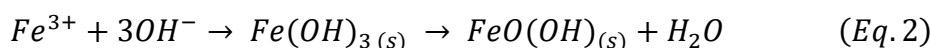
In these reactions, when the base [OH$^-$] is added to the iron mixture implies progressively hydroxylation as increased of pH, then the olation and oxolation of Fe^{2+} and Fe^{3+} ions occurred at different times. Several ferrous and ferric intermediate products (simplified as $[Fe(OH)_x]^{n-x}$ species) could form depending on the reaction conditions, and then precipitate (Eq. 2 and 3). As a result, a solid-state reaction occurs between them to produce magnetite NPs at a basic pH between 8–14 (Eq. 4). The reaction occurs rapidly within few minutes or seconds at room temperature.[28,29] The simplified reaction (Eq. 2–4) is described by the overall equation 1.

The synthesis conditions which favors crystal growth of magnetite by coprecipitation method are not easy to control because of the complex speciation of Fe^{2+} and Fe^{3+} ions in aqueous solution (where different iron-hydroxy phases and aquo-complex can coexist), as well as their respective low solubilities on the pH range (8–14) where Fe$_3$O$_4$ is formed.[30] Table 2-1 summarizes and compared some related studies where was explored the effects of changing some reaction parameters in aqueous co-precipitation method, in similar conditions to our synthesis. Barring a few examples, most of the NPs exhibit sizes < 20 nm and superparamagnetic behavior at room temperature.[8] Note that synthesis that kept Fe^{2+}:Fe^{3+} 1:2 ratio could not grow further 20 nm. The co-precipitation method is highly dependent on the stability of the iron with coexisting anions. Thus, size manipulation by changing the reaction parameters in aqueous media at room temperature resulted in a reduction in crystal size in most cases.[11]

Table 2-1 Effect of variations of the reaction parameters in co-precipitation method on magnetite crystal size.

Ferrous source	Ferric source	Fe^{2+}/Fe^{3+} molar ratio	Additive	Base reagent	T °C	pH	Time (h)	Variation/ comments	Fe_3O_4 NPs size (nm)	Magnetic behavior	Ref
$FeCl_2$	$FeCl_3$	0,5	-	NaOH	25	10.7	3	Base counter cation	9.1	SPM	12
$FeCl_2$	$FeCl_3$	0,5	-	KOH	25	ND	3		7.1	SPM	
$FeCl_2$	$FeCl_3$	0,5	-	$(C_2H_5)_4NOH$	25	ND	3		6.5	SPM	
$FeCl_2$	$FeCl_3$	0,5	-	NaOH	25	10.34	3	pH and base rate addition (Fast (F) or slow (S) at 1mL/min)	11.5 (S)/ 10.2 (F)	SPM	12
$FeCl_2$	$FeCl_3$	0,5	-	NaOH	25	12.08	3		11.0 (S)/ 9.1 (F)	SPM	
$FeCl_2$	$FeCl_3$	0,5	-	NaOH	25	12.60	3		10.7(S)/ 8.2(F)	SPM	
$FeSO_4$	$FeCl_3$	0,5	-	NaOH	25	>12	-	Ferrous source and organic additive $NaC_3H_5O_3$ [1] (BOH addition at 3,0 mL/min)	10	SPM	11
$FeSO_4$	$FeCl_3$	0,5	(1)	NaOH	25	>12	-		11.5	SPM	
$FeCl_2$	$FeCl_3$	0,5	-	NaOH	25	>12	-		9.9	SPM	
$FeCl_2$	$FeCl_3$	0,5	(1)	NaOH	25	>12	-		6.6	SPM	
$Fe(C_3H_5O_3)_2$	$FeCl_3$	0,5	-	NaOH	25	>12	-		4.9	SPM	
$FeSO_4$	$FeCl_3$	0,5	-	NaOH	25	>12	-	Ferrous /ferric ratio (Slow alkaline addition)	10	SPM	11
$FeSO_4$	$FeCl_3$	1,0	-	NaOH	25	>12	-		16.8	SPM	
$FeSO_4$	$FeCl_3$	2,0	-	NaOH	25	>12	-		24.6	FM	
$FeCl_2$	$FeCl_3$	0,5	-	NH_4OH (1:2:10)	25	>12	2 min	Iron/base ratio Fe^{2+}: Fe^{3+}: OH	15–40 (Size dist.)	n.d.	13
$FeCl_2$	$FeCl_3$	0,5	-	NH_4OH (1:2:400)	25	>12	5 min		4–10 (Size dist.)	n.d.	
$FeCl_2$	$FeCl_3$	0,5	0 mM	NH_4OH	25	11	5 min	Addition of mercapto-ethanol [C_2H_6OS]	15.03	SPM	14
$FeCl_2$	$FeCl_3$	0,5	1 mM	NH_4OH	25	11	5 min		9.02	SPM	
$FeCl_2$	$FeCl_3$	0,5	5 mM	NH_4OH	25	11	5 min		8.02	SPM	
$FeCl_2$	$FeCl_3$	0,5	OA, SDS, PVA [2]	NH_4OH	25	11	1	Addition of surfactants	9.4–11.1	SPM	15
$FeCl_2$	$FeCl_3$	0,5	-	NH_4OH	49	10.5	30 min	Base rate addition (80 mL/s to 1mL/s)	6.8–11	SPM	15
$FeCl_2$	$FeCl_3$	0,5		NH_4OH	25	10.1	1	Ferrous /ferric ratio	10	n.d.	31
$FeCl_2$	$FeCl_3$	0,5		NH_4OH	60	11.5	1		7	n.d.	
$FeCl_2$	$FeCl_3$	0,3	-	NaOH	25	9.5	1		14	n.d.	
$FeCl_2$	$FeCl_3$	0,8		NaOH	25	9.5	1		22	n.d.	
$FeCl_2$	$FeCl_3$	0,3		NaOH	25	-	1		10	n.d.	

[1] $NaC_3H_5O_3$: Sodium lactate.
[2] OA: Oleic acid, SDS: sodium dodecyl sulfate, PVA: polyvinyl alcohol.
n.d. = not determined.

Hereinafter, in this thesis in order to grow magnetite NPs and reduce the size distribution, two experimental variables were chosen using indirect co-precipitation, first the choice of a suitable base and its slow and gentle addition was proved, and second citrate presence in order to evaluate the retarding effects in the kinetics of reaction. The observed effects will be explained below.

2.3.2 The role of the base and addition rate in the synthesis of magnetic IONPs

Experimentally, magnetic IONPs were synthesized following Massart's method but instead of using ammonia solution were employed tetramethyl ammonium hydroxide (TMAOH) as a base.[1] TMAOH was chosen due to its bulky TMA$^+$ cations, which in magnetite synthesis have been described as a good peptizing agent and easy to remove when more affinity ligands are present.[1,32] In addition, TMA$^+$ acts as a surface-active agent, as a result smaller and better-stabilized NPs *in-situ* can be obtained, decreasing their aggregation in aqueous solution (in comparison with NaOH), and favoring the redispersion of dry IONPs.[33,34] It has also been reported that in hematite NPs (α-Fe$_2$O$_3$) TMA$^+$ and CTAB together improve crystallinity and decrease particle distribution.[35]

Therefore, to see the effects of the base rate addition in retarding the kinetics steps in magnetite production, three different samples were prepared varying the rate addition of the TMAOH into the previously deoxygenated Fe^{2+}/Fe^{3+} mixture. The first one by the fast addition (one-shot) (F), and two samples by the slow addition rate at 800 µL/min (S) and 80 µL/min (VS), respectively. The three black colloidal dispersions IONPs(F), IONPs(S) and IONPs(VS) were obtained, displaying a negative ζ-pot (> -35 mV) due to OH$^-$ stabilization at final synthesis pH ~12. All the dispersions were visually stable, and aggregates were not observed on TEM/STEM micrographs and after use of an external magnet indicating its superparamagnetic behavior.

In the first co-precipitation procedure, the fast addition of TMAOH solution to the Fe^{2+}/Fe^{3+} mixture, leads to the immediate burst nucleation that rapidly depletes the Fe^{2+} and Fe^{3+} ions in the solution, leading to the obtention of many small magnetic IONPs.[36] Representative HAADF-STEM and HRTEM images of the IONPs(F) sample showed the obtention of nearly-spherical NPs with an average crystal size of 7.2 ± 1.3 nm and a narrow particle distribution as depicted in Figure 2-2.

Instead, IONPs(S) and IONPs(VS) samples prepared by slow TMAOH rate addition, with a duration addition of 4 min and 50 min, respectively, resulted in NPs greater in size, with a mean diameter of 10.1 ± 2.8 nm and 11.3 ± 3.7 nm, respectively. Size distribution analysis showed that as addition rate of the alkaline solution decrease, the NPs size distribution increase, however a more polydisperse product was obtained, as shown the comparison of the three rates addition in Figure 2-3. The size of the IONPs was slightly affected by the addition rate of the alkaline solution to the solution of mixed iron ions,

indicating that fast addition favors nucleation over growth. On contrary, slow addition may have slowed the formation of the nuclei allowing NPs to growth more.[12] However, continuous nucleation of some NPs were also observed, specially at very slow rate.
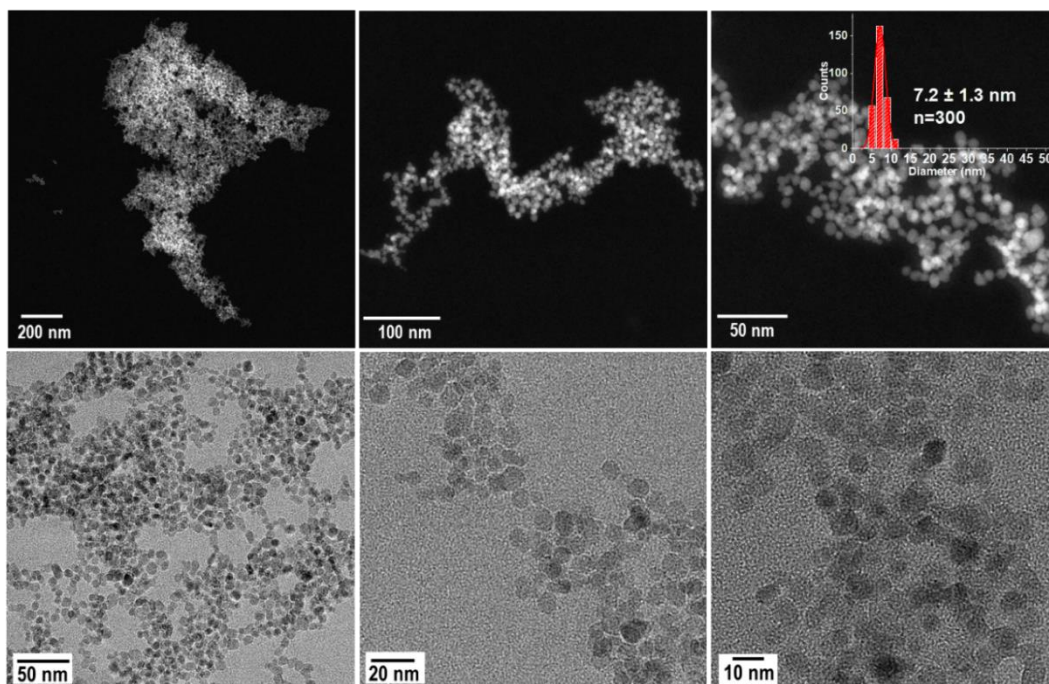
Figure 2-2. Low and high magnification HAADF-STEM and HRTEM images of IONPs synthesized via co-precipitation method by fast addition of the base and particle size distribution (scale bars: 200, 100, 50, 20 and 10 nm).
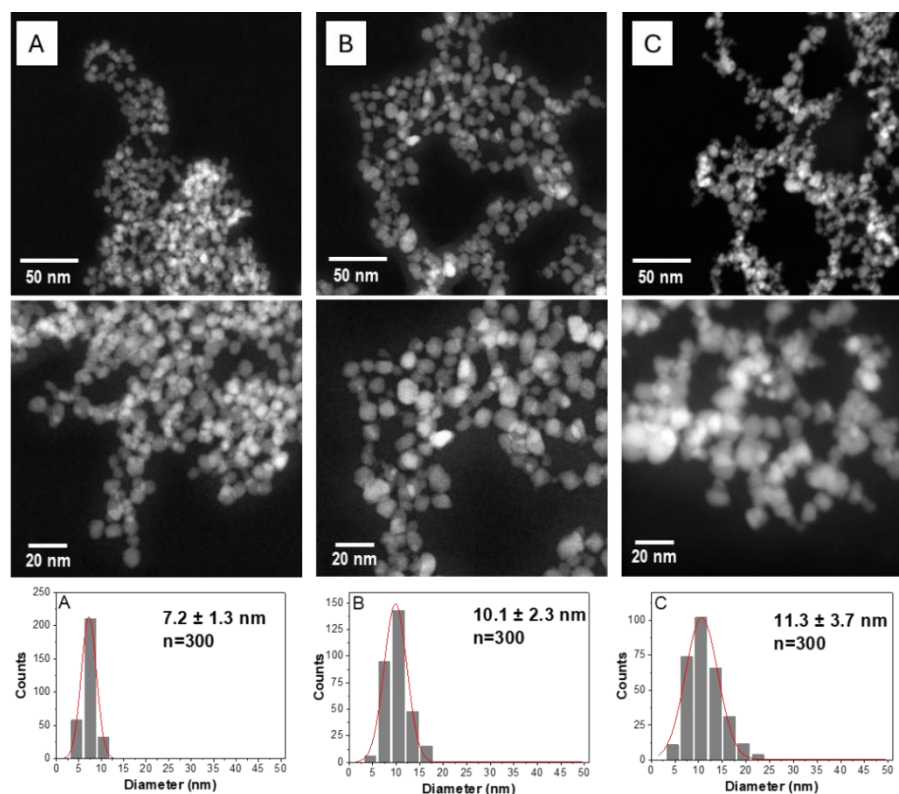
*Figure 2-3. Representative HAADF-STEM images and particle size distribution of IONPs synthesized via co-precipitation method by varying the TMAOH rate addition (**A**) F: fast addition, (**B**) S: slow addition at 800 µL/min, and (**C**) VS: very slow addition at 80 µL/min (scale bars: 50 and 20 nm).*

The crystal structure of the magnetic products was characterized by using powder XRD (Figure 2-4). The XRD spectra of all samples were indexed to the inverse spinel structure of Fe_3O_4 (JPDS: 019-0629) pattern. However, XRD could not unambiguously distinguish between the similarity in the position and intensity of the diffraction peaks of Fe_3O_4 and γ-Fe_2O_3 phases, and the low diffraction of these small crystal sizes (~7–11 nm). In addition, it is reported that magnetite crystals below 200 nm, under oxidizing conditions, tend to transform into maghemite; the transformation process occurs by cation migration at the surface which creates oxygen vacancies. This diffusion is shorter and faster as the crystal size is reduced. At the surface the cations are oxidized with the absorbed oxygen or OH groups. Thus, IONPs composition could be a Fe_3O_4 /γ-Fe_2O_3 solid solution.[29,37]
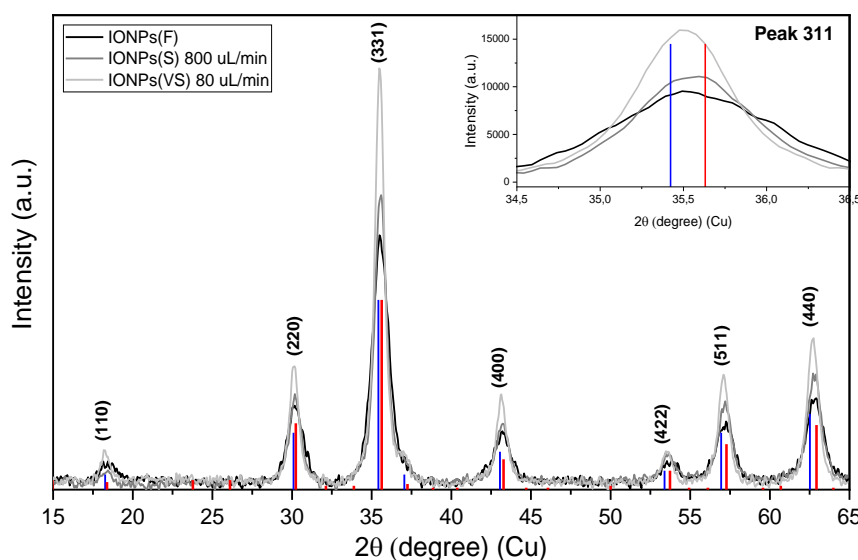
Figure 2-4. Powder XRD diffractograms of IONPs synthesized by co-precipitation method by fast (F), slow (S), and very slow (VS) addition of TMAOH solution (Blue bars: magnetite (JCPDS: 019-0629); Red bars: maghemite (JCPDS:039-1346).

The average crystal size of the samples estimated by using Scherrer's formula and other crystallographic parameters are summarized in Table 2-2.Closeness between the crystal size determined by TEM and XRD indicates the obtention of single crystal IONPs. The calculated lattice parameters for the magnetic products were between the standard lattice parameters of Fe_3O_4 (8.396 Å) and γ-Fe_2O_3 (8.346 Å), and the decrease of microstrain were consistent with the increase of the crystal size caused by the slow addition of the base.

Table 2-2. Effect of fast or slow addition of the TMAOH solution on the synthesized IONPs

Sample	Addition rate (μL/min)	D_{STEM} (nm)	D_{XRD} (nm)	Lattice Parameter (Å)[a]	Strain (ε)	ζ-pot (mV)
IONPs(F)	Fast injection	7.2 ± 1.3	8.3 ± 0.4	8.363	0.0123	-35
IONPs(S)	800	10.1 ± 2.3	10.7 ± 0.6	8.365	0.0093	-42
IONPs(VS)	80	11.3 ± 3.7	13.9 ± 0.9	8.378	0.0069	-43

[a] Reported magnetite lattice parameter: 8.3960 Å (Standard JCPDS: 019-0629).

According to classical theories, solution-based crystallization is governed by two primary stages: nucleation and growth. Nucleation occurs when the solution reaches a critical supersaturation level, leading to the formation of small nuclei.[38] These nuclei then undergo growth through the diffusion of solute ions to the surface, gradually increasing and forming larger crystals. In general, to achieve NPs with a uniform size distribution, it is important to separate the nucleation and growth steps.[38] However, in the iron coprecipitation method the separation of these steps is not easy due to the complex speciation of Fe^{2+} and Fe^{3+} in aqueous solution, and their respective low solubilities (*Kps* > 10^{-17}) on the pH range where magnetite is formed (pH 8–14).[30]

The experiments showed that variation of the base rate addition from fast (F) to slow (S) results in a small change in size from ~7 to 10 nm. However, large base rate addition (at 80 μL/min) led to the production of very polydisperse product, here continuous nucleation was favored because of the low solubility of the product and their fast crystallization. In addition, the influence of coexisting ions (i.e, Cl^- and TMA^+) and their absorption onto Fe_3O_4 surface decreases their surface potential inhibiting Fe_3O_4 growth.[11]

2.3.3 Synthesis of Citrate-coated Iron Oxide Nanoparticles (SC-IONPs) - Citrate Effect

According to the previous section, slow addition (S) of the alkaline solution allowed the formation of slightly larger NPs, this parameter was chosen to carry out the synthesis from now on. Six samples of IONPs were synthesized in the presence of different amounts of sodium citrate (SC) according to the previously described co-precipitation method. Briefly, a TMAOH solution (4 mL, 1 M) was dropped slowly (800 μL/min) into an Fe^{2+}/Fe^{3+} (1:2 ratio) deoxygenated aqueous mixture which previously contained different amounts of SC (0.5, 1.0, 2.0, 4.0, 10.0 and 20 mM). The samples were washed to remove the citrate excess and resuspended in a TMAOH solution (10 mM), final pH ~11.

Stable black colloidal dispersions of SC-IONPs were obtained in all the synthesis. All the magnetic dispersions exhibited a negative ζ-potential (> -37 mV) due to the citrate stabilization.

The HAADF-STEM images of the synthesized IONPs at different citrate concentrations are shown in Figure 2-5. The presence of citrate and slow addition of the TMAOH solution during magnetite synthesis led to the formation of SC-IONPs heterogeneous in size and shape. It was distinguished between irregular, rounded, and truncated cubic shaped NPs (Figure 2-5). The magnetic products obtained up to SC 4 mM did not show significant effects on the particle size and distribution, with a broad size distribution ranging from 4 to 20 nm (Figure A1, Annex A). However, when the citrate concentration was above 10 mM, the effects on size decrease began to be more evident. For instance, at 20 mM, the crystal size decreased significantly to 6.7 ± 1.1 nm ($D_{DLS} = 7 \pm 3$ nm) and more homogeneous spherical-shaped NPs were observed. However, as the SC concentrations were higher, more aggregation of the NPs was observed.
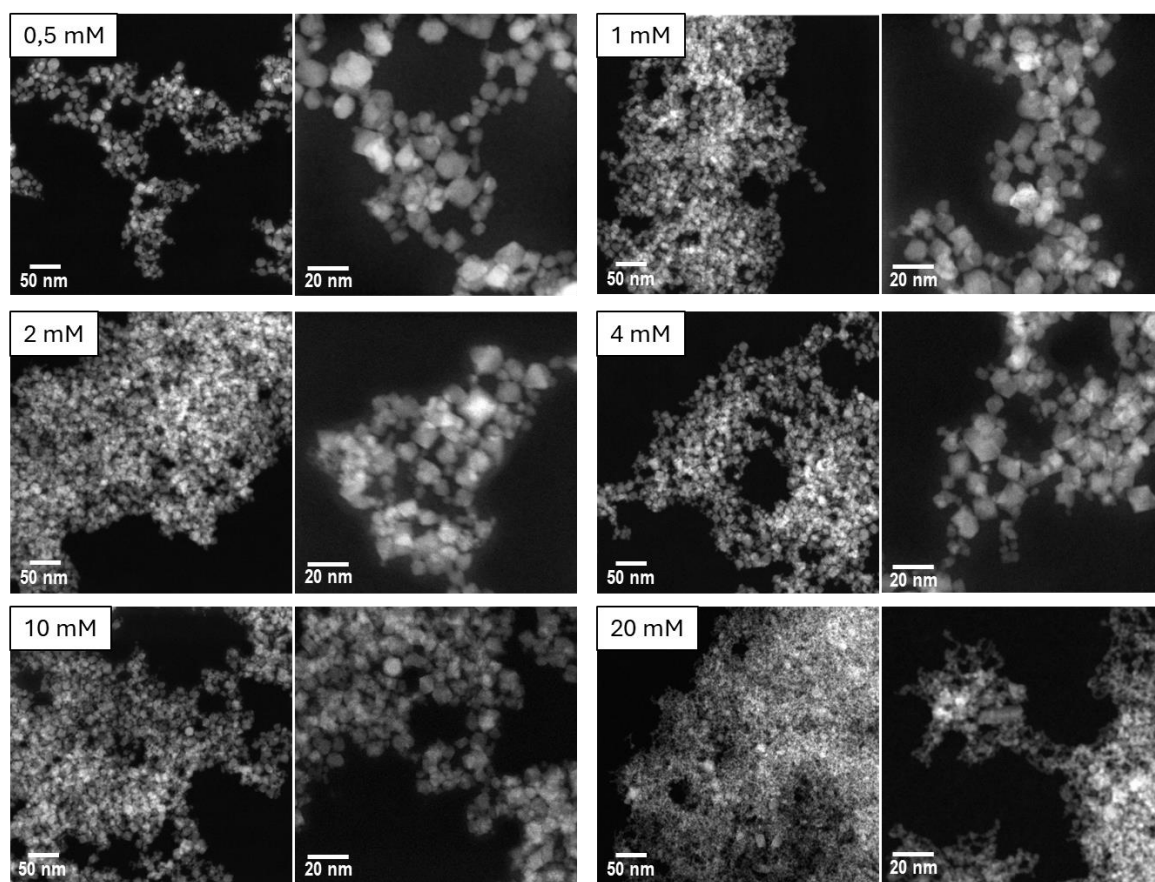
Figure 2-5. HRTEM images of magnetic SC-IONPs synthesized by co-precipitation in the presence of different SC amount (0.5 to 20 mM) (scale bars at 50 nm and 20 nm).

The powder XRD diffractograms of the SC-IONPs were indexed to the Fe_3O_4 pattern with an inverse spinel structure, as shown in Figure 2-6. The results obtained from the STEM and XRD analyses are summarized in Table 2-3. The crystallite sizes were below 14 nm, and no significant differences in crystal size or crystallographic properties were observed by XRD or STEM in the SC concentration range from 0.5 to 4.0 mM. The calculated lattice parameters were between the standard lattice parameters of Fe_3O_4 (8.396 Å) and γ-Fe_2O_3 (8.346 Å), and the broadener of the peaks and increase in microstrain with increasing SC content was consistent with the decrease in the crystal size. Despite the formation of some large particles in the precipitate, the synthesized SC-IONPs were below 20 nm, with an expected SPM behavior.
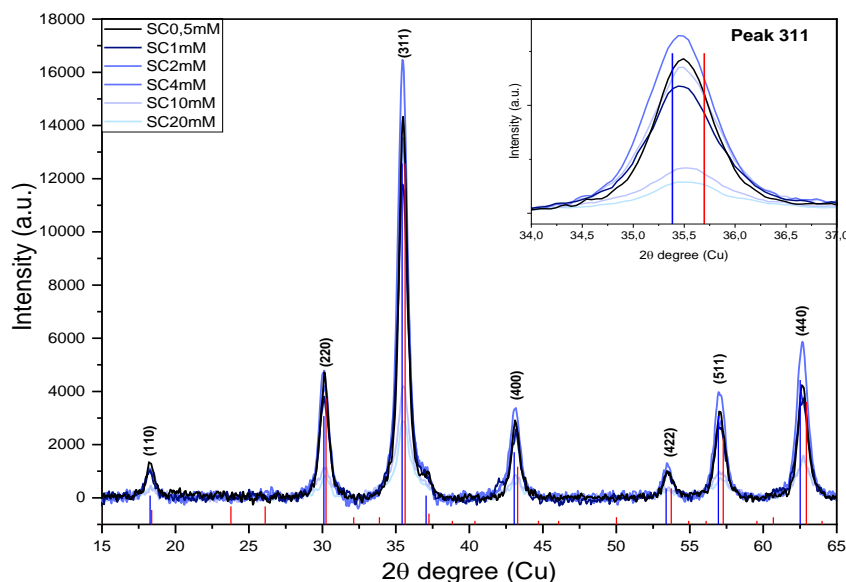
Figure 2-6. Powder XRD diffractograms of magnetic IONPs synthesized by co-precipitation in the presence of different SC amount (0.5 to 20 mM) (Blue bars: magnetite (JCPDS: 019-0629); Red bars: maghemite (JCPDS:039-1346).

Table 2-3. Effect of citrate ions on the properties of SC-IONPs.

Sample -IONPs	[SC] mM	D_{STEM} (nm)	D_{XRD} (nm)	Lattice Parameter (Å)[a]	Strain (ε)	ζ-pot (mV)
SC0.5	0.5	10.9 ± 3.4	14.0 ± 0.6	8.379	0.0069	-41
SC1	1.0	10.6 ± 3.5	11.8 ± 1.2	8.381	0.0085	-45
SC2	2.0	8.7 ± 3.4	12.1 ± 0.5	8.386	0.0083	-37
SC4	4.0	9.3 ± 3.4	11.6 ± 1.0	8.381	0.0086	-45
SC10	10.0	n.d.	10.4 ± 1.0	8.376	0.0098	-41
SC20	20.0	n.d.	6.7 ± 1.1	8.376	0.0146	-42

[a] Reported magnetite lattice parameter: 8.3960 Å (Standard JCPDS:019-0629).

n.d: not determined.

As reported, citrate effects in magnetite synthesis by the co-precipitation method lead to a decrease in the average size of the obtained magnetite NPs, usually in a size range of 4–10 nm, and superparamagnetic behavior.[2,39,40] The particle size can be tuned by increasing the relative SC/Fe concentration rate without affecting magnetite formation.[39,40]

The observed size effects in the synthesized SC-IONPs were attributed to two main factors. First, as the SC is a chelating tridentate ligand with a stronger coordination capacity because of its carboxylic groups, this strong coordination of the SC with the metal center results in a slower dissociation rate of Fe ions, reducing their availability to react and consequently preventing the nucleation and growth of the metal oxides or oxyhydroxide phases, leading to the formation of small NPs.[2,11,39,41] Second, considering the sub-stoichiometric ratio between Fe and SC ions (specifically below SC 4 mM), the complex Fe speciation in aqueous solution and Fe-citrate ligands,[42,43] and their pH dependency which vary with the progressive titration process, led to the appearance of different nucleation events that resulted in the formation of heterogeneous IONPs. While at high SC ratios, most of the Fe is fully complexed by the SC, resulting in a slow growth, small NPs and reducing the polydispersity of the NPs because the strong coordination.[44] These observations can be correlated with recent studies that have demonstrated that polynuclear iron-citrate species are the major species at low citrate concentrations, whereas mononuclear species are the major species at high citrate concentrations, and their kinetic studies have shown that polynuclear ferric-citrate complexes react more slowly than di- or trinuclear < mononuclear complexes, owing to larger steric effects.[45] Thus, at low citrate concentrations, the size of the NP may be larger.

Apart from that, some citrate ions were adsorbed on the NP surface forming a stable coating which might inhibit NP growth.[42,44,46,47] Thus, particle formation and growth could be inhibited due to ligand competition at the surface, resulting in the appearance of a mixture of products,[41] and anisotropic growth of IONPs.[48,49] In addition, the strong coordination of the carboxylate groups on the surface influences the electrostatic repulsion between the negative charged NPs to prevent their aggregation in the synthesis media.[30]

2.3.4 Surface Characterization

Surface characterization was followed by FTIR, surface charge and XPS analysis of selected samples, IONPs(S) and SC4-IONPs. The citrate surface coating in the obtained

SC-IONPs was proven by FTIR analysis by comparison with the spectra of the bared IONPs and trisodium citrate (SC) reagent, as shown in Figure 2-7A.

Representative IONPs and SC-IONPs spectra showed a broad band at 3500–3200 cm^{-1} and a stretching at 1614 cm^{-1} characteristic of O–H bending vibrations indicating the presence of hydroxyl groups or water moieties adsorbed onto NPs surface. In addition, the low frequency bands around 576 cm^{-1} and 438 cm^{-1} were referred to Fe−O vibrations in octahedral and tetrahedral sites.[50] For the SC-IONPs sample, the apparition of the two absorption peaks at 1562 and 1395 cm^{-1} were assigned to the asymmetric and symmetric stretching of the carbonyl group (COO$^-$), respectively, which confirmed the presence of citrate ions on the NPs surface.[21] Instead, IONPs showed two characteristic bands at 1488 cm^{-1} and 948 cm^{-1} assigned to the asymmetric stretching vibration of −CH$_3$ of tetramethyl ammonium hydroxide (TMAOH), which confirmed the trace amount of residual cation (TMA$^+$) on the surface.[51]

The characteristic charge of the surface material was determined by the ζ-potential curve as a function of pH, as shown in Figure 2-7B. In comparison with the bared IONPs, the isoelectric point for the SC-IONPs was shifted to lower pH values, indicating the presence of citrate ions at the NPs surface, which confers good colloidal stability in a wider range of pH.[52] However, as the SC-IONPs were washed several times they lost partially the citrate on surface having a similar behavior to the bared IONPs.
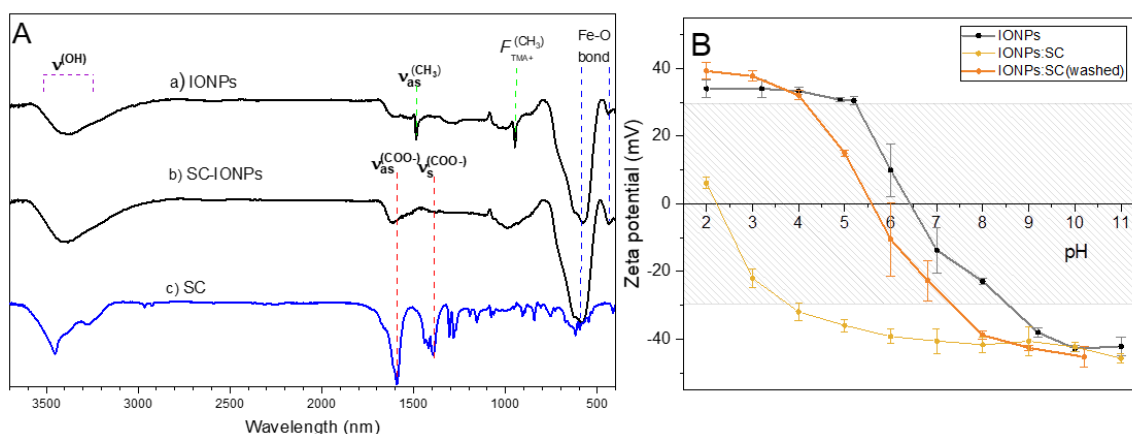
*Figure 2-7. (**A**) FTIR spectra of (a) IONPs, (b) citrate coated SC4-IONPs, and (c) trisodium citrate (SC), (**B**) zeta-potential as a function of pH for IONPs and SC-IONPs.*

XPS analysis was used to evaluate the elemental composition at the NPs surface and the oxidation states. Figure 2-8 depicts the corresponding deconvoluted XPS spectra of Fe 2p, O 1s and C 1s of the IONPs and SC-IONPs samples, respective percentage composition is shown in Table 1A (Annex A).
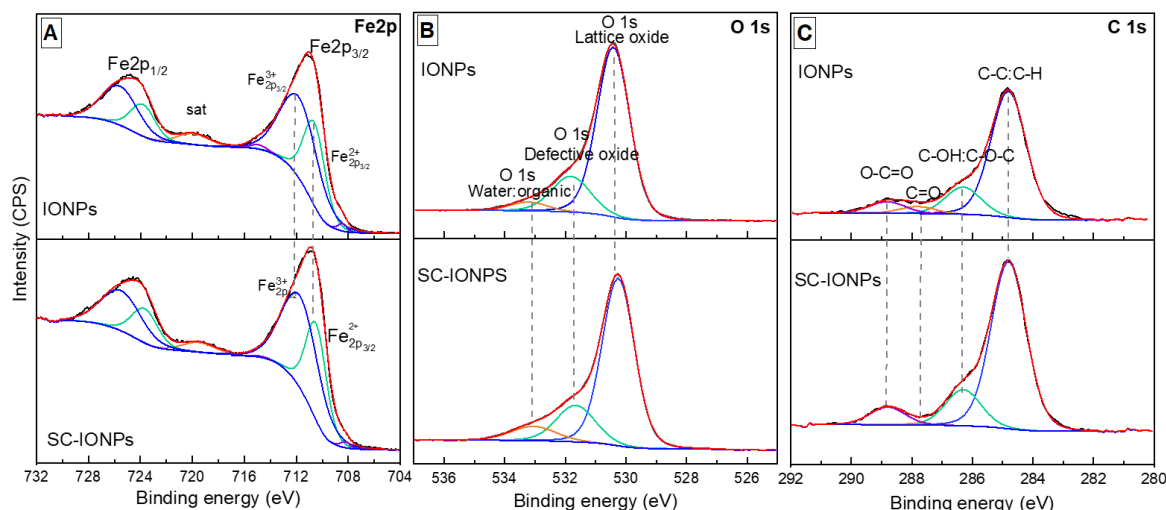
*Figure 2-8. XPS peak fitting spectra of (**A**) Fe 2p, (**B**) O 1s and (**C**) C 1s in IONPs and SC-IONPs.*

The Fe 2p spectra showed two main peaks corresponding to Fe $2p_{3/2}$ (710.8 eV) and Fe $2p_{1/2}$ (724.4 eV), which are attributed to Fe^{3+} state in Fe_3O_4 or Fe_2O_3 particles (Figure 2-8).[53] The presence of Fe^{2+} state was indicated by the broadener band at 710 eV and binding energy shift and intensity in the main peaks towards lower energies at 708 eV and 723 eV, respectively, characteristic of Fe^{2+} in Fe_3O_4.[53–56] The stoichiometry ratio between $Fe^{3+}:Fe^{2+}$ in both samples was estimated to be 1.7, which is close to the expected ratio.

The deconvoluted O 1s XPS spectra showed an sharp intense peak around 529.9 eV indicating the oxide (O^{2-}) formation in IONPs in the spinel crystal lattice as the predominant species (Figure 2-8B).[54,57] The peak broadening towards 531.5 eV and 532.8 eV revealed the presence of hydroxyl groups (OH^-) and water moieties. These hydroxyl groups can be correlated with the presence of the hydroxyl- from the SC carboxylic groups (-COOH) bonded to the surface of the SC-IONPs and residual water moieties absorbed during the sample preparation. Thus, the formation IONPs in a SC medium resulted in the attachment of carboxylic groups to the particle surface, as also demonstrated by FTIR shows. Finally, The C 1s spectra fitted to the C 1s saturated hydrocarbons (C−C: C−H) at 284.8 eV (Figure 2-8C). Although the IONPs synthesis was carried out without the presence of citrate, as observed by the lower intensity of the peak corresponding to O−C=O at 288.8 eV, organic molecules could be adsorbed on the particle surface during exposure to air.[58] On the other hand, synthesis in the SC presence exhibited higher signals both at 288.8 eV corresponding to O−C=O, as well as a more predominant shoulder at 283.3 eV corresponding to C−O−H, that appears to correspond to the carboxylic groups and a central carbon bonded to the hydroxyl group in the citrate molecule.

Finally, thermogravimetric analysis of the selected samples, IONPs and SC-IONPs was carried out from 30 to 600 °C at 10°C/min under N_2 atmosphere (Figure 2-9). The thermogram showed two gradual weight loss at ~120°C and ~230–400°C, corresponding to the loss of absorbed water between approximately 2% and 3%, and up to 5,8% corresponding to the loss of citrate molecules from the surface, respectively.[52] After 380°C, no weight loss was observed, achieving weight stability.[59]
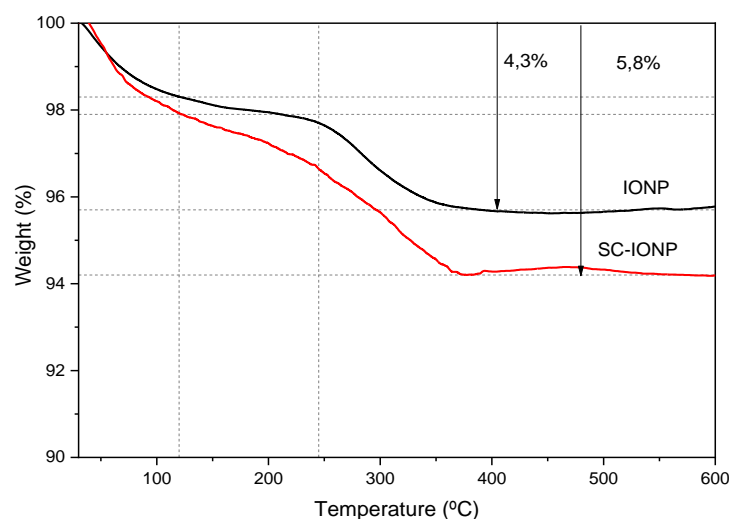
Figure 2-9. TGA weight loss of IONPs and SC-IONPs.

The citrate loss percent can be used to determine the number of citrate molecules absorbed per nm^2 of the NP surface by using the following equation 5: [52,60]

$$A = \frac{W\rho \, r \, N_A}{M_w(1-W) \times 3 \times 10^{21}} \qquad \text{(Eq. 5)}$$

Where, A= number of citrate molecules/nm^2, W= weight loss of sample, ρ= density of magnetite (5.17 g/cm^3), r = particle radius (nm), N_A = Avogadro's number (6.022x10^{23}), and M_w = molecular weight of the ligand (citric acid =192.1 amu).[52] Assuming a diameter of 11.6 nm, there are approximately ~1.9 citrate molecules per nm^2, which corresponding to ~802 molecules per each SC-IONPs. This value of ~1.9 (molecules/nm^2) seems to agree with the experimental values reported by Granath et al.[20] Although theoretically IONPs between 9-10 nm would be covered by 25-30 citrate molecules per nm^2, experimentally they found 1.6 to 2.2 citrate molecules per nm^2 depending on the pH. Their findings indicated that the surface cannot completely covered by citrate because there are other factors such as coordination spaces, preferred hydrogen bonds and equilibria between competing and interacting species of the medium as water, citrate, and ammonia.[20]

2.4 Conclusions

In this chapter, the influence of base rate addition, using TMAOH as an alkaline solution, and the effect of sodium citrate (SC) presence on the synthesis of magnetic IONPs were investigated. It was found that reducing the base rate had a slight effect on the increase in NP size from ~7 nm to ~11 nm, but a significant impact on the increase in the size distribution, which led to different nucleation events during the synthesis process. However, stable colloidal dispersions were obtained using TMAOH as the base.

The addition of sodium citrate ions to the magnetite synthesis significantly affected the size and shape of the IONPs. In general, as the SC concentration increased, the NPs size decreased. SC interacted strongly with the iron ions and at the NP surface. At low SC concentrations, they reduce the iron availability, retarding the crystallization process, observed by the obtention of some larger NPs but not homogeneous products. In contrast, at high SC concentrations, they interact strongly with the NPs surface, inhibiting their growth, favoring the formation of smaller NPs.

The difference in the size and shape of the obtained SC-IONPs can be explained by two competitive mechanisms commanded by the presence of SC and the slow titration process, which affects the availability of the iron precursor and its hydroxylation, and the overall equilibrium between nucleation and growth events.

The association of the TMA^+ and SC ions on the NPs surface was revealed by surface analysis. Both ions facilitated the colloidal stability of the IONPs, obtaining good colloidal dispersions in water, in addition to facilitating the redispersion of the dry NPs powders.

2.5   References

(1)   Massart, R. Preparation of Aqueous Magnetic Liquids in Alkaline and Acidic Media. *IEEE Trans. Magn.* **1981**, *17* (2), 1247–1248. https://doi.org/10.1109/TMAG.1981.1061188.

(2)   Bee, A.; Massart, R.; Neveu, S. Synthesis of Very Fine Maghemite Particles. *J. Magn. Magn. Mater.* **1995**, *149* (1–2), 6–9. https://doi.org/10.1016/0304-8853(95)00317-7.

(3)   Wu, L.; Mendoza-Garcia, A.; Li, Q.; Sun, S. Organic Phase Syntheses of Magnetic Nanoparticles and Their Applications. *Chem. Rev.* **2016**, *116* (18), 10473–10512. https://doi.org/10.1021/acs.chemrev.5b00687.

(4)   Kudr, J.; Haddad, Y.; Richtera, L.; Heger, Z.; Cernak, M.; Adam, V.; Zitka, O. Magnetic Nanoparticles: From Design and Synthesis to Real World Applications. *Nanomaterials* **2017**, *7* (9). https://doi.org/10.3390/nano7090243.

(5)   Shukla, S.; Khan, R.; Daverey, A. Synthesis and Characterization of Magnetic Nanoparticles, and Their Applications in Wastewater Treatment: A Review. *Environ. Technol. Innov.* **2021**, *24*, 101924. https://doi.org/10.1016/j.eti.2021.101924.

(6)   Mohammed, L.; Gomaa, H. G.; Ragab, D.; Zhu, J. Magnetic Nanoparticles for Environmental and Biomedical Applications: A Review. *Particuology* **2017**, *30*, 1–14. https://doi.org/10.1016/j.partic.2016.06.001.

(7)   Lu, A. H.; Salabas, E. L.; Schüth, F. Magnetic Nanoparticles: Synthesis, Protection, Functionalization, and Application. *Angew. Chemie - Int. Ed.* **2007**, *46* (8), 1222–1244. https://doi.org/10.1002/anie.200602866.

(8)   Kolhatkar, A. G.; Jamison, A. C.; Litvinov, D.; Willson, R. C.; Lee, T. R. *Tuning the Magnetic Properties of Nanoparticles*; 2013; Vol. 14. https://doi.org/10.3390/ijms140815977.

(9)   Du, K.; Zhu, Y.; Xu, H.; Yang, X. Multifunctional Magnetic Nanoparticles: Synthesis Modification and Biomedical Applications. *Prog. Chem.* **2011**, *23* (11), 2287–2298.

(10)   Gloag, L.; Mehdipour, M.; Chen, D.; Tilley, R. D.; Gooding, J. J. Advances in the Application of Magnetic Nanoparticles for Sensing. *Adv. Mater.* **2019**, *31* (48), 1–26. https://doi.org/10.1002/adma.201904385.

(11)   Iwasaki, T.; Mizutani, N.; Watano, S.; Yanagida, T.; Kawai, T. Size Control of Magnetite Nanoparticles by Organic Solvent-Free Chemical Coprecipitation at Room Temperature. *J. Exp. Nanosci.* **2010**, *5* (3), 251–262. https://doi.org/10.1080/17458080903490731.

(12)   Mascolo, M. C.; Pei, Y.; Ring, T. A. Room Temperature Co-Precipitation Synthesis of Magnetite Nanoparticles in a Large Ph Window with Different Bases. *Materials (Basel).* **2013**, *6* (12), 5549–5567. https://doi.org/10.3390/ma6125549.

(13)   Martínez-Mera, I.; Espinosa-Pesqueira, M. E.; Pérez-Hernández, R.; Arenas-Alatorre, J. Synthesis of Magnetite (Fe3O4) Nanoparticles without Surfactants at Room Temperature. *Mater. Lett.* **2007**, *61* (23–24), 4447–4451. https://doi.org/10.1016/j.matlet.2007.02.018.

(14)   Faiyas, A. P. A.; Vinod, E. M.; Joseph, J.; Ganesan, R.; Pandey, R. K. Dependence of PH and Surfactant Effect in the Synthesis of Magnetite (Fe3O4) Nanoparticles and Its Properties. *J. Magn. Magn. Mater.* **2010**, *322* (4), 400–404. https://doi.org/10.1016/j.jmmm.2009.09.064.

(15)   Arévalo, P.; Isasi, J.; Caballero, A. C.; Marco, J. F.; Martín-Hernández, F. Magnetic and Structural Studies of Fe3O4 Nanoparticles Synthesized via Coprecipitation and Dispersed in Different Surfactants. *Ceram. Int.* **2017**, *43* (13), 10333–10340. https://doi.org/10.1016/j.ceramint.2017.05.064.

(16)   Lee, J.; Isobe, T.; Senna, M. Magnetic Properties of Ultrafine Magnetite Particles and Their Slurries Prepared via In-Situ Precipitation. *Colloids Surfaces A Physicochem. Eng. Asp.* **1996**, *109*, 121–127. https://doi.org/10.1016/0927-7757(95)03479-X.

(17)   Ali, A.; Shah, T.; Ullah, R.; Zhou, P.; Guo, M.; Ovais, M.; Tan, Z.; Rui, Y. K. Review on Recent Progress in Magnetic Nanoparticles: Synthesis, Characterization, and Diverse Applications. *Front. Chem.* **2021**, *9* (July), 1–25. https://doi.org/10.3389/fchem.2021.629054.

(18)   Kuwahara, Y.; Miyazaki, T.; Shirosaki, Y.; Kawashita, M. Effects of Organic Polymer Addition in Magnetite Synthesis on the Crystalline Structure. *RSC Adv.* **2014**, *4* (45), 23359–23363. https://doi.org/10.1039/c4ra02073a.

(19)   Akl, M. A.; Kamel, A. M.; El-Ghaffar, M. A. A. Biodegradable Functionalized Magnetite Nanoparticles as Binary-Targeting Carrier for Breast Carcinoma. *BMC Chem.* **2023**, *17* (1), 3. https://doi.org/10.1186/s13065-023-00915-4.

(20)   Granath, T.; Mandel, K.; Löbmann, P. The Significant Influence of the PH Value on Citrate Coordination upon Modification of Superparamagnetic Iron Oxide Nanoparticles. *Part. Part. Syst. Charact.* **2022**, *39* (3). https://doi.org/10.1002/ppsc.202100279.

(21)   Nappini, S.; Magnano, E.; Bondino, F.; Píš, I.; Barla, A.; Fantechi, E.; Pineider, F.; Sangregorio, C.; Vaccari, L.; Venturelli, L.; Baglioni, P. Surface Charge and Coating of CoFe2O4 Nanoparticles: Evidence of Preserved Magnetic and Electronic Properties. *J. Phys. Chem. C* **2015**, *119* (45), 25529–25541. https://doi.org/10.1021/acs.jpcc.5b04910.

(22)   Cheng, C.; Wen, Y.; Xu, X.; Gu, H. Tunable Synthesis of Carboxyl-Functionalized Magnetite Nanocrystal Clusters with Uniform Size. *J. Mater. Chem.* **2009**, *19* (46), 8782–8788. https://doi.org/10.1039/b910832g.

(23)   Ishikawa, T.; Kataoka, S.; Kandori, K. The Influence of Carboxylate Ions on the Growth of β-FeOOH Particles. *J. Mater. Sci.* **1993**, *28* (10), 2693–2698. https://doi.org/10.1007/BF00356205.

(24)   Cornell, R. M.; Schindler, P. W. Infrared Study of the Adsorption of Hydroxycarboxylic Acids on α-FeOOH and Amorphous Fe (III)Hydroxide. *Colloid Polym. Sci. Kolloid Zeitschrift Zeitschrift für Polym.* **1980**, *258* (10), 1171–1175. https://doi.org/10.1007/BF01382462.

(25)   Ishikawa, T.; Nishimori, H.; Abe, I.; Kandori, K. Influence of the Adsorption of Citrate and Tartrate Ions upon the Formation of γ-FeOOH Particles. *Colloids Surfaces A Physicochem. Eng. Asp.* **1993**, *71* (2), 141–146. https://doi.org/10.1016/0927-7757(93)80338-F.

(26)   Atrei, A.; Mahdizadeh, F. F.; Baratto, M. C.; Scala, A. Effect of Citrate on the Size and the Magnetic Properties of Primary Fe3o4 Nanoparticles and Their Aggregates. *Appl. Sci.* **2021**, *11* (15). https://doi.org/10.3390/app11156974.

(27)   Jolivet, J. P.; Chanéac, C.; Tronc, E. Iron Oxide Chemistry. From Molecular Clusters to Extended Solid Networks. *Chem. Commun.* **2004**, *4* (5), 477–483. https://doi.org/10.1039/b304532n.

(28)   Montes-Hernandez, G.; Findling, N.; Renard, F. Direct and Indirect Nucleation of Magnetite Nanoparticles from Solution Revealed by Time-Resolved Raman Spectroscopy. *Cryst. Growth Des.* **2021**, *21* (6), 3500–3510. https://doi.org/10.1021/acs.cgd.1c00282.

(29)   Cornell, R. M.; U. Schwertmann. *The Iron Oxides: Structure, Properties, Reactions, Occurences and Uses*, Second.; Wiley VCH, Ed.; Weinheim, 2003; Vol. 664.

(30)   Mirabello, G.; Lenders, J. J. M.; Sommerdijk, N. A. J. M. Bioinspired Synthesis of Magnetite Nanoparticles. *Chem. Soc. Rev.* **2016**, *45* (18), 5085–5106. https://doi.org/10.1039/c6cs00432f.

(31)   Nyirő -Kósa, I.; Csákberényi Nagy, D.; Pósfai, M. Size and Shape Control of Precipitated Magnetite Nanoparticles. *Eur. J. Mineral.* **2009**, *21* (2), 293–302. https://doi.org/10.1127/0935-1221/2009/0021-1920.

(32)   Casals, E.; Barrena, R.; García, A.; González, E.; Delgado, L.; Busquets-Fité, M.; Font, X.; Arbiol, J.; Glatzel, P.; Kvashnina, K.; Sánchez, A.; Puntes, V. Programmed Iron Oxide Nanoparticles Disintegration in Anaerobic Digesters Boosts Biogas Production. *Small* **2014**, *10* (14), 2801–2808. https://doi.org/10.1002/smll.201303703.

(33)   Andrade, Â. L.; Valente, M. A.; Ferreira, J. M. F.; Fabris, J. D. Preparation of Size-Controlled Nanoparticles of Magnetite. *J. Magn. Magn. Mater.* **2012**, *324* (10), 1753–1757. https://doi.org/10.1016/j.jmmm.2011.12.033.

(34)   Zaitsev, V. S.; Filimonov, D. S.; Presnyakov, I. A.; Gambino, R. J.; Chu, B. Physical and Chemical Properties of Magnetite and Magnetite-Polymer Nanoparticles and Their Colloidal Dispersions. *J. Colloid Interface Sci.* **1999**, *212* (1), 49–57. https://doi.org/10.1006/jcis.1998.5993.

(35)   Giri, S.; Samanta, S.; Maji, S.; Ganguli, S.; Bhaumik, A. Magnetic Properties of α-Fe2O3

Nanoparticle Synthesized by a New Hydrothermal Method. *J. Magn. Magn. Mater.* **2005**, *285* (1–2), 296–302. https://doi.org/10.1016/j.jmmm.2004.08.007.

(36)   Altan, C. L.; Lenders, J. J. M.; Bomans, P. H. H.; de With, G.; Friedrich, H.; Bucak, S.; Sommerdijk, N. A. J. M. Partial Oxidation as a Rational Approach to Kinetic Control in Bioinspired Magnetite Synthesis. *Chem. - A Eur. J.* **2015**, *21* (16), 6150–6156. https://doi.org/10.1002/chem.201405973.

(37)   Goss, C. J. Saturation Magnetisation, Coercivity and Lattice Parameter Changes in the System Fe3O4-ГFe2O3, and Their Relationship to Structure. *Phys. Chem. Miner.* **1988**, *16* (2), 164–171. https://doi.org/10.1007/BF00203200.

(38)   Whitehead, C. B.; Özkar, S.; Finke, R. G. LaMer's 1950 Model for Particle Formation of Instantaneous Nucleation and Diffusion-Controlled Growth: A Historical Look at the Model's Origins, Assumptions, Equations, and Underlying Sulfur Sol Formation Kinetics Data. *Chem. Mater.* **2019**, *31* (18), 7116–7132. https://doi.org/10.1021/acs.chemmater.9b01273.

(39)   Kirillov, V. L.; Balaev, D. A.; Semenov, S. V.; Shaikhutdinov, K. A.; Martyanov, O. N. Size Control in the Formation of Magnetite Nanoparticles in the Presence of Citrate Ions. *Mater. Chem. Phys.* **2014**, *145* (1–2), 75–81. https://doi.org/10.1016/j.matchemphys.2014.01.036.

(40)   Ruizmoreno, R. G.; Martinez, A. I.; Castro-Rodriguez, R.; Bartolo, P. Synthesis and Characterization of Citrate Coated Magnetite Nanoparticles. *J. Supercond. Nov. Magn.* **2013**, *26* (3), 709–712. https://doi.org/10.1007/s10948-012-1790-z.

(41)   Granath, T.; Mandel, K.; Löbmann, P. Overcoming the Inhibition Effects of Citrate: Precipitation of Ferromagnetic Magnetite Nanoparticles with Tunable Morphology, Magnetic Properties, and Surface Charge via Ferrous Citrate Oxidation. *Part. Part. Syst. Charact.* **2021**, *38* (8). https://doi.org/10.1002/ppsc.202100098.

(42)   Zhang, X.; Chen, L.; Liu, R.; Li, D.; Ge, X.; Ge, G. The Role of the OH Group in Citric Acid in the Coordination with Fe3O4 Nanoparticles. *Langmuir* **2019**. https://doi.org/10.1021/acs.langmuir.9b00208.

(43)   Channei, D.; Phanichphant, S.; Nakaruk, A.; Mofarah, S.; Koshy, P.; Sorrell, C. Aqueous and Surface Chemistries of Photocatalytic Fe-Doped CeO2 Nanoparticles. *Catalysts* **2017**, *7* (12), 45. https://doi.org/10.3390/catal7020045.

(44)   Zhang, X.; Chen, L.; Yuan, L.; Liu, R.; Li, D.; Liu, X.; Ge, G. Conformation-Dependent Coordination of Carboxylic Acids with Fe 3 O 4 Nanoparticles Studied by ATR-FTIR Spectral Deconvolution. *Langmuir* **2019**, *35* (17), 5770–5778. https://doi.org/10.1021/acs.langmuir.8b03303.

(45)   Gautier-Luneau, I.; Merle, C.; Planon, D.; Lebrun, C.; Biaso, F.; Serratrice, G.; Pierre, J. L. New Trends in the Chemistry of Iron(III) Citrate Complexes: Correlations between X-Ray Structures and Solution Species Probed by Electrospray Mass Spectrometry and Kinetics of Iron Uptake from Citrate by Iron Chelators. *Chem. - A Eur. J.* **2005**, *11* (7), 2207–2219. https://doi.org/10.1002/chem.200401087.

(46)   Jing, J.; Zhang, Y.; Liang, J.; Zhang, Q.; Bryant, E.; Avendano, C.; Colvin, V. L.; Wang, Y.; Li, W.; Yu, W. W. One-Step Reverse Precipitation Synthesis of Water-Dispersible Superparamagnetic Magnetite Nanoparticles. *J. Nanoparticle Res.* **2012**, *14* (4), 827. https://doi.org/10.1007/s11051-012-0827-3.

(47)   Spiro, T. G.; Bates, G.; Saltman, P. Hydrolytic Polymerization of Ferric Citrate. II. Influence of Excess Citrate. *J. Am. Chem. Soc.* **1967**, *89* (22), 5559–5562. https://doi.org/10.1021/ja00998a009.

(48)   Muro-Cruces, J.; Roca, A. G.; López-Ortega, A.; Fantechi, E.; Del-Pozo-Bueno, D.; Estradé, S.; Peiró, F.; Sepúlveda, B.; Pineider, F.; Sangregorio, C.; Nogues, J. Precise Size Control of the Growth of Fe3O4 Nanocubes over a Wide Size Range Using a Rationally Designed One-Pot Synthesis. *ACS Nano* **2019**. https://doi.org/10.1021/acsnano.9b01281.

(49)   Rizzuti, A.; Dassisti, M.; Mastrorilli, P.; Sportelli, M. C.; Cioffi, N.; Picca, R. A.; Agostinelli, E.; Varvaro, G.; Caliandro, R. Shape-Control by Microwave-Assisted Hydrothermal Method for the Synthesis of Magnetite Nanoparticles Using Organic Additives. *J. Nanoparticle Res.* **2015**, *17* (10). https://doi.org/10.1007/s11051-015-3213-0.

(50)   Qi, Z.; Joshi, T. P.; Liu, R.; Liu, H.; Qu, J. Synthesis of Ce(III)-Doped Fe3O4 Magnetic Particles for Efficient Removal of Antimony from Aqueous Solution. *J. Hazard. Mater.* **2017**, *329*, 193–204. https://doi.org/10.1016/j.jhazmat.2017.01.007.

(51)   Bottger, G. L.; Geddes, A. L. The Infrared Spectra of the Crystalline Tetramethylammonium Halides. *Spectrochim. Acta* **1965**, *21* (10), 1701–1708. https://doi.org/10.1016/0371-1951(65)80082-0.

(52)   Hancock, M. L.; Yokel, R. A.; Beck, M. J.; Calahan, J. L.; Jarrells, T. W.; Munson, E. J.; Olaniyan, G. A.; Grulke, E. A. The Characterization of Purified Citrate-Coated Cerium Oxide Nanoparticles Prepared via Hydrothermal Synthesis. *Appl. Surf. Sci.* **2021**, *535* (August 2020), 147681. https://doi.org/10.1016/j.apsusc.2020.147681.

(53)   Grosvenor, A. P.; Kobe, B. A.; Biesinger, M. C.; McIntyre, N. S. Investigation of Multiplet Splitting of Fe 2p XPS Spectra and Bonding in Iron Compounds. *Surf. Interface Anal.* **2004**, *36* (12), 1564–1574. https://doi.org/10.1002/sia.1984.

(54)   Joseph, Y.; Ketteler, G.; Kuhrs, C.; Ranke, W.; Weiss, W.; Schlögl, R. On the Preparation and Composition of Potassium Promoted Iron Oxide Model Catalyst Films. *Phys. Chem. Chem. Phys.* **2001**, *3* (18), 4141–4153. https://doi.org/10.1039/b104263g.

(55)   Schedel-Niedrig, T.; Weiss, W.; Schlögl, R. Electronic Structure of Ultrathin Ordered Iron Oxide Films Grown onto Pt(111). *Phys. Rev. B* **1995**, *52* (24), 17449–17460. https://doi.org/10.1103/PhysRevB.52.17449.

(56)   Chen, F.; Wang, X.; Nie, Y.; Li, Q.; Ouyang, J.; Feng, Z.; Chen, Y.; Harris, V. G. Ferromagnetic Resonance Induced Large Microwave Magnetodielectric Effect in Cerium Doped Y3 Fe5 O12 Ferrites. *Sci. Rep.* **2016**, *6* (June). https://doi.org/10.1038/srep28206.

(57)   Schedel-Niedrig, T.; Weiss, W.; Schlögl, R. Electronic Structure of Ultrathin Ordered Iron Oxide Films Grown onto Pt(111). *Phys. Rev. B* **1995**, *52* (24), 17449–17460. https://doi.org/10.1103/PhysRevB.52.17449.

(58)   Moskvin, M.; Marková, I.; Malínská, H.; Miklánková, D.; Hüttl, M.; Oliyarnyk, O.; Pop-Georgievski, O.; Zhigunov, A.; Petrovský, E.; Horák, D. Cerium Oxide-Decorated γ-Fe2 O3 Nanoparticles: Design, Synthesis and in Vivo Effects on Parameters of Oxidative Stress. *Front. Chem.* **2020**, *8* (August), 1–13. https://doi.org/10.3389/fchem.2020.00682.

(59)   Marciello, M.; Connord, V.; Veintemillas-Verdaguer, S.; Vergés, M. A.; Carrey, J.; Respaud, M.; Serna, C. J.; Morales, M. P. Large Scale Production of Biocompatible Magnetite Nanocrystals with High Saturation Magnetization Values through Green Aqueous Synthesis. *J. Mater. Chem. B* **2013**, *1* (43), 5995–6004. https://doi.org/10.1039/c3tb20949k.

(60)   Larsen, E. K. U.; Nielsen, T.; Wittenborn, T.; Birkedal, H.; Vorup-Jensen, T.; Jakobsen, M. H.; Ostergaard, L.; Horsman, M. R.; Besenbacher, F.; Howard, K. A.; Kjems, J. Size-Dependent Accumulation of Pegylated Silane-Coated Magnetic Iron Oxide Nanoparticles in Murine Tumors. *ACS Nano* **2009**, *3* (7), 1947–1951. https://doi.org/10.1021/nn900330m.

Chapter 3

Magnetic Iron Oxide Nanoparticles Size Control from Single Crystal to Nanowires: The role of Lanthanide Cations

3.1 Introduction

Magnetite (Fe_3O_4) and maghemite (Fe_2O_3) NPs are important iron oxide nanoparticles (IONPs) that are used in numerous nano- and biotechnological applications. Both superparamagnetic and larger ferromagnetic IONPs, hold greater relevance for most applications in fields such as biomedicine, catalysis, environmental remediation, among others.[1–7] At the nanoscale, the magnetic properties of IONPs are extremely dependent on their size, but also its morphology, crystal structure and quality, atomic composition (such as doping, cation distribution, and crystal defects), and surface (core-shell design, functionalization, and surface doping).[8,9] Therefore, controlling the size of IONPs is crucial for fine-tuning their properties and thus their performance.

Synthesis based on metal-organic precursors and organic solvents has proven to be a very successful tool for the preparation of monodispersed IONPs with high crystallinity,

different shapes, and reduced magnetic disorder.[2] Nevertheless, over the years, aqueous synthesis at room temperature presents a green and scalable approach for producing magnetite/maghemite NPs with stability in aqueous media making them attractive for several applications.[10,11]

Among aqueous routes, the fast co-precipitation method –first reported by Massart[12]–,stands out for its simplicity, scalability, and low energy consumption. This method involves the addition of Fe^{2+} and Fe^{3+} salt precursors in a 1:2 molar ratio into a basic solution, resulting in the rapid formation of small magnetite NPs (~10 nm).[12] However, the precise size control of highly crystalline NPs is challenging. Previous efforts to manipulate NP crystallization by adjusting factors such as iron counterions, base type, pH, aging time, and the presence of organic additives have yielded varied results in terms of the average particle size.[13–16]

In contrast, magnetotactic bacteria intracellularly produce magnetite crystals between 35 and 120 nm at room temperature (RT), under aqueous, ambient conditions.[17] This process, occurring in magnetosomes, and involve a transient precursor phase, ferrihydrite $Fe(OH)_3$, whose transformation into magnetite is regulated by the biomolecular machinery.[18,19] Inspired by this approach, several studies have explored the growth of magnetite NPs *via* the Fe^{2+}-induced transformation of ferrihydrite to magnetite.[15,20,21] By carefully dosing Fe^{3+}/Fe^{2+} reactants by means of titration or controlled diffusion, the aim was to control the gradual release of Fe^{3+} from ferrihydrite, allowing the controlled growth of NPs through precursor attachment.[11,22] These approaches rely on precise control over reaction kinetics, wherein a primary metastable phase serves as a precursor for the thermodynamically stable magnetite phase.[14,15] It has been demonstrated that the nucleation and growth of magnetite involve the formation of an unstable ferrihydrite-like phase ($Fe(OH)_3$), which, by interaction with Fe^{2+} ions leads to the formation of primary magnetite particles, which grow in number and size by coalescence, redissolution, and recrystallization mechanisms, allowing the formation of magnetite crystals up to 60 nm.[15]

Alternatively, single-domain magnetite NPs with sizes in the range of 20–200 nm can also be obtained by partial oxidation of Fe^{2+}.[23–25] In this method, a ferrous precursor is precipitated in alkaline media to form ferrous hydroxide ($Fe(OH)_2$), known as white rust precursor. Subsequent partial oxidation to Fe^{3+} by a mild oxidizing agent (typically NO_3^-) and recrystallization with the remaining Fe^{2+} yields magnetite NPs.[23–25] However, thoroughly adjustment of reactant concentrations is necessary to control the reaction kinetics and achieve the desired NP size.[24,26] Modulating pH, oxidant type, or additives

offers flexibility in controlling NP morphology,[27] but the overall process remains complex due to the formation of various iron oxyhydroxides, such as goethite or lepidocrocite, under minor variations of the synthetic conditions.[28] This complexity highlights the significant challenge of consistently producing high-quality size-controlled NPs under mild chemical aqueous conditions.

Several studies have explored growing magnetite beyond the SPM limit.[28] For magnetite, it becomes a single domain below 128 nm and the magnetic dipole becomes SPM below 20 nm at RT.[29,30] For sizes above the SPM/FM transition, the permanent dipole magnetically aggregates the NPs into chain-like structures. Growing a single NC of magnetite NPs and stabilizing them beyond the Massart limit in water is challenging. According to classical mechanism, in order to grow a NC, one needs to have monomer after the burst nucleation, and the surface has to be active to incorporate new atoms while avoiding NC aggregation; otherwise, more monomers represent more NCs but not larger NCs.[31]

The challenge stems from the complex crystallization processes of magnetite and other oxides in aqueous environments,[15] which involves managing reaction intermediates and overcoming of the high surface reactivity of the NPs.[32] In these systems, the hydrolysis of precursor in aqueous solutions produces very small colloidal particles (4-8 nm), derived from intermediate species that are thermodynamically unstable but kinetically favorable.[32] NPs then grow either by the incorporation of precursor onto existing crystal domains, following the classical model, or through aggregation of amorphous primary particles, according to the non-classical model.[15] Overcoming the high interfacial energy at the oxide/water interface -dewetting- is crucial, requiring strategies to lower the activation energy.[33] Adjusting the pH and using additives (i.e., peptides (i.e., Mms6) containing moieties of negatively charged molecules, such as aspartic and glutamic acid), are the most used strategies for modulating the physicochemical properties of the species involved in the reaction, such as surface charge, wettability, and stability.[11,15,21] The pH determines the speciation, solubility, and surface state of hydroxides, ultimately impacting their stability, as illustrated by Pourbaix diagrams. Additives can decrease the reactivity of the precursor to prevent burst nucleation, stabilize intermediates by adjusting wettability, and modulate NP reactivity, thereby influencing the final size and morphology of the NPs, as well as modifying their magnetic properties.

On the other hand, several research groups have also investigated the influence of cation doping on magnetite structures ($M_xFe_{3-x}O_4$).[34–37] Rare earth (RE) elements or

lanthanide ions (Ln^{3+}) are an interesting class of dopants because their partially occupied 4f-electrons exert effects on the physical and chemical characteristics of IONPs.[38–42] The amount and type of lanthanide in magnetite usually induce magnetic and optical modifications, particularly beneficial for biomedical applications such as imaging, labeling, and hyperthermia.[37,42,43] Among the RE family, cerium (Ce) is the most abundant element, and cerium-based catalysts have received significant attention due to their excellent catalytic redox properties attributable to their ease of redox cycle Ce^{3+} and Ce^{4+}. Furthermore, cerium has also been considered a valuable doping ion, and its incorporation into magnetic iron oxide-based catalysts has shown better reactivity, and improved catalytic performance as a Fenton-like catalyst.[44–48] Moreover, its combination with magnetic IONPs allows easy magnetic separation and recovery.[47,49]

Recent studies have highlighted the influence of lanthanide doping on NCs growth, size, and phase transition during NCs synthesis.[50–52] In contrast to conventional methods, this approach requires the modification of a single parameter –the concentration of the lanthanide dopant–, offering greater precision in controlling the size and morphology of the resulting NCs.[51] However, limited research exists on the study of the effect of lanthanide in magnetite synthesis.[39,42,53–55] Particularly, using the co-precipitation method and in combination with SC, remains rather unexplored. Previous studies, such as those by Zhang et al., have found that gadolinium (Gd) doping alters both the growth process and magnetic properties. They found that 5% Gd doping increased magnetite NPs crystal size from 18 to 44 nm, holding the magnetite crystal structure with Gd^{3+} aleatory incorporated into the crystal lattice.[39] Similarly Kowalik et al., demonstrated that the size of yttrium (Y^{3+}) doped magnetite NPs increased with an increase in the Y^{3+} content. Yttrium doping at 0.1% and 1% yielded magnetite NPs of 18 and 23 nm, respectively.[42] However, both studies exhibited drawbacks such as wide size distributions, the presence of polycrystalline NPs, or the appearance of a precipitated secondary phase.

Hence, this chapter focuses on the synthesis of magnetic iron oxide (magnetite/maghemite) NPs in the presence of cerium and sodium citrate (Ce@IONPs) via aqueous co-precipitation method. Single-crystal Ce@IONPs up to 46 nm with controlled size were obtained, by adjusting the concentration of the cerium precursor in the reaction media. In particular, the effects of cerium and sodium citrate ions on the size and properties of the resulting NPs, precursor concentrations, experimental conditions, use of other lanthanides, and physicochemical and surface properties of the synthesized Ce@IONPs were also investigated.

3.2   Experimental

3.2.1 Chemicals

Iron (II) chloride tetrahydrate ($FeCl_2 \cdot 4H_2O$, >99%), Iron (III) chloride anhydrous ($FeCl_3$, >99%), tetramethylammonium hydroxide (TMAOH, 1.0 M in H_2O), trisodium citrate (SC, $Na_3C_6H_5O_7$, >99%), Cerium (III) chloride heptahydrate ($CeCl_3 \cdot 7H_2O$, >99%), Europium (III) chloride hexahydrate ($EuCl_3 \cdot 6H_2O$, >99%), Gadolinium (III) chloride hexahydrate ($GdCl_3 \cdot 6H_2O$, >99%), Erbium (III) chloride anhydrous ($ErCl_3$, >99%), Erbium (III) nitrate pentahydrate ($Er(NO_3)_3 \cdot 5H_2O$, >99.99%), Ytterbium (III) nitrate pentahydrate ($Yt(NO_3)_3 \cdot 5H_2O$, >99.99%), and Lutetium (III) nitrate pentahydrate ($Lu(NO_3)_3 \cdot 5H_2O$, >99.99%). All reagents were purchased from Sigma-Aldrich and used as received without further purification. Milli-Q water (18 MΩ cm^{-1}) was used in all the experiments. All glassware was first cleaned with aqua regia and washed with Milli-Q water prior to the experiments.

3.2.2 Synthesis of Magnetic Iron Oxide Nanoparticles (Ce@IONPs and Ln@IONPs)

Ce@IONPs were prepared by the co-precipitation method at room temperature as described below. All the aqueous solutions in Milli-Q-water were first degassed by sonication (10 min) and then purged with N_2 at least 1h before use.

In a typical reaction, in a glass vessel sealed with a rubber septum, a 92 mL solution was prepared containing trisodium citrate (SC, final concentration 4 mM) and different concentrations of $CeCl_3$ (final concentration from 0–2.0 mM) under magnetic stirring and constant N_2 bubbling for 1 h. Freshly $FeCl_2$ (2 mL, 100 mM) and $FeCl_3$ (2 mL, 200 mM) solutions (1:2 ratio, 6 mM total Fe concentration) were then quickly added to the previously degassed aqueous solution under vigorous magnetic stirring (800 rpm) and constant N_2 bubbling, followed by the addition of a TMAOH (4 mL, 1 M) solution at a constant rate of 800 μL/min. This caused the precipitation of magnetic IONPs, as indicated by a gradual color change of the solution from yellow to black. The resulting mixture was aged for 2 h while stirring under N_2 to prevent oxidation. Thereafter, the magnetic IONPs were collected by centrifugation (20 min at 6000 to 10000G, depend on the NP size) or by magnetic decantation and washed twice with water to remove the excess of ions in solution

and further redispersed in a TMAOH (10 mM) free-oxygen aqueous solution or in milli-Q-water before sample characterization. The size of Ce@IONPs NPs was controlled by adjusting the concentration of $CeCl_3$ added during the synthesis. Thus, by increasing the concentration from 0.1 mM to 1.25 mM, magnetic IONPs ranging from 10 nm to 46 nm were produced.

NPs synthesis employing other lanthanides (Ln = Eu^{3+}, Gd^{3+}, Er^{3+}, Yt^{3+}, and Lu^{3+}) were synthesized following the above-described protocol but replacing the Ce precursor by Gd, Eu, Er, Yt or Lu ones. All the samples were synthesized under the same synthetic conditions (temperature, reactant concentration, alkaline titration rate, and time). Briefly, different lanthanide (Ln) salts (at 0.3, 0.5 or 1.0 mM, final concentration) were dissolved in free-oxygen SC (4 mM) solution. Then Fe^{2+}/Fe^{3+} aqueous mixture (1:2 ratio, 6 mM total Fe concentration) were added, followed by the slow addition of a TMAOH solution (1 M, 4 mL at 800 μL/min), resulted in Ln@IONPs of similar size. The rest of the procedure was kept the same and after 24 h of reaction, the resulted Ln@IONPs were magnetically collected and washed before characterization.

3.3   Results and Discussion

3.3.1 Standard Synthesis of Magnetic Iron Oxide Nanoparticles (Ce@IONPs)

Single-domain magnetic Iron Oxide Nanoparticles (Ce@IONPs) of controlled sizes were obtained via co-precipitation reaction at room temperature in the presence of Ce^{3+} and SC ions. In a standard synthesis, aqueous solutions of ferrous ($FeCl_2$) and ferric ($FeCl_3$) (Fe^{2+}:Fe^{3+} (1:2), final concentration 6 mM) were injected into a degassed aqueous solution containing previously a mixture of a Ce^{3+} and SC ions (Ce:SC, final concentration 0.5:4 mM), followed by the slow and continuous addition of a TMAOH solution (4 mL, 1 M, at 800 μL/min). During the addition of TMAOH, the solution changed color gradually from light-yellow to brownish orange and then to dark black within minutes, indicating the formation of magnetic Ce@IONPs. TMAOH was chosen for its bulky TMA^+ cations, which stabilize NPs and prevent aggregation in aqueous solutions compared to NaOH, optimizing magnetite synthesis and reducing particle size distribution.[56] After synthesis, the NPs were either centrifuged or magnetically purified and then resuspended in a 10 mM

TMAOH solution, ensuring their stability and dispersion for subsequent use. Importantly, to avoid the co-precipitation of Ce^{3+} ions into the reaction media, two experimental conditions were established: maintaining the inert atmosphere by constant N_2 bubbling all the reaction to avoid the fast oxidation of Ce^{3+} into Ce^{4+}, and setting the SC to a final concentration of 4 mM to keep complexed cerium ions, thus modifying cerium reactivity in the reaction media.

Structural and compositional characterization was carried out from the Ce@IONPs obtained in the standard synthesis. Representative images of high-resolution transmission electron microscopy (HRTEM) and high-angle annular dark field scanning TEM (HAADF-STEM) of as-obtained Ce@IONPs are shown in Figure 3-1A. Obtained results revealed that the sample was composed of mostly spherical NPs with a diameter of 26.7 ± 4.2 nm, self-assembled magnetically in elongated structures in a wire-like morphology as they dried in the grid, as a consequence of a stronger magnetic dipole NPs interactions.[57]

The dominant structure of each wire was composed of different Fe_3O_4 crystallites, as revealed in the details of the selective area electro diffraction (SAED) from the two examples imaged of a single crystal along the [110] and [103] zone axes (Figure 3-1B). Therefore, the presence of Ce^{3+} did not disrupt the local symmetry of magnetite. The power spectra (FFT) indexation of the analyzed crystal planes indicated that each crystallite was composed of Fe_3O_4 cubic spinel structure with Fd-3m (227) space group. Remarkably, we did not observe the formation of any isolated CeO_2 crystal co-precipitated with the obtained Ce@IONPs, indicating that the nucleation of CeO_2 NPs was avoided during the 2h of synthesis.

The electron energy loss spectroscopy (EELS) analysis was performed to obtain more information on the elemental composition, which detected the presence of O, Fe, and Ce in the sample (Figure 3-2A). To extrapolate the different elements, the O K-edge at 532 eV (red), Fe L-edge at 708 eV (blue), and Ce M-edge at 883 eV (green) energies were used. By performing the quantitative analysis, the weights of Fe and O signals were 36% and 62%, respectively, while the Ce presence was in traces amounts, below 2% approximately. Interestingly, the Ce traces seemed to be homogeneously distributed over the whole nanoparticles (Figure 3-2A). In addition, EDX analysis confirmed the coexistence of Fe, Ce and O in the NPs (Figure 3-2B). The nanostructures were rich in Fe with respect to the Ce ratio, as indicated by the labeled main signals of $FeK\alpha_1$ and $CeL\alpha_1$. Signals of C and Cu

were mainly due to the TEM grids used for the analysis, and the presence of Cl and Si could be attributed to impurities present in the synthesis precursors.
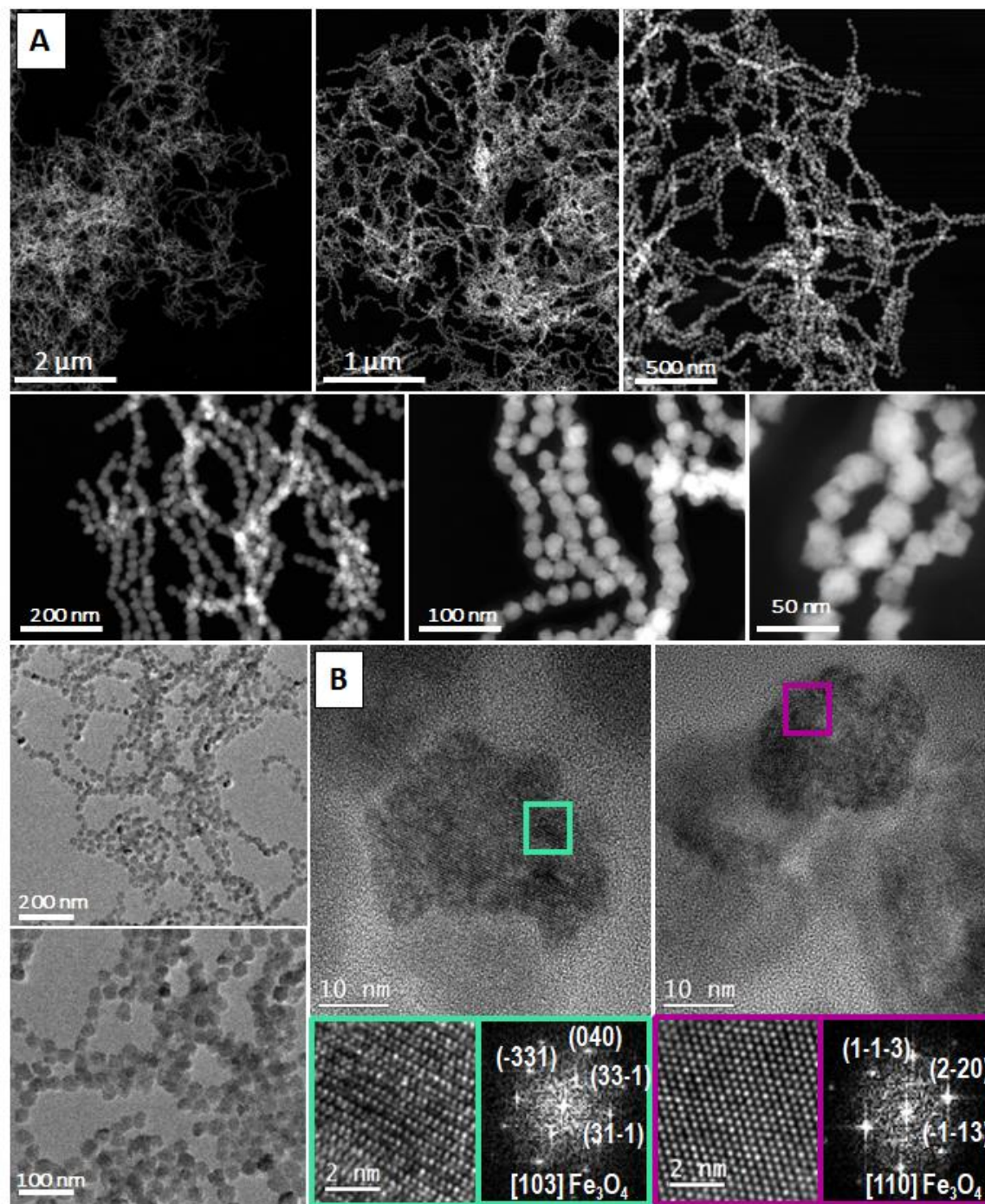
*Figure 3-1. Representative High Resolution HAADF-STEM and HRTEM images of the Ce@IONPs (26.7 ± 4.2 nm) as-obtained from the standard synthesis in the presence of Ce³⁺ and SC ions ([Ce³⁺]=0.5 mM) (**A**) low magnification and high magnification and (**B**) HRTEM images of a single NPs and their corresponding FFT patterns indexed to the magnetite crystal planes, reflections seen along the [103] and [110] zone axes (Scale bars: 10 and 2 nm).*
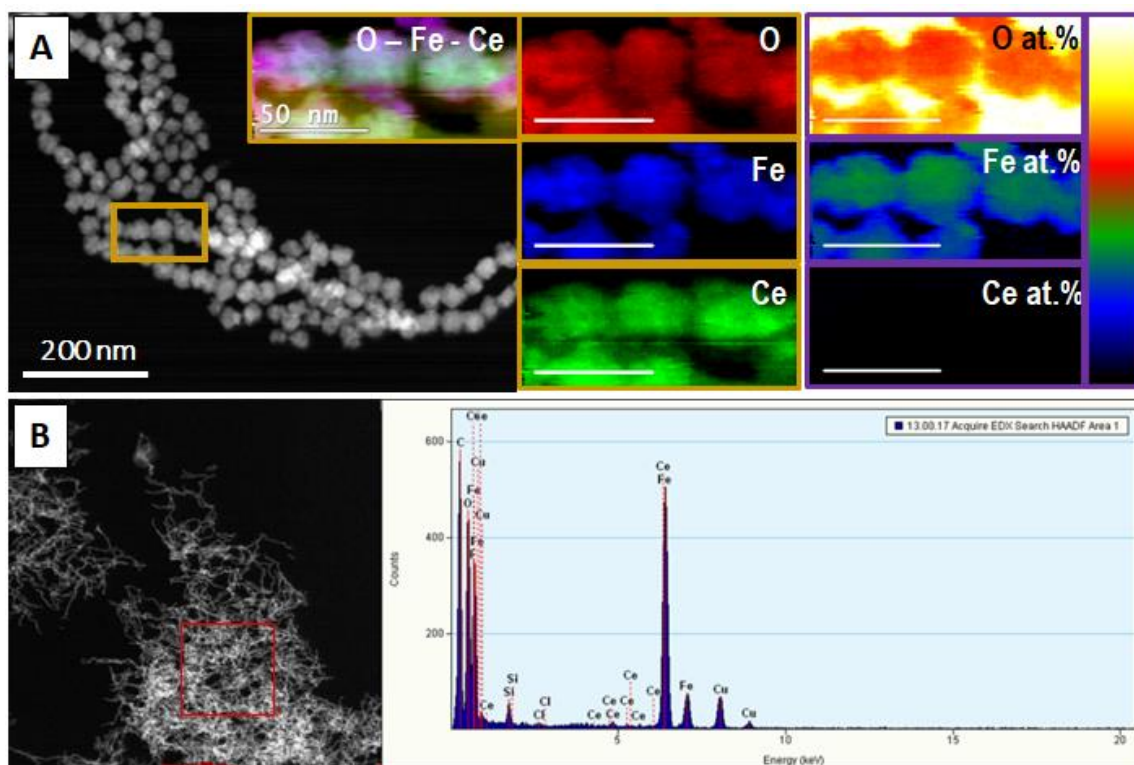
Figure 3-2. (A) HAADF STEM general view and Electron Energy Loss Spectroscopy (EELS) elemental analysis maps obtained for Ce@IONPs (26.7 ± 4.2 nm) (Scale bars: 200 nm and 50 nm), and (B) Representative Energy Dispersive X-ray spectroscopy (STEM-EDX) obtained for Ce@IONPs (26.7 ± 4.2 nm) (scale bar: 500 nm).

The X-ray diffraction (XRD) pattern matched with the cubic inverse spinel structure of magnetite (JCPDS 019-0629) (Figure 3-3), showing well-defined diffraction peaks of the (111), (220), (311), (400), (422), (511), and (440) planes. The prominent (111) peak at 18°, and the calculated lattice parameter of a = 8.380 Å, indicated that Ce@IONPs were composed mainly of magnetite phase, and no structural changes occurred upon the employ of Ce^{3+}. The average crystallite size and standard deviation was determined from the full width at half-maximum (FWHM) from the more intense peaks (i.e., (220), (311), (400), (511) and (440)) by using the Scherrer equation. Crystallite size by XRD gave a value of 24.3 ± 2.7 nm, which was close to the size distribution analysis obtained by TEM (26.7 ± 4.2 nm), indicating that the obtained particles were single crystals.
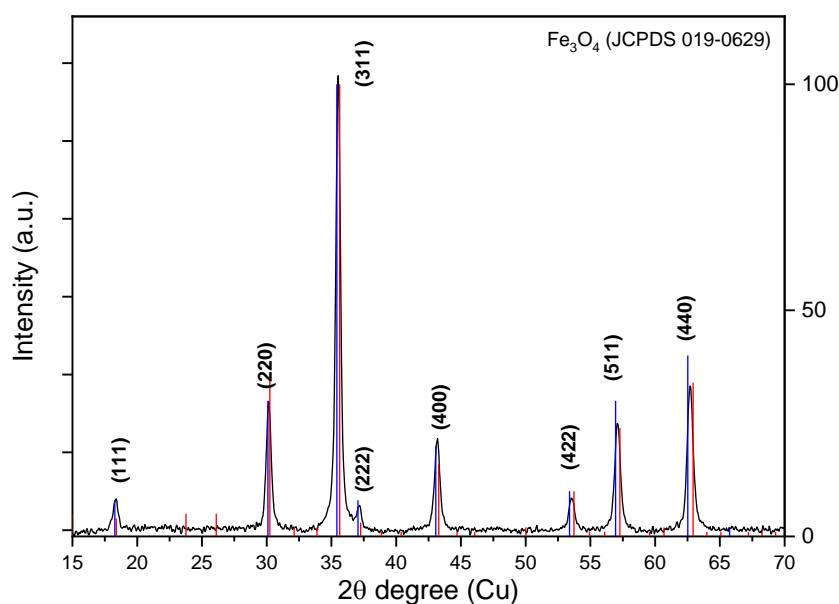
Figure 3-3. Powder XRD diffractogram of Ce@IONPs from the standard synthesis (Ce concentration at 0,5 mM) compared with the standard peaks of Fe3O4 (JCPDS 019-0629) (blue bars) and γ-Fe2O3 (JCPDS 039-1346) (red bars).

3.1.1 Size control of Ce@IONPs

Among the reaction parameters**,** the Ce concentration was found to be an important and convenient synthetic parameter to the obtention of single crystal Ce@IONPs with controllable sizes up to 46 nm.

Based on the standard synthesis described above, in the following synthesized set of samples, the final concentration of Fe^{2+}/Fe^{3+} (2:4 mM), SC (4 mM) and TMAOH (4 mL, 1 M, at 800 μL/min) were kept constant, while the concentration of $CeCl_3$ was varied from 0 to 2 mM in the premixed and oxygen-free SC solution.

Both the size and chemical composition of the obtained Ce@IONPs were affected by variations of the initial Ce^{3+} amount in the synthesis. Representative Bright field (BF) transmission electron microscopy (TEM) images of the obtained Ce@IONPs with varying sizes are shown in Figure 3-4. As shown, the increased Ce^{3+} amount from 0.1 to 1.25 mM leads to the formation of roughly spherical NPs with sizes which varying from 13.4 ± 2.7 nm to 46.3 ± 7.2 nm (Figure 3-4B-G) with a moderate narrow size distribution (Figure B1, Annex B). As expected from their size, it was possible to observe both superparamagnetic and ferromagnetic NPs. It was observed that as the NPs grew larger, they self-assembled onto the carbon-coated Cu grid. The NPs oriented one by one along the direction of their

easy magnetic axis to form string-like structures to decrease the magnetic repulsion during the grid dry, a behavior consistent with ferromagnetic NPs overcoming the steric forces associated Ce-SC coating.[57]
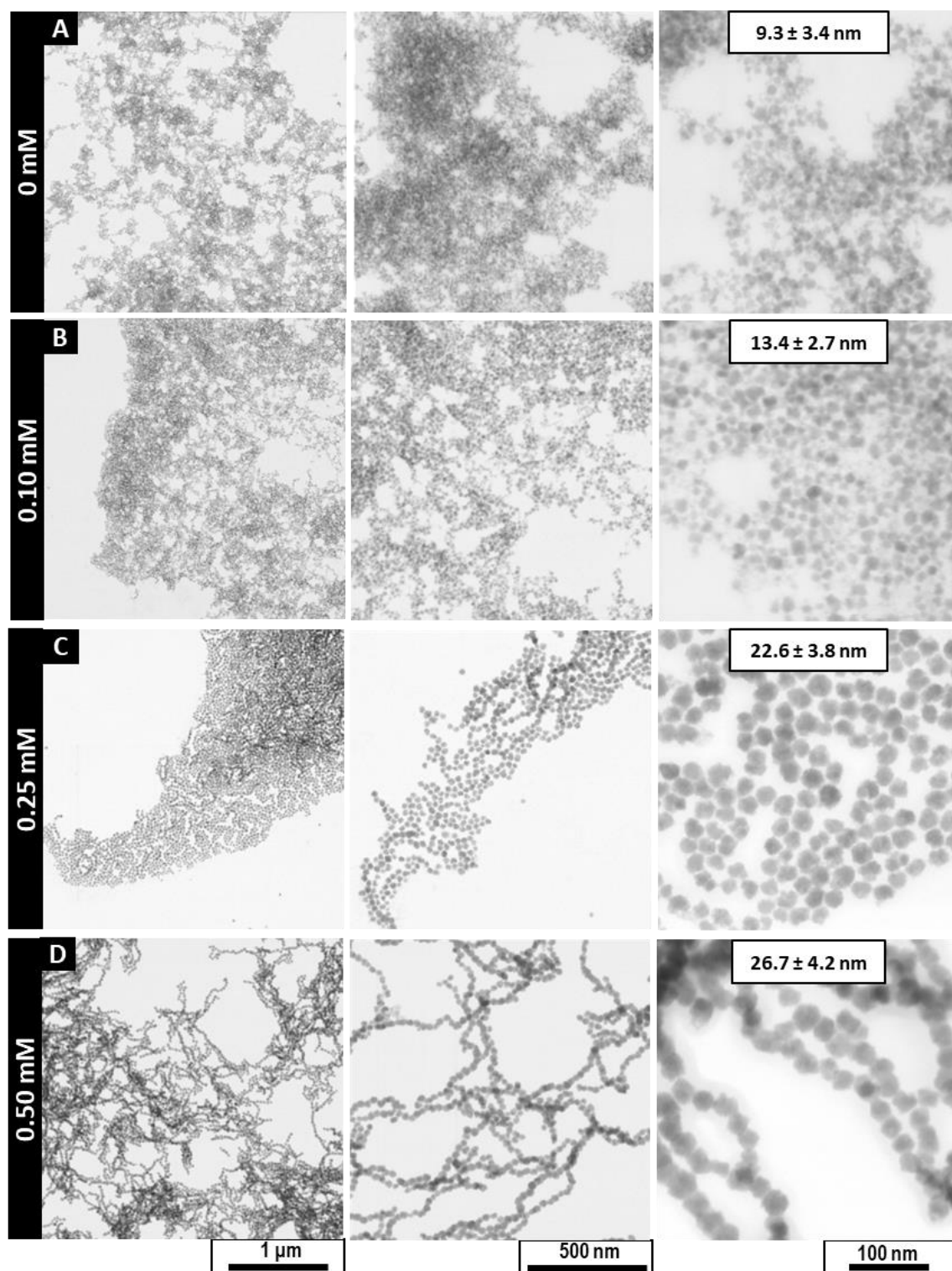
*Figure 3-4. Representative BF TEM images of the obtained Ce@IONPs synthesized with increasing Ce^{3+} concentration in the reaction media, (**A**) 9.3 ± 3.4 nm ([Ce^{3+}=0.0 mM]), (**B**) 13.4 ± 2.7 nm ([Ce^{3+}=0.10 mM]), (**C**) 22.6 ± 3.8 nm ([Ce^{3+}=0.25 mM]), (**D**) 26.7 ± 4.2 nm ([Ce^{3+}=0.50 mM]), (**E**) 34.0 ± 6.9 nm ([Ce^{3+}=0.75 mM]), (**F**) 42.3 ± 7.4 nm ([Ce^{3+}=1.00 mM]), (**G**) 46.3 ± 7.2 nm ([Ce^{3+}=1.25 mM]), (**H**) 80 ± 15 nm ([Ce^{3+}=1.60 mM]), and (**I**) 90 ± 20 nm ([Ce^{3+}=2.00 mM]). (scale bars: 1 μm, 500 nm and 100 nm).*
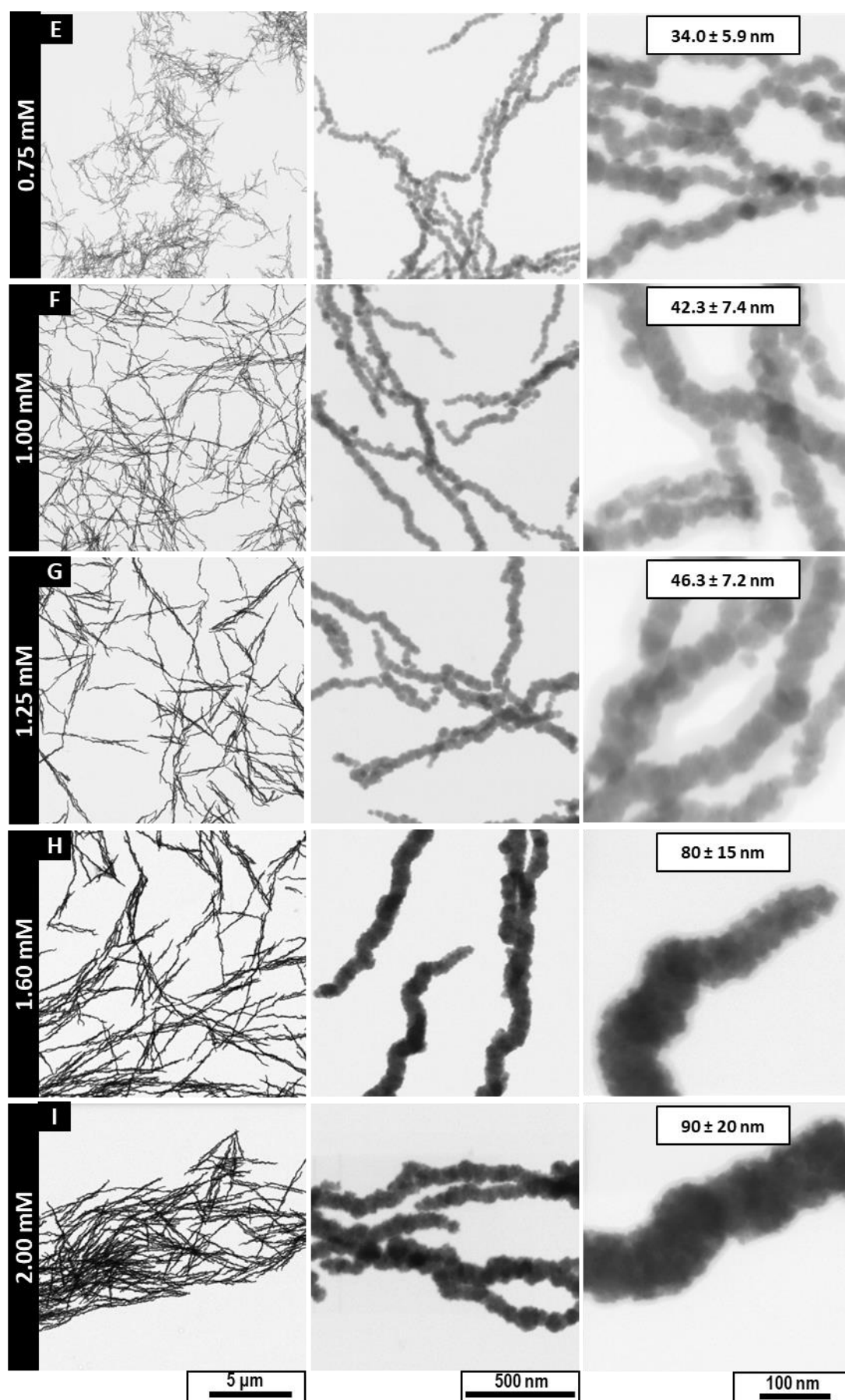
Figure 3-4. Continued. (scale bars: 5 μm, 500 nm and 100 nm).

In contrast, Ce@IONPs obtained at high Ce^{3+} concentrations (> 1.6 mM) formed dense multidomain nanowires structures by coalescence of very fine nanocrystals with sections from 80 to 90 nm in diameter and lengths extending into microns as shown in Figure 3-4H-I. Note that larger ferromagnetic NPs have greater relevance for different applications where their lower ratio of chemically active surface area per volume with respect to the core, show better stability against oxidation process, maintaining their magnetic properties for extended periods, and also offers easy and fast magnetic recovery from the work medium.

The reaction conditions, particle size measured by TEM (D_{TEM}), crystallite size calculated by XRD (D_{XRD}), crystallographic parameters, and elemental analysis of as-synthesized Ce@IONPs are summarized in Table 3-1.

Table 3-1. Summary of the physicochemical and crystallographic properties of obtained Ce@IONPs samples.

Ce^{3+} precursor (mM) [a, b]	D_{STEM} (nm)	D_{XRD} (nm)	Lattice Parameter a (Å)[c]	Volume unit cell (Å)	Strain (ε) x 10^{-3}	$X_{(Ce/Ce+Fe)}$ Precursor (%)[b]	$X_{(Ce/Ce+Fe)}$ (%)[e]	Reaction Yield [e] (%)
0.00	9.3 ± 3.4	11.6 ± 1.0	8.382	588.9	0.00860	0.0	0.0	89
0.10	13.4 ± 2.7	11.8 ± 0.3	8.381	588.7	0.00855	1.6	1.2	66
0.25	22.6 ± 3.8	17.5 ± 1.7	8.368	586.1	0.00565	4.0	3.2	69
0.50	26.7 ± 4.2	24.3 ± 2.7	8.380	588.6	0.00408	7.7	1.7	56
0.75	34.0 ± 5.9	32.2 ± 5.5	8.380	588.5	0.00307	11.1	1.6	44
1.00	42.3 ± 7.4	41.4 ± 8.5	8.379	588.3	0.00239	14.3	1.5	41
1.25	46.3 ± 7.2	47.5 ± 12.3	8.376	587.7	0.00211	17.2	1.5	32
1.60	80 ± 15[d]	46.4 ± 13.8	8.376	587.7	0.00204	21.1	1.7	30
2.00	90 ± 20[d]	44.5 ± 11.1	8.366	585.5	0.00224	25.0	1.8	17

[a] All prepared in the presence of SC (4mM).
[b] Nominal concentration of Ce^{3+} put in the reaction.
[c] Reported magnetite lattice parameter: 8.396 Å (JCPDS 019-0629).
[d] Rod width measurement.
[e] Acid digestion, ICP-OES determination.

The XRD patterns of the Ce@IONPs synthesized at different Ce^{3+} concentrations are shown in Figure 3-5A. All samples showed identical XRD diffraction patterns, and their positions and relative intensities were indexed to cubic inverse spinel structure of magnetite (JCPDS 019-0629). No other phases were observed in the analyzed samples after 2 h of reaction as indicated by the Rietveld refinement analysis (Figure B2, Annex B). The diffraction patterns of the samples showed well-defined diffraction peaks, which became

sharper and narrower with increasing Ce^{3+} concentration consistent with the progressive increase in the average crystallite size (calculated using Scherrer equation) and decreasing strain showed in Table 3-1. Comparison between the crystal sizes by TEM and XRD analysis (Figure 3-5B), indicated that Ce@IONPs synthesized with Ce^{3+} concentration from 0.1 to 1.25 mM were single crystals due to the closer values. In contrast, samples obtained with a Ce^{3+} concentration >1.6 mM were polycrystalline samples, composed of crystal approximately of 45 nm in size, similar to the larger single crystal NPs obtained. This suggests that polycrystalline nanowires grow in solution after smaller NPs form and self-assemble during the early stages of the reaction.
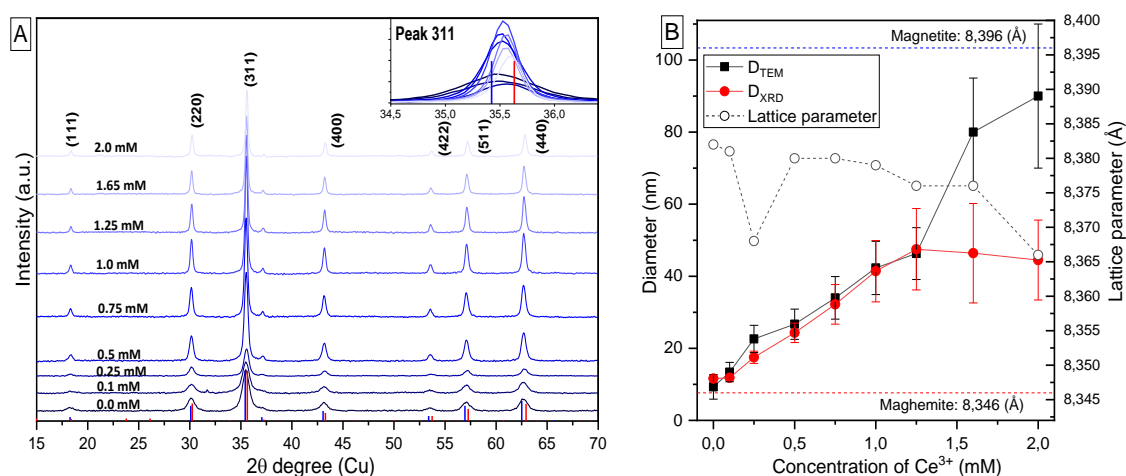
Figure 3-5. (A) Corresponding powder XRD diffractograms of Ce@IONPs synthesized by increasing Ce^{3+} concentration (0–2 mM), inset: shift of the peak (311) (blue bars: magnetite JCPDS:019-0629; red bars: maghemite JCPDS:039-1346). (B) Schematic representation of the variation of the crystal size (D_{TEM}) and (D_{XRD}), and lattice parameter as a function of the Ce^{3+} concentration.

The magnified image of the (311) peak shows a slight shift towards higher 2θ values and slight lattice parameter reduction of the Ce@IONPs with the increased Ce^{3+} amount in the media. However, on average the Ce@IONPs unit cell were between the unit cell of magnetite (591.86 Å) and maghemite (582.50 Å), which means that the obtained product was partially oxidized. No other crystallographic changes or the presence of other crystalline or amorphous phases suggesting the entry of Ce atoms into the iron oxide lattice could be inferred from the XRD analysis.

The partial oxidation could be at the NPs surface and can be attributed to the standard redox potential of the redox pairs in the reaction system, as for Ce^{4+}/Ce^{3+} is +1.61 V, while that Fe^{3+}/Fe^{2+} is +0.77 V, here the electron transfer reaction from Fe^{2+} to Ce^{4+} is a spontaneous or thermodynamically favored process as predicted by the Nerst equation.[45] The calculation to evaluate the effect of concentration at the redox pairs at the initial

conditions of the reaction, is related the standard free-energy change for the reaction, expressed as:

$$\Delta G = \Delta G° - RT\, LnQ$$

Where Q is the reaction equilibrium expression for the concentration in the reaction mixture at a given moment. Substituting $\Delta G = -nFE_{cel}$ in the previous equation gives the Nerst equation:

$$E_{cel} = E_{cel}° - \frac{RT}{nF} LnQ$$

Where, R is the ideal gas constant (J/mol K); T is the absolute temperature (K); F is Faraday's constant (96,480 C/mol); n is the number of moles of electrons transferred, and $E_{cel}°$ is equal to:

$$E_{cel}° = E_{red(catode)} - E_{red(anode)}$$

Then, assuming a well free-oxygen system, the presence of Ce^{4+} in the system, even at trace concentrations (ppt), could promote the oxidation of Fe^{2+}, leading to the formation of a partially oxidized magnetite phase.[37,46,58] In general, that condition could proceed through a trace Ce^{4+} reagent contamination, not a completely deoxygenated system, and the Ce^{3+} → Ce^{4+} conversion as the reaction pH increased, which increased the driving force for the oxidation reaction. Thermodynamic calculations are shown in Figure B3, Annex B).

ICP-OES were performed to quantify the amount of Ce and the reaction yield in the synthesized Ce@IONPs (Table 3-1). Regardless of the Ce^{3+} concentration added to the reaction mixture, Ce incorporation into the NPs remains relatively low, ranging from 1.2% to 3.2% In all the synthesis Ce values were lower than the initial amount of the Ce precursor put in the synthesis, and at Ce^{3+} concentration of 0.25 mM (NPs size ~23 nm) the percentage of Ce reached a maximum of 3.2% and started to decrease until ~1.5% as increased the NPs size, which is consisted with the decrease of surface area to volume ratio. Note that in the synthesis Ce^{3+} and SC ions mainly play the role of controlling the size of the magnetite crystal, keeping the crystal surface active for growth, some Ce^{3+} ions may be incorporated into the structure or attached to the surface, but most of them, as the magnetite crystal grows, are expelled into the reaction media. Most of Ce precursor remained in the solution complexed with the SC under the inert conditions at least during the 2 h reaction.

The limited Ce incorporation can be attributed to the large size of Ce^{3+} (1.15 Å). As reported, in general, cations with similar ionic radii to Fe (i.e., Mg, Co, Ni, or Zn) are easily incorporated within the magnetite bulk structure forming a solid solution $M_xFe_{3-x}O_4$;[35,59,60] and heavier ions as Bi, Gd, appear to be concentrated near the surface of the crystals.[37,39,61]

Considering the large ionic radius of Ce^{3+} (1.15 Å, coordination number (CN) = VI), in comparison with that of the Fe^{3+} (0.63 Å, CN = VI) and Fe^{2+} (0.78 Å, CN = VI) ions, it is expected that Ce^{3+} are distributed over the surface forming a shell structure or a capping agent bounded to the NPs surface.[60,61] Surface characterization will be discussed below.

Remarkably, increasing concentrations of Ce^{3+} significantly decrease the reaction yield, suggesting that Ce^{3+} may stabilize intermediates. Indeed, these intermediates could serve as a source of monomers for NP's growth, albeit at the cost of reduced overall yield. In other words, the presence of Ce^{3+} seems to promote growth against nucleation at the same time that reduce iron incorporation into the NPs leading to a more controlled crystallization process. This point will be further discussed in sections below.

3.3.2 Ce@IONPs Surface Characterization

Surface characterization was followed by FTIR, TGA and surface charge and XPS analysis. The surface covering with citrate as organic capping agent in the obtained Ce@IONPs was proven by FTIR analysis by comparing the Ce@IONPs spectra with the spectra of bared IONPs, citrate cover magnetite NPs (SC-IONP), trisodium citrate (SC) and SC-CeO_2 NPs, as shown in Figure 3-6.

FTIR analysis further elucidates the interaction of citrate as a capping agent and the structural modifications imparted by Ce doping. All the samples showed characteristic O–H bending vibrations signaled by the broad band at 3500–3200 cm^{-1} and a stretching at 1614 cm^{-1} (Figure 3-6), indicating the presence of hydroxyl groups or water moieties adsorbed on the NPs surface, due to the aqueous synthesis environment. media. For the Ce@IONPs, the apparition of the two absorption peaks at 1562 and 1395 cm^{-1} were assigned to the asymmetric and symmetric stretching of the carbonyl group (COO^-), respectively, which confirmed the presence of citrate ions on the surface (Figure 3-6c and d), similar to observed in the synthesized SC-IONPs (in Chapter 2).[62] Furthermore, in the far-infrared region, typical bands at low frequency around 576 cm^{-1} were referred to Fe–O vibration in octahedral and tetrahedral sites, and 438 cm^{-1} were ascribed to Fe–O vibration in octahedral sites.[49] While, the Fe–O bands in both Ce@IONPs samples, and compared with the CeO_2-SC reference spectra showed peak broadening to the right, that could be due to the increment of cation vacancies in the lattice, indicating that Ce ions may occupy some Fe sites.[63] Moreover, in some spectra (Figure 3-6a, c and d), two bands were observed at 1488 cm^{-1} and 948 cm^{-1}, and assigned to the asymmetric stretching vibration of –CH_3

characteristic of tetramethyl ammonium hydroxide (TMAOH) molecule, which confirmed the presence of TMA$^+$ cation traces on the NP surface.[64]
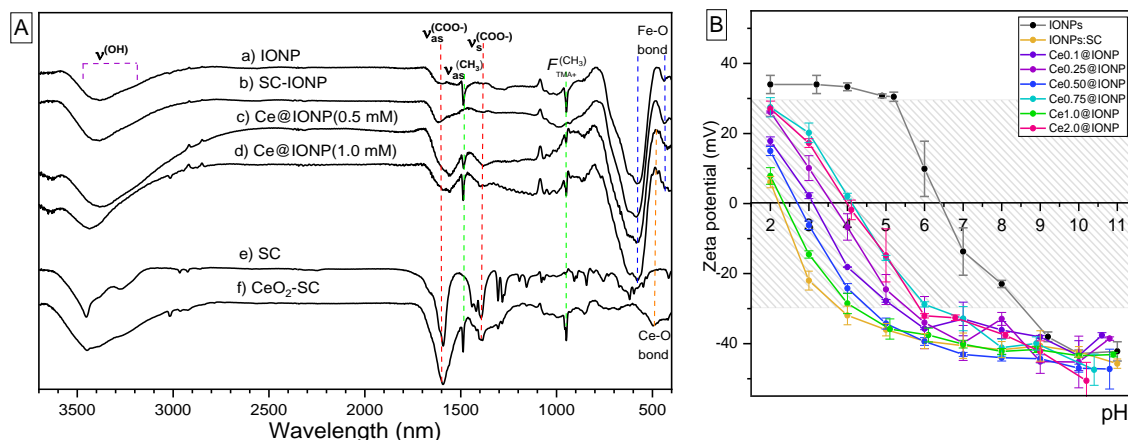
Figure 3-6.(A) FTIR spectra for Ce@IONPs of two different sizes, corresponding to Ce precursor concentrations of 0.5 and 1.0 mM (c,d), compared with those produced in the absence of Ce^{3+} and SC cations (a, b). SC (e) and citrate-coated cerium oxide NPs (f) are included for comparison. (B) Zeta potential as a function of pH for the as-synthesized magnetite NPs of different sizes, compared with those produced in the absence of Ce3+ cations (~9.3 nm) and SC (~10.1 nm).

The characteristic charge of the nanomaterial surface was determined for the Ce@IONPs by the ζ-potential curve as a function of pH and compared with the bared IONPs and SC-IONPs, as shown in Figure 3-6B.

Aqueous colloidal suspensions of the as-synthesized IONPs exhibited a negative effective surface charge > -40 mV at pH~11. Citrate-stabilized IONPs produced in the absence of Ce cations exhibit a strong negative surface charge (below -40 mV) and an isoelectric point (IEP) around pH ~2. With increasing Ce concentrations, the IEP shifts to higher pH values (2–4), indicating that Ce cations accumulate on the NP's surface. However, the presence citrate ions at the surface, granting the NPs colloidal stability across a wide pH range (5–11), that could be useful for possible biomedical applications at physiological pH.[65] In addition, thermogravimetric analysis of selected Ce@IONPs samples (Figure B4, Annex B), showed a first gradual weight loss at ~120°C corresponding to the loss of absorbed water, and a second loss at ~230–400°C, corresponding to the loss of citrate molecules at the surface from 2.9% to 7.9 %. [65] This SC loss could be related to the Ce content found in the NPs, being the major loss which had the major Ce content (Ce at 0.25 mM). After 380°C, no weight loss was observed, achieving weight stability.[10]

The Ce@IONPs surface were analyzed by XPS and compared with those of bared IONPs and SC-IONPs. XPS analysis confirmed the presence of Fe, Ce, O, and C in the Ce@IONPs samples. Corresponding deconvoluted spectra are shown in Figure B5-B8,

(Annex B). Representative survey scan XPS analysis and their individual and deconvoluted spectra of Fe 2p, Ce 3d, O 1s and C 1s from the sample Ce@IONPs (~23 nm) using Ce^{3+} at 0.5 mM are shown in Figure 3-7.
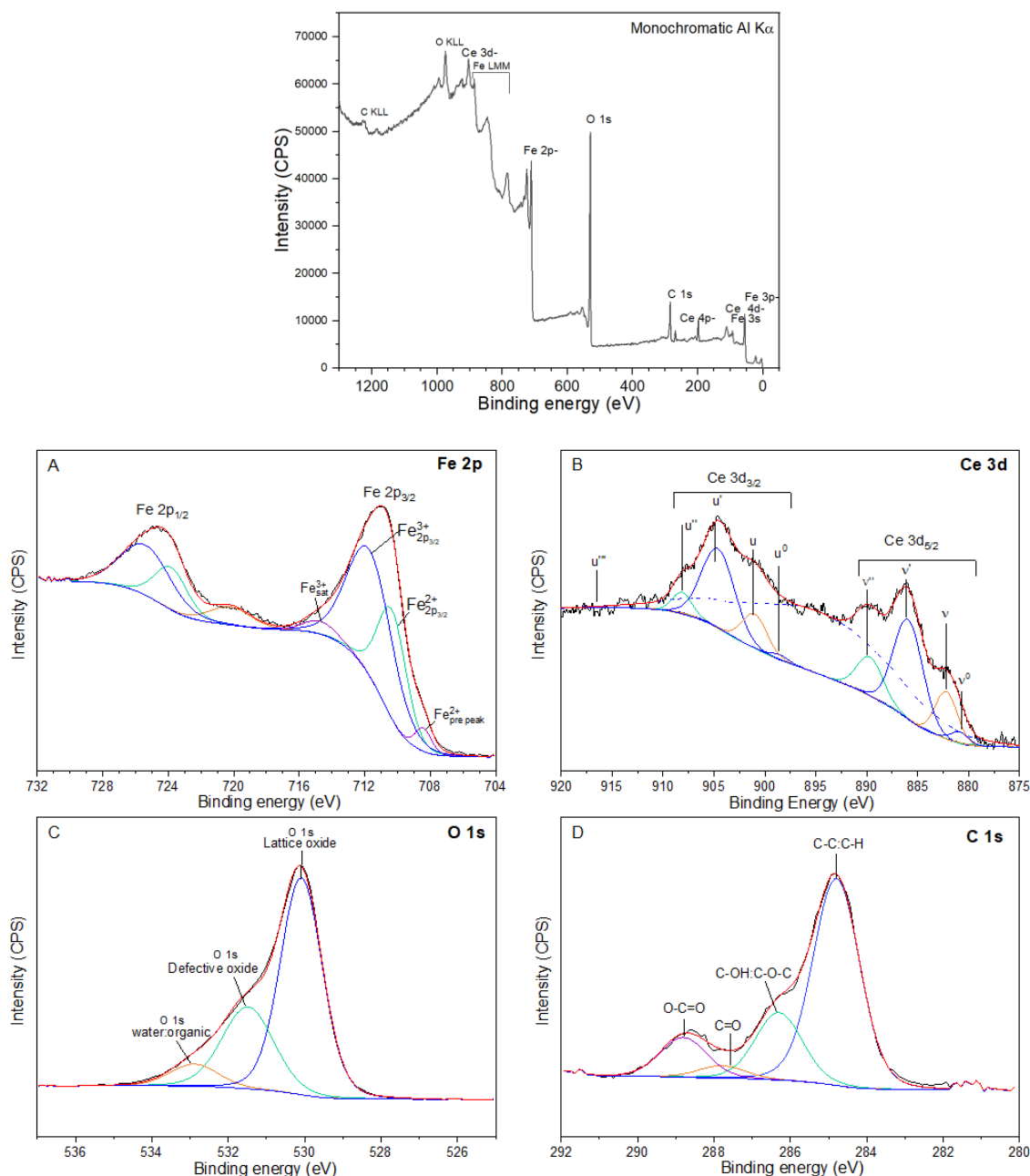
Figure 3-7. XPS survey scan of Ce@IONPs (sample Ce at 0.5 mM) and individual XPS peak fitting spectra of (A) Fe 2p, (B) Ce 3d (C) O 1s and (D) C 1s in Ce@IONPs (~23 nm) at Ce^{3+} concentration 0.5 mM.

The Fe 2p spectra showed Fe photoemission lines corresponding to Fe $2p_{3/2}$ (710.8 eV) and Fe $2p_{1/2}$ (724.4 eV), characteristic of Fe^{3+} in magnetite and maghemite particles (Figure 3-7A). The presence of Fe^{2+} was indicated by the binding energy shift and intensity for Fe $2p_{3/2}$ and Fe $2p_{1/2}$ peaks towards 708 eV and 723 eV, respectively, characteristic of iron oxides which contains both Fe^{3+} and Fe^{2+} in multivalent iron oxide Fe_3O_4.[41,66–68] The Fe^{2+}

/Fe^{3+} ratio was found to be 1:1.7, which was close to the molar ratio (1:2) put at the beginning of the reaction (Figure B5, Annex B). In addition, a satellite line at 719 eV of Fe^{3+}, which is more prominent in Fe_2O_3 was observed.[66] Thus, XPS analysis indicates a partially oxidized magnetite surface.[69]

Characteristic peaks of both Ce^{3+} and Ce^{4+} ionic mixtures were observed for the Ce@IONPs, corresponding to the $3d_{5/2}$ and $3d_{3/2}$ spin-orbital split of the Ce 3d spectra (Figure 3-7B). These contrasts with the non-doped IONPs and SC-IONPs which did not present those peaks (Figure B9, Annex B). The individual spectra of Ce@IONPs were analyzed by subtracting the Fe_3O_4 background in the range of 875–920 eV, possibly due to the Fe Al(Kα) Auger line $LM_{23}M_{23}$ at 888 eV,[70] observed in the non-doped IONP and SC-IONP samples(Figure B9, Annex B). After that, the individual contributions of the Ce^{3+} and Ce^{4+} ions to the XPS spectra were deconvoluted in their respective peak components, as exemplified for the Ce@IONPs at Ce 0.5 mM (Figure 3-7B). The Ce fitting and the sum of the individual contribution of the deconvoluted peaks allowed the Ce^{3+} (v^0, v', u^0, u') and Ce^{4+} (v, v", v''', u, u", u''') species to be differentiated. The satellite peak u''' (916.7 eV) is characteristic of Ce^{4+} ions, indicating its presence in the sample.[71]

According to the Ce 3d fitted spectra, the main contribution in the Ce@IONPs samples corresponded to the u' and v' components at 904.2 ± 0.2 eV and 885.6 ± 0.2 eV, which is characteristic of the Ce^{3+} ions. In addition, we can observe a minor contribution of the u and v components at 901.0 ± 0.1 eV and 882.5 ± 0.2 eV, which is characteristic of the Ce^{4+} ions. In some samples, the satellite peak observed at 916.5 eV confirmed surface doping with Ce^{4+} (Figure B6, Annex B). The Ce^{3+}/Ce^{4+} ratio was determined to be an average of 1.5:1, indicating that cerium was mostly in the Ce^{3+} state Therefore, the results indicate that the surface of the Ce@IONPs was doped with both Ce^{3+} and Ce^{4+} mixed oxides. The existence of a redox cycle Ce^{4+}/Ce^{3+} on the surface of the IONPs can cause the oxidation of Fe^{2+};[45] therefore, the surface might have more Fe^{3+} and Ce^{3+} states.

The O 1s XPS spectra of the Ce@IONPs consists of a sharp main peak at 530 eV indicating the oxide formation (Figure 3-7C, Figure B7-Annex B).[66,72] The peak broadening towards 531.5 eV and 532.8 eV was associated with defective oxide or hydroxyl groups (~24% intensity) and water (~6% intensity), respectively, as observed in the analyzed samples. Note that the intensities of the peaks do not directly correspond to the relative concentrations.[73,74] These hydroxyl groups can be correlated with the presence of hydroxyl- from the SC carboxylic groups, or with the formation of Ce hydroxyl groups

bonded to the surface of the NPs, similar to the results reported for Bi-doped magnetite NPs by Laguna et al.[61]

The C 1s spectra were fitted to the C 1s saturated hydrocarbons (C−C: C−H) at 284.8 eV (Figure 3-7D, Figure B8-Annex B). Apart from the main peak, synthesis of Ce@IONPs in the presence of SC exhibited two main signals at 288.8 and 287.8 eV corresponding to O−C=O and C=O bonds, respectively, as well as a predominant shoulder at 286.3eV corresponding to C−O−H bonds, which are related to the carboxylic groups and the central carbon bonded to the hydroxyl group in the citrate molecule.

Therefore, the formation IONPs in aqueous medium containing Ce^{3+} and SC ions resulted in the attachment of Ce and carboxylic groups onto the particle surface, which resulted in the formation of citrate shell around the magnetic iron oxide core, likewise to that observed in the treatment of ceria oxide or hydroxide surfaces stabilized with sodium citrate or citric acid.[75,76]

Although the structure of the shell with respect to the Ce and SC order bonding in the Ce@IONPs surface is not fully clear. According to a SEM analysis where organic coverage was observed (Figure 3-8) and similar works,[46,61,65] it is possible to assume that Ce is attached to the Fe−O surface through hydroxyl groups $M-OH_x$ formed during the titration process and at the same time is partially complexed by some SC units, as organic part. Thus, by electrostatic attraction, positively charged Ce may be attached on the NP surface forming $Fe-O-Ce(III)-L_m$ complexes, where L_m can be any Ce coordinated ligand (L_m= OH, H_2O or SC).[46]
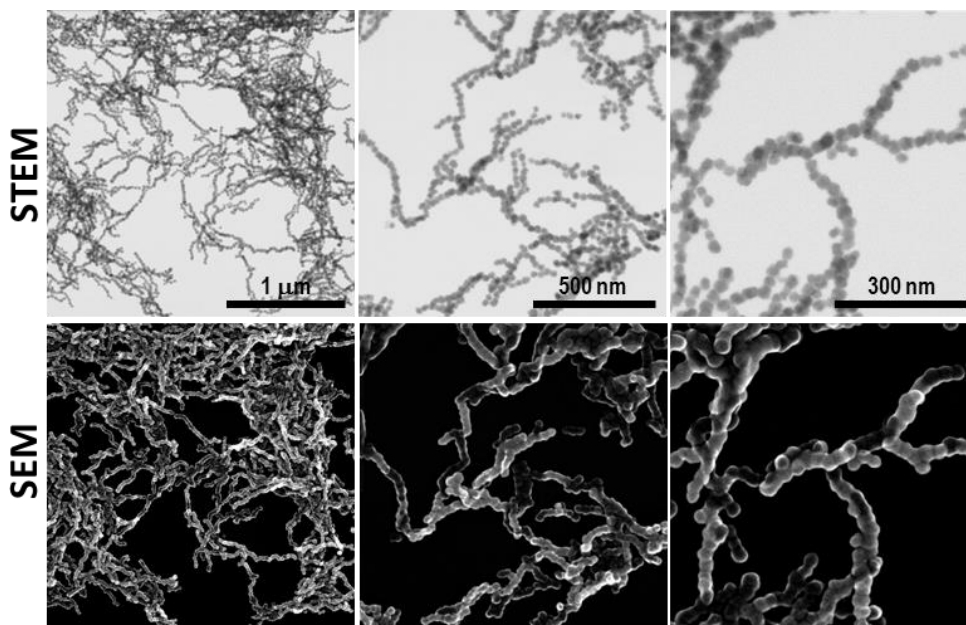
Figure 3-8. BF TEM and SEM images of Ce@IONPs at Ce3+ concentration 0.5 mM, showing a possible Ce-SC shell over the particles.

3.3.3 Magnetic Characterization

The magnetic responses for selected IONPs synthesized with increasing Ce concentration (9.3 nm, 22.6 nm, 26.7 nm, 34.0 nm and 42.3 nm ([Ce^{3+}= 0.00, 0.25, 0.50, 0.75 and 1.00 mM], respectively) were evaluated by measuring hysteresis loops at 10 K (Figure 3-9A, Table 3-2) and normalized by ICP analysis. Hysteresis loops at 10K indicate high saturation magnetization (M_s) values for all samples being the IONPs ~34 nm ([Ce^{3+}= 0.75] the ones showing the highest value (97 emu/g). The M_s values of the synthesized IONPs laying between those accepted for Fe_3O_4 (92 emu/g) and γ-Fe_2O_3 (72 emu/g) reported bulk values at 300 K.[9] The magnified inset in the origin of the hysteresis loops indicates a ferrimagnetic (FM) behavior at 10 K for all the samples and moderate coercivity (H_C) between 129 and 305 Oe, which seems to follow an increasing tendency with increasing size, at least for the samples of 23 nm, 27 nm, and 34 nm (Figure 3-9, inset).

Normalized M_S indicated that IONPs synthesized in the presence of Ce^{3+} cations above 23 nm exhibited a high magnetic susceptibility to low magnetic fields, reaching saturation already at 10 kOe, compared to the bared IONPs (Figure 3-9). This is in agreement with the higher contribution of the surface, especially in the magnetic response of the smaller NPs ~9 nm, which act as a spin-glass. This was reflected in their lower magnetic susceptibility value (χ_{HF}), which decreases with increasing NPs size. It is noteworthy that in our results we did not clearly observe an influence of Ce cation incorporation in their magnetic performance, even for sample with the highest Ce content (~23 nm; ~3.2% Ce). In fact, the *f*-electron of Ce cloud interferes with the ferromagnetic order of magnetite structure diminishing the overall magnetic moment. This behavior has been previously described in other lanthanide-doped IONPs of similar size.[39,42,53,77]

Furthermore, it is worth noting that some of the iron oxide nanoparticles (IONPs) obtained in this study fall within the optimal size range for magnetic hyperthermia (MH), which is between 20 and 26 nm.[78] These IONPs also have the advantage to present low polydispersity and are coated with SC, which can improve their performance, dispersion and stability in MH applications.[79] Thus, IONPs samples of 23 nm, 27 nm and 34 nm were further characterized by zero-field cooling (ZFC) and field-cooling (FC) methods (Figure 3-9C). For IONPs with a size of approximately ~23 nm, the overlap of the ZFC and FC curve close to 280 K, suggesting that NPs are between the FM to SPM transition at RT. In contrast, the IONPs with sizes of ~27 and ~34 nm clearly indicate that NPs are blocked at

RT or in ferrimagnetic state. This ZFC/FC analysis also suggests that IONPs with size below ~23 nm were SPM.

Table 3-2. Summary of average particle diameters by TEM, saturation magnetization (M_S), remanence (M_R), coercive field (H_C), for selected IONPs at 10 K.

Ce^{3+} (mM)	Size $_{TEM}$ (nm)	M_S (emu g^{-1})	M_R (emu g^{-1})	χ_{HF}	H_C (Oe)	T_b (K)
0.00	9.3 ± 3.4	76	16	1.5 x10^{-4}	244	n.d
0.25	22.6 ± 3.8	86	19	1.9x10^{-4}	129	~280
0.50	26.7 ± 4.2	90	23	1.8 x10^{-4}	230	>300
0.75	34.0 ± 6.9	97	26	2.5x10^{-4}	305	>300
1.00	42.3 ± 7.4	81	22	2.7 x10^{-5}	195	n.d

n.d: not determined.
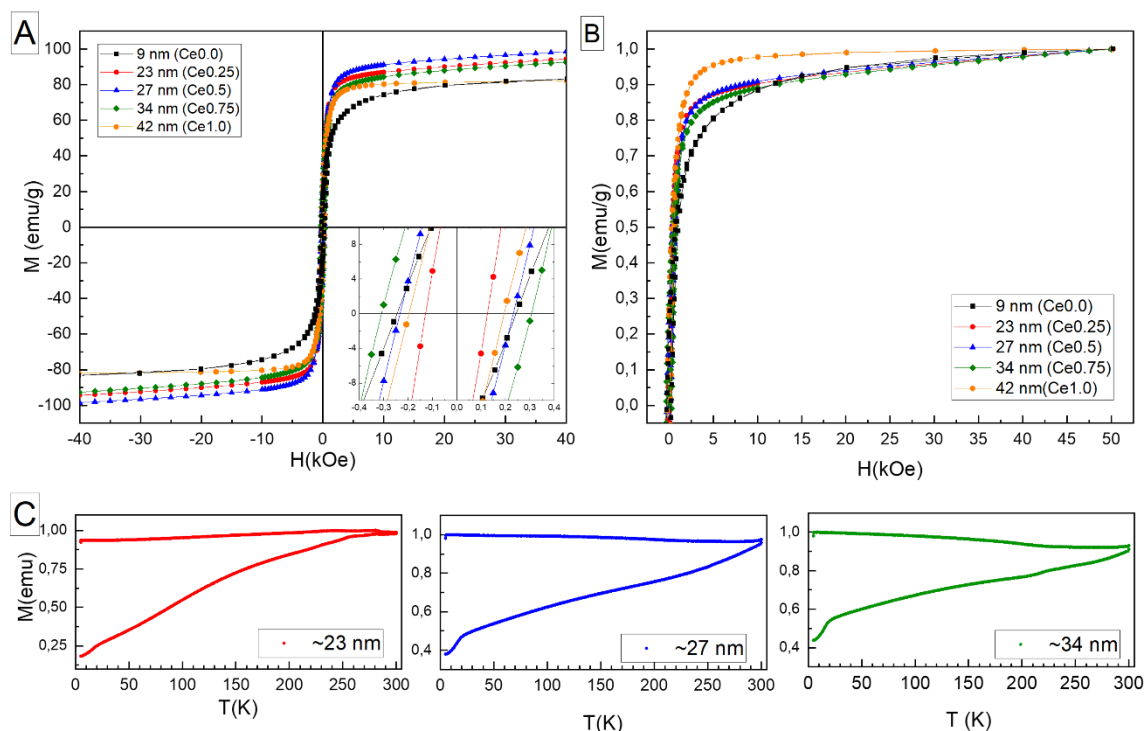
*Figure 3-9. Magnetization hysteresis at (**A**) 10 K of selected IONPs synthesized with increasing Ce concentration (9.3 nm, 22.6 nm, 26.7 nm, 34.0 nm and 42.3 nm ([Ce^{3+}= 0.00, 0.25, 0.50, 0.75 and 1.00 mM], respectively), Inset: magnified loop over the range <400 Oe. (**B**) Normalized half-magnetization curves at 10K (showing positive branch). (**C**) Zero field cooled (ZFC)/field cooled (FC, 50 Oe) curves for 23 nm, 27 nm and 34 nm IONPs ([Ce^{3+}= 0.25, 0.50, and 0.75 mM], respectively).*

3.3.4 Synthesis using other Lanthanides (Ln@IONPs)

To demonstrate the robustness of our synthetic procedure and investigate the influence of other lanthanides cations on the growth of IONPs, we extended our standard synthesis to include Eu^{3+}, Gd^{3+}, Er^{3+}, Yt^{3+}, and Lu^{3+} ones. Chloride or nitrate lanthanide salts

precursor were used for this synthesis. All samples were synthesized under the same synthetic conditions (reaction temperature, reactants concentrations (specifically [Ln^{3+}] = 0.5 mM), alkaline titration rate (800 µL/min), and time).

Representative BF TEM images of the obtained Ln@IONPs are shown in Figure 3-10. TEM images clearly show that varying the Ln cation does not significatively affect the final morphology of the IONPs, leading to the growth and to the obtention of monodispersed IONPs (<15%) (Figure B10-Annex B). The use of the same Ln concentration (0.5 mM) produced magnetic Ln@IONPs with sizes ranging from 20–27 nm. Their self-assembly in wires indicated their ferromagnetic behavior.

A comparison between the employ of lanthanide chloride (Cl$^-$) or nitrate (NO^{3-}) precursors showed that the variation in the counter ion did not significantly affect the crystal growth of Ln@IONPs (Figure 3-10). For instance, IONPs obtained using ErCl$_3$ or Er(NO$_3$)$_3$ precursors exhibited similar XRD crystal sizes (20.9 ± 1.7 and 22.0 ± 2.7, respectively) as shown in Table 3-3.
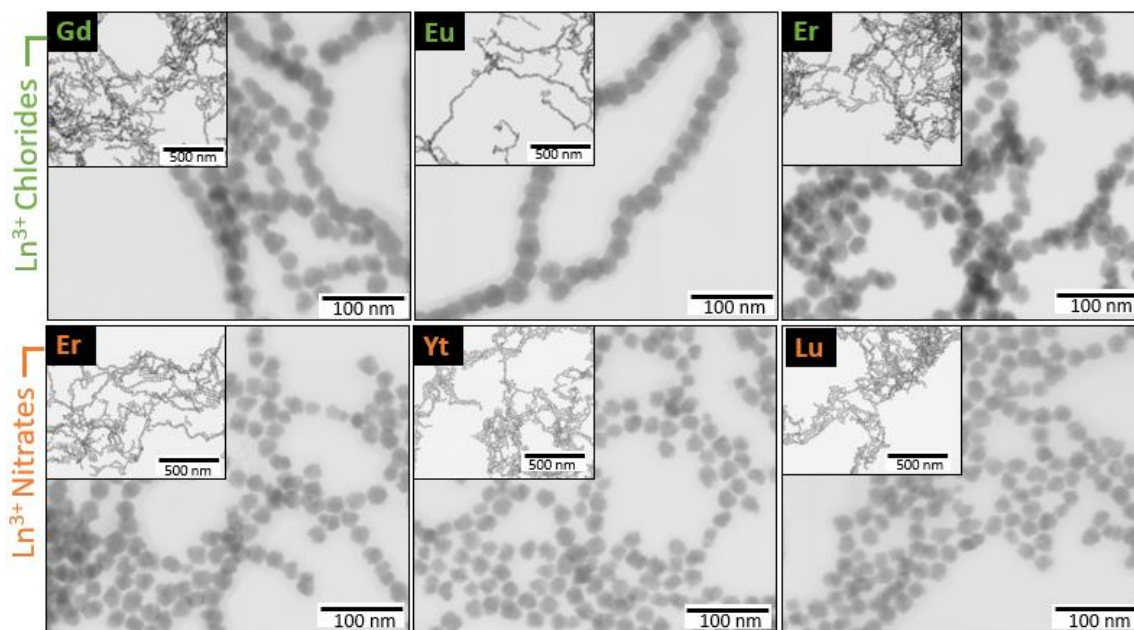
Figure 3-10. Representative BF TEM images of the obtained Ln@IONPs via the co-precipitation in the presence of SC and different lanthanide ions (Ln = Eu^{3+}, Gd^{3+}, Er^{3+}, Yt^{3+}, and Lu^{3+}) at 0.5 mM (scale bars: 500 nm and 100 nm).

Like observed with the Ce^{3+} cations, the variation of the Ln concentration in the synthesis process can achieve control over particle size, as demonstrated by the two sets of samples synthesized with Eu and Gd cations (Figure 3-11, Table 3-3). In these samples, the size of the particles gradually increases with higher Ln concentrations. This demonstrates the robustness and extensibility of our proposed synthesis method for obtaining other Ln@IONPs with tuned crystals sizes in the range of transition from SPM

to FM behavior, that could be of interest for example in magnetic hyperthermia applications.[80]
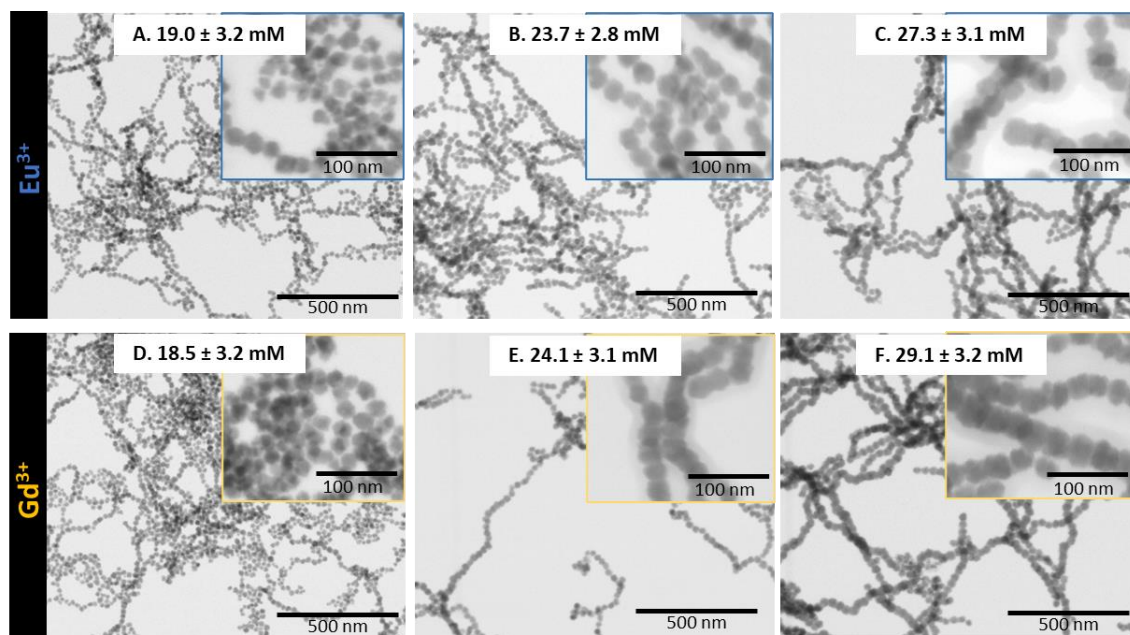
*Figure 3-11. Representative BF TEM images of the resulted IONPs synthesized in the presence of Eu^{3+} and Gd^{3+} ions at different concentrations ([Ln^{3+}] = 0.3 mM (**A, D**), 0.5 mM (**B, E**), and 1.0 mM (**C, F**)). (scale bars: 500 and 100 nm).*

XRD powder diffraction patterns of the samples were indexed to the pattern of magnetite inverse spinel structure, and no structural changes or other phases owing to the lanthanide used were observed by Rietveld refinement analysis (Figure 3-12, Figure B11-Annex B). Crystal size determined by XRD analysis were consistent with the TEM data, indicating the obtention of single-crystals Ln@IONPs (Table 3-3). The microstrain of all synthesized NPs, was consistent with their size and in general, increased as the crystal size decreased. Notably, it was observed that crystal size decreased with increasing lanthanide atomic number, probably due to the decrease in Ln ionic radii from Ce^{3+} (115 pm) to Lu^{3+} (100 pm). These findings were supported also at higher concentrations of the Ln cations used (Table 3-3).

The calculated lattice parameters of Ln@IONPs were quite close to the reported lattice parameter of magnetite (a = 8.396 Å), indicating that the synthesized particles were composed of Fe_3O_4 as the main phase (Table 3-3). Note that this proximity to the magnetite unit cell can be related to the fact that these lanthanides used only had a 3+ oxidation state (except for Eu $2^+/3^+$) (Figure B12-Annex B). Working with other Ln results easier since the oxidation of Fe^{2+} is a non-spontaneous process, in comparison when is worked with Ce^{3+}. For example, when Eu^{3+} is used, as the standard redox potential of Eu^{3+}/Eu^{2+} is
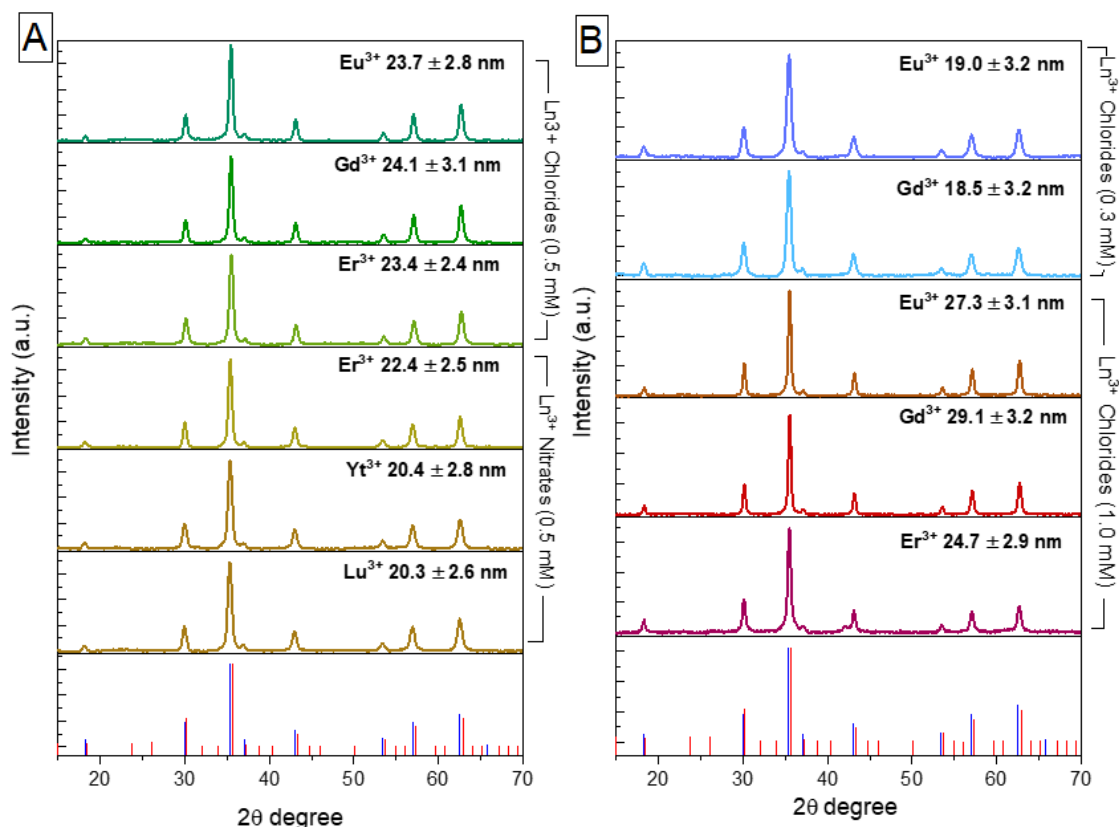
*Figure 3-12. Powder XRD diffractograms of the obtained IONPs synthesized by coprecipitation in the presence of SC and different lanthanides (Ln = Eu^{3+}, Gd^{3+}, Er^{3+}, Yt^{3+}, and Lu^{3+}) (**A**) at 0.5 mM (chlorides and nitrates precursors) and (**B**) at 0.3 and 1.0 mM (chlorides precursors). Size labels correspond to NP's diameter as determined by TEM (For NPs synthesized with Ce^{3+}, see Figure 3-5 main text). Blue bars represent the magnetite pattern, and red bars represent the maghemite pattern.*

Table 3-3. Effect of lanthanide cations on the crystallographic properties of magnetic Ln@IONPs.

Ln^{3+} Conc. (mM) [a]	Ln^{3+} precursor	D_{STEM} (nm)	D_{XRD} (nm)	Lattice parameter (Å)	Volume unit cell (Å)	Strain (ε)
0.5	$EuCl_3$	23.7 ± 2.8	24.0 ± 2.6	8.383	589.1	0.00398
0.5	$GdCl_3$	24.1 ± 3.1	24.3 ± 2.6	8.382	588.9	0.00404
0.5	$ErCl_3$	23.4 ± 2.4	20.9 ± 1.7	8.380	588.5	0.00470
0.5	$ErNO_3$	22.4 ± 2.5	22.0 ± 2.7	8.387	590.0	0.00435
0.5	$YtNO_3$	20.4 ± 2.8	19.3 ± 1.3	8.385	589.5	0.00519
0.5	$LuNO_3$	20.3 ± 2.6	19.0 ± 1.9	8.388	590.2	0.00508
0.3	$EuCl_3$	19.0 ± 3.2	18.1 ± 1.3	8.386	589.7	0.00565
0.3	$GdCl_3$	18.5 ± 3.2	18.8± 1.8	8.394	591.4	0.00564
1.0	$EuCl_3$	27.3 ± 3.1	29.1 ± 3.1	8.382	588.9	0.00340
1.0	$GdCl_3$	29.1 ± 3.2	29.7 ± 3.2	8.383	589.1	0.00332
1.0	$ErCl_3$	24.7 ± 2.9	23.9 ± 1.9	8.384	589.3	0.00415

[a] All prepared in the presence of [SC] = 4 mM.
[b] Magnetite lattice parameter reported: 8.396 Å (Standard JCPDS: 019-0629).

-0.35 V, the electron transfer reaction from Fe2+ to Eu3+ is a non-thermodynamically favored process calculated by the Nerst equation (Figure B3, Annex B). However, further surface oxidation studies of these Ln@IONPs could be of interest.

XPS characterization of the Ln@IONPs from the chloride precursors (Eu, Gd, and Er at 0.5 mM) reveled the characteristic peaks of Fe $2p_{3/2}$ and $2p_{1/2}$, O 1s and C 1s consistent for magnetite NPs, and the lanthanide spectra for Eu, Gd and Er, confirmed their incorporation within the NP's surface, respectively (Figure 3-13). Comparison of the XPS spectra of the $3d_{3/2}$ and $3d_{5/2}$ photoelectron peak energies for Eu at 1164 and 1134 eV, and for Gd at 1219 and 1187 eV (Figure 3-13D and E), with a previously XPS reported for these ions, showed similar binding energy positions and shapes to those of Eu_2O_3 and Gd_2O_3 oxide references,[39,53,70] indicating that IONPs surface contain Eu^{3+} and Gd^{3+} ion states. XPS spectra of Er@IONPs sample (Figure 3-13F) showed a characteristic Er 4d binding energy at 168,0 eV, which confirms the presence of Er_2O_3 at the surface.[81]
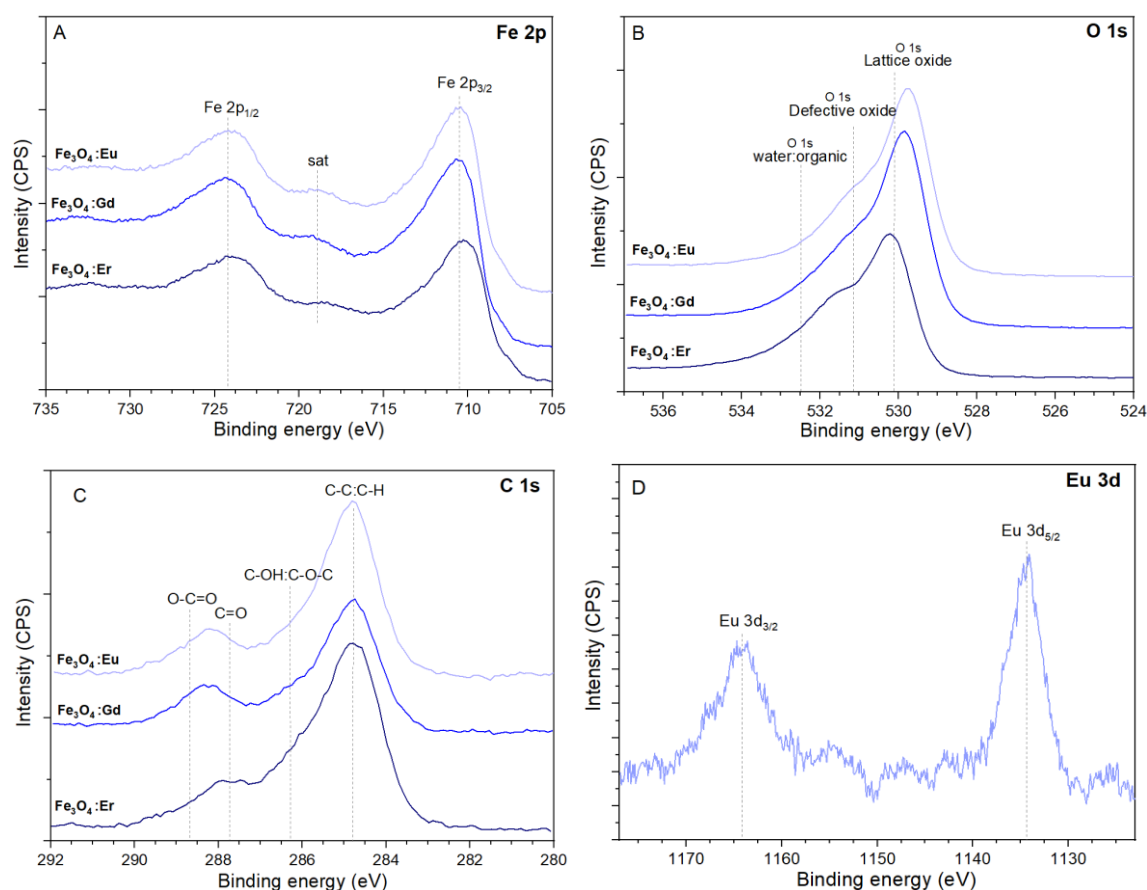
Figure 3-13. XPS spectra for (A) Fe 2p, (B) 0 1s, (C) C 1s, (D) Eu 3d, (E) Gd 3d and (F) Er 4d for Ln@IONPs synthesized in presence of Eu, Gd and Er at 0.5 mM.
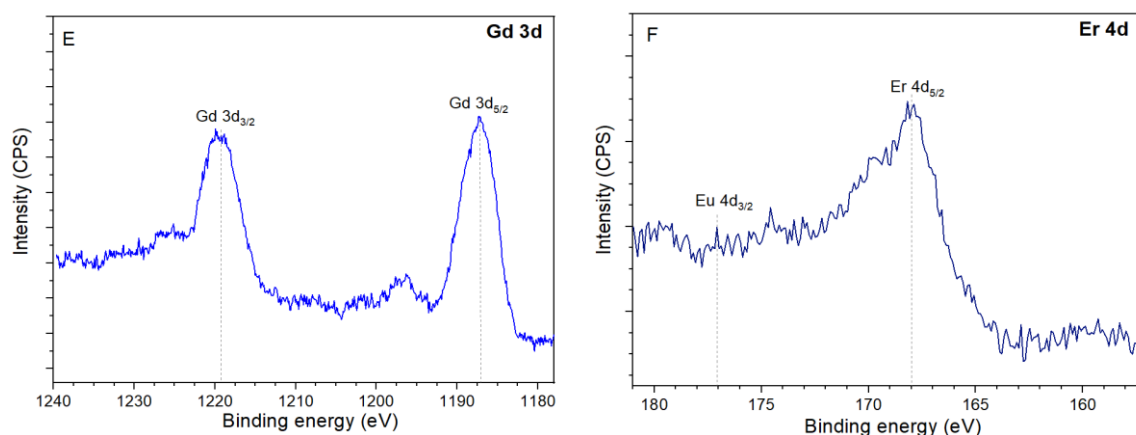
Figure 3-13. Continued.

As evidenced, the obtained results confirm that Ln cations consistently promote the controlled growth of NPs regardless of their valence. Control experiments involving other monovalent (K^+) and divalent (Ca^{2+}, Ba^{2+}) cations, as well as Au^{3+}, resulted in NPs with distinct morphologies and phases (Figure 3-14). XRD patterns of samples produced in the presence of K^+, Ca^{2+}, and Ba^{2+} indicate the production of maghemite phase, indicated also by their magnetism and brown color, with very small crystal sizes. In contrast, samples obtained in the presence of Au^{3+} were non-magnetic and exhibited XRD peaks corresponding to metallic Au and goethite (α-FeOOH), highlighting the acidic conditions promoted by Au^{3+}.[77] These findings identify the unique effectiveness of lanthanide cations in ensuring consistent growth of magnetic IONPs under these conditions.
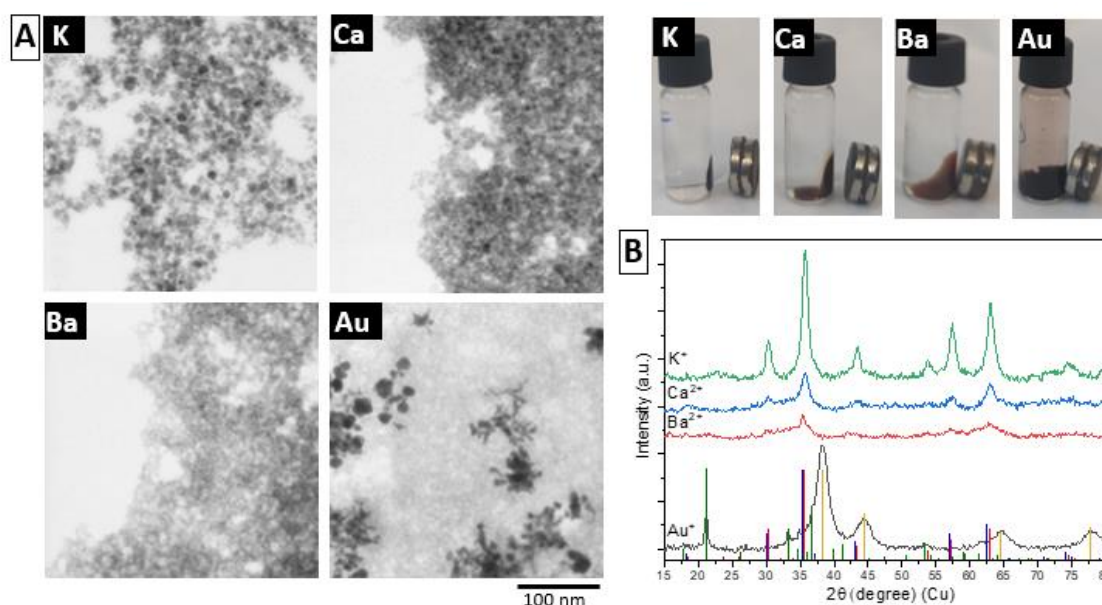
Figure 3-14. (A)Representative STEM images of different magnetic IONPs synthesized by coprecipitation of Fe^{2+} and Fe^{3+} in presence of SC (4 mM) and KCl, $CaCl_2$, $BaCl_2$ or $HAuCl_3$ and (B) XRD analysis of the corresponding products. Blue bars (Fe_3O_4, JCPDS 019-0629), red bars ($γ$-Fe_2O_3, JCPDS 039-1346), yellow bars (Gold syn, JCPDS 004-0784) and green bars (Goethite, JCPDS 0029-0713).

3.3.5 Insights into the mechanism of Ce@IONPs

3.3.5.1 Effect of Synthesis Parameters

There are key factors for the reproducible production of monodispersed Ce@IONPs with controllable sizes from 13 to 46 nm: 1) the presence of sodium citrate, 2) the concentration of cerium ions, 3) the addition rate of the alkaline solution, and 4) temperature.

Control experiments demonstrate the essential role of both SC and Ce^{3+} cations, and the effect of the above-mentioned key parameters on the produced IONPs. In these experiments reagents ratio was kept constant and while each factor (highlighted in red) was varied. Representative STEM images are shown in Figure 3-15.

As discussed in the previous chapter, in the absence of both SC and Ce^{3+} cations, the co-precipitation product, commonly known as Massart's product, was synthesized by co-precipitation of the iron salts (Fe^{2+}: Fe^{3+} (1:2 molar ratio)) by the slow addition of a TMAOH solution (800 μL/min). This product consists of nearly spherical single-crystal IONPs, with an average crystal size of ~10.1 ± 2.3 nm (D_{TEM}) in the SPM domain (Figure 3-15A).

Interestingly, the addition of SC (4 mM) with the slow addition of the base (800 μL/min) led to the obtention of citrate covered SC-IONPs, with in a broader size distribution (4–20 nm), increased heterogeneity in both size and shape, including the presence of smaller NPs of about 9.3 ± 3.4 nm (D_{TEM}) (Figure 3-15B). The observed size effects were attributed to three main roles of SC: *i*) as a chelating agent, resulting in a slower dissociation of Fe ion, *ii*) as pH buffering agent, controlling the iron hydroxylation and, *iii*) as a surface coating agent that could inhibit NP growth.[13,82–86] Unfortunately, these IONPs and SC-IOPNs previously prepared by the co-precipitation method often results in polydisperse and superparamagnetic NPs, and it is well known that for the production of monodisperse NPs, a homogenous nucleation and subsequent slow and controlled growth is critical.

On the other hand, Figure 3-15C exemplifies the coprecipitation product of a mixture containing Fe^{2+}: Fe^{3+}: Ce^{3+} (2:4:0.5 mM) in the absence of SC ions. The STEM images showed the formation of larger magnetic IONPs alongside a secondary non-magnetic amorphous Ce-Fe-hydroxide gel phase (Figure 3-15B). The largest amount of both products was magnetically isolated from each other and according to the XRD analysis,

the sample was composed principally of a magnetite/maghemite phase and a secondary non-magnetic amorphous phase (Figure 3-16).
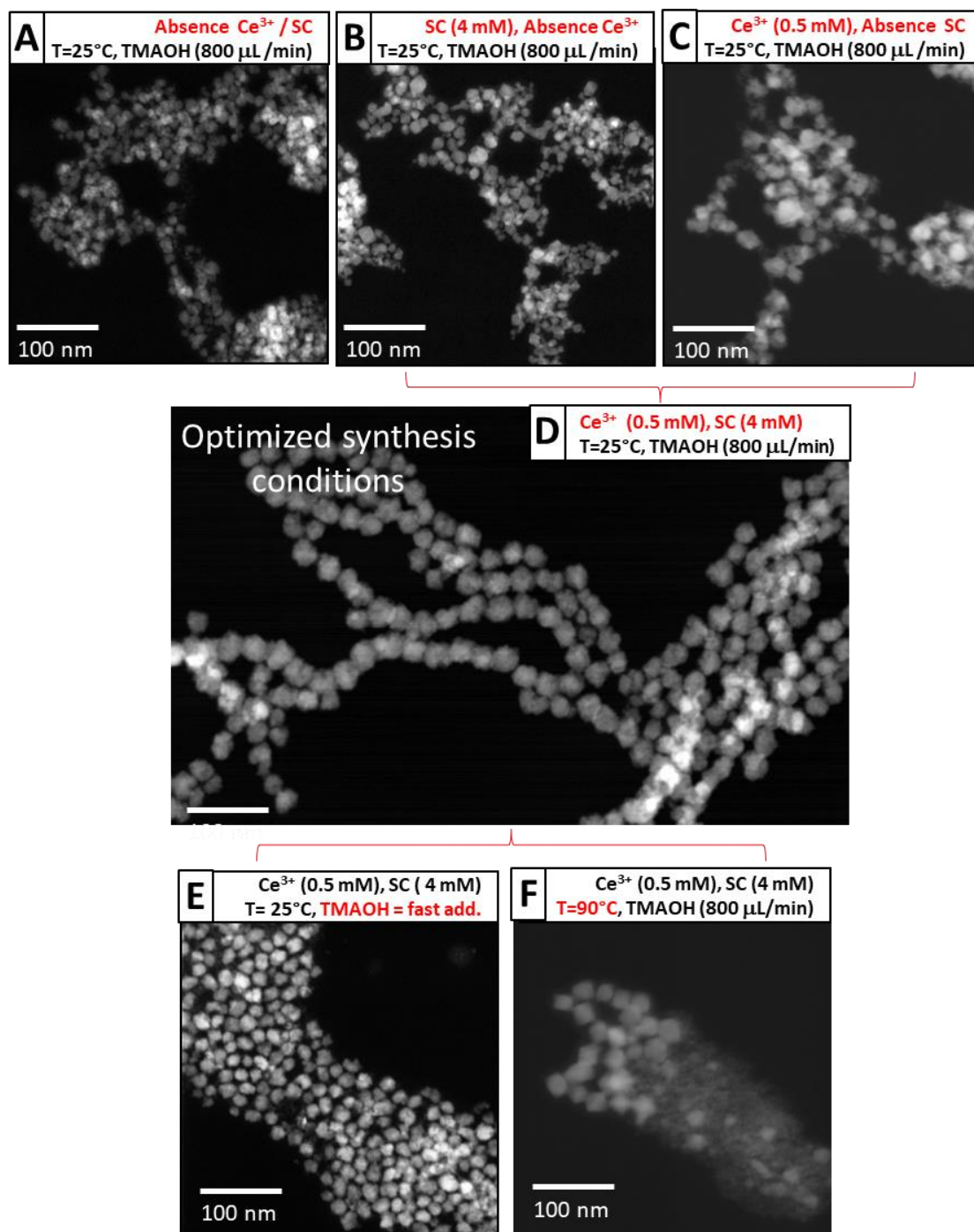
*Figure 3-15. Effect of Synthesis Parameters as visualized by HAADF STEM. (**A**) In the absence of both SC and Ce³⁺ cations, Massart's product yielded nearly spherical single-crystal NPs with an average size of ~10.1 ± 2.3 nm. (**B**) In the absence of Ce³⁺ and the presence of SC resulted in smaller NPs (9.3 ± 3.4 nm) with a broader size distribution (4–20 nm) and increased heterogeneity in both size and shape -spherical, truncated cubes, and cubic- NPs, (**C**) In the absence of SC, the co-precipitation of Fe²⁺/Fe³⁺/Ce³⁺ resulted in the formation of larger magnetic NPs alongside a secondary non-magnetic amorphous Ce-Fe-hydroxide gel phase. (**D**) Controlled addition of TMAOH solution promoted precise nucleation and growth of NPs (26.7 ± 4.2 nm), whereas (**E**) synthesis D at high temperature at 90°C and (**F**) rapid TMAOH addition results in smaller magnetite sizes (16.2 ± 1.3 nm)*
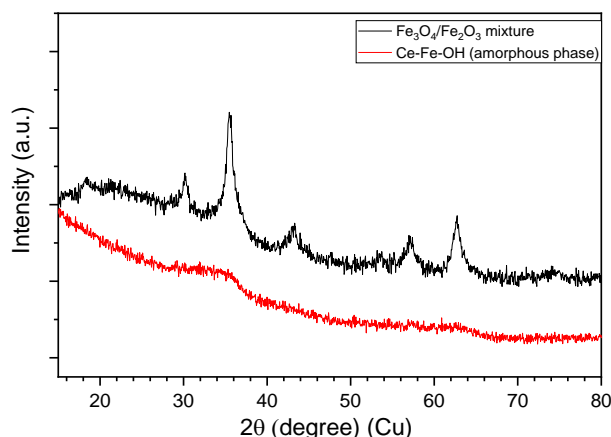
Figure 3-16. Powder XRD diffractograms of the magnetic (black line) and non-magnetic (red line) isolated products obtained from the coprecipitation of a mixture containing Fe^{2+}: Fe^{3+}: Ce^{3+} (2:4:0.5 mM) ions without SC.

As previously shown, the magnetic reaction yield significantly decreases with increasing concentrations of Ce^{3+} cations (Table 3-1). At low Ce^{3+} concentrations, the iron precursor is primarily converted into magnetite NPs, though some of it remains as an amorphous gel phase. However, at higher Ce^{3+} concentrations (>1.5 mM), the predominant product shifts towards the amorphous phase. These findings are consistent with Zhang et al., who observed that the presence of Ce^{3+} in the Fe^{2+}/Fe^{3+} (1:2 ratio) system impedes magnetite formation. [87,88] On the other hand, the lack of SC leads to the fast co-precipitation of Ce^{3+}, probably in the form of $Ce(OH)_3 \leftrightarrow Ce(OH)_{4\ (S)}$ as the reaction increases the pH. Then, the oxidation to Ce^{4+} is a thermodynamically and kinetically favored process, and as Ce^{4+} is a good oxidant, it can caused the oxidation and depletion of Fe^{2+} from the media, which can reduced the formation of the magnetic product.[88,89]

Under optimized conditions (Figure 3-15D), the main parameter to control the size of the IONPs was the variation in the amount of Ln^{3+} cations. However, the presence of SC benefits the reaction by acting as a chelating agent. SC binds to cationic Fe^{2+}/Fe^{3+} ions through its acidic residues, forming complexes that reduce the reactivity of the cations and slow their release, thereby facilitating controlled growth.[27,90] Additionally, SC play a crucial role in controlling the pH of the reaction, providing a precise control over basicity and regulating the availability of hydroxide intermediate species.[13,83,86] Moreover, by chelating Ce^{3+} cations, SC prevents the nucleation of CeO_2 NPs, resulting in a precursor with significantly lower oxidation and hydrolysis rates, as observed by UV-vis spectra (Figure B13 -Annex B).[91]

Therefore, the size of Ln@IONPs could be controlled by adjusting the concentration of Ln^{3+} to SC. In this sense, it is known that lanthanide doping can play an important role

in influencing the physicochemical properties, as well as the phase, size and shape of several NCs.[50,51] If we consider the large ionic radius of Ln^{3+} cations and its positive charge, this can play an important role on the surface of the primary particles, modifying the growth kinetics of the crystals, which is also limited or regulated by an constant equilibrium with the SC of the medium. Both Ln^{3+} and SC, may operate by competitive effects over the same surface sites, changing the electrostatic properties of the oxide-water interface, in this case is probably by the formation of a Ln-SC complex in solution.[34] Furthermore, Ln^{3+} can act as a growth activator, reducing the chemical potential of monomers and the potential of some planes, suggesting that the amount of Ln^{3+} could promote homogenous growth and average NP size.[25,42] Other studies have shown tuning of magnetite NPs by varying the lanthanide (Gd^{3+} and Y^{3+}) concentration.[39,42] However, as far as we know, this is the first report that use Ce^{3+} complexed with SC ions previously, for regulation of magnetite NP size in an important size range (9–46 nm) of applications, obtaining homogeneous size and avoiding secondary co-precipitation products.

In this context, the reaction benefits also from the slow addition of the TMAOH solution, which was also necessary to achieve fine-tuning of the IONPs crystal size. As shown, precise nucleation and growth of NPs (26.7 ± 4.2 nm) were achieved with slow addition of TMAOH solution, while rapid addition resulted in smaller sizes (16.2 ± 1.3 nm) (Figure 3-15F). Here fast addition favors the fast nucleation, determining the formation of magnetite nanoparticles smaller in size.[92] Nature of the base cation could be also important, although no determined its influence in the scope of this thesis, it has been reported that TMAOH has been used in many inorganic syntheses where plays a role of template, influencing their size and shape of NCs; For instance, in acicular α-FeOOH, nanosquare TiO_2, layered TiO_2, and highly oriented zeolite films.[93,94]

Noteworthy, the morphology of IONPs appears to be dependent on the reaction temperature. Thus, running the reaction at 25°C, resulted in a final spherical product (Figure 3-15), whereas an increase in temperature to 90°C increased the conversion through a more cubic product (Figure 3-15E, Figure B14-Annex B). However, increasing the synthesis temperature at ~90°C had a side effect in promoting the formation of by-products, including CeO_2 crystallites.

In summary, it was possible concluded that SC acts as a chelator, controlling the oxidation kinetics and achieving slow, continuous nucleation and growth process. It also acts as a pH buffer, controlling hydroxyl availability to form oxides, and finally as a capping agent or stabilizer of the electric double layer (EDL). In contrast, Ce cations

modify the growth kinetics of the crystal, acting as a growth activator at the surface of the primary NPs, reducing the surface energy of the magnetite monomers, and stabilizing the amorphous iron precursor phase for the magnetite formation. In addition, because of its large ionic radii, was incorporated in the NPs shell. Finally, OH$^-$ ions are required to promote the hydroxylation of Fe^{2+} and Fe^{3+} ions and conversion into magnetite, but they are also involved in the formation of several intermediate species or complexes, including Ce species, and selective precipitation of the involved phases was controlled by the slow addition of the base and SC buffering.

3.3.5.2　Temporal Evolution Reaction Ce@IONPs

To investigate the magnetite formation, a standard synthesis of Ce@IONPs (Ce: SC: Fe^{2+}: Fe^{3+} (0.5:4:2:4 mM)) was monitored; however, this procedure was altered reducing the addition rate of the TMAOH solution (4 mL, 1 M) at 100 µL/min to slow down the precipitation. While the alkaline solution was added, aliquots were periodically extracted from the reaction mixture. These aliquots were centrifuged to separate the precipitate from the supernatant, and then analyzed by BF TEM and UV-vis. We specifically chose IONPs with an average diameter of 27 nm for this analysis. This size, at the transition limit between the FM and SPM states, is large enough to allow effective growth monitoring, yet small enough to prevent chain formation, which ensures the observation of individual particles rather than aggregates.

Obtained results followed by TEM analysis are summarized in Figure 3-17. The initial solution containing a mixture of Ce^{3+} and SC, has a pH of ~ 7. Upon adding the iron precursors, the pH drops sharply to ~2. At this point, TMAOH base is continuously added at a rate of 100 µL/min for 40 minutes, with aliquots periodically extracted starting from the initiation of base addition. Aliquots taken in the first 10 minutes of the reaction were too low in product conversion to perform STEM analysis. After 12 min of reaction, when the pH reaches approximately 6, the precipitation of a non-magnetic amorphous iron oxide precursor phase was observed (Figure 3-17A). While Fe^{2+} may form Fe(OH)$_2$, the solubilities of Fe^{3+} and Fe^{2+} hydroxides differ. Under this relatively low pH, the ferrihydrite phase, which is the most insoluble, is assumed to predominate as the primary precipitated species.[14] At this stage, NPs have not yet formed and the amorphous phase persists until 20 minutes, when the pH reaches ~12 (Figure 3-17 C-B). After 30 min, small particle formation was observed when most of the base (75%) had been added (Figure 3-17D).
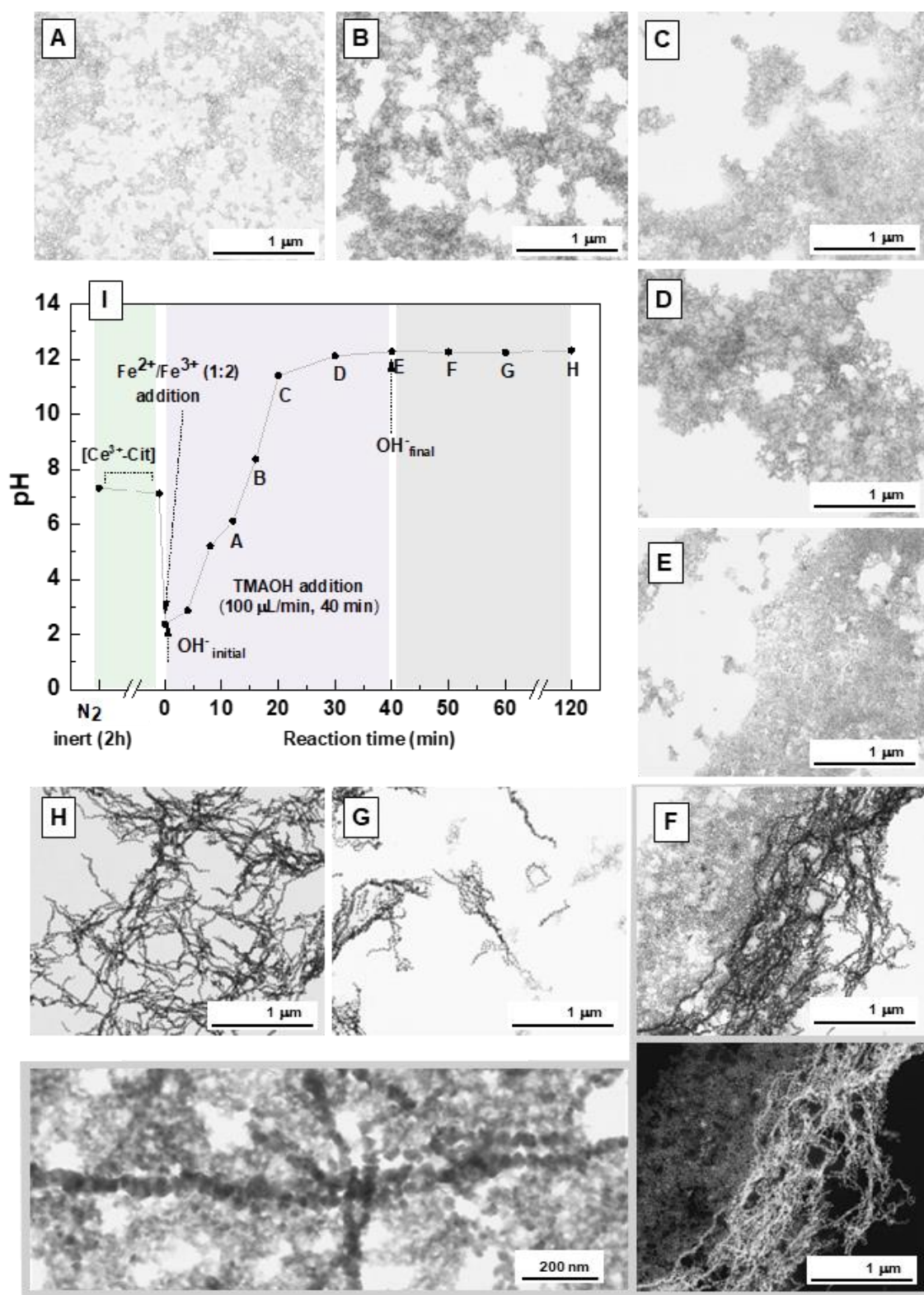
Figure 3-17. Time evolution formation of IONPs (~27 nm) synthesized by co-precipitation method by slow addition of the TMAOH solution at 100 μL/min in presence of Ce^{3+}:SC (0.5:4 mM). The BF TEM images are arranged in clockwise order: (A) 12 min, (B) 16 min, (C) 20 min, (D) 30 min, (E) 40 min, (F) 50 min, (G) 60 min and (H) 120 min. (I) Time-dependent pH evolution after the addition of TMAOH. Aliquots were periodically extracted during the addition of the alkaline solution.

After complete base addition (from 40 min), the number of magnetite NPs grew in number and the size became more uniform, while the amorphous iron oxide precursor phase gradually disappeared (Figure 3-17E-F). This morphological transition change from the iron oxide precursor phase to magnetite NPs suggests that it was possibly formed through solid-state conversion via the addition of Fe^{2+} ions to ferrihydrite-like precursor.[14,15,95] After 2 hours of reaction, the NPs seems to reach their final size ~27 nm and semi- spherical morphology. As expected from their size and ferromagnetic behavior, they self-assembled into single-chain structures and double or multiple wires likely due dipolar magnetic interaction between NPs (Figure 3-17G-H). The wavelength time-dependent absorption of the UV-vis measurements are shown in Figure B15(Annex B). As the reaction progressed, the supernatant presented an oscillation correlated with the consumption of Fe ions in the reaction media, while the absorption peaks of the precipitate showed a decrease in the average absorption around 260–300 nm, indicating the advance through a black magnetite phase.

3.3.5.3 Transformation Experiments of Ferrihydrite as Precursor of the Ln@IONPs

To demonstrate that the magnetic Ce@IONPs may have arisen from the rapid solid-state transformation of a ferrihydrite-like precursor by the addition of Fe^{2+} ions, four transformation experiments were performed varying the Fe^{2+} concentration in the media whit respect to the initial Fe^{3+}, based on Aeppli et al.,[96] and Raghav et al.,[97] studies. All samples were synthesized according to the standard synthesis of Ce@IONPs, using the same synthetic conditions: day, reactants concentrations (Ce: SC: Fe^{3+}: TMAOH (0.5: 4: 4: 40 mM)), alkaline titration rate (800 µL/min), N_2 inert atmosphere, and room temperature. However, the Fe^{2+} concentration was varied from 0.5 to 4 mM to obtain either goethite or magnetite as a transformation product (experimental concentration in Table B2, in Annex B). The collected precipitates were washed twice and dried under vacuum conditions.

As shown in Table 3-4, ferrihydrite precursor can be interconverted to several iron oxides of higher crystallinity. Ferrihydrite conversion occurs over a wide range of pH (3–14), and increases in pH, temperature, and Fe^{2+} amount accelerates their transformation.[34] However, the experimental conditions that favor their transformation into goethite or magnetite, high pH (~12), presence of Fe^{2+}, and inert atmosphere, and low temperature, were established in our experiment.

Table 3-4. Ferrihydrite transformation to iron oxides.[34]

Precursor	Product	Type of transformation	Preferred medium
Ferrihydrite	Goethite	Dissolution / reprecipitation	Aqueous solution pH 3–14
	Magnetite	Dissolution / reprecipitation	Alkaline solution with M^{2+}
	Hematite / maghemite	Thermal dehydration/ dehydroxylation	Gas / vacuum
	Akaganéite	Dissolution / reprecipitation	Acidic media; presence of Cl
	Lepidocrocite	Dissolution / reprecipitation	pH 6, presence of cysteine
	Hematite	Aggregation, short range crystallization within ferrihydrite aggregate	Aqueous solution at pH 6–8

Figure 3-18A shows the XRD spectra of the products obtained after 2 h of reaction corresponding to the Fe^{2+}:Fe^{3+} ratio used. At very low Fe^{2+} concentration (1:8 ratio), XRD indicated the obtention of a very small non-crystalline product corresponding possibly to the 2-line ferrihydrite (Fh) precursor, as signaled by the two broad *hkl* lines 110 ($2\theta \approx 30$) and 300 ($2\theta \approx 60$), respectively.[34]

As the Fe^{2+} increases to (1:4), it leads to a slow conversion into intermediate goethite and magnetite phases signaled by the prominent goethite *hkl* 101($2\theta =21.2$) and magnetite *hkl* 311($2\theta=35.4$) diffraction peaks. However, during the 2 h of reaction, the transformation was not completed. Increasing the Fe^{2+} to 1:2 and 1:1 ratio directly drives to the obtention of magnetite as the major phase in both cases. There, the continuous magnetic stirring exposed the ferrihydrite precursor to a homogeneous and high concentration of Fe^{2+} in the reaction media, leading to magnetite formation.[97]

The transformation of ferrihydrite to more stable phases involve a competitive process, which is defined by the reaction conditions and time. Figure 3-18B shows the final product obtained from the conversion of the 1:8 ratio after one week keeping the system closed, which leads to goethite as the major phase and a secondary phase of CeO_2 NPs.

HAADF-STEM images of the product (1:8) after 2h of reaction showed very small particles which agree with the formation of ferrihydrite precursor. In addition, the HR-TEM image showed some transformation to a needle-shaped goethite (~100 nm in length). (Figure 3-18C). In contrast, STEM images of the products (1:2) and (1:4) showed the typical magnetic Ce@IONPs formed.

EDX analysis confirmed the coexistence of Fe and Ce in the ferrihydrite precursor (product 1:8) (Figure 3-18D). From the two different areas analyzed, as indicated by the labeled main signals of $FeK\alpha_1$ and $CeL\alpha_1$, the bright areas (*Area 1*) were very rich in Ce with respect to the Fe, and the dark area (*Area 2*) was rich in Fe with respect to Ce,

suggesting that Ce^{3+} was adsorbed onto the ferrihydrite precursor. As the specific surface area of ferrihydrite is approximately 600 m^2/g, which is higher than the transformation products magnetite (90 m^2/g) and goethite (54 m^2/g),[97] it is reasonable that ferrihydrite absorbs a higher quantity of Ce ions, stabilizing and influencing its transformation to the size-controlled magnetic Ce@IONPs.
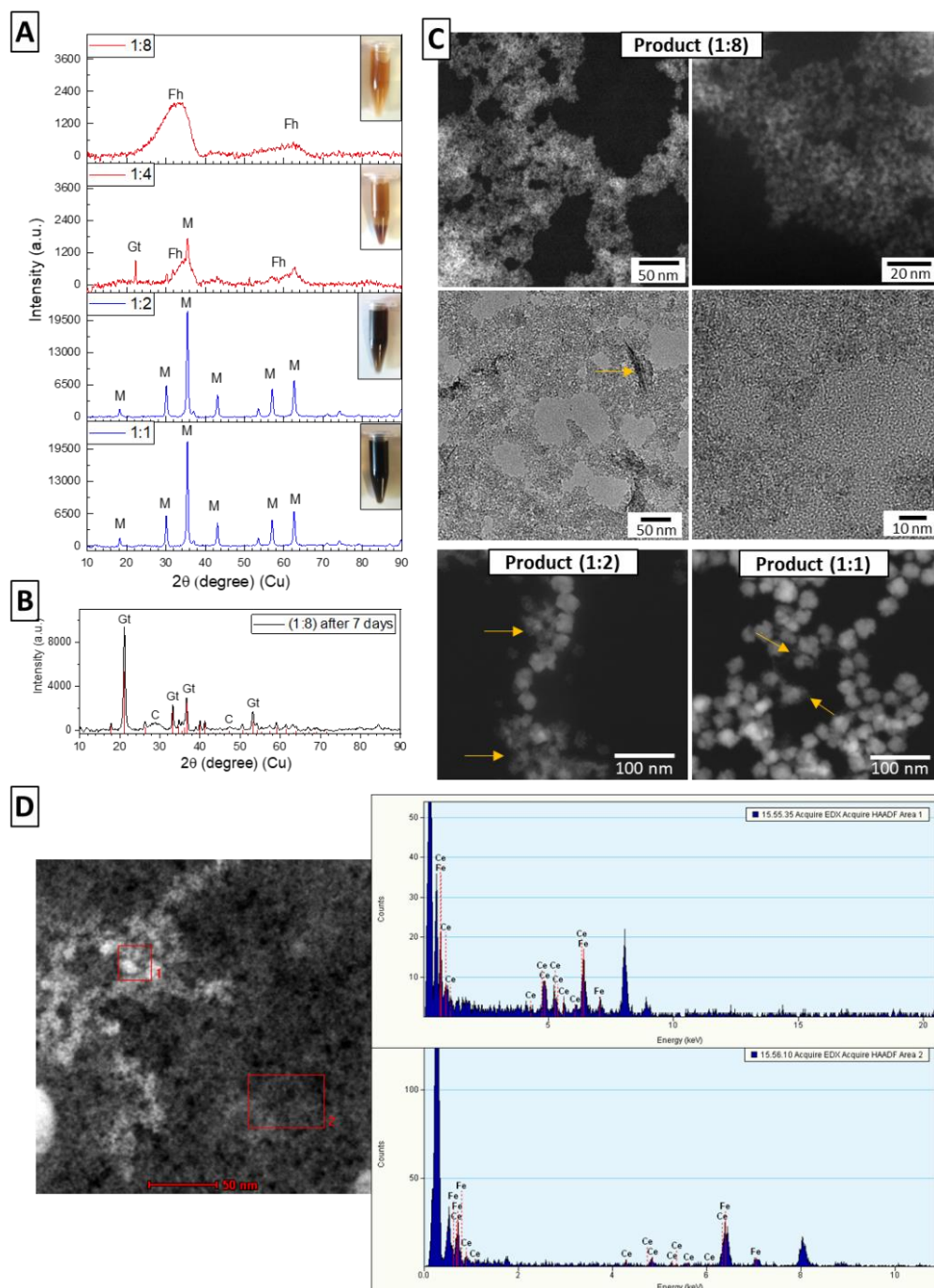
Figure 3-18. (A) XRD spectra of the precipitate (magnetic or non-magnetic) obtained from ferrihydrite transformation experiments at 2h reaction by changed Fe^{2+}: Fe^{3+} ratio (1:8 to 1:1) in presence of Ce^{3+}:SC (0.5:4 mM). (Fh: ferrihydrite; Gt: goethite; M: magnetite/maghemite), (B) evolution product of Fe^{2+}: Fe^{3+} ratio (1:8) after one week (Gt: goethite; C: ceria or residual Fh). (C) Representative HAADF and HRTEM of the product (Fe^{2+}: Fe^{3+}) 1:8 ratio and STEM-HAADF of the products (Fe^{2+}:Fe^{3+}) 1:2 and 1:1 ratio, respectively, and (D) EDX analysis of the product (Fe^{2+}:Fe^{3+}) 1:8 ratio after 2h reaction.

The previous hypothesis was contrasted with the following experiments. In the first experiment, magnetite NPs were first coprecipitated from $Fe^{2+}:Fe^{3+}$ (2:4 mM), washed and resuspended in a free oxygen solution containing Ce^{3+} ions (0.25 mM). The first coprecipitation product exhibited a ζ-potential of -41 mV indicating the typical surface charge with OH^- of magnetite NPs, after incubation with Ce^{3+} the ζ-potential was changed to +36 mV, indicating the sorption of Ce on the NPs. Thereafter, a second precipitation $Fe^{2+}:Fe^{3+}$ (1:2) step was repeated over the former particles in order to know if the primary magnetite NPs could grow mediated by the Ce ions on the surface. The illustrated experiment and the obtained IONPs are shown in Figure 3-19. There was not any significative change in the size of the NPs after the second precipitation step, indicated that NPs does not growth continuously over magnetite the seeds. Instead, a new nucleation event produced new IONPs of similar size.
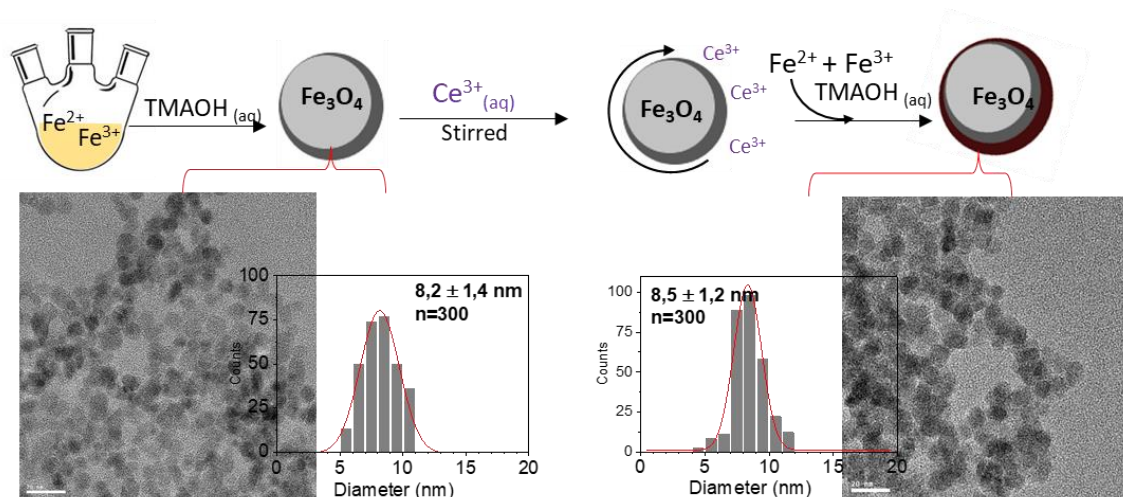
Figure 3-19. Illustrated scheme, HR-TEM images, and size distribution analysis (before and after) of seeded growth magnetite experiment through absorption of Ce^{3+}.

The second experiment, was carried out the standard synthesis of $Fe^{2+}:Fe^{3+}$ (2:4 mM) in the presence of Ce:SC (0.25:4 mM) followed by the slow addition of TMAOH (800 µL/min), and after 10 min of reaction was made a second addition of the iron precursors, $Fe^{2+}:Fe^{3+}$ (1:2 mM) or Fe^{2+} (3mM). As a result, the subsequent addition of the iron precursors did not produce significant NP growth in comparison to the control experiment (Figure 3-20). It was noticed that, the subsequent addition of $Fe^{2+}:Fe^{3+}$ produced a more polydisperse product and amorphous solid, which possibly could be the $Ce\text{-}Fe\text{-}OH_X$ gel or ferrihydrite precursor surrounding the IONPs. However, the addition of Fe^{2+} led to a second nucleation event, and smaller magnetite IONPs were observed. Both experiments suggest that Ce ions influence were at the very early stage of the reaction, in a very low pH >8 in the stabilization of the amorphous intermediates.
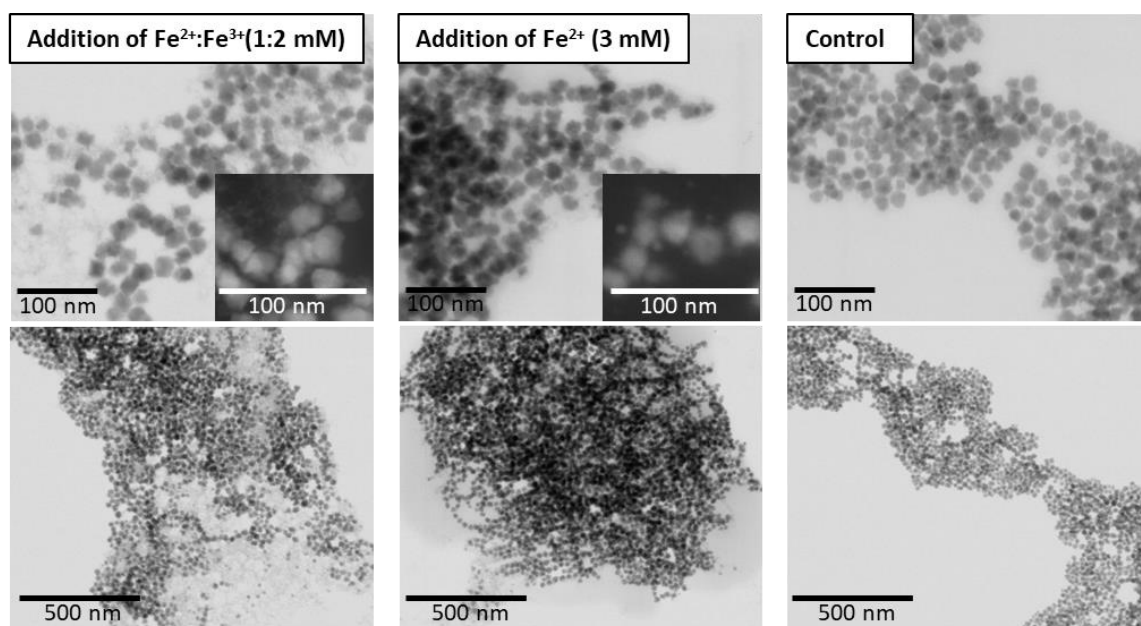
Figure 3-20. Representative STEM images of the double addition of iron precursors to the standard synthesis in presence of Ce:SC (0.25:4 mM): first experiment addition of Fe^{2+}: Fe^{3+} (1:2 mM), second experiment addition of Fe^{2+} (3 mM) and control (scale bar: 100 nm and 500 nm).

3.3.5.4   Proposed Ln@IONPs reaction mechanism

As reported, growth of magnetite particles via coprecipitation can be achieved by the very slow and continuous titration of a solution containing both Fe^{2+} and Fe^{3+} precursors, which results in particles above the SPM domain, mimicking the pathways used by magnetotactic bacteria.[16] As reported by Baumgartner et al.,[15] in an Fe^{2+} and Fe^{3+} system, initial increase in pH (Eq. 1) or slow OH^- influx produces the first nucleation event, corresponding to the precipitation of Fe^{3+} as ferrihydrite $Fe(OH)_3$ at pH ~3 (Eq. 2). Although Fe^{+2} may form solid ferrous hydroxide as pH increases (Eq. 3), Fe^{3+} and Fe^{2+} hydroxides exhibit different solubilities; then at low pH values ferrihydrite predominated as precipitated primary phase, and $Fe(OH)_2$ remained soluble.

$$N(CH_3)_4^+ OH^- + H_2O \rightarrow N(CH_3)_4^+ + OH^- \qquad (1)$$
$$Fe^{3+} + 3OH^- \rightarrow Fe(OH)_3 \qquad\qquad pH{\sim}3 \quad (2)$$
$$Fe^{2+} + 2OH^- \rightarrow Fe(OH)_2 \qquad\qquad pH{\sim}8 \quad (3)$$
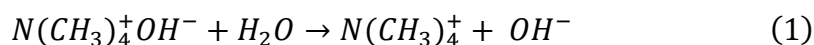
Thereafter, a second nucleation event occurs when the pH rose to ~8, where magnetite could be obtained. Magnetite is formed through solid-state conversion via the addition of Fe^{2+} to the ferrihydrite $Fe(OH)_3$ precursor (Eq. 2+3). Afterwards, growth of magnetite proceeds through the attachment of small particles ~ 1 nm on the crystal surface, and by dehydration transformed to magnetite at increased pH (8 to 14).

$$2Fe(OH)_3 + Fe^{2+} + 2OH^- \rightarrow Fe_3O_4 + 4H_2O \qquad (2+3)$$
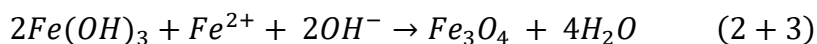
The obtained results in this thesis suggest the role of Ln cations in modifying the crystal growth kinetics of the Fe^{2+}/Fe^{3+} coprecipitation reaction. With the progressive variation of the pH, Ln^{3+} cations through electrostatic attractions could surround the surface of the iron oxide precursors, but with the impossibility of being incorporated into the structure because of its large cation radii remaining at the surface. As demonstrated by Jolivert et al.,[98] variations in oxide particle size and shape are closely linked to changes in the electrostatic surface charge density, which affect the oxide-solution interfacial tension and reduce the surface energy. This reduction enables more precise control over the surface area of the system. This modification in the reaction kinetics probably occurs either by stabilizing the amorphous hydroxy intermediate species during the reaction and/or by adsorption onto the negatively charged magnetite surface, thereby reducing the surface energy for growth.

Similar to bioinspired synthesis methods that use various biomolecules to manipulate intermediate species during magnetite NP synthesis, the combination of SC and Ln cations enables the precise adjustment of NP size. Similarly, as described by Kuhtrs et al.[33], by using polyarginine a peptide (positively charged) and by fine control of the pH. Then, the adsorption of Ln cations and SC can act in a similar form, either by passivating the crystal through reducing surface energy and/or stabilizing the Fe^{3+}-rich hydroxide precursor. The presence of Ln cations may enhance wettability by stabilizing amorphous hydroxy intermediate species.[33] This mechanism promotes the formation of larger magnetite NPs from $Fe(OH)_3$ by maintaining the wetness of the growing NP surface, which is an important step during ferrihydrite transformation.

Moreover, it has been shown that acidic amino acids (negatively charged) regulate crystal size by acting as nucleation inhibitors, stabilizing intermediates through iron coordination.[11] The presence of SC may allow controlling the pH changes at the interface ferrihydrite precursor/magnetite NPs.[33] This SC inducing a buffering effect and complexation that directly impacts in the stability of the iron oxy- or hydroxy- species in the reaction media, as pH and complexation determine the speciation, solubility, and surface state of the species formed according to Pourbaix and speciation diagrams.[99] [100]

However, various uncertainties still arise from the experimental conditions in this system; their metal-citrate equilibria in aqueous media with progressive hydroxylation can be an interesting subject of study. These include the complexes formed, the number and

strength of the complexes and their hydrolysis, the determination of the intermediary species in the system and its transformation, the stability and oxidation of Fe(II), which allows magnetite crystallization, and the sorption or interaction of the Ln^{3+} cations and SC at the $Fe(OH)_3$ and magnetite surface, may operate either competitive or synergistic effects.[101,102] Although the formation of Ln@IONPs may involve several complicated steps, the combination of Ln^{3+} and SC ions clearly slowed the process of magnetite formation, both acting as growth control agents, homogeneously regulating the size of the produced magnetic IONPs.

3.4 Conclusions

In this chapter, a novel co-precipitation method at room temperature for synthesized single-crystal magnetic IONPs with controlled size from ~13 nm to ~46 nm by employ of Ce^{3+} and SC ions in aqueous media was described. The size of the IONPs was controlled by varying the concentration of Ce^{3+} in the reaction media. Higher Ce concentrations led to the formation of polycrystalline nanowires with diameters up to 90 nm and lengths extending into microns. The presence of Ce^{3+} allows crystal growth homogeneously, possibly by stabilizing or modifying the kinetics of the amorphous iron precursor phase, or by modifying the NPs surface energy. In addition, the SC presence and slow titration also demonstrated to be important reaction parameters to fine tuning the NPs size. The SC acted as a chelator and pH buffer, controlling the oxidation kinetics, and achieving slow, continuous nucleation and growth processes.

Both Ce and SC were found adsorbed on the surface amorphous precursor and magnetite NPs, as demonstrated by the characterization techniques. The robustness of these synthesis was extended to other lanthanide cations (3+) such as Eu, Gd, Er, Yt, and Lu, producing single crystal IONPs of similar sizes. The IONPs in this study were synthesized using a simple and practical aqueous coprecipitation method at room temperature, offering an environmentally friendly approach for generating monodisperse and tunable IONPs in size and surface, which can be potentially functionalized and used for example in biomedicine or in catalytic applications.

3.5 References

(1)   Du, K.; Zhu, Y.; Xu, H.; Yang, X. Multifunctional Magnetic Nanoparticles: Synthesis Modification and Biomedical Applications. *Prog. Chem.* **2011**, *23* (11), 2287–2298.

(2)   Wu, L.; Mendoza-Garcia, A.; Li, Q.; Sun, S. Organic Phase Syntheses of Magnetic Nanoparticles and Their Applications. *Chem. Rev.* **2016**, *116* (18), 10473–10512. https://doi.org/10.1021/acs.chemrev.5b00687.

(3)   Kudr, J.; Haddad, Y.; Richtera, L.; Heger, Z.; Cernak, M.; Adam, V.; Zitka, O. Magnetic Nanoparticles: From Design and Synthesis to Real World Applications. *Nanomaterials* **2017**, *7* (9). https://doi.org/10.3390/nano7090243.

(4)   Shukla, S.; Khan, R.; Daverey, A. Synthesis and Characterization of Magnetic Nanoparticles, and Their Applications in Wastewater Treatment: A Review. *Environ. Technol. Innov.* **2021**, *24*, 101924. https://doi.org/10.1016/j.eti.2021.101924.

(5)   Gloag, L.; Mehdipour, M.; Chen, D.; Tilley, R. D.; Gooding, J. J. Advances in the Application of Magnetic Nanoparticles for Sensing. *Adv. Mater.* **2019**, *31* (48), 1–26. https://doi.org/10.1002/adma.201904385.

(6)   Mohammed, L.; Gomaa, H. G.; Ragab, D.; Zhu, J. Magnetic Nanoparticles for Environmental and Biomedical Applications: A Review. *Particuology* **2017**, *30*, 1–14. https://doi.org/10.1016/j.partic.2016.06.001.

(7)   Díez, A. G.; Rincón-Iglesias, M.; Lanceros-Méndez, S.; Reguera, J.; Lizundia, E. Multicomponent Magnetic Nanoparticle Engineering: The Role of Structure-Property Relationship in Advanced Applications. *Mater. Today Chem.* **2022**, *26* (October), 101220. https://doi.org/10.1016/j.mtchem.2022.101220.

(8)   Kolhatkar, A. G.; Jamison, A. C.; Litvinov, D.; Willson, R. C.; Lee, T. R. *Tuning the Magnetic Properties of Nanoparticles*; 2013; Vol. 14. https://doi.org/10.3390/ijms140815977.

(9)   Guardia, P.; Labarta, A.; Batlle, X. Tuning the Size, the Shape, and the Magnetic Properties of Iron Oxide Nanoparticles. *J. Phys. Chem. C* **2011**, *115* (2), 390–396. https://doi.org/10.1021/jp1084982.

(10)   Marciello, M.; Connord, V.; Veintemillas-Verdaguer, S.; Vergés, M. A.; Carrey, J.; Respaud, M.; Serna, C. J.; Morales, M. P. Large Scale Production of Biocompatible Magnetite Nanocrystals with High Saturation Magnetization Values through Green Aqueous Synthesis. *J. Mater. Chem. B* **2013**, *1* (43), 5995–6004. https://doi.org/10.1039/c3tb20949k.

(11)   Lenders, J. J. M.; Mirabello, G.; Sommerdijk, N. A. J. M. Bioinspired Magnetite Synthesis via Solid Precursor Phases. *Chem. Sci.* **2016**, *7* (9), 5624–5634. https://doi.org/10.1039/C6SC00523C.

(12)   Massart, R. Preparation of Aqueous Magnetic Liquids in Alkaline and Acidic Media. *IEEE Trans. Magn.* **1981**, *17* (2), 1247–1248. https://doi.org/10.1109/TMAG.1981.1061188.

(13)   Bee, A.; Massart, R.; Neveu, S. Synthesis of Very Fine Maghemite Particles. *J. Magn. Magn. Mater.* **1995**, *149* (1–2), 6–9. https://doi.org/10.1016/0304-8853(95)00317-7.

(14)   Lenders, J. J. M.; Altan, C. L.; Bomans, P. H. H.; Arakaki, A.; Bucak, S.; De With, G.; Sommerdijk, N. A. J. M. A Bioinspired Coprecipitation Method for the Controlled Synthesis of Magnetite Nanoparticles. *Cryst. Growth Des.* **2014**, *14* (11), 5561–5568. https://doi.org/10.1021/cg500816z.

(15) Baumgartner, J.; Dey, A.; Bomans, P. H. H.; Le Coadou, C.; Fratzl, P.; Sommerdijk, N. A. J. M.; Faivre, D. Nucleation and Growth of Magnetite from Solution. *Nat. Mater.* **2013**, *12* (4), 310–314. https://doi.org/10.1038/nmat3558.

(16) Mirabello, G.; Lenders, J. J. M.; Sommerdijk, N. A. J. M. Bioinspired Synthesis of Magnetite Nanoparticles. *Chem. Soc. Rev.* **2016**, *45* (18), 5085–5106. https://doi.org/10.1039/c6cs00432f.

(17) Faivre, D.; Schüler, D. Magnetotactic Bacteria and Magnetosomes. *Chem. Rev.* **2008**, *108* (11), 4875–4898. https://doi.org/10.1021/cr078258w.

(18) Siponen, M. I.; Legrand, P.; Widdrat, M.; Jones, S. R.; Zhang, W. J.; Chang, M. C. Y.; Faivre, D.; Arnoux, P.; Pignol, D. Structural Insight into Magnetochrome-Mediated Magnetite Biomineralization. *Nature* **2013**, *502* (7473), 681–684. https://doi.org/10.1038/nature12573.

(19) Baumgartner, J.; Morin, G.; Menguy, N.; Gonzalez, T. P.; Widdrat, M.; Cosmidis, J.; Faivre, D. Magnetotactic Bacteria Form Magnetite from a Phosphate-Rich Ferric Hydroxide via Nanometric Ferric (Oxyhydr)Oxide Intermediates. *Proc. Natl. Acad. Sci. U. S. A.* **2013**, *110* (37), 14883–14888. https://doi.org/10.1073/pnas.1307119110.

(20) Baumgartner, J.; Antonietta Carillo, M.; Eckes, K. M.; Werner, P.; Faivre, D. Biomimetic Magnetite Formation: From Biocombinatorial Approaches to Mineralization Effects. *Langmuir* **2014**, *30* (8), 2129–2136. https://doi.org/10.1021/la404290c.

(21) Baumgartner, J.; Bertinetti, L.; Widdrat, M.; Hirt, A. M.; Faivre, D. Formation of Magnetite Nanoparticles at Low Temperature: From Superparamagnetic to Stable Single Domain Particles. *PLoS One* **2013**, *8* (3), 1–6. https://doi.org/10.1371/journal.pone.0057070.

(22) Kuhrts, L.; Macías-Sánchez, E.; Tarakina, N. V.; Hirt, A. M.; Faivre, D. Shaping Magnetite with Poly- l -Arginine and PH: From Small Single Crystals to Large Mesocrystals. *J. Phys. Chem. Lett.* **2019**, *10* (18), 5514–5518. https://doi.org/10.1021/acs.jpclett.9b01771.

(23) Sugimoto, T.; Matijević, E. Formation of Uniform Spherical Magnetite Particles by Crystallization from Ferrous Hydroxide Gels. *J. Colloid Interface Sci.* **1980**, *74* (1), 227–243. https://doi.org/10.1016/0021-9797(80)90187-3.

(24) Vergés, M. A.; Costo, R.; Roca, A. G.; Marco, J. F.; Goya, G. F.; Serna, C. J.; Morales, M. P. Uniform and Water Stable Magnetite Nanoparticles with Diameters around the Monodomain-Multidomain Limit. *J. Phys. D. Appl. Phys.* **2008**, *41* (13). https://doi.org/10.1088/0022-3727/41/13/134003.

(25) Luengo, Y.; Morales, M. P.; Gutiérrez, L.; Veintemillas-Verdaguer, S. Counterion and Solvent Effects on the Size of Magnetite Nanocrystals Obtained by Oxidative Precipitation. *J. Mater. Chem. C* **2016**, *4* (40), 9482–9488. https://doi.org/10.1039/c6tc03567a.

(26) Vereda, F.; de Vicente, J.; Hidalgo-Alvarez, R. Oxidation of Ferrous Hydroxides with Nitrate: A Versatile Method for the Preparation of Magnetic Colloidal Particles. *J. Colloid Interface Sci.* **2013**, *392* (1), 50–56. https://doi.org/10.1016/j.jcis.2012.09.064.

(27) Lenders, J. J. M.; Bawazer, L. A.; Green, D. C.; Zope, H. R.; Bomans, P. H. H.; de With, G.; Kros, A.; Meldrum, F. C.; Sommerdijk, N. A. J. M. Combinatorial Evolution of Biomimetic Magnetite Nanoparticles. *Adv. Funct. Mater.* **2017**, *27* (10), 1–9. https://doi.org/10.1002/adfm.201604863.

(28) Wu, J.; Shi, M.; Feng, F.; Hao, J.; Zhao, D.; Wang, X.; Li, J.; Zhang, W.; Wang, Q.; Ke, Y.; Yan, X.; Lin, Z.; Chai, L. Recent Advances in Magnetite Crystallization:

Pathway, Modulation, and Characterization. *Cryst. Growth Des.* **2023**, *23* (8), 6201–6218. https://doi.org/10.1021/acs.cgd.3c00530.

(29) Kittel, C. Theory of the Structure of Ferromagnetic Domains in Films and Small Particles. *Phys. Rev.* **1946**, *70* (11–12), 965–971. https://doi.org/10.1103/PhysRev.70.965.

(30) Leslie-Pelecky, D. L.; Rieke, R. D. Magnetic Properties of Nanostructured Materials. *Chem. Mater.* **1996**, *8* (8), 1770–1783. https://doi.org/10.1021/cm960077f.

(31) Whitehead, C. B.; Özkar, S.; Finke, R. G. LaMer's 1950 Model for Particle Formation of Instantaneous Nucleation and Diffusion-Controlled Growth: A Historical Look at the Model's Origins, Assumptions, Equations, and Underlying Sulfur Sol Formation Kinetics Data. *Chem. Mater.* **2019**, *31* (18), 7116–7132. https://doi.org/10.1021/acs.chemmater.9b01273.

(32) Bastús, N. G.; Casals, E.; Vázquez-Campos, S.; Puntes, V. Reactivity of Engineered Inorganic Nanoparticles and Carbon Nanostructures in Biological Media. *Nanotoxicology* **2008**, *2* (3), 99–112. https://doi.org/10.1080/17435390802217830.

(33) Kuhrts, L.; Prévost, S.; Chevrier, D. M.; Pekker, P.; Spaeker, O.; Egglseder, M.; Baumgartner, J.; Pósfai, M.; Faivre, D. Wettability of Magnetite Nanoparticles Guides Growth from Stabilized Amorphous Ferrihydrite. *J. Am. Chem. Soc.* **2021**, *143* (29), 10963–10969. https://doi.org/10.1021/jacs.1c02687.

(34) Cornell, R. M.; U. Schwertmann. *The Iron Oxides: Structure, Properties, Reactions, Occurences and Uses*, Second.; Wiley VCH, Ed.; Weinheim, 2003; Vol. 664.

(35) Fantechi, E.; Innocenti, C.; Albino, M.; Lottini, E.; Sangregorio, C. Influence of Cobalt Doping on the Hyperthermic Efficiency of Magnetite Nanoparticles. *J. Magn. Magn. Mater.* **2015**, *380*, 365–371. https://doi.org/10.1016/j.jmmm.2014.10.082.

(36) Lee, J. H.; Huh, Y. M.; Jun, Y. W.; Seo, J. W.; Jang, J. T.; Song, H. T.; Kim, S.; Cho, E. J.; Yoon, H. G.; Suh, J. S.; Cheon, J. Artificially Engineered Magnetic Nanoparticles for Ultra-Sensitive Molecular Imaging. *Nat. Med.* **2007**, *13* (1), 95–99. https://doi.org/10.1038/nm1467.

(37) Luengo, Y.; Roldan, M. A.; Varela, M.; Herranz, F.; Morales, M. P.; Veintemillas-Verdaguer, S. Doped-Iron Oxide Nanocrystals Synthesized by One-Step Aqueous Route for Multi-Imaging Purposes. *J. Phys. Chem. C* **2019**, *123* (12), 7356–7365. https://doi.org/10.1021/acs.jpcc.9b00512.

(38) Aghazadeh, M.; Karimzadeh, I.; Maragheh, M. G.; Ganjali, M. R. Gd3+ Doped Fe3O4 Nanoparticles with Proper Magnetic and Supercapacitive Characteristics: A Novel Synthesis Platform and Characterization. *Korean J. Chem. Eng.* **2018**, *35* (6), 1341–1347. https://doi.org/10.1007/s11814-018-0027-7.

(39) Zhang, H.; Malik, V.; Mallapragada, S.; Akinc, M. Synthesis and Characterization of Gd-Doped Magnetite Nanoparticles. *J. Magn. Magn. Mater.* **2017**, *423* (August 2016), 386–394. https://doi.org/10.1016/j.jmmm.2016.10.005.

(40) Vakil, Z.; Kumar, A.; Jain, A.; Gupta, K. M.; Najim, M.; Singh, D. Effect of Cerium (Ce3+) Doping on Structural, Magnetic and Dielectric Properties of Barium Ferrite (BaFe12O19). *Proc. 2015 IEEE Int. Conf. Electr. Comput. Commun. Technol. ICECCT 2015* **2015**, 9–12. https://doi.org/10.1109/ICECCT.2015.7225982.

(41) Chen, F.; Wang, X.; Nie, Y.; Li, Q.; Ouyang, J.; Feng, Z.; Chen, Y.; Harris, V. G. Ferromagnetic Resonance Induced Large Microwave Magnetodielectric Effect in Cerium Doped Y3 Fe5 O12 Ferrites. *Sci. Rep.* **2016**, *6* (June). https://doi.org/10.1038/srep28206.

(42) Kowalik, P.; Mikulski, J.; Borodziuk, A.; Duda, M.; Kamińska, I.; Zajdel, K.;

Rybusinski, J.; Szczytko, J.; Wojciechowski, T.; Sobczak, K.; Minikayev, R.; Kulpa-Greszta, M.; Pazik, R.; Grzaczkowska, P.; Fronc, K.; Lapinski, M.; Frontczak-Baniewicz, M.; Sikora, B. Yttrium-Doped Iron Oxide Nanoparticles for Magnetic Hyperthermia Applications. *J. Phys. Chem. C* **2020**, *124* (12), 6871–6883. https://doi.org/10.1021/acs.jpcc.9b11043.

(43)   Goderski, S.; Kanno, S.; Yoshihara, K.; Komiya, H.; Goto, K.; Tanaka, T.; Kawaguchi, S.; Ishii, A.; Shimoyama, J.; Hasegawa, M.; Lis, S. Lanthanide Luminescence Enhancement of Core–Shell Magnetite–SiO 2 Nanoparticles Covered with Chain-Structured Helical Eu/Tb Complexes. *ACS Omega* **2020**, *5* (51), 32930–32938. https://doi.org/10.1021/acsomega.0c03746.

(44)   Orooji, Y.; Haddad Irani-nezhad, M.; Hassandoost, R.; Khataee, A.; Rahim Pouran, S.; Joo, S. W. Cerium Doped Magnetite Nanoparticles for Highly Sensitive Detection of Metronidazole via Chemiluminescence Assay. *Spectrochim. Acta Part A Mol. Biomol. Spectrosc.* **2020**, *234*, 118272. https://doi.org/10.1016/j.saa.2020.118272.

(45)   Xu, L.; Wang, J. Magnetic Nanoscaled Fe3O4/CeO2 Composite as an Efficient Fenton-like Heterogeneous Catalyst for Degradation of 4-Chlorophenol. *Environ. Sci. Technol.* **2012**, *46* (18), 10145–10153. https://doi.org/10.1021/es300303f.

(46)   Haviv, A. H.; Grenèche, J. M.; Lellouche, J. P. Aggregation Control of Hydrophilic Maghemite (γ-Fe2O 3) Nanoparticles by Surface Doping Using Cerium Atoms. *J. Am. Chem. Soc.* **2010**, *132* (36), 12519–12521. https://doi.org/10.1021/ja103283e.

(47)   Li, K.; Zhao, Y.; Song, C.; Guo, X. Magnetic Ordered Mesoporous Fe 3 O 4 /CeO 2 Composites with Synergy of Adsorption and Fenton Catalysis. *Appl. Surf. Sci.* **2017**, *425*, 526–534. https://doi.org/10.1016/j.apsusc.2017.07.041.

(48)   Santos de Lima, A.; Fernandes Pupo Nogueira, R. Cerium-Modified Iron Oxides Applied as Catalysts in the Heterogeneous Fenton System for Degradation of Cephalexin. *Environ. Sci. Pollut. Res.* **2021**, *28* (19), 23767–23777. https://doi.org/10.1007/s11356-020-11238-5.

(49)   Qi, Z.; Joshi, T. P.; Liu, R.; Liu, H.; Qu, J. Synthesis of Ce(III)-Doped Fe3O4 Magnetic Particles for Efficient Removal of Antimony from Aqueous Solution. *J. Hazard. Mater.* **2017**, *329*, 193–204. https://doi.org/10.1016/j.jhazmat.2017.01.007.

(50)   Chen, D.; Wang, Y. Impurity Doping: A Novel Strategy for Controllable Synthesis of Functional Lanthanide Nanomaterials. *Nanoscale* **2013**, *5* (11), 4621–4637. https://doi.org/10.1039/c3nr00368j.

(51)   Wang, F.; Han, Y.; Lim, C. S.; Lu, Y.; Wang, J.; Xu, J.; Chen, H.; Zhang, C.; Hong, M.; Liu, X. Simultaneous Phase and Size Control of Upconversion Nanocrystals through Lanthanide Doping. *Nature* **2010**, *463* (7284), 1061–1065. https://doi.org/10.1038/nature08777.

(52)   Wang, G.; Peng, Q.; Li, Y. Lanthanide-Doped Nanocrystals: Synthesis, Optical-Magnetic Properties, and Applications. **2011**, *44* (5).

(53)   Silva, C. R. De; Smith, S.; Shim, I.; Pyun, J.; Gutu, T.; Jiao, J. Lanthanide (III)-Doped Magnetite Nanoparticles of Current Interest , Due Largely to Their Advanced Technological And. *J. Am. Chem. Soc.* **2009**, *131* (3), 6336–6337.

(54)   Jiang, P. S.; Drake, P.; Cho, H. J.; Kao, C. H.; Lee, K. F.; Kuo, C. H.; Lin, X. Z.; Lin, Y. J. Tailored Nanoparticles for Tumour Therapy. *J. Nanosci. Nanotechnol.* **2012**, *12* (6), 5076–5081. https://doi.org/10.1166/jnn.2012.4890.

(55)   Aashima; Uppal, S.; Arora, A.; Gautam, S.; Singh, S.; Choudhary, R. J.; Mehta, S. K. Magnetically Retrievable Ce-Doped Fe3O4 Nanoparticles as Scaffolds for the Removal of Azo Dyes. *RSC Adv.* **2019**, *9* (40), 23129–23141. https://doi.org/10.1039/c9ra03252e.

(56) Andrade, Â. L.; Valente, M. A.; Ferreira, J. M. F.; Fabris, J. D. Preparation of Size-Controlled Nanoparticles of Magnetite. *J. Magn. Magn. Mater.* **2012**, *324* (10), 1753–1757. https://doi.org/10.1016/j.jmmm.2011.12.033.

(57) Moya, C.; Abdelgawad, A. M.; Nambiar, N.; Majetich, S. A. Magnetic Properties of Cube-Shaped Fe 3 O 4 Nanoparticles in Dilute, 2D, and 3D Assemblies. *J. Phys. D. Appl. Phys.* **2017**, *50* (32), 325003. https://doi.org/10.1088/1361-6463/aa7b11.

(58) Leontyev, I. N.; Kuriganova, A. B.; Leontyev, N. G.; Hennet, L.; Rakhmatullin, A.; Smirnova, N. V.; Dmitriev, V. Size Dependence of the Lattice Parameters of Carbon Supported Platinum Nanoparticles: X-Ray Diffraction Analysis and Theoretical Considerations. *RSC Adv.* **2014**, *4* (68), 35959–35965. https://doi.org/10.1039/c4ra04809a.

(59) Sun, S.; Zeng, H.; Robinson, D. B.; Raoux, S.; Rice, P. M.; Wang, S. X.; Li, G. Monodisperse MFe 2 O 4 (M = Fe, Co, Mn) Nanoparticles. *J. Am. Chem. Soc.* **2004**, *126* (1), 273–279. https://doi.org/10.1021/ja0380852.

(60) Almessiere, M. A.; Slimani, Y.; Baykal, A. Synthesis and Characterization of Co1–2Ni Mn Ce Fe2–O4 Nanoparticles. *J. Rare Earths* **2020**, *38* (2), 188–194. https://doi.org/10.1016/j.jre.2019.07.005.

(61) Laguna-Marco, M. A.; Piquer, C.; Roca, A. G.; Boada, R.; Andrés-Vergés, M.; Veintemillas-Verdaguer, S.; Serna, C. J.; Iadecola, A.; Chaboy, J. Structural Determination of Bi-Doped Magnetite Multifunctional Nanoparticles for Contrast Imaging. *Phys. Chem. Chem. Phys.* **2014**, *16* (34), 18301–18310. https://doi.org/10.1039/c4cp01392a.

(62) Nappini, S.; Magnano, E.; Bondino, F.; Píš, I.; Barla, A.; Fantechi, E.; Pineider, F.; Sangregorio, C.; Vaccari, L.; Venturelli, L.; Baglioni, P. Surface Charge and Coating of CoFe2O4 Nanoparticles: Evidence of Preserved Magnetic and Electronic Properties. *J. Phys. Chem. C* **2015**, *119* (45), 25529–25541. https://doi.org/10.1021/acs.jpcc.5b04910.

(63) Petrova, N.; Todorovsky, D.; Angelova, S.; Mehandjiev, D. Synthesis and Characterization of Cerium Citric and Tartaric Complexes. *J. Alloys Compd.* **2008**, *454* (1–2), 491–500. https://doi.org/10.1016/j.jallcom.2007.01.005.

(64) Bottger, G. L.; Geddes, A. L. The Infrared Spectra of the Crystalline Tetramethylammonium Halides. *Spectrochim. Acta* **1965**, *21* (10), 1701–1708. https://doi.org/10.1016/0371-1951(65)80082-0.

(65) Hancock, M. L.; Yokel, R. A.; Beck, M. J.; Calahan, J. L.; Jarrells, T. W.; Munson, E. J.; Olaniyan, G. A.; Grulke, E. A. The Characterization of Purified Citrate-Coated Cerium Oxide Nanoparticles Prepared via Hydrothermal Synthesis. *Appl. Surf. Sci.* **2021**, *535* (August 2020), 147681. https://doi.org/10.1016/j.apsusc.2020.147681.

(66) Joseph, Y.; Ketteler, G.; Kuhrs, C.; Ranke, W.; Weiss, W.; Schlögl, R. On the Preparation and Composition of Potassium Promoted Iron Oxide Model Catalyst Films. *Phys. Chem. Chem. Phys.* **2001**, *3* (18), 4141–4153. https://doi.org/10.1039/b104263g.

(67) Schedel-Niedrig, T.; Weiss, W.; Schlögl, R. Electronic Structure of Ultrathin Ordered Iron Oxide Films Grown onto Pt(111). *Phys. Rev. B* **1995**, *52* (24), 17449–17460. https://doi.org/10.1103/PhysRevB.52.17449.

(68) Grosvenor, A. P.; Kobe, B. A.; Biesinger, M. C.; McIntyre, N. S. Investigation of Multiplet Splitting of Fe 2p XPS Spectra and Bonding in Iron Compounds. *Surf. Interface Anal.* **2004**, *36* (12), 1564–1574. https://doi.org/10.1002/sia.1984.

(69) Goss, C. J. Saturation Magnetisation, Coercivity and Lattice Parameter Changes in the System Fe3O4-ΓFe2O3, and Their Relationship to Structure. *Phys. Chem. Miner.* **1988**, *16* (2), 164–171. https://doi.org/10.1007/BF00203200.

(70) Briggs, D. X-Ray Photoelectron Spectroscopy (XPS). *Handb. Adhes. Second Ed.* **2005**, 621–622. https://doi.org/10.1002/0470014229.ch22.

(71) Bêche, E.; Charvin, P.; Perarnau, D.; Abanades, S.; Flamant, G. Ce 3d XPS Investigation of Cerium Oxides and Mixed Cerium Oxide (Ce XTiyOz). *Surf. Interface Anal.* **2008**, *40* (3–4), 264–267. https://doi.org/10.1002/sia.2686.

(72) Schedel-Niedrig, T.; Weiss, W.; Schlögl, R. Electronic Structure of Ultrathin Ordered Iron Oxide Films Grown onto Pt(111). *Phys. Rev. B* **1995**, *52* (24), 17449–17460. https://doi.org/10.1103/PhysRevB.52.17449.

(73) Maslakov, K. I.; Teterin, Y. A.; Popel, A. J.; Teterin, A. Y.; Ivanov, K. E.; Kalmykov, S. N.; Petrov, V. G.; Petrov, P. K.; Farnan, I. XPS Study of Ion Irradiated and Unirradiated CeO 2 Bulk and Thin Film Samples. *Appl. Surf. Sci.* **2018**, *448*, 154–162. https://doi.org/10.1016/j.apsusc.2018.04.077.

(74) Ferreira, J. M.; Souza, K. P.; Queiroz, F. M.; Costa, I.; Tomachuk, C. R. Electrochemical and Chemical Characterization of Electrodeposited Zinc Surface Exposed to New Surface Treatments. *Surf. Coatings Technol.* **2016**, *294* (May), 36–46. https://doi.org/10.1016/j.surfcoat.2016.03.023.

(75) Ferreira, J. M.; Souza, K. P.; Queiroz, F. M.; Costa, I.; Tomachuk, C. R. Electrochemical and Chemical Characterization of Electrodeposited Zinc Surface Exposed to New Surface Treatments. *Surf. Coatings Technol.* **2016**, *294* (May), 36–46. https://doi.org/10.1016/j.surfcoat.2016.03.023.

(76) Moskvin, M.; Marková, I.; Malínská, H.; Miklánková, D.; Hüttl, M.; Oliyarnyk, O.; Pop-Georgievski, O.; Zhigunov, A.; Petrovský, E.; Horák, D. Cerium Oxide-Decorated γ-Fe2 O3 Nanoparticles: Design, Synthesis and in Vivo Effects on Parameters of Oxidative Stress. *Front. Chem.* **2020**, *8* (August), 1–13. https://doi.org/10.3389/fchem.2020.00682.

(77) Liang, X.; Wang, X.; Zhuang, J.; Chen, Y.; Wang, D.; Li, Y. Synthesis of Nearly Monodisperse Iron Oxide and Oxyhydroxide Nanocrystals. *Adv. Funct. Mater.* **2006**, *16* (14), 1805–1813. https://doi.org/10.1002/adfm.200500884.

(78) Gavilán, H.; Avugadda, S. K.; Fernández-Cabada, T.; Soni, N.; Cassani, M.; Mai, B. T.; Chantrell, R.; Pellegrino, T. Magnetic Nanoparticles and Clusters for Magnetic Hyperthermia: Optimizing Their Heat Performance and Developing Combinatorial Therapies to Tackle Cancer. *Chem. Soc. Rev.* **2021**, *50* (20), 11614–11667. https://doi.org/10.1039/d1cs00427a.

(79) Vassallo, M.; Martella, D.; Barrera, G.; Celegato, F.; Coïsson, M.; Ferrero, R.; Olivetti, E. S.; Troia, A.; Sözeri, H.; Parmeggiani, C.; Wiersma, D. S.; Tiberto, P.; Manzin, A. Improvement of Hyperthermia Properties of Iron Oxide Nanoparticles by Surface Coating. *ACS Omega* **2022**. https://doi.org/10.1021/acsomega.2c06244.

(80) Guardia, P.; Riedinger, A.; Kakwere, H.; Gazeau, F.; Pellegrino, T. Magnetic Nanoparticles for Magnetic Hyperthermia and Controlled Drug Delivery. *Bio-Bioinspired Nanomater.* **2014**, *9783527335*, 139–172. https://doi.org/10.1002/9783527675821.ch06.

(81) Foong, Y. M.; Hsieh, J.; Li, X.; Chua, D. H. C. Comparative Study between Erbium and Erbium Oxide-Doped Diamondlike Carbon Films Deposited by Pulsed Laser Deposition Technique. *J. Vac. Sci. Technol. A Vacuum, Surfaces, Film.* **2010**, *28* (3), 449–455. https://doi.org/10.1116/1.3372335.

(82) Iwasaki, T.; Mizutani, N.; Watano, S.; Yanagida, T.; Kawai, T. Size Control of Magnetite Nanoparticles by Organic Solvent-Free Chemical Coprecipitation at Room Temperature. *J. Exp. Nanosci.* **2010**, *5* (3), 251–262. https://doi.org/10.1080/17458080903490731.

(83) Kirillov, V. L.; Balaev, D. A.; Semenov, S. V.; Shaikhutdinov, K. A.; Martyanov,

O. N. Size Control in the Formation of Magnetite Nanoparticles in the Presence of Citrate Ions. *Mater. Chem. Phys.* **2014**, *145* (1–2), 75–81. https://doi.org/10.1016/j.matchemphys.2014.01.036.

(84)   Granath, T.; Mandel, K.; Löbmann, P. Overcoming the Inhibition Effects of Citrate: Precipitation of Ferromagnetic Magnetite Nanoparticles with Tunable Morphology, Magnetic Properties, and Surface Charge via Ferrous Citrate Oxidation. *Part. Part. Syst. Charact.* **2021**, *38* (8). https://doi.org/10.1002/ppsc.202100098.

(85)   Jing, J.; Zhang, Y.; Liang, J.; Zhang, Q.; Bryant, E.; Avendano, C.; Colvin, V. L.; Wang, Y.; Li, W.; Yu, W. W. One-Step Reverse Precipitation Synthesis of Water-Dispersible Superparamagnetic Magnetite Nanoparticles. *J. Nanoparticle Res.* **2012**, *14* (4), 827. https://doi.org/10.1007/s11051-012-0827-3.

(86)   Zhang, X.; Chen, L.; Liu, R.; Li, D.; Ge, X.; Ge, G. The Role of the OH Group in Citric Acid in the Coordination with Fe3O4 Nanoparticles. *Langmuir* **2019**. https://doi.org/10.1021/acs.langmuir.9b00208.

(87)   Zhang, Y.; Yang, M.; Gao, Y.; Wang, F.; Huang, X. Preparation and Adsorption Mechanism of Rare Earth-Doped Adsorbent for Arsenic(V) Removal from Groundwater. *Sci. China, Ser. B Chem.* **2003**, *46* (3), 252–258. https://doi.org/10.1360/02yb0136.

(88)   Zhang, Y.; Yang, M.; Dou, X. M.; He, H.; Wang, D. S. Arsenate Adsorption on an Fe-Ce Bimetal Oxide Adsorbent: Role of Surface Properties. *Environ. Sci. Technol.* **2005**, *39* (18), 7246–7253. https://doi.org/10.1021/es050775d.

(89)   Wells, W. H.; Wells, V. L. The Lanthanides, Rare Earth Elements. *Patty's Toxicol.* **2012**, *1*, 817–840. https://doi.org/10.1002/0471435139.tox043.pub2.

(90)   Dey, A.; Lenders, J. J. M.; Sommerdijk, N. A. J. M. Bioinspired Magnetite Formation from a Disordered Ferrihydrite-Derived Precursor. *Faraday Discuss.* **2015**, *179*, 215–225. https://doi.org/10.1039/C4FD00227J.

(91)   Piella, J.; Gónzalez-Febles, A.; Patarroyo, J.; Arbiol, J.; Bastús, N. G.; Puntes, V. Seeded-Growth Aqueous Synthesis of Colloidal-Stable Citrate-Stabilized Au/CeO2 Hybrid Nanocrystals: Heterodimers, Core@Shell, and Clover- And Star-Like Structures. *Chem. Mater.* **2019**, *31* (19), 7922–7932. https://doi.org/10.1021/acs.chemmater.9b02005.

(92)   Mascolo, M. C.; Pei, Y.; Ring, T. A. Room Temperature Co-Precipitation Synthesis of Magnetite Nanoparticles in a Large Ph Window with Different Bases. *Materials (Basel).* **2013**, *6* (12), 5549–5567. https://doi.org/10.3390/ma6125549.

(93)   Krehula, S.; Popovi, S.; Musić, S. Synthesis of Acicular α-FeOOH Particles at a Very High PH. *Mater. Lett.* **2002**, *54* (2–3), 108–113. https://doi.org/10.1016/S0167-577X(01)00546-8.

(94)   Chen, Y.; He, X.; Zhao, X.; Yuan, Q.; Gu, X. Preparation, Characterization, and Growth Mechanism of a Novel Aligned Nanosquare Anatase in Large Quantities in the Presence of TMAOH. *J. Colloid Interface Sci.* **2007**, *310* (1), 171–177. https://doi.org/10.1016/j.jcis.2007.01.046.

(95)   Liu, Y.; Ding, Y.; Sheng, A.; Li, X.; Chen, J.; Arai, Y.; Liu, J. Fe(II)-Catalyzed Transformation of Ferrihydrite with Different Degrees of Crystallinity. *Environ. Sci. Technol.* **2023**, *57* (17), 6934–6943. https://doi.org/10.1021/acs.est.3c00555.

(96)   Aeppli, M.; Kaegi, R.; Kretzschmar, R.; Voegelin, A.; Hofstetter, T. B.; Sander, M. Electrochemical Analysis of Changes in Iron Oxide Reducibility during Abiotic Ferrihydrite Transformation into Goethite and Magnetite. *Environ. Sci. Technol.* **2019**, *53* (7), 3568–3578. https://doi.org/10.1021/acs.est.8b07190.

(97)   Raghav, M.; Sáez, A. E.; Ela, W. P. Understanding Abiotic Ferrihydrite Re-Mineralization by Ferrous Ions. *Int. J. Environ. Sci. Technol.* **2015**, *12* (6), 1945–

1956. https://doi.org/10.1007/s13762-014-0599-7.

(98)   Jolivet, J. P.; Froidefond, C.; Pottier, A.; Chanéac, C.; Cassaignon, S.; Tronc, E.; Euzen, P. Size Tailoring of Oxide Nanoparticles by Precipitation in Aqueous Medium. A Semi-Quantitative Modelling. *J. Mater. Chem.* **2004**, *14* (21), 3281–3288. https://doi.org/10.1039/b407086k.

(99)   Channei, D.; Phanichphant, S.; Nakaruk, A.; Mofarah, S.; Koshy, P.; Sorrell, C. Aqueous and Surface Chemistries of Photocatalytic Fe-Doped CeO2 Nanoparticles. *Catalysts* **2017**, *7* (12), 45. https://doi.org/10.3390/catal7020045.

(100)   Abellan, P.; Moser, T. H.; Lucas, I. T.; Grate, J. W.; Evans, J. E.; Browning, N. D. The Formation of Cerium (III) Hydroxide Nanoparticles by a Radiation Mediated Increase in Local PH. *RSC Adv.* **2017**, *7* (7), 3831–3837. https://doi.org/10.1039/C6RA27066B.

(101)   Silva, A. M. N.; Kong, X.; Parkin, M. C.; Cammack, R.; Hider, R. C. Iron(Iii) Citrate Speciation in Aqueous Solution. *Dalt. Trans.* **2009**, No. 40, 8616–8625. https://doi.org/10.1039/b910970f.

(102)   Königsberger, L. C.; Königsberger, E.; May, P. M.; Hefter, G. T. Complexation of Iron (III) and Iron (II) by Citrate. Implications for Iron Speciation in Blood Plasma. *J. Inorg. Biochem.* **2000**, *78* (3), 175–184. https://doi.org/10.1016/S0162-0134(99)00222-6.

Chapter 4

Evaluating the Applicability of Iron Oxide Nanoparticles

4.1 Introduction

The remarkable attention in magnetic IONPs is reflected in extensive published research across synthesis methodologies to their wide use in nanotechnology applications. The IONPs developed in this thesis, especially Ce@IONPs, can be versatile and useful NPs to be used in diverse areas, from environmental remediation to innovative biomedical applications. Their customizable size, combined with their inherent magnetic properties, and cerium ions on their surface, make them ideal for catalytic and therapeutic purposes.

Inorganic nanomaterials have been reported to have intrinsic enzyme-like catalytic activity.[1] Since the discovery in 2007 that ferrimagnetic iron oxide nanoparticles (IONPs) –previously considered inert–, exhibit inherent peroxidase-like activity, were introducing the enzyme study methodologies into nanotechnology.[2] Known today as "nanozymes", these are simply inorganic nanoparticles catalysts. To date, more than 300 nanomaterials with enzymatic activity have been reported, leading to the broad acceptance and rapid development of the nanozymes field.[1,3]

Nanozymes are distinct from enzyme-integrated nanoparticles or nanomaterial hybrid enzymes (i.e., enzymes conjugated to AuNPs,[4,5] or IONPs[6]), where the nanomaterials

themselves are generally considered catalytically inert.[7,8] In the case of nanozymes, the catalytic activity directly originates from the nanomaterial itself which distinguishes them from the above-mentioned materials.[2,3]

Like biological enzymes, nanozymes possess several features that allow them to catalyze biochemical reactions under physiological conditions. However, being heterogeneous inorganic catalysts, they are not biological enzymes.[9] These provide nanozymes several advantages to make them robust alternatives to natural enzymes, including enhanced stability and durability, lower cost, high catalytic activity, ease of production, and a broad range of applications, while they are not effective at very low substrate concentrations, as enzymes are.[1,10]

Nanozymes are composed of inorganic or organic nanomaterials with specific physicochemical properties. They usually follow similar enzymatic kinetics, most of them the Michaelis-Menten kinetics model, characterized by an asymptotic curve, where the initial slope represents the reaction rate and the plateau indicates the reaction equilibrium.[3] Nanozymes catalytic activity can also be regulated depending or their specific design or by modifying the reaction conditions; for example, carbon nanospheres selectively nitrogen-doped could mimic four different enzyme-like activities (oxidase, peroxidase, catalase and superoxide dismutase) used for ROS regulation (production/scavenging).[11]

The size, morphology, and surface characteristics of nanozymes, such as crystal form, lattice planes, defects, and vacancies, critically impact their activity.[11] These nanoscale factors offer a strategic advantage for fine-tuning their catalytic efficiency. For instance, IONPs display peroxidase-like activity (POD) at acidic pH and catalase-like activity (CAT) at physiological pH, making them versatile for various applications.[12,13] In addition, nanozymes exhibit other physicochemical properties, for example magnetism, fluorescence, and photothermal effects, which provides more advantages in practical applications and in the design of bioanalytical sensors.[14]

Ferromagnetic IONPs are one of the most studied and used nanozyme. Their high surface-to-volume ratio support various catalytic sites, which result in high surface reactivity.[15,16] To enhance the efficiency or selectivity of nanozymes, their catalytic activity can be improved or modulated though methods such as atomic doping or creating hybrid nanostructures.[17–19] Cerium ions are particularly effective as doping agents. Cerium-based nano-catalysts have gained significant attention due to their exceptional catalytic redox properties, high oxygen storage capacity, non-toxicity and the ease of redox cycle between Ce^{3+} to Ce^{4+} and vice versa.[20–25] Incorporating cerium into magnetic iron oxide-based

catalysts has demonstrated higher reactivity, and improved catalytic performance as Fenton-like heterogenous catalyst by increasing HO· generation and Fe redox recycling.[18,21,26–28] Additionally, its combination with the magnetic properties of IONPs offers the advantage of easy magnetic separation and recovery, apart from their low toxicity.

Magnetic IONPs are also employed for cancer treatment, and their use in magnetic hyperthermia therapy (MHT) is well-recognized.[29,30] Magnetic NPs convert electromagnetic energy into heat when exposed to an alternating magnetic field (AMF), and this energy is maximized in the size range between the SPM and FM transition.[31] However, increased NPs size distribution leads to a reduction in the heating effect and small changes in NP size and aggregation can also produce significant effects at the biological level.[32] The NPs heating efficiency can be translated into SAR values –also known as specific loss power (SLP)–, and current research aims to optimize the magneto-energy conversion to administer the lowest NPs amount to patients.[31]

Recent studies have demonstrated the benefits of MH with IONPs in affecting the tumor microenvironment and sensitizing tumor cells to other therapies.[32,33] In this regard, current therapeutic strategies are focused on the use multimodal MNPs, which can enhance their therapeutic efficacy through thermally induced mechanisms, using magnetic hyperthermia and photothermal therapies.[33,34] For instance, in one study, magnetic heating generated by Fe_3O_4 nanozymes has been shown to exert dual effects, proving effective for tumor growth inhibition and removal by accelerating the production of HO· radicals at 42°C in the tumor microenvironment.[35] In another study, a $MnFe_2O_3$ NPs surface modified with a lipophilic Iridium(III) complex as mitochondrial target, when exposed to an AMF, induced localized hyperthermia causing mitochondrial damage, and cytotoxic damage by ROS generated.[36]

Hence, the objective of this chapter was to investigate and compare the peroxidase-mimicking activity of the previously synthesized Ce@IONPs in a heterogeneous catalysis approach. This study aims to demonstrate that the presence of Ce on the IONPs surface considerably enhances the oxidation of 3,3´,5,5´-tetramethylbenzydine (TMB) (an enzymatic substrate) due to the combination of the Fe and Ce redox couple. Furthermore, the performance of Ce@IONPs in magnetic hyperthermia will be tested, because the synthesized NPs have a tunable size, high monodispersity, and high magnetic saturation, which could be of interest for MHT. These results highlight the improved performance of Ce@IONPs, making them ideal for potential bio-technological applications.

4.2   Experimental

4.2.1 Chemicals and materials

3,3´,5,5´-tetramethylbenzydine (TMB, ≥99%), hydrogen peroxide solution (H$_2$O$_2$, 30% w/w, *puriss* p.a.), dimethyl sulfoxide (DMSO, **>99%**), sodium acetate anhydrous (NaAc, **>99%**), acetic acid (HAc, **>99%**). All reagents were purchased from Sigma-Aldrich and used as received without further purification. Prepared NaAc-HAc buffer solution 0.01M, adjusted to pH 5.0. Milli-Q water (18 MΩ cm^{-1}) was used in all the experiments. In-house-made nanoparticles SC-IONPs (~9 nm), Ce@IONPs (13–46 nm) obtained using Ce concentration from 0.1 to 2.0 mM (showed in chapter 3). Leaching solution was obtained by using Centricon amicon ultra® 100 kDa (6 nm pore) and centrifuged at 5000G for 3 min.

4.2.2 Mimicking Peroxidase-like Catalytic Activity of Ce@IONPs

Determination of the mimicking peroxidase-catalytic activity of the Ce@IONPs was based on the oxidation of TMB in the presence of H$_2$O$_2$ as a heterogeneous catalysis approach. All catalytic assays were performed at pH 5 and room temperature, unless otherwise stated. Stock aqueous dispersions of IONP and Ce@IONPs were prepared at concentration of 0.2 mg/mL in a TMAOH (2 mM) aqueous solution. The catalytic assays were carried out in 4.5 mL PS-disposable cuvettes and monitored by UV-vis spectroscopy. As TMB and H$_2$O$_2$ solutions are susceptible to degradation, H$_2$O$_2$ and TMB were freshly prepared before the kinetic assays, and the experiments were performed in the dark to minimize interference with illumination.

For the catalytic activity, in a typical experiment, 2 mL of NaAc-HAc buffer solution (0.010 M, pH 5.0) containing different amounts of Ce@IONPs (0, 5, 10, 15, 20, and 30 μg) were placed in disposable cuvettes. Then, 20 μL of TMB solution (5 mg mL^{-1} in DMSO) (final concentration, 0.204 mM) was added to the cuvette and mixed, followed by the addition of 32 μL of H$_2$O$_2$ (final concentration, 150 mM) to start the reaction. Immediately after the substrates were added, a blue-color reaction was observed. The intensity of the absorption peak at 652 nm was monitored by UV-vis spectroscopy as a function of time every 10 s for up to 600 s. This process was repeated for each amount from each different

Ce@IONPs size. Control experiments were performed for each Ce@IONPs by using the highest amount of NPs (30 μg), first by performing the reaction in the absence of H_2O_2, and second by performing the reaction with the leaching solution (LS). The LS is the resultant solution obtained from NPs incubation in the acidic buffer during 40 min to ensure that catalytic activity is not caused by the release or leaching of iron ions from the catalyst in the solution.

The effect of the buffer solution and ionic strength on the catalytic activity of 20 μg of the non-doped IONPs was evaluated. In addition, the effect of pH was evaluated within the pH range of 3.0–6.5 at 25ºC, and the influence of the temperature between 20 to 50 ºC.

Their apparent kinetic parameters were determined for 5 μg of the IONPs and Ce0.25@IONPs by varying the substrate concentrations of TMB (0.02–0.8 mM) at fixed concentration of H_2O_2 (150 mM), or H_2O_2 (0.07–2 M) at fixed concentration of TMB (0,406 mM), in an NaAc-HAc buffer solution (0.010 M, pH 5.0) at room temperature. The apparent parameters were calculated following a Michaelis-Menten kinetics model.

4.2.3 Magnetic Hyperthermia Characterization

The determination of the heating performance of the Ce@IONPs samples were evaluated by calorimetric measurements conducted in a commercially available set up (magneTherm nanoTherics Ltd). Selected Ce@IONPs (~13 nm, ~23 nm, ~27 nm, and ~ 34 nm ([Ce^{3+}] at 0.10, 0.25, 0.50 and 0.75 mM, respectively), at concentration around ~9 to 22 mg/mL in water were evaluated. Briefly, a 500 μL of water-soluble Ce@IONPs dispersion was introduced into a sample holder thermally isolated from the environment to achieve a quasi- or close-to-adiabatic (QA) conditions. The samples were exposed to an alternating magnetic field (AMF) 17.5 kA/m and 156 kHz frequency for 1 minute, while the temperature of the sample was recorded by an optical thermal fibber probe at 0.15 s scan rate. All measurements were performed in water and normalized by the amount of Ce@IONPs (g/L of sample). SLP reported values and error bars were obtained from at least four experimental measurements and calculated according to the following equation:

$$SLP\left(W/g\right) = \left(\frac{C}{m} \cdot \frac{dT}{dt}\right) \approx \left(\frac{C}{m} \cdot \frac{\Delta T}{\Delta t}\right)_{QA}$$

Where C is the specific heat capacity of the water dispersion medium water (C_{water} = 4185 J/ L·K) per unit volume, m is the concentration of the magnetic material (in g/L of

Fe) in solution, and $\Delta T/\Delta t_{QA}$ is the calculated initial slope of the temperature versus time curve, under the quasi-adiabatic conditions.

4.2.4 Cytotoxicity Assay

To evaluate the cytotoxicity of the Ce0.25@ IONPs in an in-vitro model, we evaluated cell viability using THP1 cells after incubation with different amounts of nanoparticles. The THP1 cell line was cultured in RPMI1640 medium (ATCC), supplemented with 10% heat inactivated FBS (ATCC), 100 μg/mL streptomycin, and 100 units/mL penicillin (Sigma Aldrich) and maintained at 37°C in a 5% CO_2 atmosphere. Initially, cells were seeded in a 24-well plate at an initial density of ~$1x10^6$ cells/mL and incubated for 24 hours under standard conditions.

After 24 hours, the cells were treated with a final concentration of 0.1, 0.2 and 0.5 mg/mL of Ce0.25@IONPs (~23 nm) for an additional 24 hours. Afterwards, cells were centrifuged, washed in PBS and then incubated in complete RMPI medium to separate them from non-endocytosed NPs. Cell viability was determined using Trypan Blue exclusion test at 24 h and 72 h by comparison with the control cells under an optical microscope.

4.3   Results and Discussion

4.3.1 Mimicking Peroxidase-like Catalytic Activity of Ce@IONPs

4.3.1.1   Oxidation of TMB chromogenic substrate

The synthesized Ce@IONPs were evaluated for their catalytic performance using a peroxidase-like mimicking assay. This specific assay was selected because ferromagnetic Fe_3O_4 NPs were the first nanomaterial known to possess intrinsic enzyme-like catalytic activity.[2] In addition, other nanomaterials as CeO_2 NPs or hybrid Ce-IONPs, have been studied for their enzymatic-like characteristics, and applied in bioanalytical assays.[1,18,23,37–39] Additionally, key nanoscale factors such as particle size, morphology, surface chemistry and surface coating can significantly influence their catalytic activity.

We catalyzed the oxidation of 3,3´,5,5´-tetramethylbenzydine (TMB) as the substrate in the presence of H_2O_2. While other common colorimetric substrates like o-phenylenediamine (OPD), 2,2'-azino-bis(3-ethylbenzothiazoline-6-sulfonic acid) (ABTS), and 3,3'-diaminobenzidine (DAB) are available, TMB is frequently chosen. TMB is preferred due to its non-toxicity, high sensitivity, and the intense blue color that produces at 652 nm, which does not overlap with the IONPs absorbance.[40]

Figure 4-1 illustrates the scheme of the TMB oxidation reaction and its following by UV-vis spectroscopy. The oxidation of TMB is both favorable and stable in an acidic pH. During this process, one-electron oxidation of TMB diamine produces a TMB+· cation free radical, which is in equilibrium with the charge-transfer complex (T2). Studies have shown that this equilibrium is almost entirely shifted towards the product.[41] The T2 complex exhibited two maximum absorbance peaks at 370 nm and 652 nm, which are observed as a blue color reaction (Figure 4-1A). Further two-electron oxidation results in the formation of diimine oxidized TMB with a maximum peak absorbance at 450 nm, causing a transition color from blue to green and finally leading to a bright yellowish color at longer reaction times (Figure 4-1B).[41] The two consecutive reactions, each one-electron transition, can be treated separately. The absorption peak at 652 nm is useful for subsequent analyses, as the peak at 370 nm overlaps with the diimine peak (450 nm).[41]
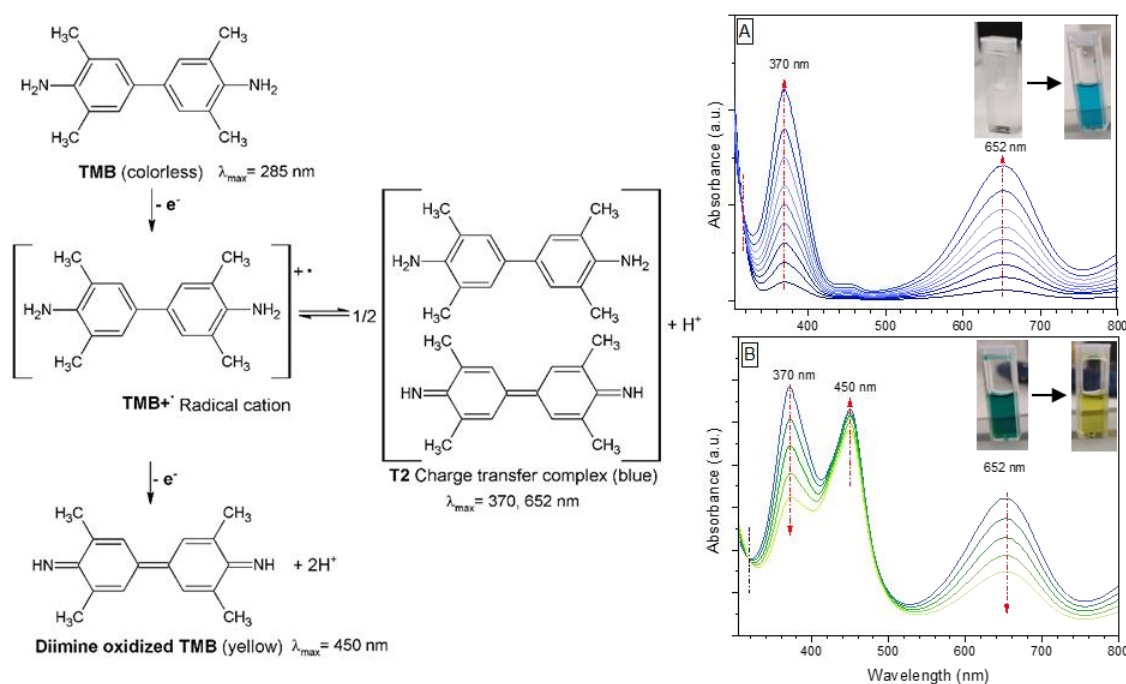

Figure 4-1. Scheme of the oxidation process of 3,3´,5,5´-tetramethylbenzydine (TMB) and UV-vis spectra monitoring during this reaction in the presence of H_2O_2, catalyzed by Ce0.25@IONPs at pH 5, (A) the oxidation reaction begins with the formation of the T2 complex, and (B) ending in diimine TMB at longer reaction times.

In the reaction, maintaining the stability of the blue charge-transfer complex (T2) over time-reaction is important as the reaction is followed by monitoring the absorption peak at 652 nm. This can be achieved through the evaluation and optimization of the reaction parameters, such as pH, buffers type, ionic strength, and substrates concentration.

4.3.1.2 Optimization of the TMB Oxidation Reaction

The oxidation of TMB in presence of H_2O_2 displays a controlled reaction, which can be used to quantitatively analyze and to compare the catalytic activity of NPs. Although this study initially aimed to follow the standardized protocol by Jiang et al.,[14] used for testing the peroxide-like activity of various nanomaterials, among them Fe_3O_4 NPs with a sizes range of 30–250 nm, we needed to make several adjustments in the experimental conditions. These adjustments were necessary to measure the kinetics within the linear range of our UV-vis spectrophotometer, especially for smaller crystal sizes and Ce@IONPs samples, where in those conditions the catalytic activity was higher and not possible to recorded.

First, in comparison with the standardized protocol,[14] it was necessary to decrease the amounts of both substrates, in our experiments we used: 0.1 mg of TMB substrate instead of 1 mg, an H_2O_2 concentration of 0.150 M rather than 1 M. The incubation temperature was at room temperature (25ºC) instead of 37ºC, for practical purposes.

In addition, considerations regarding the concentration of protons (H^+) and ionic strength of the medium influenced the catalytic activity of the TMB substrate and the IONPs. Since TMB is a chromogenic reactive that works in acidic media, and the surface of the synthesized IONPs contain ionizable groups such as citrate, the pH and buffer salt chosen may change their activity or promote NPs aggregation. Figure 4-2 displays the tests carried out with 20 µg of the SC-IONPs (~9 nm) using acetate (NaAc:AcH) or citrate (NaCit:CitH) buffers at two different pH (3.6 and 5.6) and ionic strengths (10 mM and 100 mM).
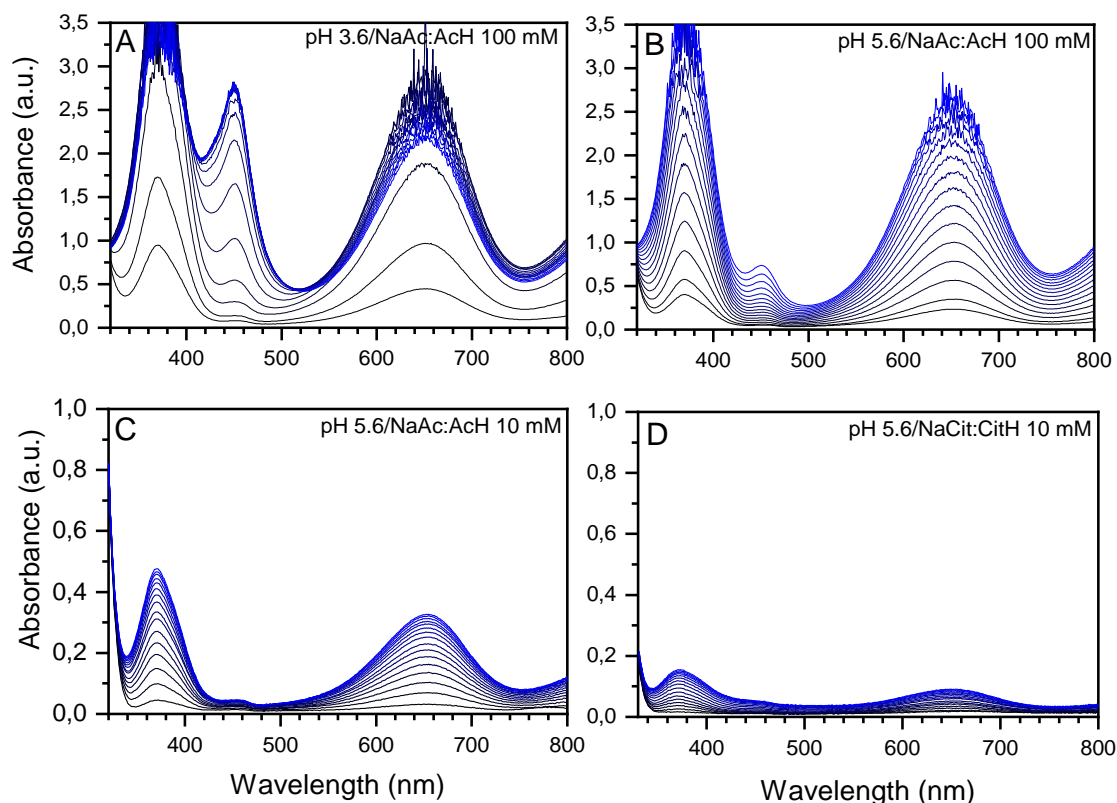
*Figure 4-2. UV-vis spectra of the reaction times curves for the catalytic oxidation of TMB (0.1 mg) by H_2O_2 (150 mM) using 20 μg of IONPs (~9 mM) by varying the buffer NaAc: AcH (**A**) 100 mM at pH 3.6, (**B**) 100 mM at pH 5.6, (**C**) 10 mM at pH 5.6 and (**D**) buffer NaCit:CitH 10 mM at pH5.6. Time interval between the measurements ΔT = 10 s up to 600 s.*

As observed in the UV-Vis spectra (Figure 4-2A), the first reaction condition using acetate buffer 100 mM at an acidic pH of 3.6, the reaction rate proceed faster, and the two-electron transfer product (diimine) was also produced. That was indicated by the rapidly increased absorption peak at 450 nm and manifested in the reaction mixture as a rapid color change from blue to green and finally yellowish solution, indicating that these conditions were not favorable. Despite this, the high ionic strength and low pH (3.6) caused rapid aggregation of the nanoparticles over time, making the experiments difficult and not completely reproducible. To address this, we reduced the ionic strength to 10 mM and worked in a more suitable pH range 5–6, within of the determined colloidal stability of the NPs (Figure 3-6, in chapter 3) and within the reported pH range for peroxidase-like behavior assays.[15]

As expected, the reaction rate decreased when the pH was raised to 5.6 (Figure 4-2B). This reduction occurred because, as their TMB pKa is approximately 4.17, at the lower pHs the amino groups can partially exists in the protonated form.[40] Hydrogen donor substrates that works at acidic media, such as ABTS, TMB, and OPD, are pH dependent.[42]

This positively charge facilitates their attraction to the negatively charged NPs surface, leading to a faster reaction. In addition, the stability and formation of the reactive HO· in Fenton reaction decreases at higher pH.[43] The reduction of ionic strength to 10 mM, also resulted in a further decrease in the reaction rate, which can be attributed to the lower proton concentration in the media (Figure 4-2C). Additionally, we tested a 10 mM citrate buffer and observed an even greater reduction in the reaction rate compared to the acetate buffer (Figure 4-2D). In the citrate buffer, the nanoparticles surface became completely covered by citrate ions, which blocked their interaction with the TMB or H_2O_2 substrates.

Figure 4-3 presents the reaction time curves at the maximum absorbance of 652 nm from the experiments described above. These curves showed that the 10 mM NaAc:AcH buffer at pH 5.6 provided the apparent steady-state conditions of a Michaelis-Menten kinetic model across different NPs concentrations (Figure 4-3B). The conditions depicted in Figure 4-3A were unsuitable due to the rapid production of the diimine product at pH 3.6 and by the observed aggregation of the IONPs with the time at the high ionic strength of 100 mM. Furthermore, the conditions shown in Figure 4-3C were discarded due to the lowest absorption observed due to citrate coats the NPs surface forming a strong coordination complex with the Ce and Fe ions decreasing its reactivity. In addition, the sigmoidal behavior at each NP concentration, indicating a deviation from the M-M kinetic model. This deviation was mainly caused by the equilibrium between the citrate groups at the NP surface and the pH buffer.
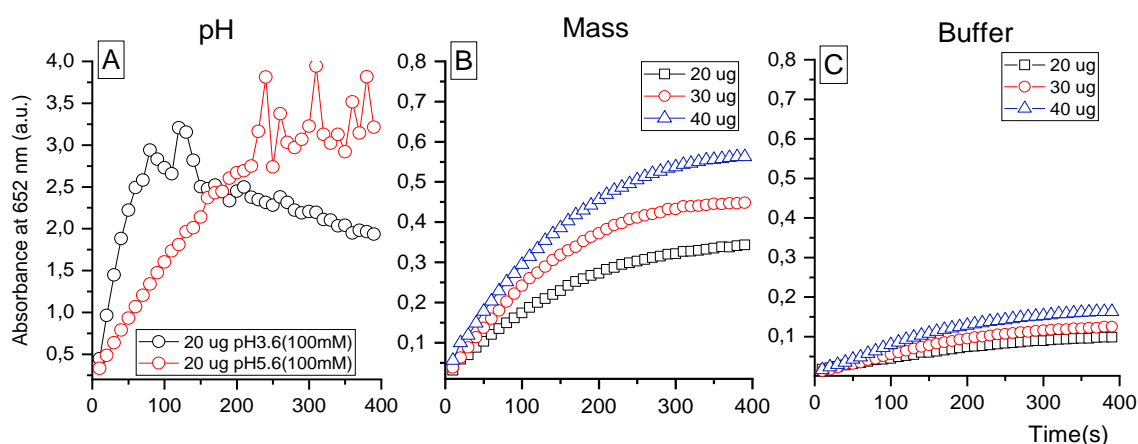
Figure 4-3. UV-vis reaction times curves (λ_{max} = 652 nm) for the oxidation of TMB (0.1 mg) in presence of H_2O_2 (150 mM) catalyzed by IONPs (~9 mM) as a function of their mass (µg), by varying: (A) IONPs (20 µg) buffer NaAc:AcH 100 mM at pH 3.6 and 5.6, (B) IONPs (20, 30 and 40 µg) buffer NaAc:AcH 10 mM at pH 5.6 and (C) IONPs (20, 30 and 40 µg) buffer NaCit:CitH at pH 5.6. Time interval between the measurements ΔT = 10 s up to 400 s.

The catalytic response of the IONPs at different pH (3.0–6.5) and temperatures (20–50 ℃) was evaluated, the normalized relative activities are shown in Figure 4-4. The catalytic activity are both pH and temperature dependent, similar to horseradish peroxidase (HRP) enzyme.[2] The highest activity occurred at around pH 4.5, however, pH 4.0 and 5.0 also demonstrating high catalytic responses above 90%. Although pH below 4.0 showed good activity, the solutions turned greenish, indicating the rapid production of the diimine oxidation product. Conversely, at pH above 5.0, the catalytic activity gradually decreased, dropping from 60% at pH 5.5 to 10% at pH 6.5.

The optimal temperature range for mimicking peroxidase catalytic activity was between 35 and 40 ℃. However, the effect temperature changes within the tested range were less significant than pH changes, with catalytic activity remaining above 83 % from 20 to 50℃.
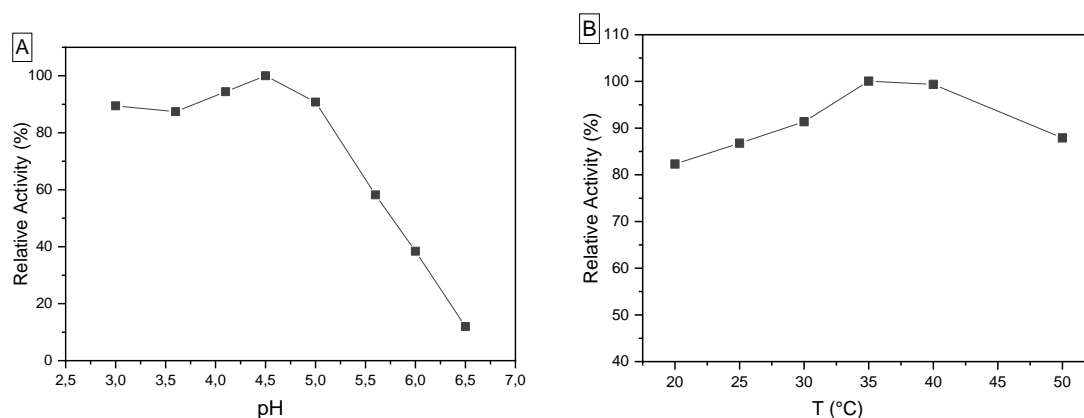
Figure 4-4. Effect of (A) pH and (B) temperature as relative activity (%) for the catalytic oxidation of TMB (0.1 mg) catalyzed by 20 μg of IONPs (~9 mM) in presence of H_2O_2 (150 mM) buffer NaAc:AcH (10 mM).

Finally, we established the experimental conditions with 0.1 mg of TMB substrate, 0.150 M of H_2O_2 concentration, NaAc:AcH buffer 10 mM at pH 5 to avoid the NPs aggregation, and incubation at room temperature (25℃) for practical purposes. Since the initial velocity of the reaction depends on the concentrations of the substrates, the amount of nanoparticle, the pH, temperature, and reaction products, the values obtained under these conditions will be lower than those of the standardized protocol, making direct comparisons unfeasible. However, NPs measured under the same conditions can be compared with each other, providing an indication of their catalytic activity under the specified parameters.

4.3.1.3 Determining the catalytic activity of the Ce@IONPs

The catalytic activity of the synthesized single crystals Ce@IONPs from ~10–46 nm (Ce^{3+} at 0.1 to 1.25 mM) and the polycrystalline Ce@IONPs structures (Ce^{3+} at 2.0 mM) described in chapter 3 were evaluated and compared with the SC-IONPs (~9 nm), under the same test conditions.

As an example, Figure 4-5A-B depicts the reaction times curves of TMB colorimetric reaction catalyzed by non-doped IONPs and Ce@IONPs (Ce at 0.25 mM) at the maximum absorbance (652 nm) as a function of their mass (0–30 µg) until 10 min reaction, respectively. The mimicking peroxidase-like activity of both IONPs and Ce@IONPs at each mass followed a Michaelis-Menten (M-M) kinetic model, previously described for other NPs.[19,23] To determine the initial velocity, it was analyzed at the first part of the reaction curve, in the linear portion up to 60 seconds. These segments exhibited a good linear regression coefficient with slopes significantly different from zero.

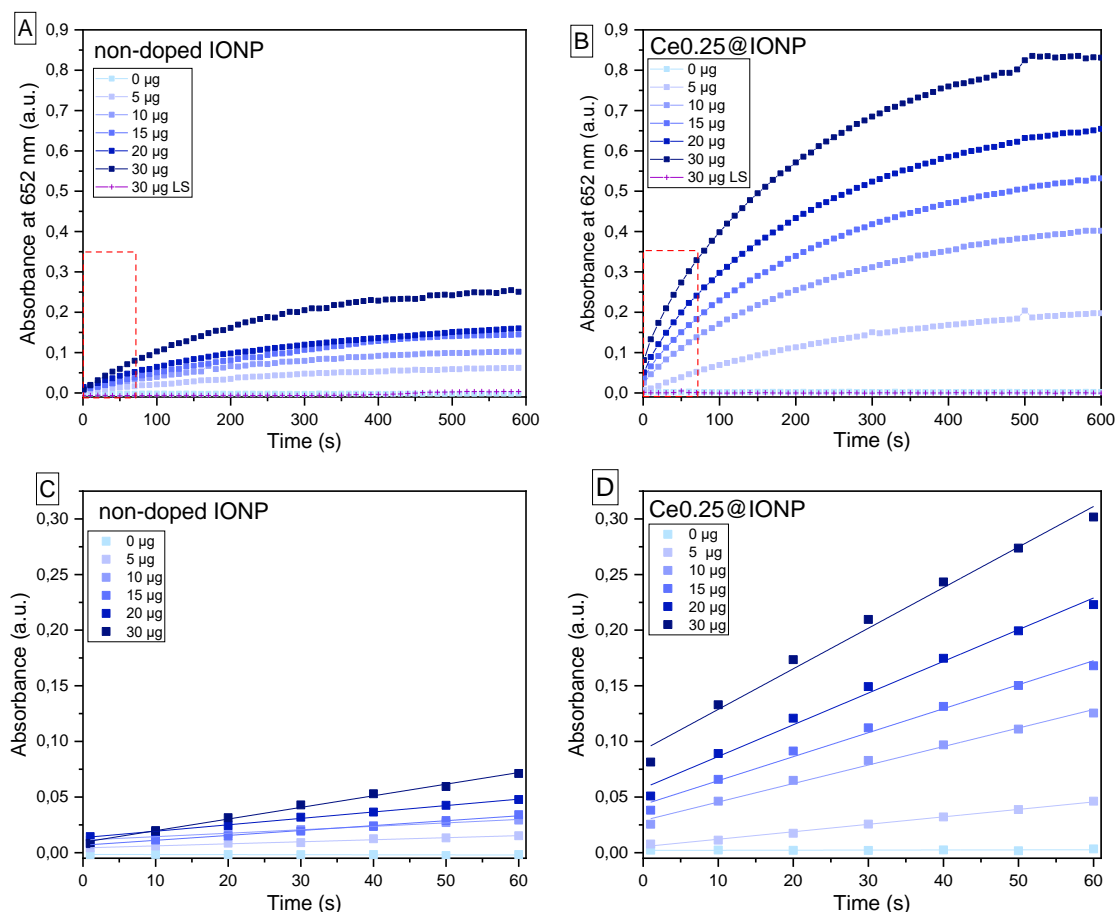*Figure 4-5. Comparison of the reaction times curves at 652 nm absorbance of TMB chromogenic oxidation reaction catalyzed by (**A**) IONPs and (**B**) Ce@IONPs (at Ce 0.25 mM) as a function of their mass (µg). Time interval between the measurements ΔT = 10 s up to 600 s. Magnification of the linearization until 60s reaction (**C**) IONPs and (**D**) Ce@IONPs (at Ce 0.25 mM).*

In addition, it is important to note that we carry out leaching solution test (LS) for each type of NPs to ensure that the observed response was not due to ions leaching from the NPs. For these tests, were incubated 30 μg of each NPs in the buffer for at least 40 minutes, then separated them from the solution using a centricon filter. The resulting solution was tested under the same reaction conditions. None of the leaching solutions exhibited peroxidase activity, indicating that the catalytic activity was at the NPs surface.

The reaction time curves for the most active Ce@IONPs samples, specifically (Ce at 0.1 and Ce0.25) with their respective controls are shown in Figure C1 and C2 (in Annex C). Additionally, Annex C includes an independent plot of the absorbance at 652 nm against its mass for each IONPs tested sample and the LS (Figure C3-Annex C).

Peroxidase-like activity can be expressed in units of activity (U_{NP}), is defined as the micromoles of substrate transformed per minute catalyzed by the NPs,[14] and is given by *Eq.1*:

$$U_{NP} = \frac{V}{\varepsilon \cdot l} \left(\frac{\Delta_{Abs}}{\Delta t} \right) \qquad (Eq.\,1)$$

Where V is the total volume of the reaction; ε is the molar absorption coefficient of the TMB at 652 nm (39000 M^{-1} cm^{-1}); *l* is the path length of the cuvette (cm); and Δ_{Abs}/Δ_t is the slope at the first part of the reaction curve.

As a result, gathering each slope and plotted as a function of their mass (in mg) gave a linear correlation which is the specific catalytic activity (SA),[14] which is given by *Eq.2*:

$$SA = \frac{U}{m} \qquad (Eq.\,2)$$

The catalytic activity determined for each Ce@IONPs as a function of their mass, is shown in Figure 4-6.

Comparison between the catalytic activity by mass from the different synthesized Ce@IONPs showed that Ce doping significantly improved the peroxidase-like activity properties at the surface of the IONPs (Figure 4-7). The results indicate that magnetic Ce@IONPs (synthesized at Ce 0.1 to 1.0 mM) from 13 to 42 nm crystal size exhibited higher catalysis of the TMB substrate, in comparison with the non-doped IONPs of ~9 nm crystal size. The Ce0.25@IONPs (~23 nm) showed the highest catalytic activity, as indicated by their high slope (Figure 4-6). This high activity could be related because it was found to be the Ce@IONPs with the highest concentration of cerium atoms determined by ICP analysis ($\chi_{(Ce/Ce+Fe)}$ = 3.2%). Therefore, Ce@IONPs activity decreased gradually as the Ce concentration decreased and as the diameter of NPs increased. The order of activity

by mass was according to the Ce mM concentration used in the reaction: Ce0.25 > Ce0.10 > Ce0.5 > Ce0.75 > Ce1.0 > non-doped IONPs > Ce1.25 > Ce2.0.
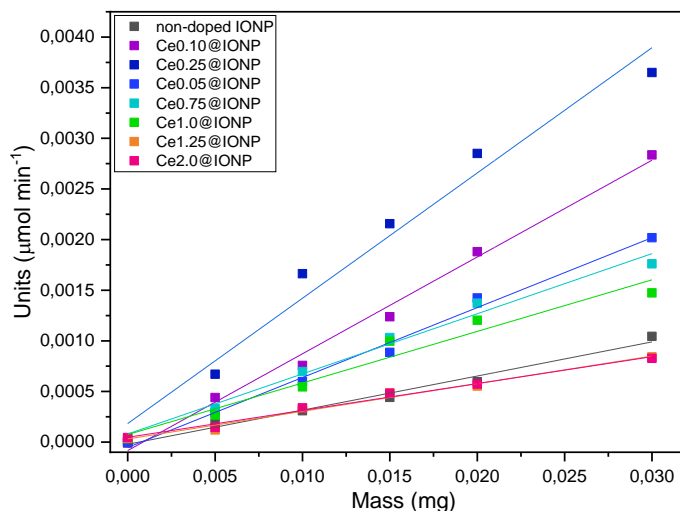
Figure 4-6. Linearization of the catalytic activities of the IONPs and Ce@IONPs as a function of their mass.

On the other hand, normalization of the catalytic activity by NPs surface area showed that Ce surface doping improved the catalytic activity of the IONPs in all size range, including the self-assembled (Ce > 0.75) and the large polycrystalline NPs (Ce2.0) in comparison to the bared IONPs (Figure 4-7). Those large structures showed the additional advantage of an easier and faster recovery with an external magnet. The catalytic activity of Ce@IONPs are summarized in Table C1 (in Annex C).
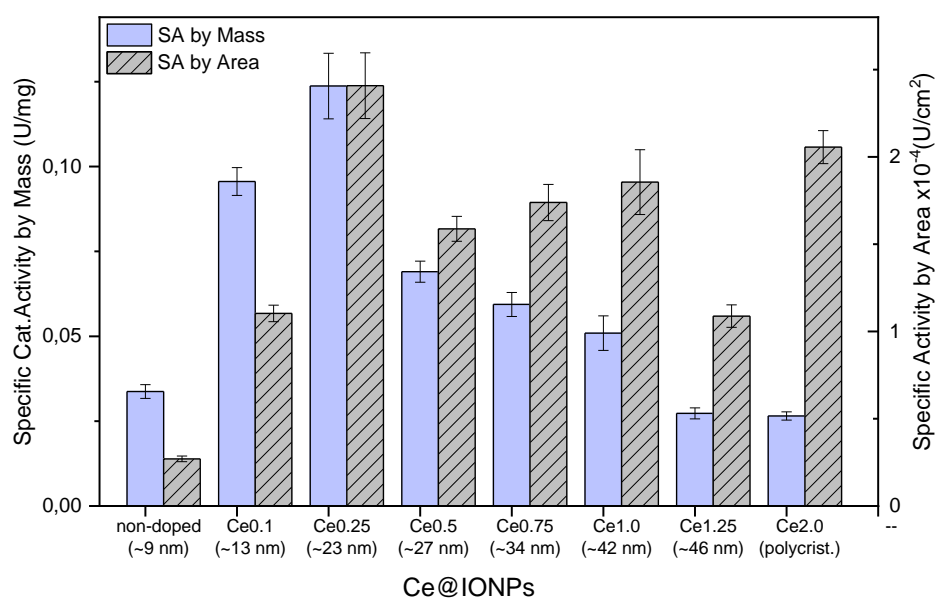
Figure 4-7. Comparison of the specific catalytic activities of the IONPs and Ce@IONPs normalized by mass and by nanoparticle surface area.

The increased peroxidase-like activity of the IONPs through surface doping with cerium (Ce) ions enhances the reaction efficiency by promoting the •OH generation and the recycling of Fe^{2+} and Fe^{3+}.[24,25] The following reaction mechanism, based on the classical Fenton reaction under acidic conditions, explains this process. Initially, surface-bound $\equiv Fe^{2+}$ reacts with H_2O_2, producing short-lived reactive hydroxyl radicals (HO·), while $\equiv Fe^{2+}$ is oxidized to $\equiv Fe^{3+}$ (*Eq.3*). Similarly, $\equiv Fe^{3+}$ reacts with H_2O_2, producing hydroperoxyl radicals (HO$_2$·), while $\equiv Fe3+$ is reduced back to $\equiv Fe^{2+}$ (*Eq. 4*). Meanwhile, other pathways lead to the Fe^{2+} regeneration (*Eq. 5*).[44] Likewise, cerium ions also react with the H_2O_2 to produce HO· species, following a similar mechanism to the Fenton reaction (*Eq. 6 and 7*). The presence of both redox pairs Ce^{4+}/Ce^{3+} (E°= +1.44V) and Fe^{3+}/Fe^{2+} (E°= +0.77 V), facilitate the electron transfer from Fe^{2+} to Ce^{4+}, which is a thermodynamically favorable proce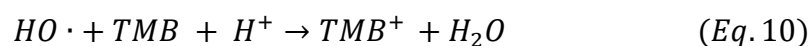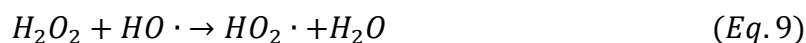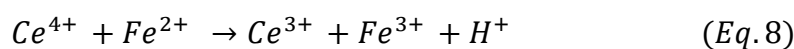ss (*Eq. 8*).[24] This synergistic activity between cerium and iron accelerates Fe^{2+} regeneration, which is the determining step in the Fenton reaction. The decomposition of H_2O_2 provides more HO$_2$·, maintaining the dynamic equilibrium through the formation of Fe^{2+} or Ce^{3+} species (*Eq. 9*). Primarily, the HO· species generated on the IONPs surface and released into the solution attacks the TMB substrate, which results in its oxidized from (*Eq. 10*).

$$Fe^{2+} + H_2O_2 + H^+ \rightarrow Fe^{3+} + HO\cdot + H_2O \qquad (Eq.3)$$

$$Fe^{3+} + H_2O_2 \rightarrow Fe^{2+} + HO_2\cdot + H^+ \qquad (Eq.4)$$

$$Fe^{3+} + HO_2\cdot \rightarrow Fe^{2+} + O_2 + H^+ \qquad (Eq.5)$$

$$Ce^{3+} + H_2O_2 + H^+ \rightarrow Ce^{4+} + HO\cdot + H_2O \qquad (Eq.6)$$

$$Ce^{4+} + HO_2\cdot \rightarrow Ce^{3+} + O_2 + H^+ \qquad (Eq.7)$$

$$Ce^{4+} + Fe^{2+} \rightarrow Ce^{3+} + Fe^{3+} + H^+ \qquad (Eq.8)$$

$$H_2O_2 + HO\cdot \rightarrow HO_2\cdot + H_2O \qquad (Eq.9)$$

$$HO\cdot + TMB + H^+ \rightarrow TMB^+ + H_2O \qquad (Eq.10)$$
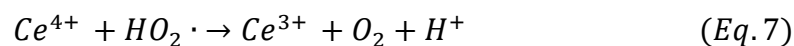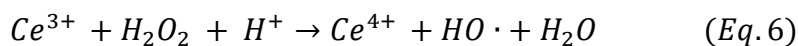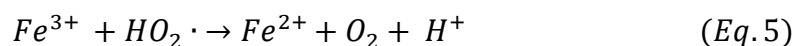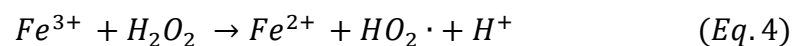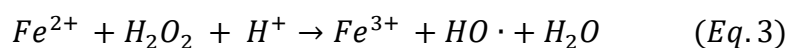
The previously proposed Fenton reaction over the Ce@IONPs surface is depicted in Scheme 1. Thus, the development of nanosized Ce@IONPs enhances their activity in the heterogeneous Fenton reaction. Additionally, after the TMB oxidation reaction, these NPs can be easily separated from the reaction mixture using an external magnetic field, facilitating catalyst recovery and reuse.
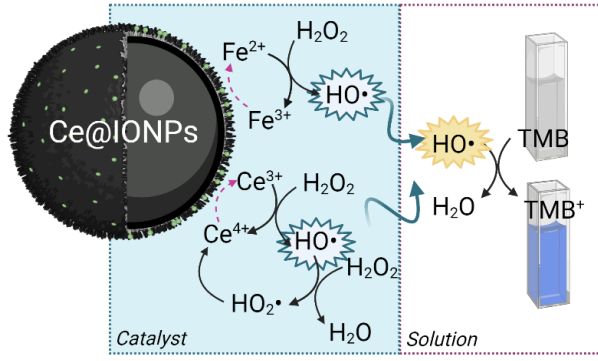
Schem 1. TMB oxidation proposed mechanism in the presence of Ce@IONPs and H_2O_2.

4.3.1.4 Evaluation of the Michaelis-Menten kinetic parameters of Ce@IONPs

Nanozyme usually follows a Michaelis-Menten kinetics model, and the determination of the apparent steady-ready kinetics parameters, including K_m and V_{max} are used to evaluate their affinity to the substrate in the peroxidase reaction and allow them compared their activity with other nanozymes. A comparative study of the kinetic properties of both synthesized IONPs ~9 nm and Ce@IONPs ~23nm ($[Ce^{3+} = 0.25$ mM]) was carried out and described using a Michaelis–Menten model. This analysis is intended to demonstrate the activity of the Ce cations at the NPs surface by comparison with the bared IONPs and HRD enzyme.

The model depicts a hyperbolic relationship between reaction velocity and the substrate concentration, as described by the following equation:

$$V_0 = \frac{V_{max}\,[S]}{K_m + [S]} \qquad (Eq.\,11)$$

Where K_m represents the M-M constant, V_{max} is the maximum reaction velocity, and $[S]$ is the substrate concentration. This reaction model describes a first-order kinetics, where the velocity depends on the substrate concentration, expressed as:

$$[S] \ll K_m \quad \therefore V_0 = \frac{V_{max}}{K_m}\,[S] \qquad (Eq.\,12)$$

It also describes a zero-order kinetics, where the reaction velocity is independent of the substrate concentration, as follows:

$$[S] \gg K_m \quad \therefore V_0 = \frac{V_{max}[S]}{\sim[S]} = \ \sim V_{max} \qquad (Eq.\,13)$$

Figure 4-8 illustrates the reaction velocity curves using 5 µg of the IONPs (~9 nm) and Ce@IONPs (~23nm) with varying the concentration of the substrates, TMB and H_2O_2, respectively. The data we fitted to a hyperbolic function in order to obtain the kinetic parameters, which are summarized in Table 4-1.
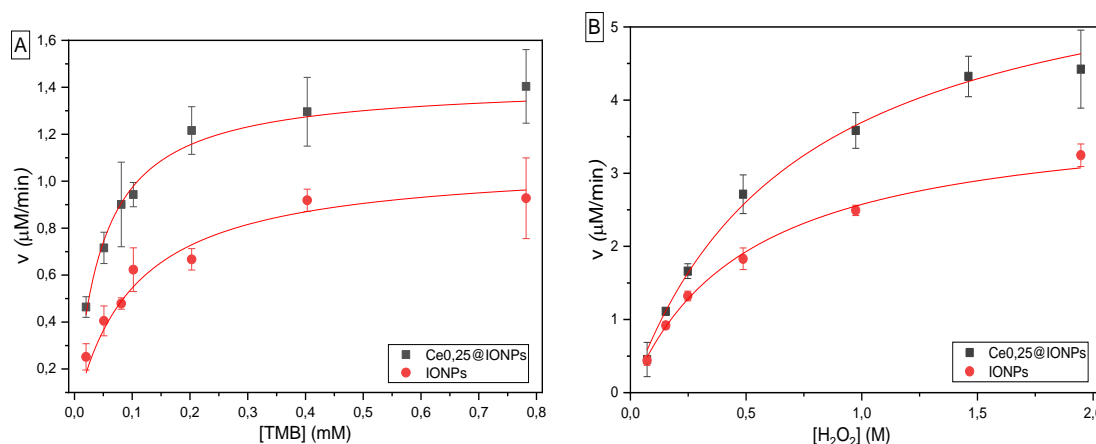
Figure 4-8. Comparison of the reaction velocity measured using 5 µg of IONPs (~9 nm) (red points) and Ce@IONPs (~23 nm) (black squares) in buffer NaAc:AcH (10 mM) at pH 5 and room temperature. (A) TMB concentration was varied at fixed H_2O_2 concentration (150 mM), and (B) H_2O_2 concentration was varied at fixed TMB concentration (0,406 mM). Error bars corresponding to three independent measurements.

Table 4-1. Comparison of the apparent kinetic parameters determined for 5 µg of IONPs or Ce0.25@IONPs at pH 5 and room temperature.

Sample	D_{STEM}	NPs	Substrate TMB		Substrate H_2O_2	
	(nm)	number[b]	Km (mM)	Vmax (M/s)	Km (mM)	V max (M/s)
SC-IONPs	9.3 ± 3.4	1.15E x10^{12}	0.099	1.807x10^{-8}	502	6.445 x10^{-8}
Ce0.25@IONPs	22.6 ± 3.8	8.68 x10^{10}	0.046	2.366 x10^{-8}	713	1.055 x10^{-7}
HRP[a]	-	2.5 x10^{-11} M	0.434	10.00 x10^{-8}	3.70	8.71 x10^{-8}

[a] Reported by Gao et al.[2] at pH 3.5 and 40°C.

[b] [NPs] = 1.08E^{-5} M

The Michaelis constant (K_m) is related to the velocity constants at each reaction stage and is used as an affinity parameter. Thus, the lower the K_m value the higher the affinity for the substrate, and vice-versa. For the TMB substrate, Ce0.25@IONPs (~23nm) exhibited the lowest Km value of 0.046 mM, indicating a higher affinity for TMB in comparison to the SC-IONPs (~9 nm), which had a K_m value of 0.099 mM. Both of these values are significantly lower than the K_m reported for horseradish peroxidase (HRP) enzyme, which is 0.434 mM. These values, which are 10-fold and 4-fold lower than HPR, for Ce@IONPs and SC-IONPs respectively, indicate a much higher affinity of TMB for the Ce0.25@IONPs. This increased affinity is related to the greater number of iron ions on

the IONPs surface compared to the single iron ion in the HRP enzyme.[2] Additionally, this study also indicates that the presence of Ce in the IONPs significantly enhances their peroxidase activity, suggesting that Ce atoms aids in the recycling of Fe^{2+} on the nanoparticle surface, effectively doubling the catalytic activity compared to non-doped IONPs.

On the other hand, for the H_2O_2 substrate, both IONPs and Ce0.25@IONPs exhibited high K_m values, indicating a lower affinity for this substrate compared to the HRP enzyme. This indicates that higher concentrations of peroxide are required to reach their maximum activity of the IONPs. As observed the M-M curve tends to plateau above 0.5 M of H_2O_2. However, even higher concentrations might be necessary to fully achieve maximal activity. It has been reported that this high oxidizing environment is characteristic in the use of the hydrogen donor substrates that works at acidic media, such as ABTS, TMB, and OPD, and is also related to the stability of the produced OH• as a function of the pH. [2,42]

4.3.2 Magnetic Hyperthermia

Magnetic IONPs have been the most studied NPs for MH treatment due to their promising efficacy, which is heavily influenced by their specific physicochemical characteristics in terms of size, magneto-energy conversion, surface chemistry and aggregation state.[33] To assess the potential of the synthesized Ce@IONPs as a possible therapeutic agent for cancer treatment through magnetic hyperthermia, calorimetric magnetic hyperthermia characterization was conducted. The heating power of magnetic IONPs is delimited the magnetic energy dissipation, which is highly dependent on the size of the NPs. Typically, in the case of IONPs employed in magnetic hyperthermia must exhibit exceptional magnetic properties and have a size withing the range of 20–26 nm, between the transition from SPM to FM at RT.[45]

In this context, the synthesized samples would be ideal candidates for evaluating their performance in magnetic hyperthermia. For this reason, experiments were carried out to evaluate Ce@IONPs dispersions, including NPs with diameters of 13 ± 3, 23 ± 4, 27 ± 4, and 34 ± 6 nm (Ce0.1, Ce0.25, Ce0.5 and Ce0.75@IONPs, respectively). The NPs were then exposed to an alternating magnetic field (Field (H) = 17.5 kA/m, and frequency (f) = 156 kHz). Note that H x f product is equal to 2.7×10^9 A/m·s, value which is below the recommended threshold (5×10^9 A/m·s) for safe biomedical application, indicating that the conditions were mild hyperthermia.

Figure 4-9 depicts the time-dependent temperature increase of the evaluated Ce@IONPs under the applied AMF. For all samples, the temperature was maintained constant for at least one minute before the magnetic field was turned on. Upon activation of the magnetic field, all samples exhibited a temporary increase in temperature. As magnetic hyperthermia was evaluated by a calorimetric method, the thermodynamic properties of the material or specific power loss (SLP) determination should be performed under adiabatic conditions, which are experimentally difficult to achieve, and typically quasi-adiabatic conditions were assumed. Since heat losses, the estimation of SLP was typically calculated from the initial slope ($\Delta T/\Delta t$), or at the maximum slope of time-dependent temperature curve.[46,47]
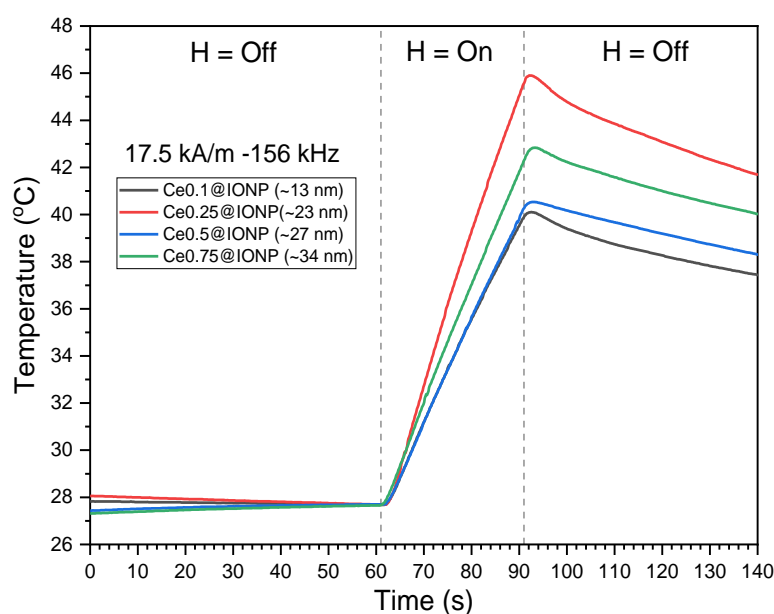
Figure 4-9. Temperature versus time curves for the different spherical Ce@IONPs exposed to an alternating magnetic field (H= 17.5 kA/m, and f = 156 kHz), where H = Off/On indicates the exposition to the magnetic field.

The specific power loss (SLP) values for these samples were calculated as the mean values of four independent measurements using the following equation:

$$SLP\left(W/g\right) = \left(\frac{C}{m} \cdot \frac{dT}{dt}\right) \approx \left(\frac{C}{m} \cdot \frac{\Delta T}{\Delta t}\right)_{QA}$$

The obtained SLP values for these samples are shown in Figure 4-10, reaching a maximum SLP value of 137 ± 5 W/g for the sample Ce0.25@IONPs (23 ± 4 nm nm). This maximum value aligns with previous reports for magnetite NPs where the highest efficiency for MH has been reported for NPs at sizes around 22 nm.[48]

The values obtained in this study are comparable to those previously reported for iron oxide nanocubes,[49] and cobalt ferrite nanocubes,[50] of a similar size (~22–24 nm), both synthesized by thermal decomposition and measured under slightly lower AMF conditions (~105 kHz and 16 kA/m). Additionally, the obtained SAR values can be compared with those reported for multicore IONPs, where values of approximately 95 ± 20 W/g were achieved at higher frequencies and higher applied magnetic field (163 kHz at 24 kA/m).[51]
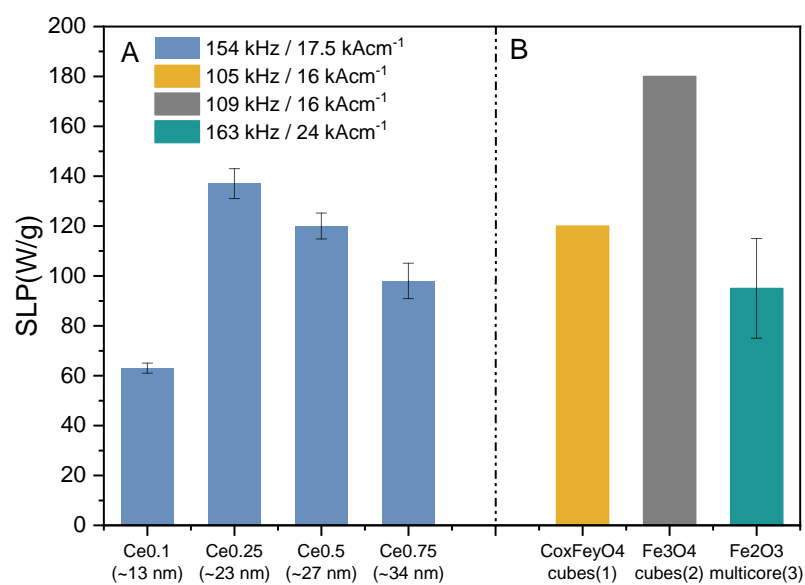
Figure 4-10. (A) Variation of the obtained SAR values for the Ce@IONPs as a function their size (13–34 nm), and (B) comparison with the reported values from the literature as (1) [49], (2)[50] and (3)[51].

It is worth noting that the reported NPs were produced under sophisticated synthesis conditions, at high temperatures, and using organic chemicals, resulting in IONPs with improved crystal quality. Additionally, it is important to consider that SAR values are influenced by factors such as size, crystal quality, magnetocrystalline anisotropy, shape anisotropy, phase composition, and surface coating.[52] However, the Ce@IONPs reported in this study were produced through a more feasible aqueous synthesis at room temperature and shorter synthesis time, by utilizing green chemicals, resulting in an environmentally friendly approach for obtaining tunable IONPs crystal sizes.

4.3.3 Cytotoxicity Assay

For biomedical applications, it is necessary to evaluate the potential cytotoxic effects of the synthesized NPs in diverse cells lines. In order to determine whether the interaction NPs -cell is cytotoxic, monocytes cells were exposed to the NPs to evaluate the use of these for therapeutic purposes. Ce0.25@IONPs (~23 nm) were selected to evaluate the cytotoxic

capabilities because they presented the highest peroxidase-like catalytic activity and highest SAR value in the above tests. Additionally, this Ce0.25@IONPs also is within the typical size range used for IONPs in biomedical applications.

The in vitro cytotoxicity of Ce0.25@IONPs (~23 nm) was assessed using THP-1 (human leukemia monocytes) cells line. Cell viability was determined using Trypan Blue exclusion test. The cells were exposed to three different concentrations of Ce0.25@IONPs (0.1, 0.2, and 0.5 mg/mL), and compared with the control cells incubated without NPs for 24 and 72 h (Figure 4-11). The results showed that there was not significative difference between the controls cells and the cells treated at the tested NPs concentrations, as indicated by the calculated F statistic value were below the F critical values, meaning that both variances are similar. The Excel output for this ANOVA analysis is presented in Table C2-Annex C. Therefore, none of the evaluated concentrations showed significant toxicity or decreased cell viability after 72 h of treatment. As expected, this confirmed that either cerium or iron ions at the NPs surface were nontoxic at any NPs concentration evaluated.
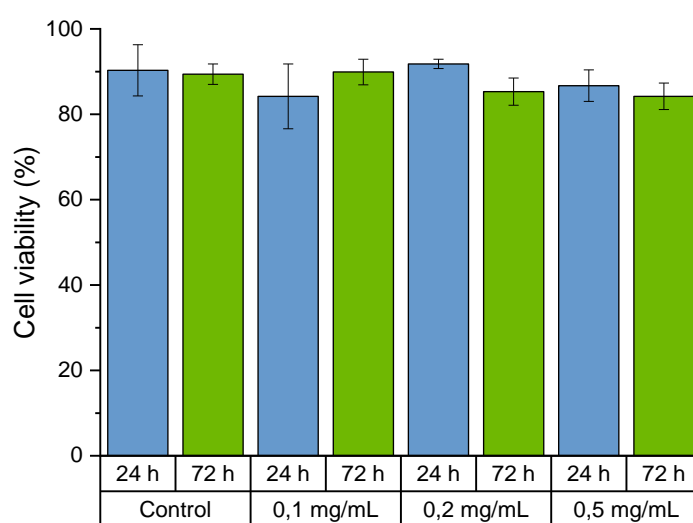
Figure 4-11. THP-1 cell viability after Ce0.25@IONPs incubation by using different NPs concentrations and evaluated at 24 h and 72 h. Data values are expressed as average ± standard deviation. Two-way ANOVA was performed to test the significance (p ≤0.05) in order to evaluate the effect of the NPs in each time point.

4.4 Conclusions

This study highlights the enhanced catalytic and thermal properties of the synthesized magnetic Ce@IONPs evaluated through peroxidase-like mimicking assays and magnetic hyperthermia.

The catalytic efficiency was significantly influenced mainly by NP size and surface chemistry, suggesting that their optimization can yield highly effective nanocatalysts. Evaluation and optimization of the reaction parameters (pH, temperature, buffer type, ionic strength, and substrate concentration), leading to identify their effects and optimal reaction conditions for the catalytic activity of IONPs. Magnetic Ce@IONPs from ~13 nm to 42 nm (synthesized at Ce^{3+} 0.1–1.0 mM) showed superior catalytic activity compared to bared IONPs (~9 nm). Ce0.25@IONPs (~23 nm) exhibited the highest catalytic activity per mass due to their high cerium doping, and presented the lowest Km value, indicating a higher affinity for TMB substrate.

Ce@IONPs ~13–34 nm (synthesized at Ce^{3+} at 0–0.75 mM) dispersions were suitable for magnetic hyperthermia studies. The Ce0.25@IONPs (~23 nm) exhibited the highest SLP value under mild hyperthermia conditions (17.5 kA/m–156 kHz). These values are consistent with those reported for nanocubes and multicore IONPs produced under organic synthesis conditions. Their excellent biocompatibility and low toxicity of the Ce@IONPs indicated their high potential for several catalytic and biomedical applications.

4.5　References

(1)　Liang, M.; Yan, X. Nanozymes: From New Concepts, Mechanisms, and Standards to Applications. *Acc. Chem. Res.* **2019**, *52* (8), 2190–2200. https://doi.org/10.1021/acs.accounts.9b00140.

(2)　Gao, L.; Zhuang, J.; Nie, L.; Zhang, J.; Zhang, Y.; Gu, N.; Wang, T.; Feng, J.; Yang, D.; Perrett, S.; Yan, X. Intrinsic Peroxidase-like Activity of Ferromagnetic Nanoparticles. *Nat. Nanotechnol.* **2007**, *2* (9), 577–583. https://doi.org/10.1038/nnano.2007.260.

(3)　Editor, S.; Lockwood, D. J. *Nanozymology*; Yan, X., Ed.; Nanostructure Science and Technology; Springer Singapore: Singapore, 2020. https://doi.org/10.1007/978-981-15-1490-6.

(4)　Tang, Y.; Chen, Q. A Simple and Practical Method for the Preparation of Magnetite Nanowires. *Chem. Lett.* **2007**, *36* (7), 840–841. https://doi.org/10.1246/cl.2007.840.

(5)　Ha, T. H.; Jeong, J. Y.; Chung, B. H. Immobilization of Hexa-Arginine Tagged Esterase onto Carboxylated Gold Nanoparticles. *Chem. Commun.* **2005**, No. 31, 3959–3961. https://doi.org/10.1039/b504184h.

(6)　Landarani-Isfahani, A.; Taheri-Kafrani, A.; Amini, M.; Mirkhani, V.; Moghadam, M.; Soozanipour, A.; Razmjou, A. Xylanase Immobilized on Novel Multifunctional Hyperbranched Polyglycerol-Grafted Magnetic Nanoparticles: An Efficient and Robust Biocatalyst. *Langmuir* **2015**, *31* (33), 9219–9227. https://doi.org/10.1021/acs.langmuir.5b02004.

(7)　Xu, J.; Sun, J.; Wang, Y.; Sheng, J.; Wang, F.; Sun, M. Application of Iron Magnetic Nanoparticles in Protein Immobilization. *Molecules* **2014**, *19* (8), 11465–11486. https://doi.org/10.3390/molecules190811465.

(8)　Katz, E.; Willner, I. Integrated Nanoparticle-Biomolecule Hybrid Systems: Synthesis, Properties, and Applications. *Angew. Chemie - Int. Ed.* **2004**, *43* (45), 6042–6108. https://doi.org/10.1002/anie.200400651.

(9)　Robert, A.; Meunier, B. How to Define a Nanozyme. *ACS Nano* **2022**, *16* (5), 6956–6959. https://doi.org/10.1021/acsnano.2c02966.

(10)　Singh, S. Nanomaterials Exhibiting Enzyme-like Properties (Nanozymes): Current Advances and Future Perspectives. *Front. Chem.* **2019**, *7* (FEB), 1–10. https://doi.org/10.3389/fchem.2019.00046.

(11)　Fan, K.; Xi, J.; Fan, L.; Wang, P.; Zhu, C.; Tang, Y.; Xu, X.; Liang, M.; Jiang, B.; Yan, X.; Gao, L. In Vivo Guiding Nitrogen-Doped Carbon Nanozyme for Tumor Catalytic Therapy. *Nat. Commun.* **2018**, *9* (1). https://doi.org/10.1038/s41467-018-03903-8.

(12)　Chen, Z.; Yin, J.; Zhou, Y.; Zhang, Y.; Song, L.; Song, M.; Hu, S.; Gu, N. Dual Enzyme-like Activities of Iron Oxide Nanoparticles and Their Implication for Diminishing Cytotoxicity. *ACS Nano* **2012**, *6* (5), 4001–4012. https://doi.org/10.1021/nn300291r.

(13)　Fan, J.; Yin, J.-J.; Ning, B.; Wu, X.; Hu, Y.; Ferrari, M.; Anderson, G. J.; Wei, J.; Zhao, Y.; Nie, G. Direct Evidence for Catalase and Peroxidase Activities of Ferritin–Platinum Nanoparticles. *Biomaterials* **2011**, *32* (6), 1611–1618. https://doi.org/10.1016/j.biomaterials.2010.11.004.

(14)　Jiang, B.; Duan, D.; Gao, L.; Zhou, M.; Fan, K.; Tang, Y.; Xi, J.; Bi, Y.; Tong, Z.; Gao, G. F.; Xie, N.; Tang, A.; Nie, G.; Liang, M.; Yan, X. Standardized Assays for Determining the Catalytic Activity and Kinetics of Peroxidase-like Nanozymes. *Nat. Protoc.* **2018**, *13* (7), 1506–1520. https://doi.org/10.1038/s41596-018-0001-1.

(15)   Gao, L.; Fan, K.; Yan, X. Iron Oxide Nanozyme: A Multifunctional Enzyme Mimetic for Biomedical Applications. *Theranostics* **2017**, *7* (13), 3207–3227. https://doi.org/10.7150/thno.19738.

(16)   Ali, A.; Shah, T.; Ullah, R.; Zhou, P.; Guo, M.; Ovais, M.; Tan, Z.; Rui, Y. K. Review on Recent Progress in Magnetic Nanoparticles: Synthesis, Characterization, and Diverse Applications. *Front. Chem.* **2021**, *9* (July), 1–25. https://doi.org/10.3389/fchem.2021.629054.

(17)   Liu, Y.; Wang, X.; Li, X.; Qiao, S.; Huang, G.; Hermann, D. M.; Doeppner, T. R.; Zeng, M.; Liu, W.; Xu, G.; Ren, L.; Zhang, Y.; Liu, W.; Casals, E.; Li, W.; Wang, Y. C. A Co-Doped Fe3O4Nanozyme Shows Enhanced Reactive Oxygen and Nitrogen Species Scavenging Activity and Ameliorates the Deleterious Effects of Ischemic Stroke. *ACS Appl. Mater. Interfaces* **2021**, *13* (39), 46213–46224. https://doi.org/10.1021/acsami.1c06449.

(18)   Zhang, S.; Ruan, H.; Xin, Q.; Mu, X.; Wang, H.; Zhang, X. D. Modulation of the Biocatalytic Activity and Selectivity of CeO2 Nanozymes via Atomic Doping Engineering. *Nanoscale* **2023**, *15* (9), 4408–4419. https://doi.org/10.1039/d2nr05742e.

(19)   Moreno-Castilla, C.; Naranjo, Á.; Victoria López-Ramón, M.; Siles, E.; López-Peñalver, J. J.; de Almodóvar, J. M. R. Influence of the Hydrodynamic Size and ζ Potential of Manganese Ferrite Nanozymes as Peroxidase-Mimicking Catalysts at PH 4 in Different Buffers. *J. Catal.* **2022**, *414*, 179–185. https://doi.org/10.1016/j.jcat.2022.09.010.

(20)   García, A.; Cámara, J. A.; Boullosa, A. M.; Gustà, M. F.; Mondragón, L.; Schwartz, S.; Casals, E.; Abasolo, I.; Bastús, N. G.; Puntes, V. Nanoceria as Safe Contrast Agents for X-Ray CT Imaging. *Nanomaterials* **2023**, *13* (15). https://doi.org/10.3390/nano13152208.

(21)   Wu, Y.; Yang, Y.; Zhao, W.; Xu, Z. P.; Little, P. J.; Whittaker, A. K.; Zhang, R.; Ta, H. T. Novel Iron Oxide-Cerium Oxide Core-Shell Nanoparticles as a Potential Theranostic Material for ROS Related Inflammatory Diseases. *J. Mater. Chem. B* **2018**, *6* (30), 4937–4951. https://doi.org/10.1039/c8tb00022k.

(22)   Orooji, Y.; Haddad Irani-nezhad, M.; Hassandoost, R.; Khataee, A.; Rahim Pouran, S.; Joo, S. W. Cerium Doped Magnetite Nanoparticles for Highly Sensitive Detection of Metronidazole via Chemiluminescence Assay. *Spectrochim. Acta Part A Mol. Biomol. Spectrosc.* **2020**, *234*, 118272. https://doi.org/10.1016/j.saa.2020.118272.

(23)   Deng, H. H.; Luo, B. Y.; He, S. Bin; Chen, R. T.; Lin, Z.; Peng, H. P.; Xia, X. H.; Chen, W. Redox Recycling-Triggered Peroxidase-like Activity Enhancement of Bare Gold Nanoparticles for Ultrasensitive Colorimetric Detection of Rare-Earth Ce 3+ Ion. *Anal. Chem.* **2019**, *91* (6), 4039–4046. https://doi.org/10.1021/acs.analchem.8b05552.

(24)   Xu, L.; Wang, J. Magnetic Nanoscaled Fe3O4/CeO2 Composite as an Efficient Fenton-like Heterogeneous Catalyst for Degradation of 4-Chlorophenol. *Environ. Sci. Technol.* **2012**, *46* (18), 10145–10153. https://doi.org/10.1021/es300303f.

(25)   Galyamin, D.; Ernst, L. M.; Fitó-Parera, A.; Mira-Vidal, G.; Bastús, N. G.; Sabaté, N.; Puntes, V. Nanoceria Dissolution at Acidic PH by Breaking off the Catalytic Loop. *Nanoscale* **2022**, *14* (38), 14223–14230. https://doi.org/10.1039/d2nr03586c.

(26)   Moskvin, M.; Marková, I.; Malínská, H.; Miklánková, D.; Hüttl, M.; Oliyarnyk, O.; Pop-Georgievski, O.; Zhigunov, A.; Petrovský, E.; Horák, D. Cerium Oxide-Decorated γ-Fe2 O3 Nanoparticles: Design, Synthesis and in Vivo Effects on Parameters of Oxidative Stress. *Front. Chem.* **2020**, *8* (August), 1–13.

https://doi.org/10.3389/fchem.2020.00682.

(27) Huang, F.; Wang, J.; Chen, W.; Wan, Y.; Wang, X.; Cai, N.; Liu, J.; Yu, F. Synergistic Peroxidase-like Activity of CeO2-Coated Hollow Fe3O4 Nanocomposites as an Enzymatic Mimic for Low Detection Limit of Glucose. *J. Taiwan Inst. Chem. Eng.* **2018**, *83*, 40–49. https://doi.org/10.1016/j.jtice.2017.12.011.

(28) Shlapa, Y.; Siposova, K.; Veltruska, K.; Maraloiu, V. A.; Garcarova, I.; Rajnak, M.; Musatov, A.; Belous, A. Design of Magnetic Fe3O4/CeO2 "Core/Shell"-Like Nanocomposites with Pronounced Antiamyloidogenic and Antioxidant Bioactivity. *ACS Appl. Mater. Interfaces* **2023**, *15* (42), 49346–49361. https://doi.org/10.1021/acsami.3c10845.

(29) Kallumadil, M.; Tada, M.; Nakagawa, T.; Abe, M.; Southern, P.; Pankhurst, Q. A. Suitability of Commercial Colloids for Magnetic Hyperthermia. *J. Magn. Magn. Mater.* **2009**, *321* (10), 1509–1513. https://doi.org/10.1016/j.jmmm.2009.02.075.

(30) Kacem, M.; Essoumhi, A.; Dib, M. Magnetic Iron Oxide-Based Materials and Their Hyperthermia Application: A Review. *Inorg. Chem. Commun.* **2024**, *166* (September 2023), 112510. https://doi.org/10.1016/j.inoche.2024.112510.

(31) Laurent, S.; Bridot, J. L.; Elst, L. Vander; Muller, R. N. Magnetic Iron Oxide Nanoparticles for Biomedical Applications. *Future Med. Chem.* **2010**, *2* (3), 427–449. https://doi.org/10.4155/fmc.09.164.

(32) Luengo, Y.; Díaz-Riascos, Z. V.; García-Soriano, D.; Teran, F. J.; Artés-Ibáñez, E. J.; Ibarrola, O.; Somoza, Á.; Miranda, R.; Schwartz, S.; Abasolo, I.; Salas, G. Fine Control of In Vivo Magnetic Hyperthermia Using Iron Oxide Nanoparticles with Different Coatings and Degree of Aggregation. *Pharmaceutics* **2022**, *14* (8). https://doi.org/10.3390/pharmaceutics14081526.

(33) Gavilán, H.; Avugadda, S. K.; Fernández-Cabada, T.; Soni, N.; Cassani, M.; Mai, B. T.; Chantrell, R.; Pellegrino, T. Magnetic Nanoparticles and Clusters for Magnetic Hyperthermia: Optimizing Their Heat Performance and Developing Combinatorial Therapies to Tackle Cancer. *Chem. Soc. Rev.* **2021**, *50* (20), 11614–11667. https://doi.org/10.1039/d1cs00427a.

(34) Gupta, R.; Chauhan, A.; Kaur, T.; Kuanr, B. K.; Sharma, D. Enhancing Magnetic Hyperthermia Efficacy through Targeted Heat Shock Protein 90 Inhibition: Unveiling Immune-Mediated Therapeutic Synergy in Glioma Treatment. *ACS Nano* **2024**. https://doi.org/10.1021/acsnano.4c03887.

(35) Wu, H.; Liu, L.; Song, L.; Ma, M.; Gu, N.; Zhang, Y. Enhanced Tumor Synergistic Therapy by Injectable Magnetic Hydrogel Mediated Generation of Hyperthermia and Highly Toxic Reactive Oxygen Species. *ACS Nano* **2019**, *13* (12), 14013–14023. https://doi.org/10.1021/acsnano.9b06134.

(36) Shen, J.; Rees, T. W.; Zhou, Z.; Yang, S.; Ji, L.; Chao, H. A Mitochondria-Targeting Magnetothermogenic Nanozyme for Magnet-Induced Synergistic Cancer Therapy. *Biomaterials* **2020**, *251* (January), 120079. https://doi.org/10.1016/j.biomaterials.2020.120079.

(37) Jansman, M. M. T.; Hosta-Rigau, L. Cerium- and Iron-Oxide-Based Nanozymes in Tissue Engineering and Regenerative Medicine. *Catalysts* **2019**, *9* (8), 691. https://doi.org/10.3390/catal9080691.

(38) Honarasa, F.; Keshtkar, S.; Eskandari, N.; Eghbal, M. Catalytic and Electrocatalytic Activities of Fe3O4/CeO2/C-Dot Nanocomposite. *Chem. Pap.* **2021**, *75* (6), 2371–2378. https://doi.org/10.1007/s11696-020-01443-4.

(39) Xiao, G.; Li, H.; Zhao, Y.; Wei, H.; Li, J.; Su, H. Nanoceria-Based Artificial Nanozymes: Review of Materials and Applications. *ACS Appl. Nano Mater.* **2022**,

5 (10), 14147–14170. https://doi.org/10.1021/acsanm.2c03009.

(40) Chung, K. T.; Chen, S. C.; Wong, T. Y.; Li, Y. S.; Wei, C. I.; Chou, M. W. Mutagenicity Studies of Benzidine and Its Analogs: Structure-Activity Relationships. *Toxicol. Sci.* **2000**, *56* (2), 351–356. https://doi.org/10.1093/toxsci/56.2.351.

(41) Josephy, P. D.; Eling, T.; Mason, R. P. The Horseradish Peroxidase-Catalyzed Oxidation of 3,5,3',5'-Tetramethylbenzidine. Free Radical and Charge-Transfer Complex Intermediates. *J. Biol. Chem.* **1982**, *257* (7), 3669–3675. https://doi.org/10.1016/s0021-9258(18)34832-4.

(42) Drozd, M.; Pietrzak, M.; Parzuchowski, P. G.; Malinowska, E. Pitfalls and Capabilities of Various Hydrogen Donors in Evaluation of Peroxidase-like Activity of Gold Nanoparticles. *Anal. Bioanal. Chem.* **2016**, *408* (29), 8505–8513. https://doi.org/10.1007/s00216-016-9976-z.

(43) Fischbacher, A.; von Sonntag, C.; Schmidt, T. C. Hydroxyl Radical Yields in the Fenton Process under Various PH, Ligand Concentrations and Hydrogen Peroxide/Fe(II) Ratios. *Chemosphere* **2017**, *182*, 738–744. https://doi.org/10.1016/j.chemosphere.2017.05.039.

(44) Wang, C.; Liu, H.; Sun, Z. Heterogeneous Photo-Fenton Reaction Catalyzed by Nanosized Iron Oxides for Water Treatment. *Int. J. Photoenergy* **2012**, *2012* (1). https://doi.org/10.1155/2012/801694.

(45) Rajan, A.; Sahu, N. K. Review on Magnetic Nanoparticle-Mediated Hyperthermia for Cancer Therapy. *J. Nanoparticle Res.* **2020**, *22* (11). https://doi.org/10.1007/s11051-020-05045-9.

(46) Liu, X.; Zhang, Y.; Wang, Y.; Zhu, W.; Li, G.; Ma, X.; Zhang, Y.; Chen, S.; Tiwari, S.; Shi, K.; Zhang, S.; Fan, H. M.; Zhao, Y. X.; Liang, X. J. Comprehensive Understanding of Magnetic Hyperthermia for Improving Antitumor Therapeutic Efficacy. *Theranostics* **2020**, *10* (8), 3793–3815. https://doi.org/10.7150/thno.40805.

(47) Obaidat, I. M.; Narayanaswamy, V.; Alaabed, S.; Sambasivam, S.; Muralee Gopi, C. V. V. Principles of Magnetic Hyperthermia: A Focus on Using Multifunctional Hybrid Magnetic Nanoparticles. *Magnetochemistry* **2019**, *5* (4), 67. https://doi.org/10.3390/magnetochemistry5040067.

(48) Guardia, P.; Di Corato, R.; Lartigue, L.; Wilhelm, C.; Espinosa, A.; Garcia-Hernandez, M.; Gazeau, F.; Manna, L.; Pellegrino, T. Water-Soluble Iron Oxide Nanocubes with High Values of Specific Absorption Rate for Cancer Cell Hyperthermia Treatment. *ACS Nano* **2012**, *6* (4), 3080–3091. https://doi.org/10.1021/nn2048137.

(49) Guardia, P.; Riedinger, A.; Nitti, S.; Pugliese, G.; Marras, S.; Genovese, A.; Materia, M. E.; Lefevre, C.; Manna, L.; Pellegrino, T. One Pot Synthesis of Monodisperse Water Soluble Iron Oxide Nanocrystals with High Values of the Specific Absorption Rate. *J. Mater. Chem. B* **2014**, *2* (28), 4426–4434. https://doi.org/10.1039/c4tb00061g.

(50) Sathya, A.; Guardia, P.; Brescia, R.; Silvestri, N.; Pugliese, G.; Nitti, S.; Manna, L.; Pellegrino, T. CoxFe3-XO4 Nanocubes for Theranostic Applications: Effect of Cobalt Content and Particle Size. *Chem. Mater.* **2016**, *28* (6), 1769–1780. https://doi.org/10.1021/acs.chemmater.5b04780.

(51) Mekseriwattana, W.; Guardia, P.; Herrero, B. T.; de la Fuente, J. M.; Kuhakarn, C.; Roig, A.; Katewongsa, K. P. Riboflavin-Citrate Conjugate Multicore SPIONs with Enhanced Magnetic Responses and Cellular Uptake in Breast Cancer Cells. *Nanoscale Adv.* **2022**, *4* (8), 1988–1998. https://doi.org/10.1039/d2na00015f.

(52) Sojková, T.; Rizzo, G. M. R.; Di Girolamo, A.; Avugadda, S. K.; Soni, N.; Milbrandt, N. B.; Tsai, Y. H.; Kuběna, I.; Sojka, M.; Silvestri, N.; Samia, A. C.; Gröger, R.; Pellegrino, T. From Core-Shell FeO/Fe3O4 to Magnetite Nanocubes: Enhancing Magnetic Hyperthermia and Imaging Performance by Thermal Annealing. *Chem. Mater.* **2023**, *35* (16), 6201–6219. https://doi.org/10.1021/acs.chemmater.3c00432.

Chapter 5

General Conclusions and Perspectives

The purpose of this thesis was to investigate a co-precipitation method for the synthesis of magnetic Iron Oxide Nanoparticles (IONPs) with controlled size and morphology in aqueous media at room temperature. It covered the study of the impact of lanthanide cations and sodium citrate on the synthesis of monodispersed single-crystal nanoparticles ranging in size from 13 nm to 46 nm and large nanowires. The findings revealed that by adjusting the lanthanide concentration in the presence of sodium citrate ions, it was possible to achieve controlled growth and regulate the size of the NPs. Additionally, the study explored the effect of base rate addition and sodium citrate, which also played and important role on the synthesis of magnetite.

The process of controlling the size of NPs was thoroughly explained in this context, along with the introduction of a plausible reaction mechanism to elucidate the role of each synthesis component. Thus, the presence of Ln cations facilitates crystal growth by passivating and modifying the energy surface of either the amorphous precursor phase or the magnetite NPs. Sodium citrate has a pH buffering effect and also acts at the particle interface. Comprehensive characterization and analysis enabled a better understanding of the reaction system, revealing that Ln cations and SC accumulate at the NP shell, which is related to the nature, kinetics, and crystallization of magnetic iron oxide NPs. However, the precise mechanism of induced size control remains unclear, as it is not known whether

these components play a crucial role in the initial nucleation steps, NP growth, or both stages. Further studies, including kinetic and thermodynamic analyses, calculations, and theoretical simulations, will be beneficial for gaining a deeper understanding of these phenomena.

The development of magnetic iron-oxide NPs, particularly magnetite and maghemite, continues to attract significant interest for various nano- and biotechnological applications. The proposed methodology allows control of size NPs and consequently its magnetic behavior. Their lanthanide and citrate covering make them useful at physiological pH which is of particular interesting in the fields of biomedicine. Here, its catalytic activity was tested for mimicking peroxidase activity in the oxidation of TMB substrate by H_2O_2, demonstrating improved performance by Ce incorporation. Furthermore, the defined size of these NPs falls within the SPM to FM transition range, making them ideal for hyperthermia applications. Combined with chemo dynamic therapy, these NPs could serve as a powerful therapeutic agent for cancer treatment. Moreover, they have potential applications in environmental remediation, catalysis, sensing, and biomedicine.

The versatility of this synthetic procedure was demonstrated by expanding its use with other lanthanide ions, thereby demonstrating its capability to obtain similar controlled-size NPs and its potential functionalization for a wide range of applications. This study offers a simple, novel, and practical aqueous coprecipitation method and environmentally friendly approach for the synthesis of magnetic IONPs.

Although several additives have been described to synthesize magnetite NPs, we believe that the combination of lanthanides and citrate and the ability to control the size and distribution of the NPs is particularly exceptional. In this study, we demonstrate the influence of these additives on magnetite growth, but they can potentially be used to control other mineral oxide systems of technological interest, such as non-magnetic iron oxides, ferrites, and zinc and aluminum oxides. Where the use of lanthanide cations is not intended to incorporate into the structure, but to shape the NCs, inducing control over the intermediate phases and influencing the final product

Experimental Section: Techniques

6.1 Characterization Techniques

Electron Microscopy (EM)

Samples for STEM analysis were prepared by drying a dispersion of the washed particles on carbon-coated Cu grids and allowing the grid to dry for at least 24 h. Images were acquired using a FEI Magellan 400 L XHR scanning electron microscope (SEM). High Resolution Transmission (HRTEM) and electron energy loss spectroscopy (EELS) spectrum images (SIs) were acquired using a FEI Tecnai F20 S/TEM operating at 200 kV equipped with a Quantum GIF EELS spectrometer and an dispersive X-ray spectroscopy (EDX) detector system.

Average size and size distribution were determined by counting around 300 particles by calibrated BF TEM and /or angle annular dark field (HAADF) scanning TEM (STEM) images (HAADF) images in the ImageJ software. The crystal sizes are reported as mean ± standard deviation.

X-ray Powder Diffraction (MPD)

X-ray diffraction patterns were collected with an X´pert PRO MPD from a PANalytical diffractometer using a Cu radiation source Kα1 (λ = 1.5406 Å) at 40 kV and 40 mA. Scans were made over a 2θ range of 10-110° with a total exposure time of 60 min, step size of 0.0501°, and counting time of 226.7 s/step. The samples were prepared on silica

holders as fine deposition films and dried in vacuum at room temperature. The average crystallite size was determined from the full width at half-maximum (FWHM) by X`pert Pro suit program, and Crystallographic parameters were calculated using FullProf Suite software. Comparisons were made to the Fe_3O_4 phase (JCPDS 019-0629).

Zeta Potential Measurements

Hydrodynamic size and surface charge analyses were performed using a Malvern ZetaSizer Nano ZS instrument (Malvern Instruments, U.K.). The aqueous dilution of the NPs 1:10 in Milli-Q-water was analyzed using DTS1070 cells at 25°C.

Superconducting quantum interference device (SQUID) magnetometry

Magnetic properties of the samples were measured by a Superconducting Quantum Interference Device (SQUID) magnetometer at temperatures of 10 K and applied fields up to 50 kOe.

X-ray photoelectron spectroscopy (XPS)

XPS measurements were performed at room temperature with a SPECS PHOIBOS 150 hemispherical analyzer (SPECS GmbH, Berlin, Germany)) in a base pressure of 5×10^{-10} mbar using monochromatic Al Kα radiation source (1486.74 eV) as operated at 300 W. The energy resolution as measured by the FWHM of the Ag $3d_{5/2}$ peak for a sputtered silver foil was 0.62 eV. The spectrum was calibrated with respect to the C1s at 284.8eV using the Casa XPS software.

UV-Vis spectroscopy (UV-vis)

UV-visible spectra were acquired with an Agilent Cary-60 UV-Vis spectrophotometer using a PS-disposable cuvette in the range of 300–800 nm at room temperature.

Inductively coupled plasma optical emission spectroscopy (ICP-OES)

The Ce and Fe content was determined with an Agilent 5900 ICP-OES. from the UAB chemical Analysis Service. Acid digestions were externalized, briefly aliquots of the digested sample solutions were digested by concentrated acids (HNO_3 (65%)) and diluted in 10 mL volumetric flasks with Milli-Q-water.

Magnetic Hyperthermia Characterization

The heating efficiency of the samples were evaluated by calorimetric measurements conducted in a magneTherm nanoTherics Ltd., commercially available set up. Briefly, 500 uL of water soluble IONPs sample solution was introduced into a sample holder thermally isolated from the environment in order to achieve a quasi-adiabatic condition (QA). The samples were exposed to an alternating magnetic field (AMF) (17.5 kA/m) and 156 kHz frequency for 1 minute while the temperature was recorded by an optical thermal fibber probe at a scan rate of 0.15 seconds. All measurements were performed in water (C_{water} = 4185 J/L K) and normalized by the amount of IONPs (g/L of sample).

Thermogravimetric Analysis.

TGA experiments were carried out in a Perkin-Elmer-TGA-8000G under a N_2 atmosphere from 30 to 600 °C at a heating rate of 10°C/min.

6.2   Experimental Synthesis Setup

For the synthesis of the magnetic nanoparticles two different setups were used in this thesis. The first setup (Figure 1 A) was used for reactions carried out at room temperature and consists of: (1) a glass vessel sealed with a rubber septum, (2) magnetic stirring plate, (3) N2 gas, and (4) syringe pump. The inert conditions were achieved through continuous N2 bubbling, and the reagents were added through injection using syringes. A small needle in the septum allows the gas to escape to avoid the overpressure in the system.

The second setup (Figure 6-1) was used for reactions carried out at high temperature and consist of: (1) Schlenk line setup – N2 line in/out, (2) vacuum pump, (3) three-necked round flask sealed with rubber septum, (4) condenser tube, (5) heating mantle, (6) thermocouple, (7) magnetic stirring plate, and (8) syringe pump.
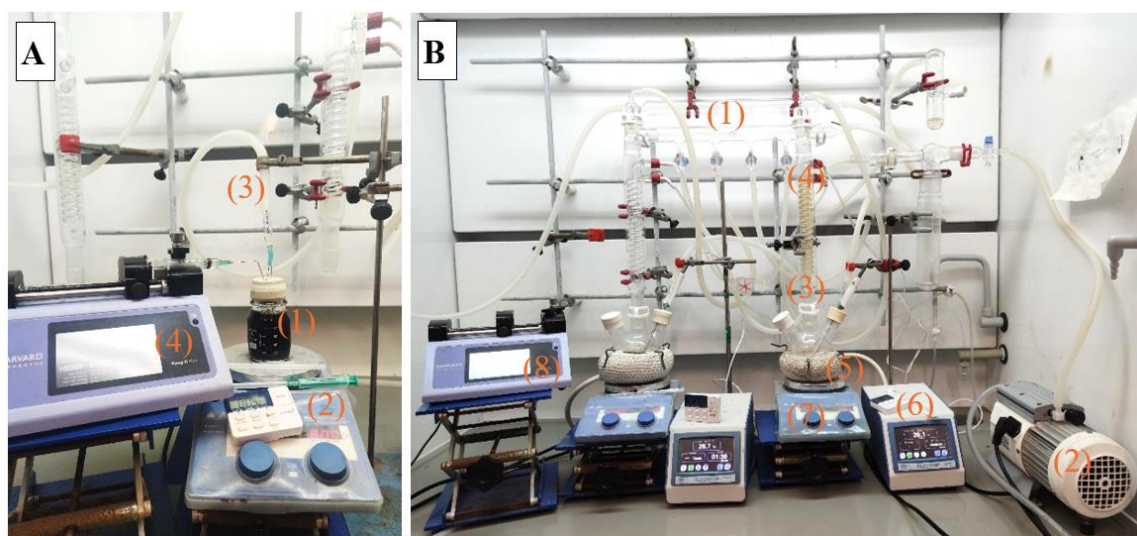
*Figure 6-1. Experimental setups used at (**A**) room and (**B**) high temperature synthesis.*

Appendix A

Magnetism of Nanomaterials

Magnetic nanoparticles (MNPs) are small particles, typically ranging from 1 to 100 nm, that exhibit magnetic properties. Their small size and magnetic properties give them unique physical and chemical characteristics that set them apart from bulk materials.

Magnetism is a physical phenomenon produced by the magnetic moment of the electrons.[1] At nanoscale, MNPs exhibit remarkable magnetic behaviors, dominated by finite size-effects which determine the magnetic behavior of NPs, such as superparamagnetism.[2] Their size, shape, composition and surface chemistry are critical in determining their functionality and efficiency across different applications,[3] such as biomedicine, energy, engineering, data storage, and environmental remediation. [4]

7.1 Magnetic Properties

Magnetism in materials results from the spin of electrons and their orbital motion around the nucleus that causes magnetic field on the atomic level. Each electron, which rotates around its own axis, behaves as a magnetic dipole and possesses a dipole moment, μB (Bohr magneton). The motion of electrons in atoms has both an orbital angular moment (m_l), and a spin moment (m_s), which is proportional to the spin (s):[1] [5]

The coupling of m_l and m_S results in the spin–orbit coupling. In a material, interactions between pairs of neighboring atoms can be expressed in terms of a Hamiltonian, which refers to the way in which electrons are coupled and is governed by Pauli's principle; two electrons cannot simultaneously occupy the same quantum state. [1]

Based on the intrinsic magnetic behavior of materials, their magnetic dipole, and net magnetization in the presence or absence of an external magnetic field, materials can be classified as weak magnetic, which include diamagnetic and paramagnetic substances, or strong magnetic, which includes ferromagnetic, antiferromagnetic, and ferrimagnetic materials, as illustrated in Figure 7-1 and described below: [3,6]

Diamagnetic: This is a general property found in all the substances, where magnetic dipoles are absent, or the substance lacks unpaired electrons. However, when an external magnetic field is applied, it causes a slight imbalance of the orbital electrons, producing a very week magnetic dipole that generates a negative response, with a magnetic susceptibility in the order of $\chi_M = 10^{-6}$ opposed to the applied field. While all materials exhibit this response, which is independent of the temperature, it is typically masked by positive magnetic responses such as paramagnetism, ferromagnetism, etc. Examples of diamagnetic materials are copper (Cu), bismuth (Bi), and water.
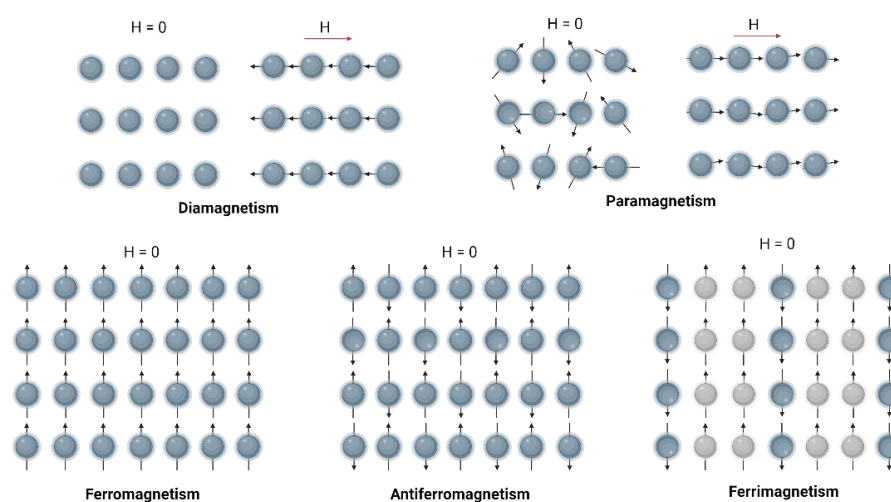
Figure 7-1.Graphic illustration of the net magnetic dipole arrangement in absence or presence of an external magnetic field and their magnetism classification.

Paramagnetic: are materials with unpaired electrons that are randomly oriented on different atoms, resulting in a net magnetic moment of zero in the crystal structure. However, upon an external magnetic field, these materials exhibited a small positive magnetic susceptibility (χ_M) response. This effect arises due to the parallel alignment of

magnetic dipole moments of atoms or molecules in response to the magnetic field. Paramagnetic materials display magnetic susceptibilities ranging from $\chi_M = 10^{-2}$ to 0, which vanishes once the magnetic field is removed. As an example, molecular oxygen (O_2), aluminum, and calcio are paramagnetic substances.

Ferromagnetic: are substances that contain unpaired electrons, whose magnetic moments are partially aligned in the absence of a magnetic field, resulting in a net positive magnetic moment. Therefore, ferrimagnetic materials are attracted to external magnetic fields. In ferromagnet substances, the electron spin alignment is parallel, and the magnetic susceptibilities ranged from $\chi_M = 10^{-2}$ to 10^6. Examples of ferromagnetic materials are cobalt (Co), iron (Fe) and nickel (Ni).

Ferrimagnetic: Like ferromagnetic substances, have net magnetic dipole moments in the absence of an external magnetic field. These materials consist of at least two different types of atoms or arrangements that vary in their magnetic moment magnitudes. Upon applied magnetic field, the electron spin alignment is antiparallel; however, as the moments are not of the same magnitude, exhibited a positive net magnetic moment in one direction. Examples of ferrimagnetic materials include magnetite (Fe_3O_4) and ferrites.

Antiferromagnetic: Similar to those of ferromagnetic materials, however, in the presence of a magnetic field the adjacent dipole moments are oriented in opposite directions or antiparallel way. As a result, the net magnetic moment is canceled. Antiferromagnetic materials display small magnetic susceptibilities from $\chi_M = 10^{-1}$ to 0. For instance, chromium (Cr) and manganese (Mn) in solid state and room temperature are antiferromagnetic.

7.2   Magnetism at Nanoscale

At the nanoscale, the reduction in the size of NPs and their magnetic properties are mainly influenced by two key features, finite-size effects and surface/interface effects.[7] Finite-size effects arise from the quantum confinement of the electrons. As NPs contain about a few hundred to ~10^5 atoms, they are governed in a state between quantum and solid-state chemistry. The most relevant finite-size effects are the single magnetic domain (SD) and superparamagnetism (SPM).[8]

Magnetic nanoparticles are typically divided into magnetic domains, which are regions of uniform magnetization (Figure 7-2). Large magnetic NPs are multidomain structures,

where different magnetic domains are separated by domain-walls. The formation of these domain-walls helps to decrease the magnetostatic energy (ΔE_{MS}) as the volume of the nanomaterial increases. However, as the particle size decreases, finite-size effects begin to become significant, where it is energetically more favorable to sustain the ΔE_{MS} of the single-domain state rather than forming domain walls.[2]

Thus, below a certain critical diameter (D_c), nanoparticles exist in a single-domain (SD) state, where the magnetic dipoles are uniformly aligned in the same direction, or along preferred axis of magnetization ("easy axis").[9] This D_c is typically below than 100 nm and depends on the material composition, size and shape.[7] In this D_c the coercivity (H_c) reaches their maximum (Figure 7-2). As the particle size continues to decrease below D_c, the coercivity gradually decreases as a function of their diameter due to thermal effects, until reach another critical diameter (D_{sp}), where the H_c becomes zero. The relationship between coercivity and particle diameter is given by: [5]

$$H_c = g - \frac{h}{D^{3/2}}$$

Where g, and h are constants.

At D_{sp} a superparamagnetic state emerges, where thermal fluctuations can randomize the direction of magnetization. NPs sizes which exhibited a strong magnetic response under an applied external field, and a magnetic moment equal to zero in absence of an external field are called superparamagnetic NPs. [3,7]

The NPs magnetic behavior is governed by the anisotropy energy (E), that vary depending on the deviation in the magnetization direction (angle θ) from the easy axis and the effective anisotropy constant (K), as given by:

$$E(\theta) = KV sin^2(\theta)$$

Where V, is the volume of the particle, and KV is the anisotropy energy barrier ($E_B^{(0)}$ = KV). In a spherical particle there two preferred orientations of the easy axis in a zero magnetic field, superspin up ($\theta = 0$) or down ($\theta = \pi$), separated for the energy barrier (KV). Because the dipolar interaction between the NPs is no longer negligible compared to the exchange energy. At high temperature, the thermal fluctuations are greater than the anisotropy barrier (thus is $kT \gg KV$), which causes that the magnetization vector to start to fluctuate between this both states. The temperature range in which these fluctuations

occur $f(V)$, is called the superparamagnetic (SPM) regime. However, at low temperature, the superspin is blocked. The time taken for the magnetization to fluctuate between two states of minimum energy is known as the Néel relaxation time, and follows the Arrhenius's law:[2]

$$\tau = \tau_0 exp\left(\frac{E_B}{kT}\right)$$

Where, τ (is a time scale), τ_0 is the specific relaxation time of the material ($\sim 10^{-9}$ s), and E_B is the energy barrier and is equal to KV without an applied external magnetic field.

The observed magnetic behavior can be distinguished between the difference of the measuring time and the relaxation time. When $\tau \gg \tau_0$(experimental time scale), the magnetic moment of the particle is blocked, exhibiting ferromagnetic behavior, and is observed by a hysteresis loop in the magnetization curve. On the contrary, if the $\tau_0 \gg \tau$, the magnetic moment fluctuates repeatedly on τ_0, then the average magnetic moment will be equal to zero.[9] The main characteristic within SPM regime is observed as the absence of a coercivity field in the hysteresis curves.

Thus, the superparamagnetic transition depends on the NPs composition, size, and shape, and it can be described as the critical size when they are still blocked at room temperature, or in terms of temperature in which the superparamagnetic transition occurs.[9]

Therefore, the blocking temperature (Tb) is defined as:

$$T_b = \frac{KV}{k_B} \ln \frac{\tau_{exp}}{\tau_0}$$

Where, K_B is the Boltzmann constant. For instance, Fe_3O_4 NPs with a diameter of 26 nm ($K= 1.1x\ 10^4$ J m^{-1}) the blocking temperature around 300 K. Thus, these NPs behavior will be superparamagnetic < 26 nm > ferromagnetic at 300 K.[9] Experimentally, T_b can be determined using zero field-cooled (ZFC) and field-cooled (FC) curves. These curves measure the magnetization of a sample as a function of the temperature. The difference lies that ZFC curve is obtained by cooling the sample in absence of a magnetic field at low temperature ($\sim$2K), while the FC curve the sample is cooled in the presence of a magnetic field ($\sim$50 Oe). Then gradually increasing the temperature. Both curves are merged and the maximum point of the ZFC indicates the T_b.

In summary, Figure 7-2 illustrates the transition between single domain to multi-domain magnetic states (characterized by domain walls). It shows a single-domain nanoparticle before and after the superparamagnetic limit (D_{sp}), in the representation the

curved arrows represent random spin fluctuations, while straight arrows indicate the blocked state. The corresponding behavior of their hysteresis loops is also depicted, highlighting the changes in magnetic properties during this transition.
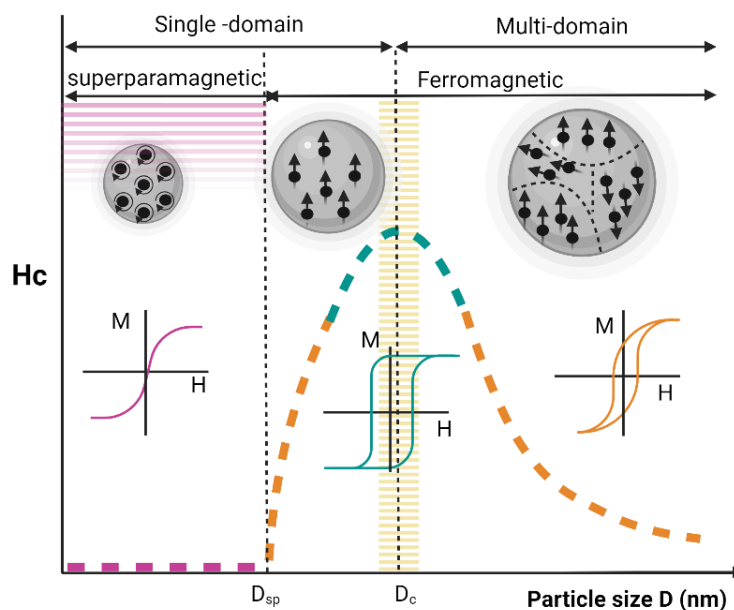

Figure 7-2. Schematic variation of the coercivity with the particle diameter, from magnetic single domain to multi-domain. Graphic based on Mohapatra et al.[10]

Another crucial aspect at the nanoscale is the impact of surface and interface effects. As particle size decreases, a significant percentage of atoms in the NP are surface atoms, making the surface and interface effects more prominent. These surface effects arise from the lack of transitional symmetry at the particle boundary, leading to surface spin disorder or misalignment respect to the core spins.[2,7] Consequently, the surface spins can greatly influence the magnetization of the NPs, remarkably in smaller particles.

Surface spin disorder can lead to a decrease of the saturation magnetization (M_s) in small particles compared to their bulk counterparts. This reduction has been associated with the existence of a magnetically dead layer on the particle surface. However, the existence of spin canting of the surface spins has been demonstrated. Spin-canting occurs, where the surface spins are slightly titled relative to the easy axis alignment. These phenomena can also affect the lattice constant and atom coordination.[7]

Another surface effect is the increase in magnetic anisotropy, K_{eff}, as the particle size decreases, known as surface anisotropy. This anisotropy value can surpass that obtained from crystalline and shape anisotropy. For instance, for a spherical particle with diameter (D), volume (V), and surface area (s), K_{eff} can be described in terms of the contributions

by bulk anisotropy per unit volume (K_v) and surface anisotropy (K_s) by the following equation:

$$K_{eff} = K_V + \frac{6}{D} K_s$$

This relationship highlights how surface effects become more pronounced as particle size diminishes, significantly influencing the overall magnetic properties. In addition, surfaces modifications, coating or adsorption of different molecules, can influence the contribution of the surface anisotropy to K_{eff}.[2,7]

7.3 Nanoparticle Magnetic Self-assembly

Single domain NPs are characterized by a preferred axis of magnetization and can act as tiny magnets (Figure 7-3A). The magnetic dipole moment (µ) of a sphere particle, is given by is volume times its saturation magnetization (per volume), and can be described as:

$$\mu = \frac{4\pi}{3} a_m^3 M_s$$

Where a_m is the particle radius of the magnetic core, and M_s is the material saturation magnetization. Then the magnetic moment scales as particle volume increases.
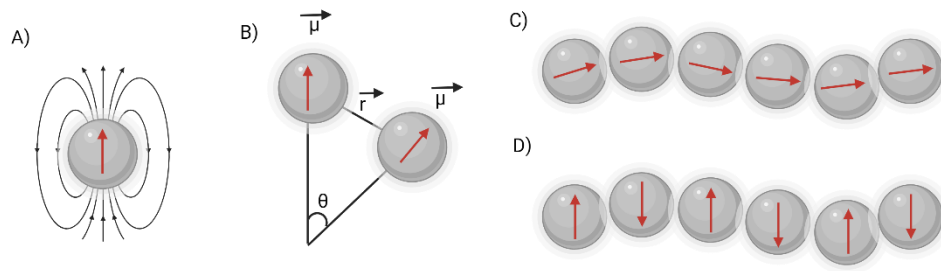
*Figure 7-3. (**A**) Magnetic field lines in a single domain magnetic NP, (**B**) interaction between two particles, (**C**) parallel, and (**D**) antiparallel alignment. Adapted from ref. 9.*

Non-interacted particles, in a superparamagnetic state and zero field (H=0), result in a magnetic moment of the sample (M) = 0, due to the random orientation of all magnetic moments. Upon a magnetic field the particle magnetic dipoles are aligned in the field direction. The magnetic moment (M) per unit volume as a function of the magnetic field (H) follows a Langevin equation: [9]

$$M(H) = M_s \varphi \left(\cot h(\alpha) - \frac{1}{(\alpha)} \right)$$

Where α is a Langevin parameter, which depends on the particle radius (a_m), temperature (T) and external magnetic field (H), as described by:

$$M(H) = M_s \varphi \left(\cot h \left(\frac{\mu_0 \mu H}{k_B T} \right) - \left(\frac{k_B T}{\mu_0 \mu H} \right) \right)$$

The interaction energy (U) between two magnetic particles depends on the strength of the magnetic dipole moments (μ), their relative orientation (θ), and the separation vector between them ($\vec{r}$). The interactions between magnetic NPs can be attractive or repulsive (Figure 7-3B).[9]

The dipole-dipole energy (U_{dd}) of interaction between the centers of two particles, is given by (Figure 7-3B):

$$U_{dd} = \frac{\vec{\mu_1} \cdot \vec{\mu_2} - 3(\vec{\mu_1} \cdot \vec{r})(\vec{\mu_2} \cdot \vec{r})}{4\pi r^3}$$

Where ($\vec{r}$) is the separation vector which connect the two particles. According to the previous Equation, particle attraction is maximal where the magnetic dipoles are in parallel or head-to-tail orientation (Figure 7-3C), and can be described by:

$$U_p = \frac{-(\mu^2)}{2\pi\mu_0 r^3}$$

While the antiparallel organization of the magnetic dipoles makes repulsion between them (Figure 7-3D), as given by:

$$U_{ap} = \frac{-(\mu^2)}{4\pi\mu_0 r^3}$$

The dipole-dipole energy (U) increases linearly with an increase in NP volume. Nanoparticles in the superparamagnetic state, the interaction potential depends on the distance between the two particles. For small separations, the interaction is strong and scales to r^{-3}, leading to the alignment of the particles. At large distances, dipole-dipole interactions are weaker and scale with the distance to r^{-6}. Large particles with a fixed magnetic moment, the dipole-dipole interactions are long-ranged (r^{-3}).[9]

The process of self-assembly can be achieved using an external magnetic field, which induces the formation of particle arrays in linear or ring aggregates, or by formation of the oriented anisotropic structures (i.e., strings).[9] Elongated or string-like structures are energetically favorable arrays because the magnetization is parallel to their magnetic easy long axis. This shape anisotropy results in an anisotropic response to an applied magnetic field (H), leading to slight differences in the hysteresis loop when the field is applied perpendicular or parallel to their long axis. However, these differences are not as pronounced as those observed in plates or nanowires structures.[11] In addition, van der Waals forces become more important as the particle size decreases, leading to the attraction between the magnetic core and repulsion from the surfactant layer.[9] Thus, magnetic NPs self-assembly results from a delicate equilibrium between attractive and repulsive forces. The strength of these interactions is influenced by factors as NPs size, composition, morphology, temperature concentration, reaction media, surface ligands, and the intensity of an applied external magnetic field.[12]

7.4   References

(1)   Nguyen T. K. Thanh. *Magnetic Nanoparticles: From Fabrication to Clinical Applications*; 2012.

(2)   Batlle, X.; Labarta, A. Finite-Size Effects in Fine Particles: Magnetic and Transport Properties. *Journal of Physics D: Applied Physics* **2002**, *35* (6). https://doi.org/10.1088/0022-3727/35/6/201.

(3)   Kolhatkar, A. G.; Jamison, A. C.; Litvinov, D.; Willson, R. C.; Lee, T. R. *Tuning the Magnetic Properties of Nanoparticles*; 2013; Vol. 14. https://doi.org/10.3390/ijms140815977.

(4)   Ali, A.; Shah, T.; Ullah, R.; Zhou, P.; Guo, M.; Ovais, M.; Tan, Z.; Rui, Y. K. Review on Recent Progress in Magnetic Nanoparticles: Synthesis, Characterization, and Diverse Applications. *Frontiers in Chemistry* **2021**, *9* (July), 1–25. https://doi.org/10.3389/fchem.2021.629054.

(5)   Cullity, B. D.; Graham, C. D. *Introduction to Magnetic Materials*; Wiley, 2008; Vol. 11. https://doi.org/10.1002/9780470386323.

(6)   Cornell, R. M.; U. Schwertmann. *The Iron Oxides: Structure, Properties, Reactions, Occurences and Uses*, Second.; Wiley VCH, Ed.; Weinheim, 2003; Vol. 664.

(7)   Lu, A. H.; Salabas, E. L.; Schüth, F. Magnetic Nanoparticles: Synthesis, Protection, Functionalization, and Application. *Angewandte Chemie - International Edition* **2007**, *46* (8), 1222–1244. https://doi.org/10.1002/anie.200602866.

(8)   Muro-Cruces, J.; Roca, A. G.; López-Ortega, A.; Fantechi, E.; Del-Pozo-Bueno, D.; Estradé, S.; Peiró, F.; Sepúlveda, B.; Pineider, F.; Sangregorio, C.; Nogues, J. Precise Size Control of the Growth of Fe3O4 Nanocubes over a Wide Size Range Using a Rationally Designed One-Pot Synthesis. *ACS Nano* **2019**. https://doi.org/10.1021/acsnano.9b01281.

(9)   Singamaneni, S.; Bliznyuk, V. N.; Binek, C.; Tsymbal, E. Y. Magnetic Nanoparticles: Recent Advances in Synthesis, Self-Assembly and Applications. *Journal of Materials Chemistry* **2011**, *21* (42), 16819. https://doi.org/10.1039/c1jm11845e.

(10)   Mohapatra, J.; Liu, J. P. *Rare-Earth-Free Permanent Magnets: The Past and Future*, 1st ed.; Elsevier B.V., 2018; Vol. 27. https://doi.org/10.1016/bs.hmm.2018.08.001.

(11)   Lisjak, D.; Mertelj, A. Anisotropic Magnetic Nanoparticles: A Review of Their Properties, Syntheses and Potential Applications. *Progress in Materials Science* **2018**, *95*, 286–328. https://doi.org/10.1016/j.pmatsci.2018.03.003.

(12)   Nandakumaran, N.; Barnsley, L.; Feoktystov, A.; Ivanov, S. A.; Huber, D. L.; Fruhner, L. S.; Leffler, V.; Ehlert, S.; Kentzinger, E.; Qdemat, A.; Bhatnagar-Schöffmann, T.; Rücker, U.; Wharmby, M. T.; Cervellino, A.; Dunin-Borkowski, R. E.; Brückel, T.; Feygenson, M. Unravelling Magnetic Nanochain Formation in Dispersion for In Vivo Applications. *Advanced Materials* **2021**, *33* (24). https://doi.org/10.1002/adma.202008683.

Appendix B

Speciation and Pourbaix Diagrams

A speciation diagram provides an indication of the species around and their relative concentrations formed during the hydration process of the soluble and precipitated species under equilibrium conditions. However, these diagrams assume no interaction between species and consider only absolute hydrolysis, considering just the transference of protons at given pH.[1] The speciation diagram for the iron-water system is shown in Figure 8-1. Intersections of two species curves indicate identical concentrations at specific pH.[1] For Fe^{3+}, the curve shows progressive hydrolysis with increasing pH, forming species such as $Fe(OH)_2^+$, $Fe(OH)_3^+$, $Fe(OH)_4^-$. This indicates that Fe^{3+} in aqueous media is stable in its ionic form only at very low pH, preferring to be in a hydrolyzed form at higher pH levels. In contrast, the Fe^{2+} curve shows that free Fe^{2+} ions are more stable at higher pH, being the predominant species up to pH ~9. Meanwhile it shows a minor hydrolysis progression with increasing pH, achieving a maximum at pH above 10. This highlights the different stability and hydrolysis behavior of Fe^{3+} and Fe^{2+} ions in varying pH.

Pourbaix diagrams, also known as potential-pH equilibrium diagrams, indicate the thermodynamic stability of various soluble, hydrated or solid species as function of pH and their redox potential. For the iron aqueous system, 32 iron species have been identified, from which only 17 are considered relevant for Pourbaix diagram calculations (Figure 8-2).[2]

142
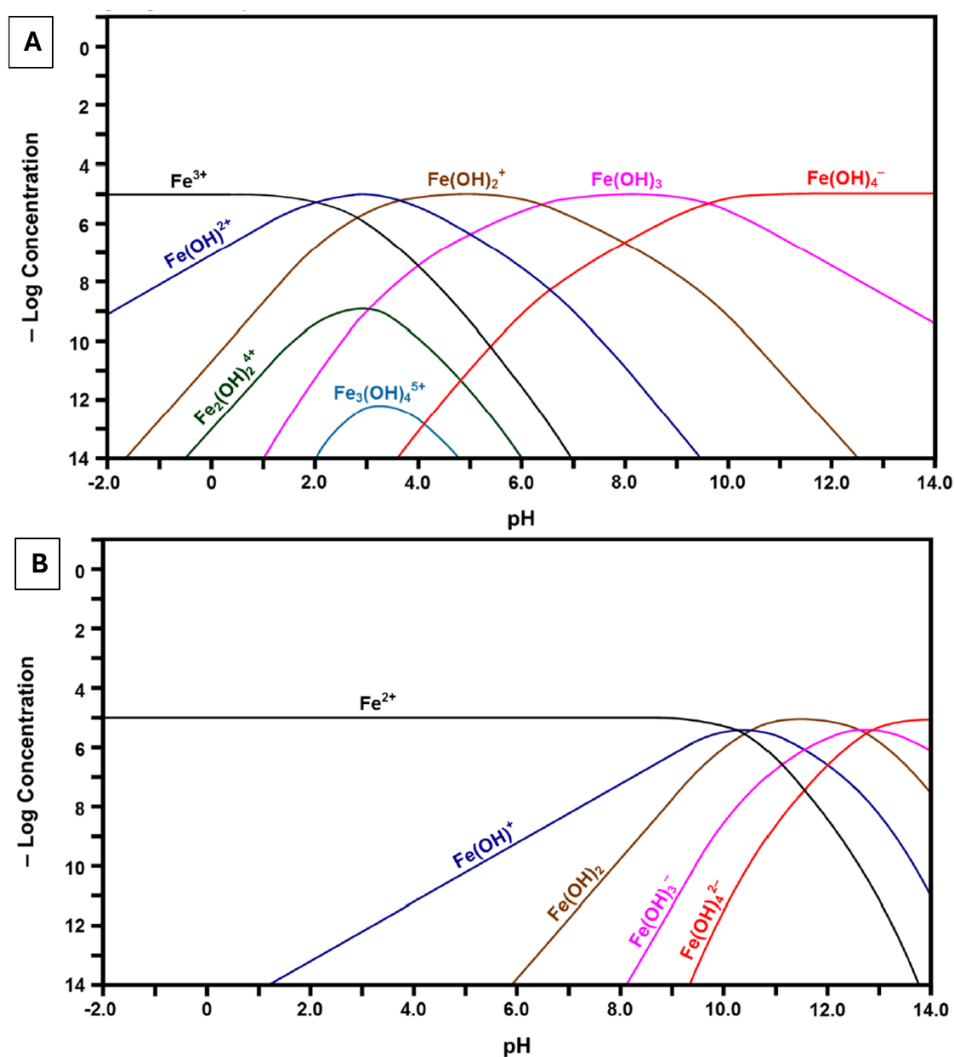
Figure 8-1. Calculated speciation diagram for Fe³⁺ and Fe²⁺ - H₂O system, assuming a [Fe]$_{total}$= 10 µM, at RT. Reproduced from [1]

The different areas of this diagram show the stable state in which iron is found, including $Fe^{2+}_{(aq)}$ and $Fe^{3+}_{(aq)}$ in solution, metallic $Fe_{(s)}$ and $Fe_3O_{4(s)}$ and $Fe_2O_{3(s)}$ oxides. The phases are separated by three types of boundary lines, which indicates the equilibrium between two species. Horizontal lines represent equilibrium between pure redox reactions and vertical lines indicate proton transfer reactions. While inclined lines show reactions involving both proton and electron transfer, with their potentials varying according to pH. According to the Pourbaix diagram, in the zone within the water stability region, magnetite (Fe_3O_4) forms at alkaline pH under de-aerated conditions, as indicated by the hydrogen reduction line (Figure 8-2). Similarly, maghemite (γ-Fe_2O_3) forms at alkaline pH but in oxygen presence. [3]

143
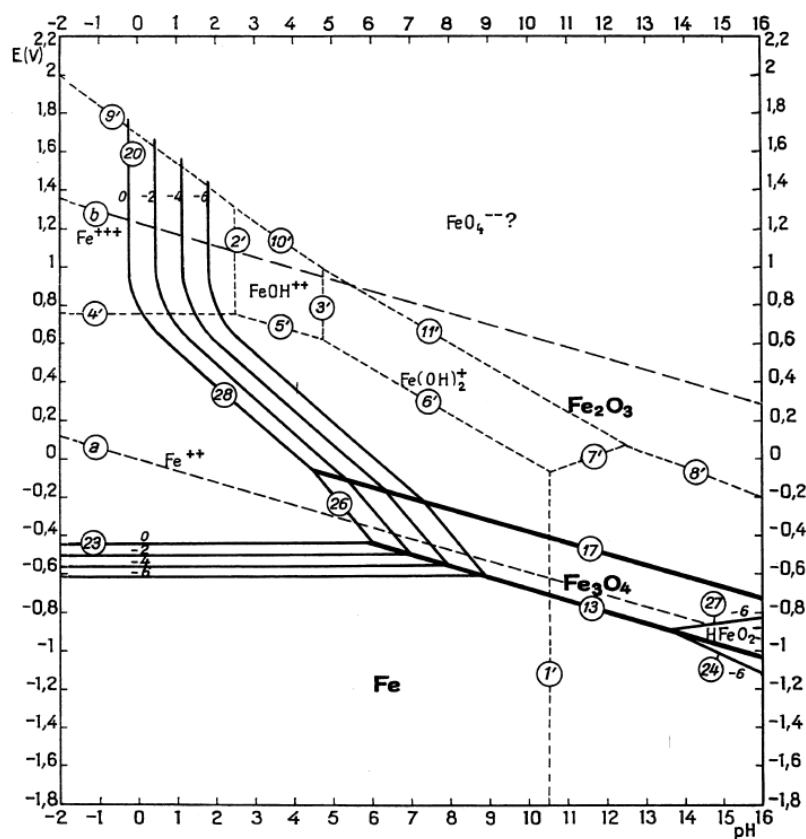
Figure 8-2. Pourbaix diagram of Fe-H₂O system at 25 °C.

Since the proposed synthesis of magnetic IONPs in this thesis employs cerium cations in aqueous media, the speciation and Pourbaix diagrams for Ce^{3+} cations are shown in Figure 8-3A. The aqueous speciation curve for Ce^{3+} depicts the stability of Ce^{3+} with increasing pH, remaining as a highly concentrated species up to pH 8. Meanwhile, progressively hydrolyzed species appear during increasing pH, leading to the formation of $Ce(OH)^{2+}$, $Ce(OH)_2^+$, and $Ce(OH)_3$.[1] Pourbaix diagram shows the domains of Ce^{3+}, CeO_2 phase, and hydrolyzed forms of $Ce(OH)_3$ and $Ce(OH)_4$ within the water stability region. Under reducing conditions, Ce^{3+} precipitated in the form of $Ce(OH)_3$ at pH ~10 (Figure 8-3B), however under oxidizing conditions precipitated in CeO_2 form.[1,4]

Despite the challenges that come from the synthesis in aqueous media, it has become increasingly attractive approach for the green and scalable production of IONPs at room temperature and low energy conpsumption.[5] One of the primary advantages of using aqueous media is the inherent stability of these particles in water, which enhances their biocompatibility compared to those synthesized in organic solvents.[5,6] This stability makes aqueous synthesis particularly appealing for biomedical applications, where biocompatibility is crucial.
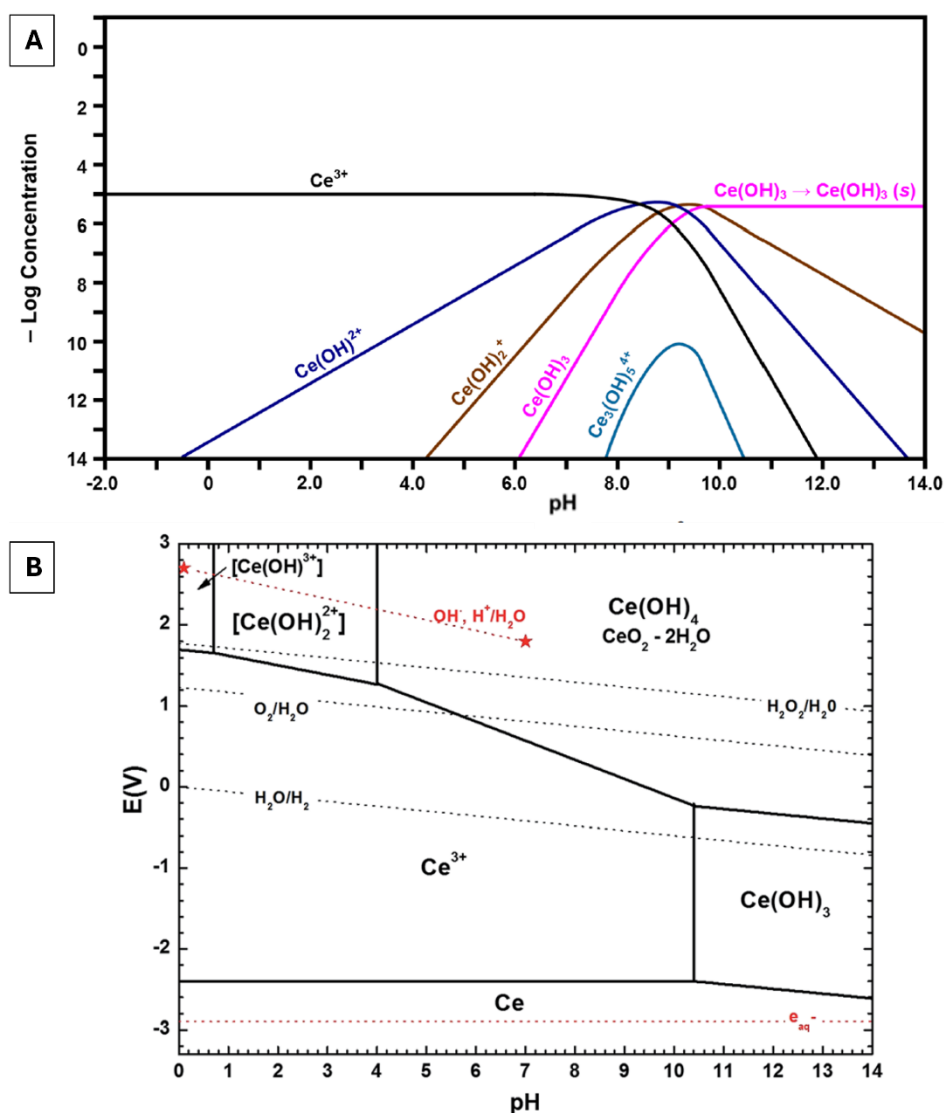
*Figure 8-3. (**A**) Calculated speciation diagram for Ce^{3+}-H$_2$O system, assuming a [Ce]$_{total}$= 10 μM, at RT (Reproduced from ref. [1]), and (**B**)Pourbaix diagram of Ce-H$_2$O system at 25 °C for 0.1 mM (Reproduced from ref. [4]).*

8.1 References

(1)   Channei, D.; Phanichphant, S.; Nakaruk, A.; Mofarah, S.; Koshy, P.; Sorrell, C. Aqueous and Surface Chemistries of Photocatalytic Fe-Doped CeO2 Nanoparticles. *Catalysts* **2017**, *7* (12), 45. https://doi.org/10.3390/catal7020045.

(2)   Beverskog, B. Revised Diagrams for Iron At 25-300 ° C. *Science (80-.).* **1996**, *38* (12), 2121–2135.

(3)   Pourbaix, M. *Atlas of Electrochemical Equilibria in Aqueous Solutions*, Second.; Houston, Texas, 1974.

(4)   Abellan, P.; Moser, T. H.; Lucas, I. T.; Grate, J. W.; Evans, J. E.; Browning, N. D. The Formation of Cerium (III) Hydroxide Nanoparticles by a Radiation Mediated Increase in Local PH. *RSC Adv.* **2017**, *7* (7), 3831–3837.

https://doi.org/10.1039/C6RA27066B.

(5)   Marciello, M.; Connord, V.; Veintemillas-Verdaguer, S.; Vergés, M. A.; Carrey, J.; Respaud, M.; Serna, C. J.; Morales, M. P. Large Scale Production of Biocompatible Magnetite Nanocrystals with High Saturation Magnetization Values through Green Aqueous Synthesis. *J. Mater. Chem. B* **2013**, *1* (43), 5995–6004. https://doi.org/10.1039/c3tb20949k.

(6)   Lenders, J. J. M.; Mirabello, G.; Sommerdijk, N. A. J. M. Bioinspired Magnetite Synthesis via Solid Precursor Phases. *Chem. Sci.* **2016**, *7* (9), 5624–5634. https://doi.org/10.1039/C6SC00523C.

ANNEX A: Chapter 2

Figure A1. *Size distribution of magnetic SC-IONPs synthesized by co-precipitation in the presence of SC (0.5 to 4 mM).*

Table A1. *Percentage composition from the deconvoluted XPS spectra for IONPs(S) and SC4-IONPs Fe2p, O1s, and C1s peak fitting.*

	Fe 2p	Fe2+ 2p3/2		Fe3+ 2p3/2		Sat Fe2+		Ratio
	Sample	Pos. (eV)	% at.	Pos. (eV)	% at.	Pos. (eV)	% at.	Fe3+/Fe2+
A	IONP	710.6	23.7	711.8	40.3	714.9	0.9	1.70
B	SC-IONP	710.5	23.98	711.7	40.8	714.7	0.3	1.70

	O 1s	Lattice oxide		Defective oxide		Water:organic oxide	
	Sample	Pos. (eV)	% at.	Pos. (eV)	% at.	Pos. (eV)	% at.
A	IONP	530.4	76.7	531.8	18.9	533.2	4.4
B	SC-IONP	530.2	72.5	531.6	18.9	533.0	8.6

	C 1s	C-C:C-H		C-OH:C-OC		C=O		O-C=O	
	Sample	Pos. (eV)	% at	Pos. (eV)	% at	Pos. (eV)	% at	Pos. (eV)	% at
A	IONP	284.8	73.5	286.3	15.9	287.8	4.0	288.8	6.6
B	SC-IONP	284.8	75.0	286.3	16.3	287.8	0.7	288.8	8.0

ANNEX B: Chapter 3
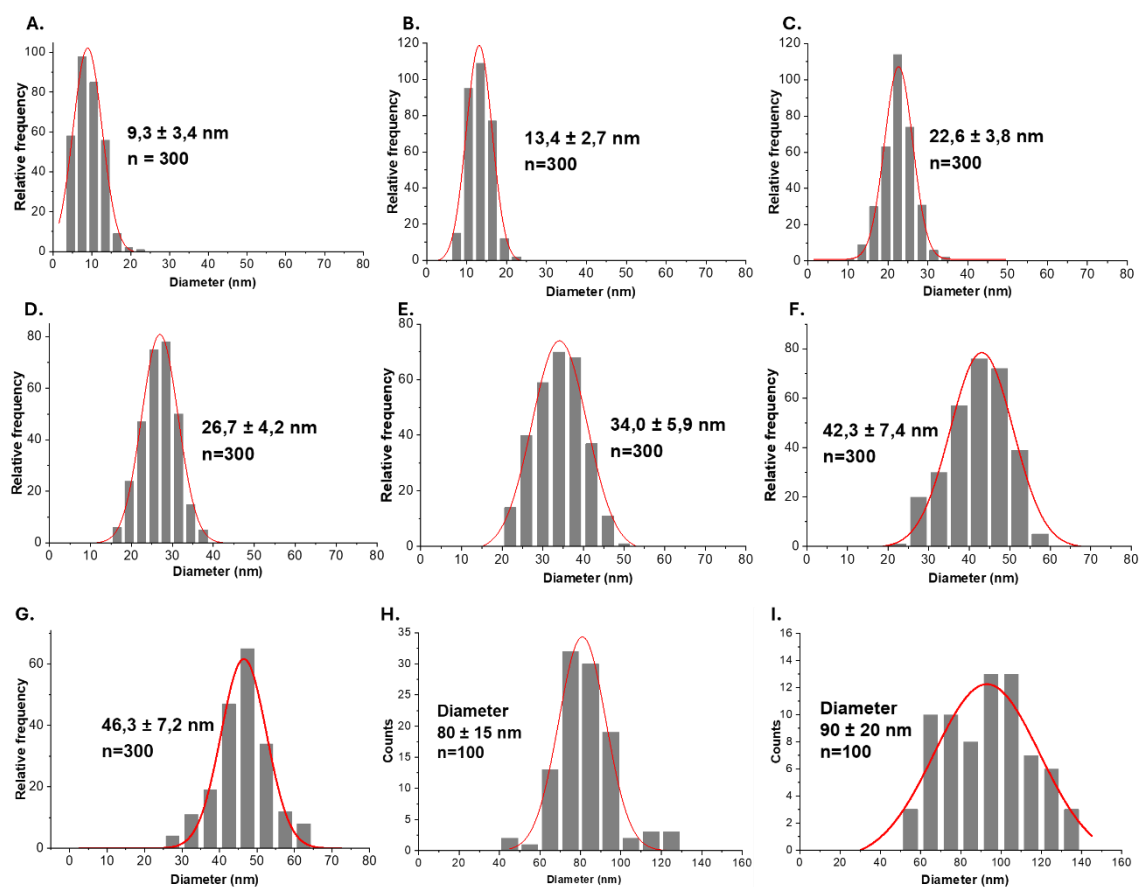
Figure B1. *Corresponding size distribution of the obtained Ce@IONPs synthesized with increasing Ce³⁺ concentration (0.00 to 2.00 mM) shown in Figure 3-1.*
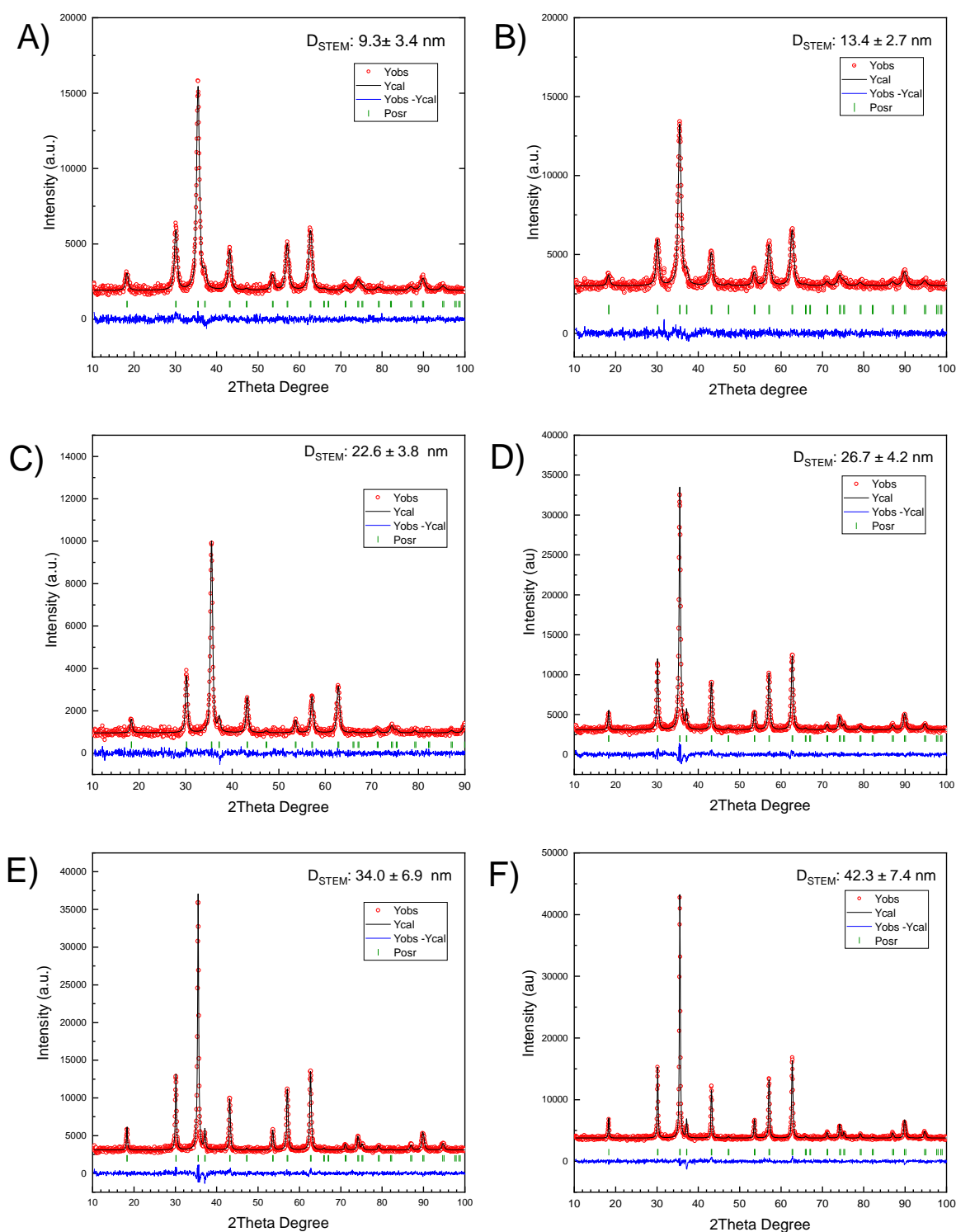
Figure B2. *XRD pattern and Rietveld refinement analysis (using FullProf Suite) for the obtained IONPs synthesized with increasing Ce³⁺ concentration in the reaction media: (A) 9.3 ± 3.4 nm ([Ce³⁺=0.0 mM]), (B) 13.4 ± 2.7 nm ([Ce³⁺=0.10 mM]), (C) 22.6 ± 3.8 nm ([Ce³⁺=0.25 mM]), (D) 26.7 ± 4.2 nm ([Ce³⁺=0.50 mM]), (E) 34.0 ± 6.9 nm ([Ce³⁺=0.75 mM]), (F) 42.3 ± 7.4 nm ([Ce³⁺=1.0 mM]), (G) 46.3 ± 7.2 nm ([Ce³⁺=1.25 mM]), (H) 80 ± 15 nm ([Ce³⁺=1.6 mM]), and (I) 90 ± 20 nm ([Ce³⁺=2. 0 mM]).*

Figure B2. *Continued.*

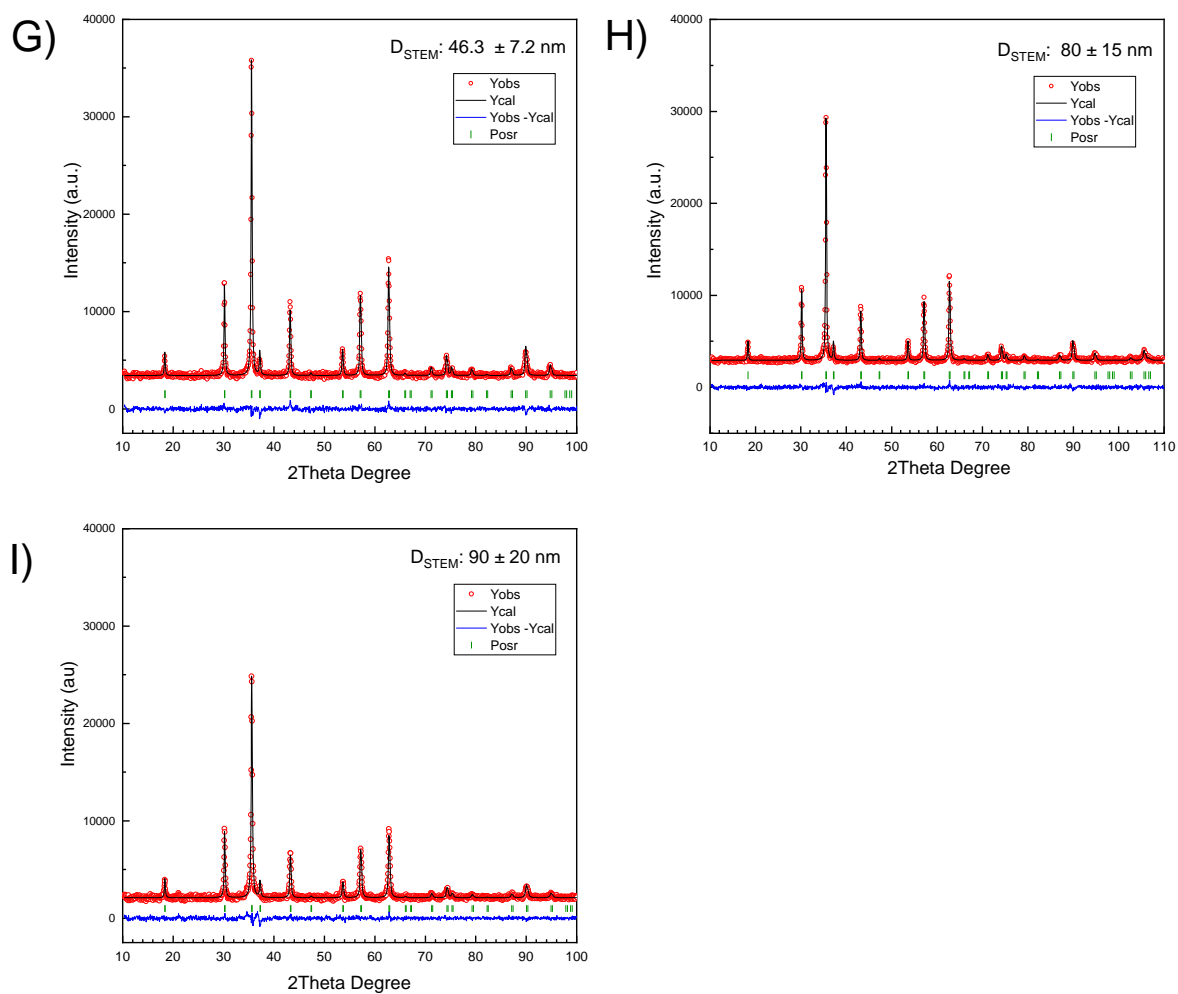|		Rxn	$[Fe^{3+}]_{(aq)}+[Fe^{2+}]_{(aq)}$----$>$$[Fe3O4]_{(s)}$		
R (J/mol K)	8,314	Half(red)	$[Fe^{3+}]_{(aq)}+1e$----$>$$[Fe^{2+}]_{(aq)}$	$[Ce^{4+}]+1e$----$>$$[Ce^{3+}]$	$[Eu^{3+}]+1e$----$>$$[Eu^{2+}]$
T (K)	298	Half(ox)	$[Fe^{2+}]_{(aq)}$--$>$$[Fe^{3+}]^{(aq)}+1e$-	$[Ce^{3+}]$--$>$$[Ce^{4+}]+1e$-	$[Eu^{2+}]$--$>$$[Eu^{3+}]+1e$-
n (mol e)	1				
F (C/mole e)	96485		$[Fe3+]+[Ce3+]$--$>$$[Fe2+]+[Ce4+]$	$[Fe2+]+[Ce4+]$--$>$ $[Fe3+]+[Ce3+]$	$[Fe2+]+[Eu3+]$--$>$$[Fe3+]+[Eu2+]$
			[Ln]i=0,1	[Ln]i=0,1	[Ln]i=0,1
[Conc]inicial	(mM)				
Fe^{2+}	2	Q	5,00E-06	Q	2,00E+05	Q	2,00E-05
Fe^{3+}	4	E	-3,13E-01	E	3,13E-01	E	-2,78E-01
Ce^{3+}	0,1	Ec	-0,84	Ec	0,84	Ec	-1,12
Ce^{3+}	0,5						
Ce^{3+}	2	E	-0,53	E	0,53	E	-0,84216635
Ce^{4+}	1,00E-06	-	No spontaneous	+	spontaneous	-	No spontaneous
Eu^{3+}	0,1						
Eu^{3+}	0,5		$[Fe3+]+[Ce3+]$----$>$$[Fe2+]+[Ce4+]$	$[Fe2+]+[Ce4+]$----$>$ $[Fe3+]+[Ce3+]$	$[Fe2+]+[Eu3+]$----$>$$[Fe3+]+[Eu2+]$
Eu^{3+}	2		[Ln]i=0,5	[Ln]i=0,5	[Ln]i=0,5
Rxn	E (red)	Q	1,00E-06	Q	1,00E+06	Q	4,00E-06
$Ce^{4+}+1e$- --$>$$Ce^{3+}$	1,61	E	-3,55E-01	E	3,55E-01	E	-3,19E-01
$Fe^{3+}+1e$- --$>$$Fe^{2+}$	0,77	Ec	-0,84	Ec	0,84	Ec	-1,12
$Eu^{3+}+1e$- --$>$$Eu^{2+}$	-0,35						
		E	-0,49	E	0,49	E	-0,80
		-	No spontaneous	+	spontaneous	-	No spontaneous
$E_{cel}=E_{red (catodo)}-E_{red(anado)}$							
Se oxida ---$>$	Anodo		$[Fe3+]+[Ce3+]$----$>$$[Fe2+]+[Ce4+]$	$[Fe2+]+[Ce4+]$--$>$ $[Fe3+]+[Ce3+]$	$[Fe2+]+[Eu3+]$----$>$$[Fe3+]+[Eu2+]$
Se reduce ---$>$	Catodo		[Ln]i=2,0	[Ln]i=2,0	[Ln]i=2,0
		Q	2,50E-07	Q	4,00E+06	Q	1,00E-06
		E	-3,90E-01	E	3,90E-01	E	-3,55E-01
		Ec	-0,84	Ec	0,84	Ec	-1,12
		E	-0,45	E	0,45	E	-0,77
		-	No spontaneous	+	spontaneous	-	No spontaneous

Figure B3. Calculations using the Nest equation in nonstandard conditions form an system reaction $Fe^{2+}:Fe^{3+}$ (2:4 mM) in the presence of the redox pairs $Ce^{3+}:Ce^{4+}$ and $Eu^{2+}:Eu^{3+}$.
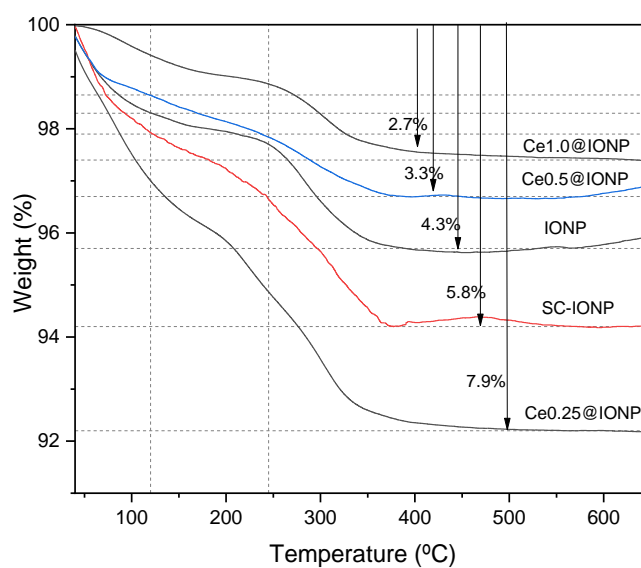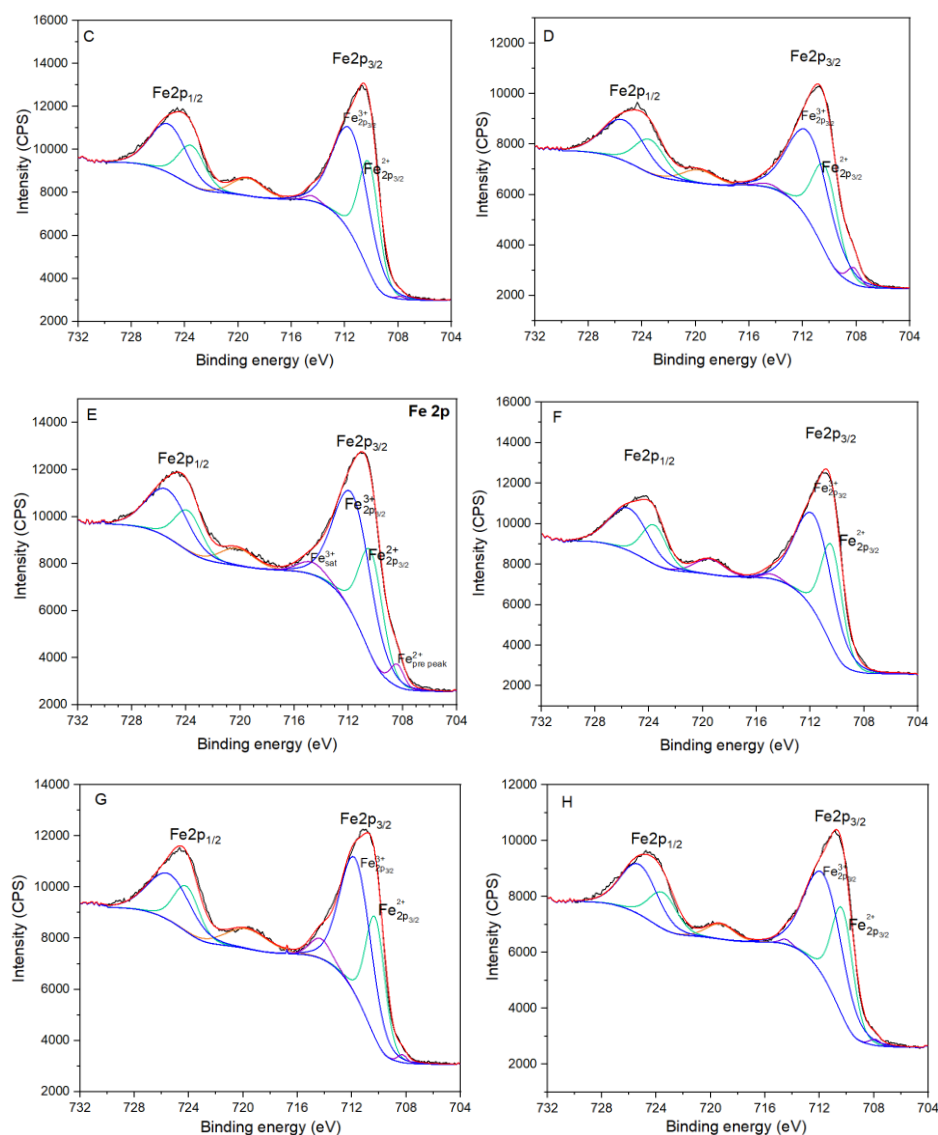

Figure B4. TGA weight loss for Ce@IONPs of three different sizes, corresponding to Ce^{3+} concentration of 0.25, 0.5 and 1.0 mM, compared with bared IONPs and SC-IONPs.

151

	Fe 2p	Fe^{2+} 2p3/2		Fe^{3+} 2p3/2		Sat Fe^{2+}		Ratio
	Sample	Pos. (eV)	% at.	Pos. (eV)	% at.	Pos. (eV)	% at.	Fe3+/Fe2+
A	IONP	710.6	23.7	711.8	40.3	714.9	0.9	1.70
B	SC-IONP	710.5	23.98	711.7	40.8	714.7	0.3	1.70
C	Ce0.1@IONP	710.1	23.2	711.5	39.5	714.5	0.9	1.70
D	Ce0.25@IONP	710.3	23.3	711.4	39.6	714.6	0.8	1.70
E	Ce0.5@IONP	710.3	22.7	711.6	38.6	714.7	3.4	1.70
F	Ce1.0@IONP	710.4	23.7	711.7	40.4	714.9	0.9	1.70
G	Ce1.25@IONP	710.3	21.2	711.7	38.1	714.3	3.7	1.79
H	Ce2.0@IONP	710.3	23.8	711.6	40.5	714.5	0.6	1.70

Figure B5. XPS spectra for Fe 2p peak fitting for Ce@IONPs at Cerium concentration C) 0.1 mM, D) 0.25 mM, E) 0.5 mM, F)1.0 mM, G) 1.25 mM and H) 2.0 mM. A) IONP and B) SC-IONP are showed for comparative purposes (presented in chapter 2).
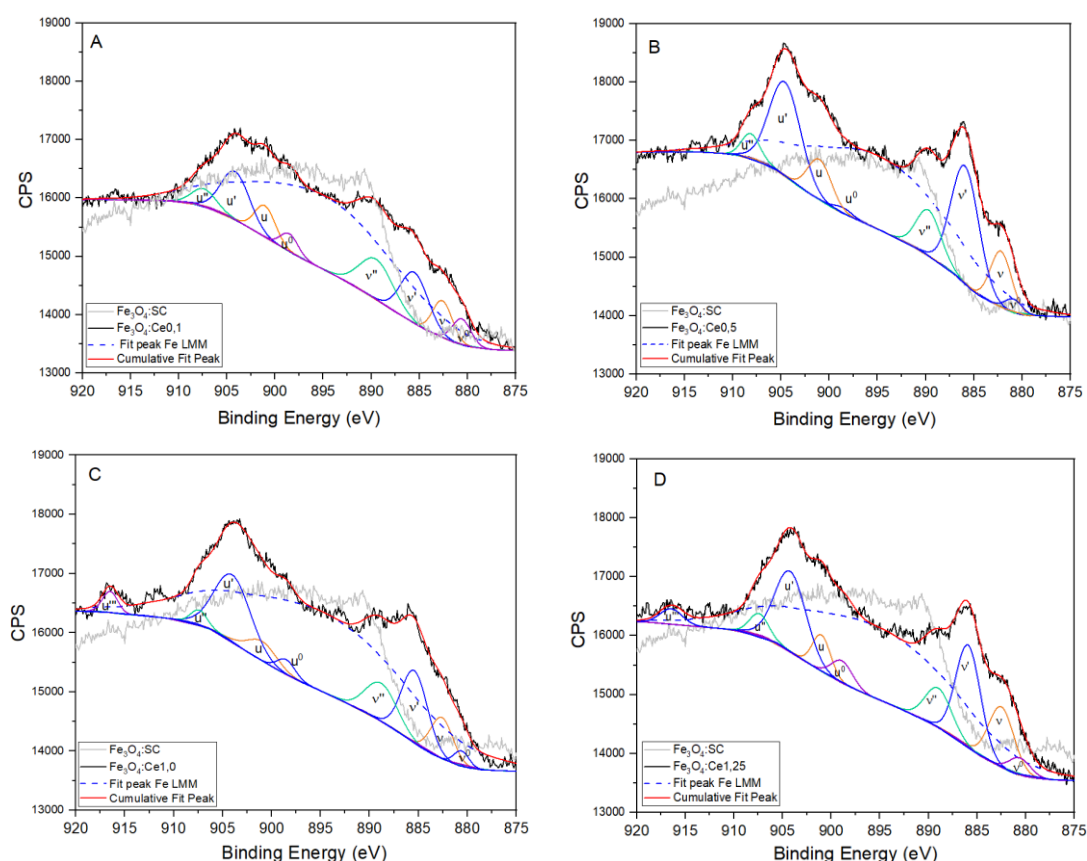
Sample		A. Ce0.1 @IONPs		B. Ce0.5@IONPs		C. Ce1.0@IONPs		D. Ce1.25@IONPs	
Component	Specie	Pos. (eV)	% at.	Pos. (eV)	% at.	Pos. (eV)	% at.	Pos. (eV)	% at.
v0	3+	880.6	7.2	880.9	2.3	880.6	2.9	880.6	3.8
v	4+	882.6	10.8	882.2	11.6	882.6	11.4	882.5	15.6
v'	3+	885.5	21.1	885.9	32.0	885.4	23.5	885.9	25.7
v"	4+	889.5	20.3	889.7	10.9	888.8	14.8	889.0	10.3
v'''	4+	-	-	-	-	-	-	-	-
u0	3+	898.5	4.7	898.6	1.0	898.5	3.4	898.9	4.8
u	4+	901.0	9.7	901.0	9.4	901.0	7.1	901.0	6.7
u'	3+	904.1	20.4	904.6	28.6	904.0	30.1	904.2	25.6
u"	4+	907.4	5.9	908.1	4.2	907.4	2.8	907.4	4.0
u'''	4+	-	-	-	-	916.5	4.0	916.4	3.5
Fit Fe FMM	-	895.0	-	894.9	-	895.0	-	895.5	-

***Figure B6**. XPS spectra for Ce3 $d_{3/2}$ and Ce3 $d_{5/2}$ peak fitting for Ce@IONPs samples at Cerium concentration A) 0.1 mM. B) 0.5 mM, C)1.0 mM and, D) 1.25 mM.*
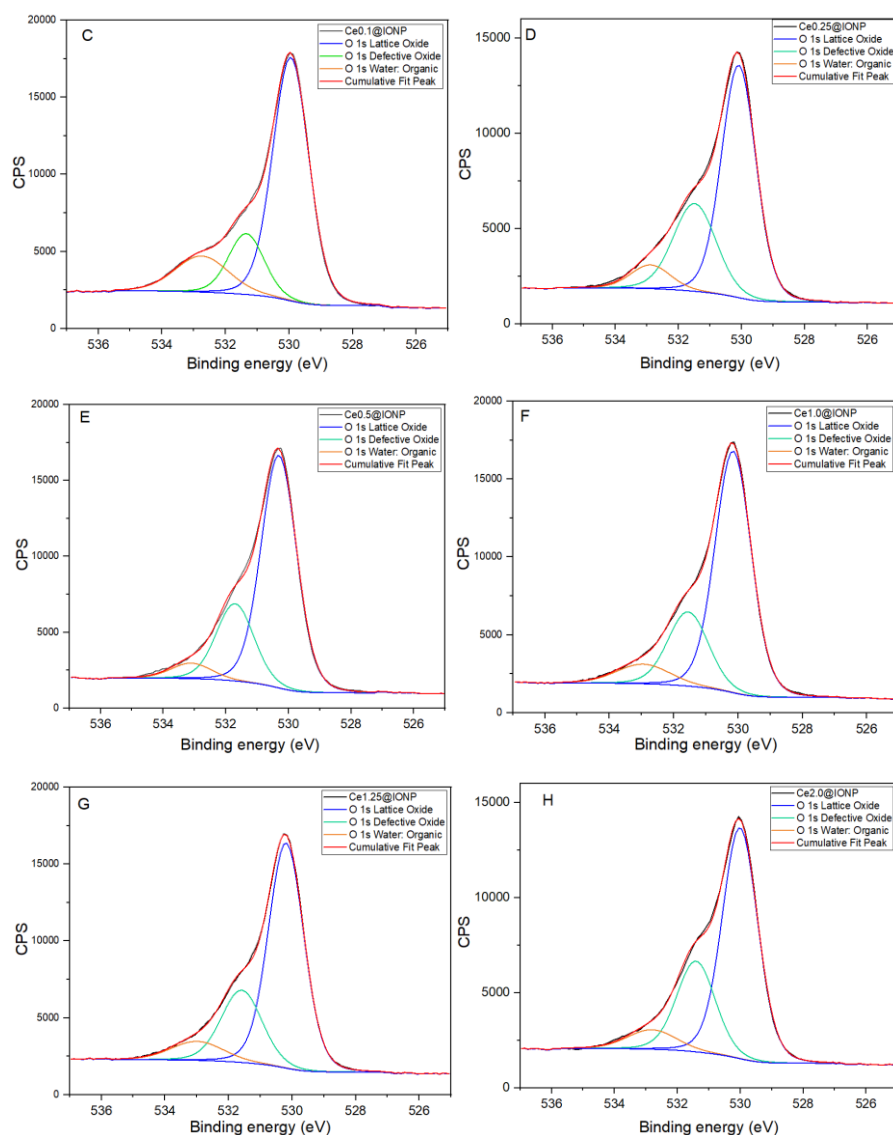
	O 1s	**Lattice oxide**		**Defective oxide**		**Water:organic oxide**	
	Sample	**Pos. (eV)**	**% at.**	**Pos. (eV)**	**% at.**	**Pos. (eV)**	**% at.**
A	IONP	530.4	76.7	531.8	18.9	533.2	4.4
B	SC-IONP	530.2	72.5	531.6	18.9	533.0	8.6
C	Ce0.1@IONP	530.0	68.4	531.4	16.7	532.8	14.9
D	Ce0.25@IONP	530.1	63.2	531.4	29.4	532.9	7.4
E	Ce0.5@IONP	530.3	70.1	531.7	24.6	533.1	5.3
F	Ce1.0@IONP	530.1	68.4	531.5	23.4	533.9	8.2
G	Ce1.25@IONP	530.1	67.0	531.6	24.6	533.0	8.4
H	Ce2.0@IONP	530.0	65.0	531.4	27.5	532.8	7.5

Figure B7. XPS spectra for O 1s peak fitting for Ce@IONPs at Cerium concentration C) 0.1 mM, D) 0.25 mM, E) 0.5 mM, F)1.0 mM, G) 1.25 mM and H) 2.0 mM. A) IONP and B) SC-IONP are showed for comparative purposes (presented in chapter 2).
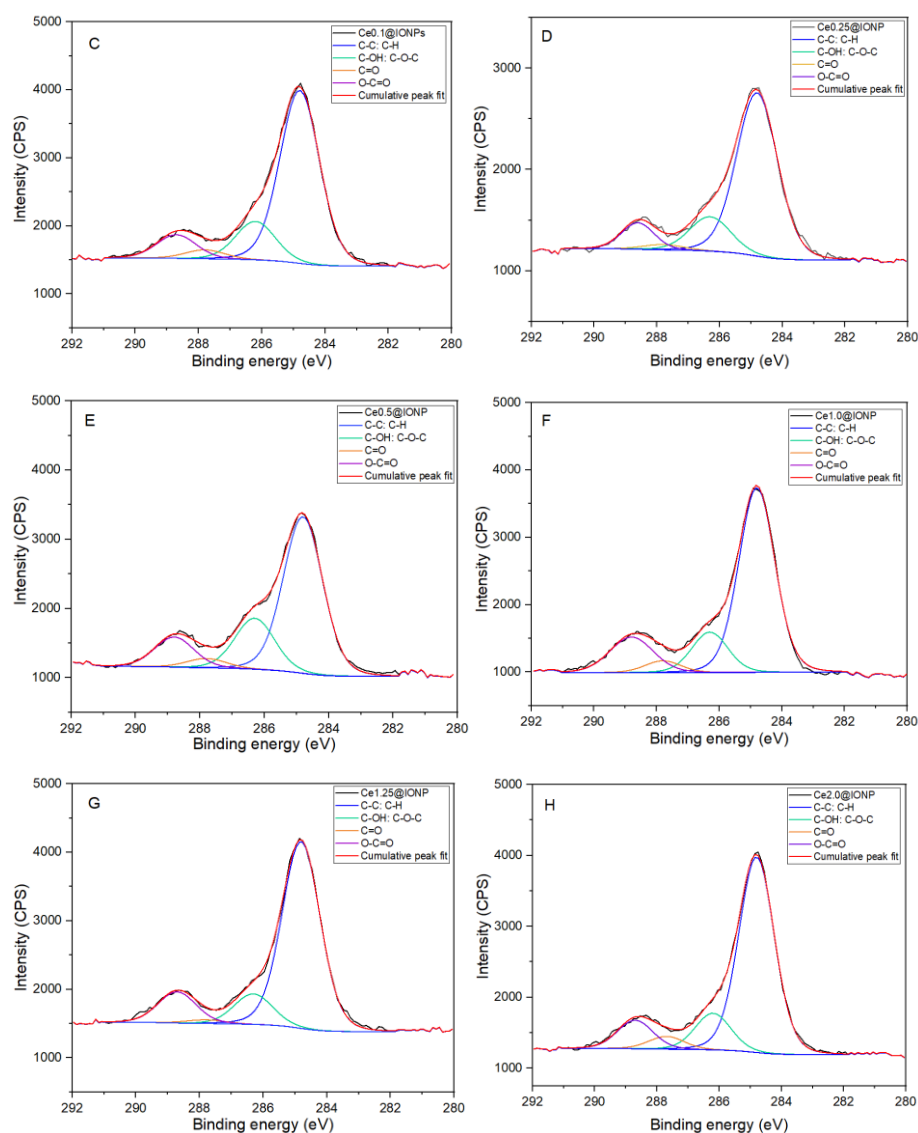
	C 1s	C-C:C-H		C-OH:C-OC		C=0		O-C=O	
	Sample	Pos. (eV)	% at	Pos. (eV)	% at	Pos. (eV)	% at	Pos. (eV)	% at
A	IONP	284.8	73.5	286.3	15.9	287.8	4.0	288.8	6.6
B	SC-IONP	284.8	75.0	286.3	16.3	287.8	0.7	288.8	8.0
C	Ce0.1@IONP	284.8	70.9	286.2	15.8	287.8	3.7	288.7	9.7
D	Ce0.25@IONP	284.8	72.9	286.3	15.3	287.8	2.4	288.7	9.4
E	Ce0.5@IONP	284.8	63.4	286.3	20.7	287.8	3.8	288.8	12.1
F	Ce1.0@IONP	284.8	66.0	286.3	14.5	287.8	4.2	288.8	15.3
G	Ce1.25@IONP	284.8	74.1	286.3	12.1	287.8	1.5	288.7	12.3
H	Ce2.0@IONP	284.8	71.5	286.2	13.4	287.7	4.6	288.7	10.4

Figure B8. XPS spectra for C 1s peak fitting for Ce@IONPs at Cerium concentration C) 0.1 mM, D) 0.25 mM, E) 0.5 mM, F)1.0 mM, G) 1.25 mM and H) 2.0 mM. A) IONP and B) SC-IONP are showed for comparative purposes (presented in chapter 2).
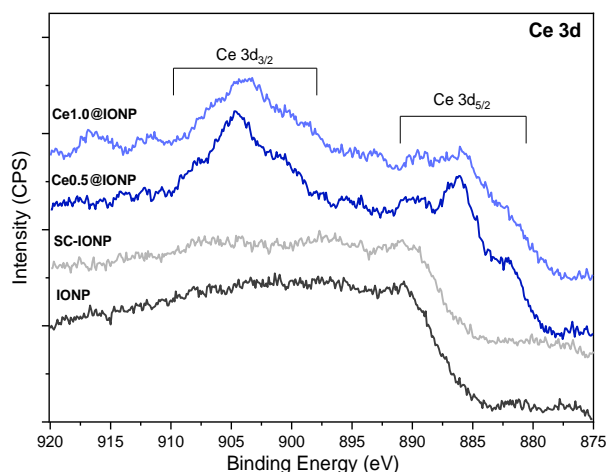
***Figure B9**. XPS spectra of Ce 3d in Ce@IONPs (at Ce precursor concentration 0.5 and 1.0 mM) compared with the bared IONPs and SC-IONPs.*
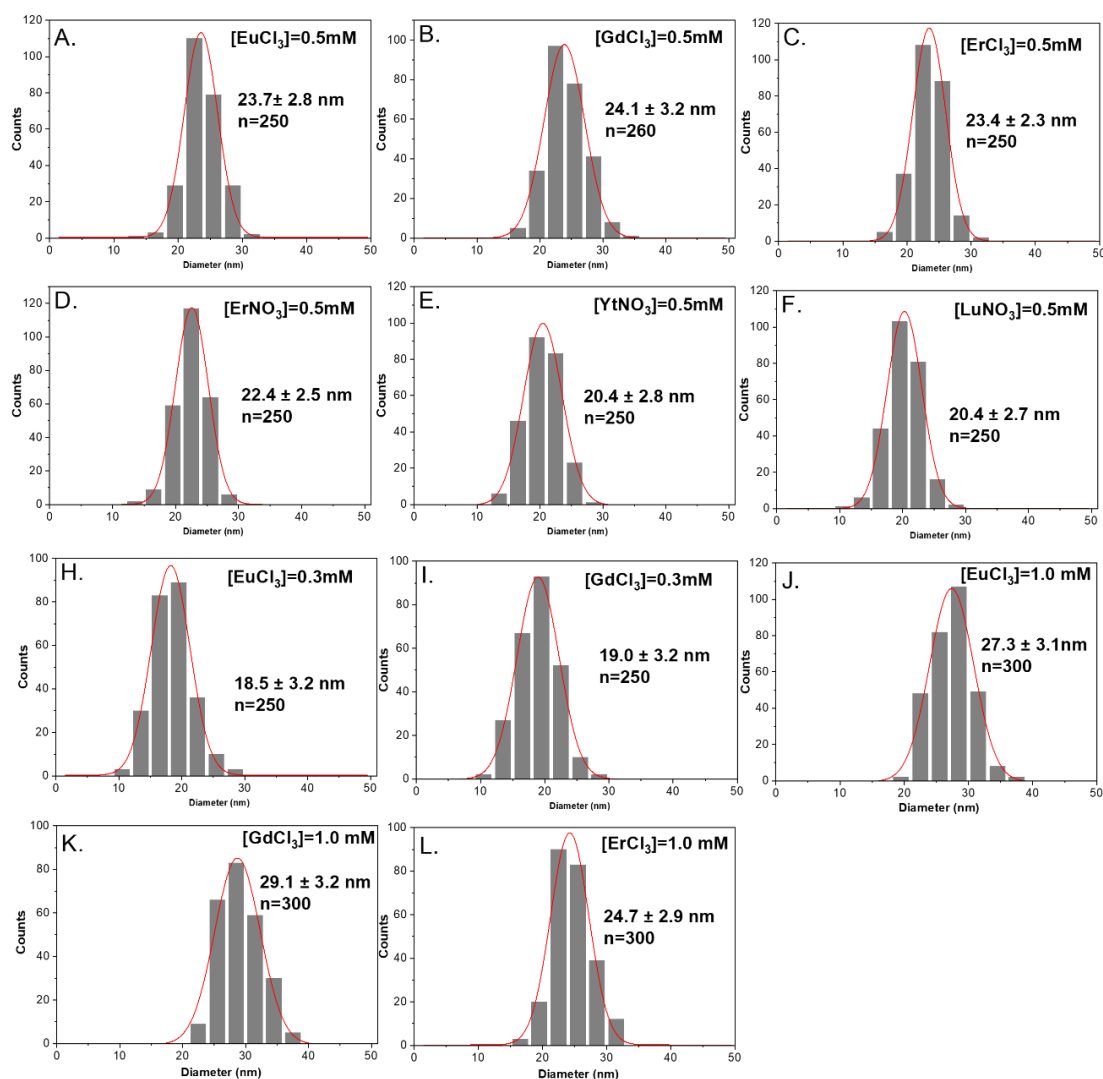

***Figure B10.** Size distribution of the obtained magnetite NPs synthesized at different Lanthanide ions (Ln = Eu^{3+}, Gd^{3+}, Er^{3+}, Yt^{3+}, and Lu^{3+}) and concentration at 0.3, 0.5 and 1.0 mM. For Ce^{3+} size distribution See Figure B1.*
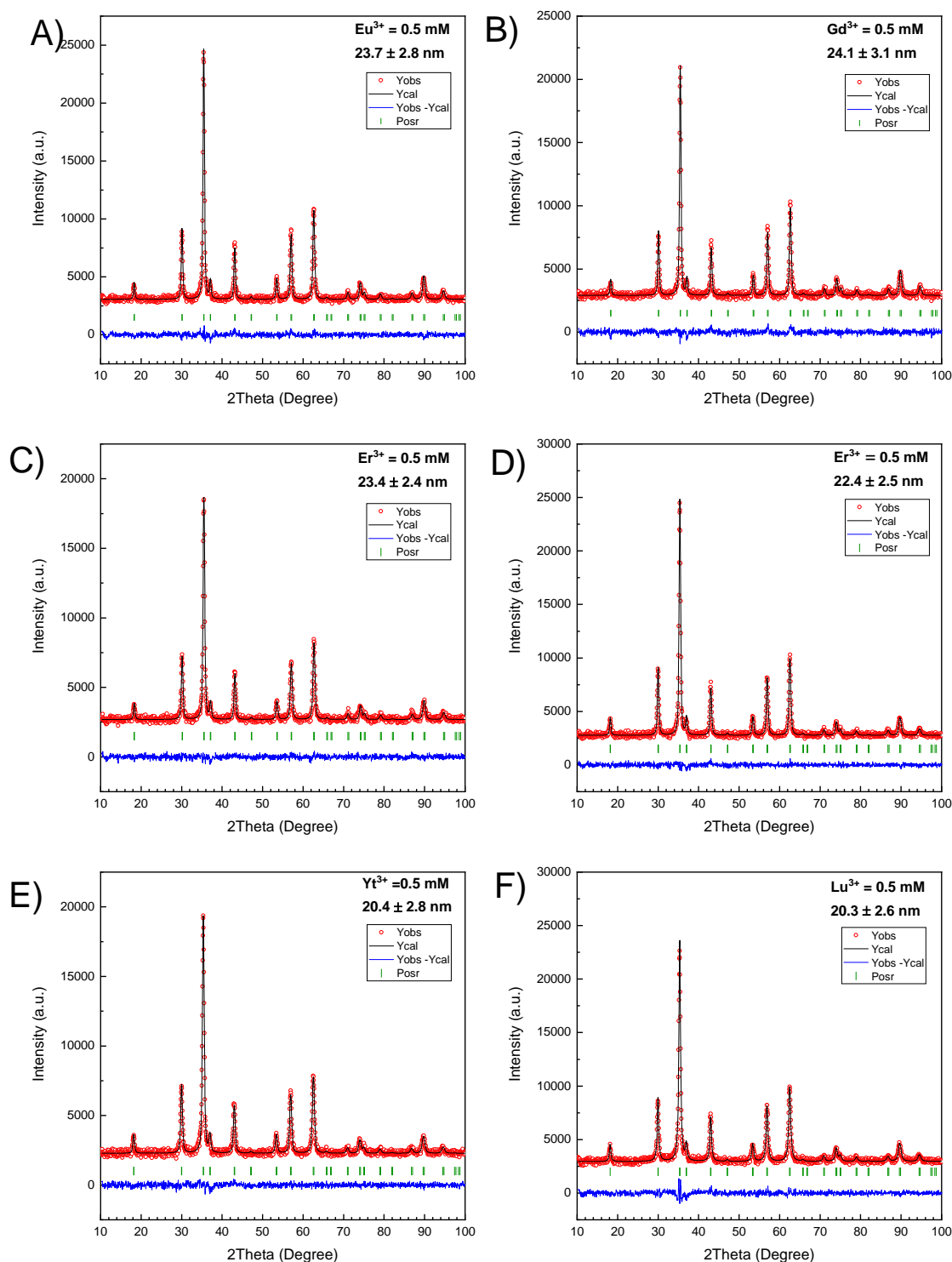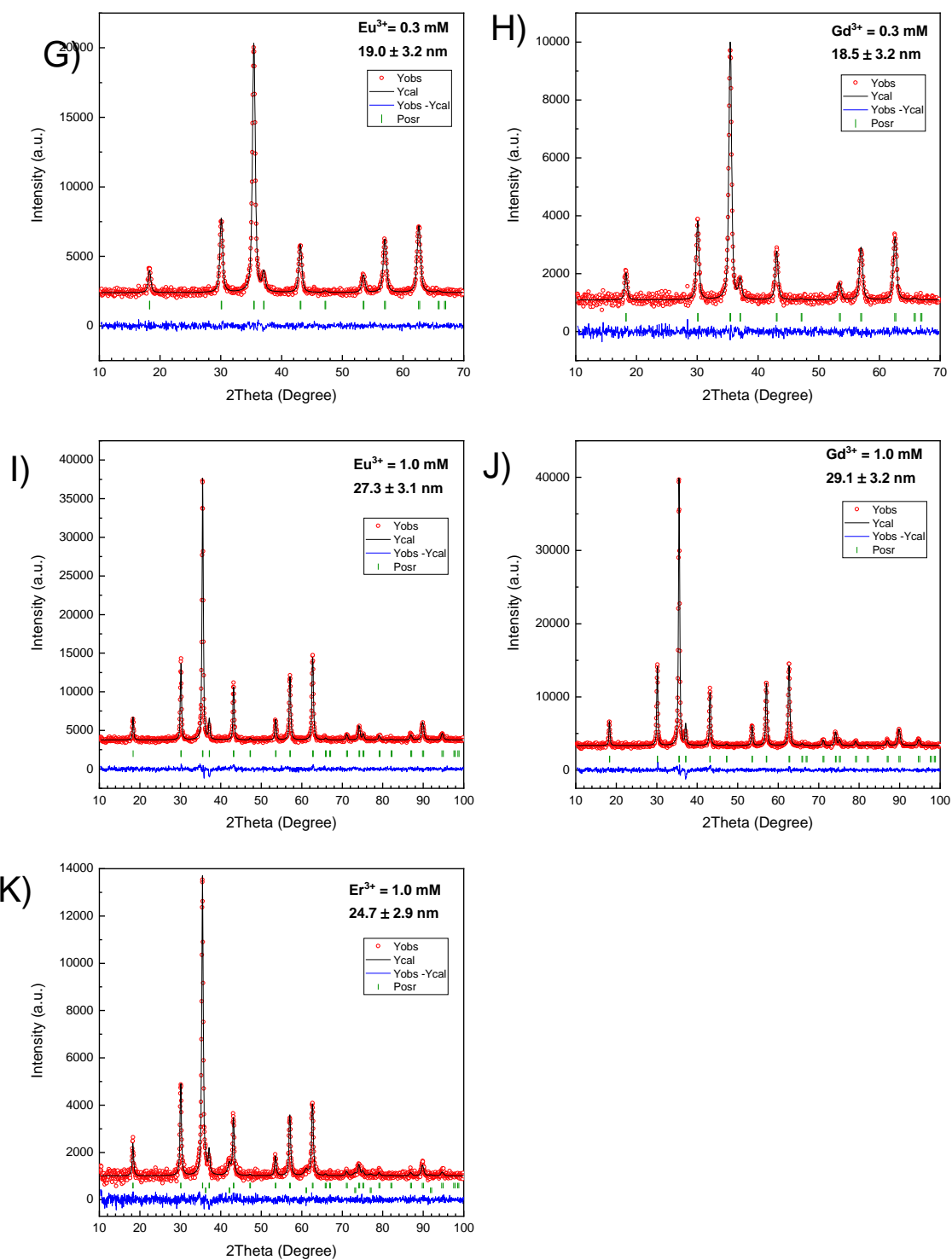
Figure B11. *XRD pattern and Rietveld refinement analysis (using FullProf Suite) for the obtained IONPs synthesized with different lanthanides (Ln = Eu³⁺, Gd³⁺, Er³⁺, Yt³⁺, and Lu³⁺) (A-F) at 0.5 mM (chlorides and nitrates precursors), (H-I) at 0.3 (chlorides precursors) and (J-L) 1.0 mM (chlorides precursors). Size labels correspond to NP's diameter as determined by TEM.*
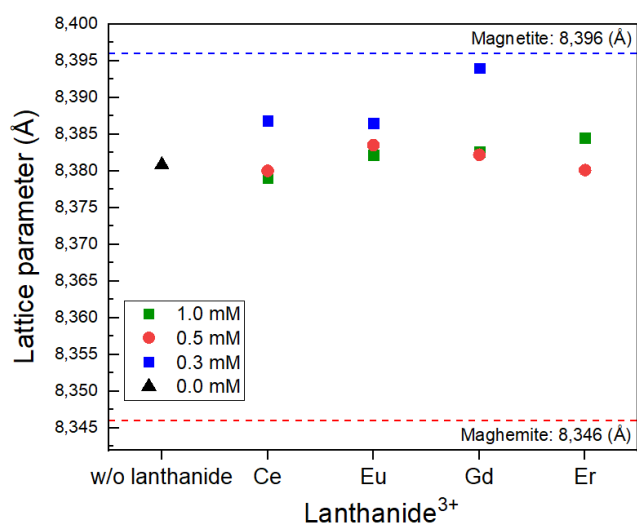
.

Figure B11. *Continued.*

Figure B12. *Comparison between lattice parameters of the obtained Ln@IONPs (LnCl₃ = Ce, Eu, Gd and Er) at 0.3 mM, 0.5 mM and 1.0 mM lanthanide concentration.*
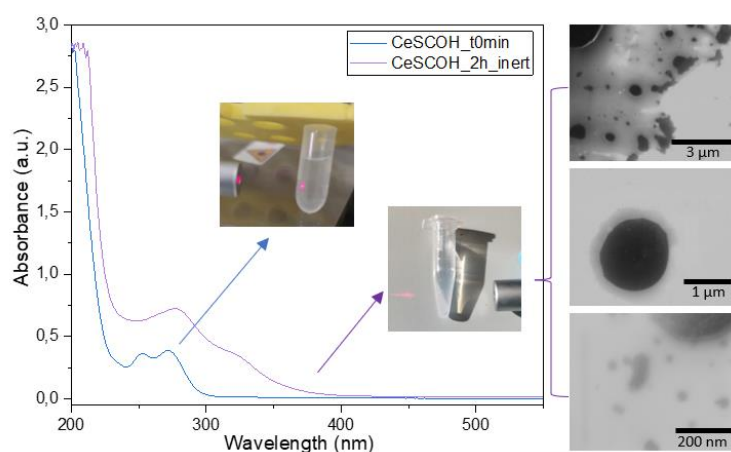

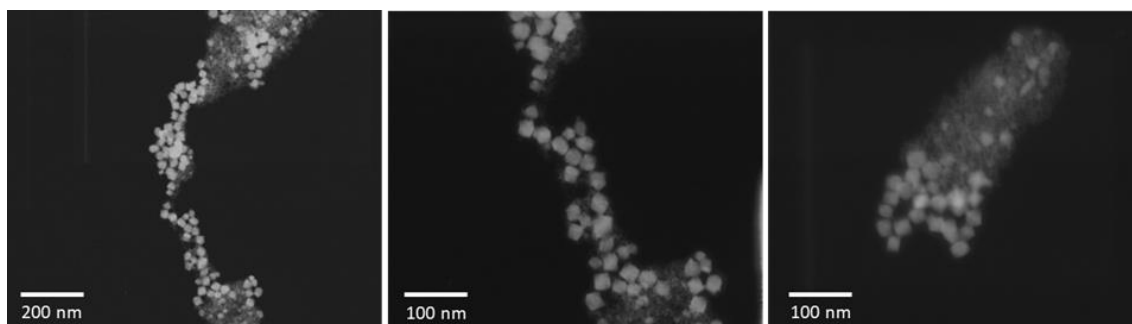**Figure B13.** *Oxidation process of Ce-SC complex at 2h reaction.*

Figure B14. *Representative HAADF STEM images of magnetite NPs synthesized via coprecipitation of Fe^{2+}/ Fe^{3+} in the presence of Ce^{3+} ([Ce^{3+}=0.50 mM]) and SC ions at high temperature at 90ºC.*
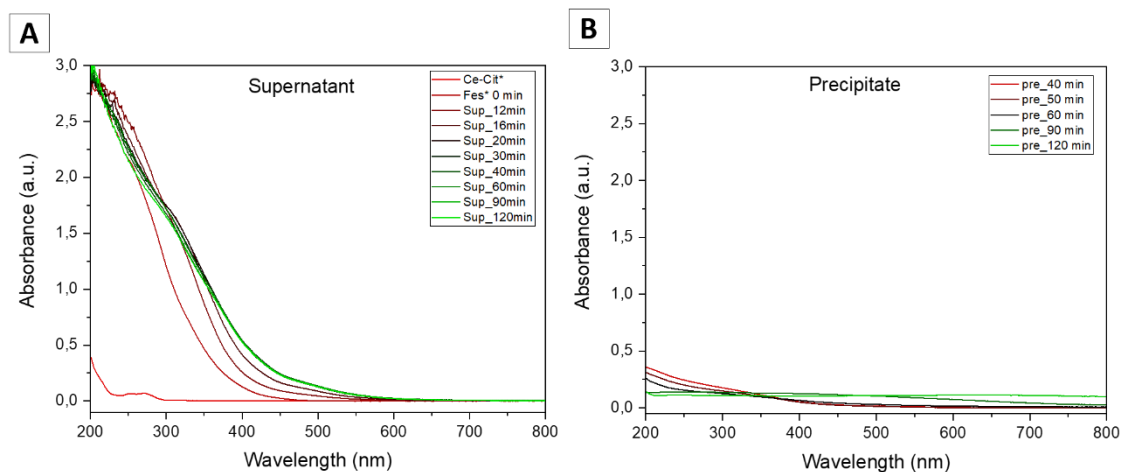
159

Figure B15. *UV-vis spectra of the time evolution formation of IONPs (~27 nm) synthesized by co-precipitation method by slow addition of the TMAOH solution at 100 μL/min in presence of Ce³⁺:SC (0.5:4 mM).*

Table B2. *Summary of the reagent concentration for transformation of ferrihydrite experiments.*

Reagents concentration	SC (mM)	Ce³⁺ (mM)	Fe²⁺ (mM)	Fe³⁺ (mM)	Ratio Fe²⁺: Fe³⁺	TMAOH (mM)
Exp 1	4	0.5	0.5	4	1:8	4 mL, 1 M, at 800 µL/min
Exp 2	4	0.5	1	4	1:4	
Exp 3	4	0.5	2	4	1:2	
Exp 4	4	0.5	4	4	1:1	

Annex C: Chapter 4

Figure C1*. UV-vis spectra of the reaction times curves of Ce0.1@IONPs for the catalytic oxidation of TMB (0.1 mg) by H₂O₂ (150 mM) by varying the NPs amount from 0 to 30 ug, ΔT = 10 s up to 600 s. 30 ug of NPs were used for blank and leaching solution experiments.*
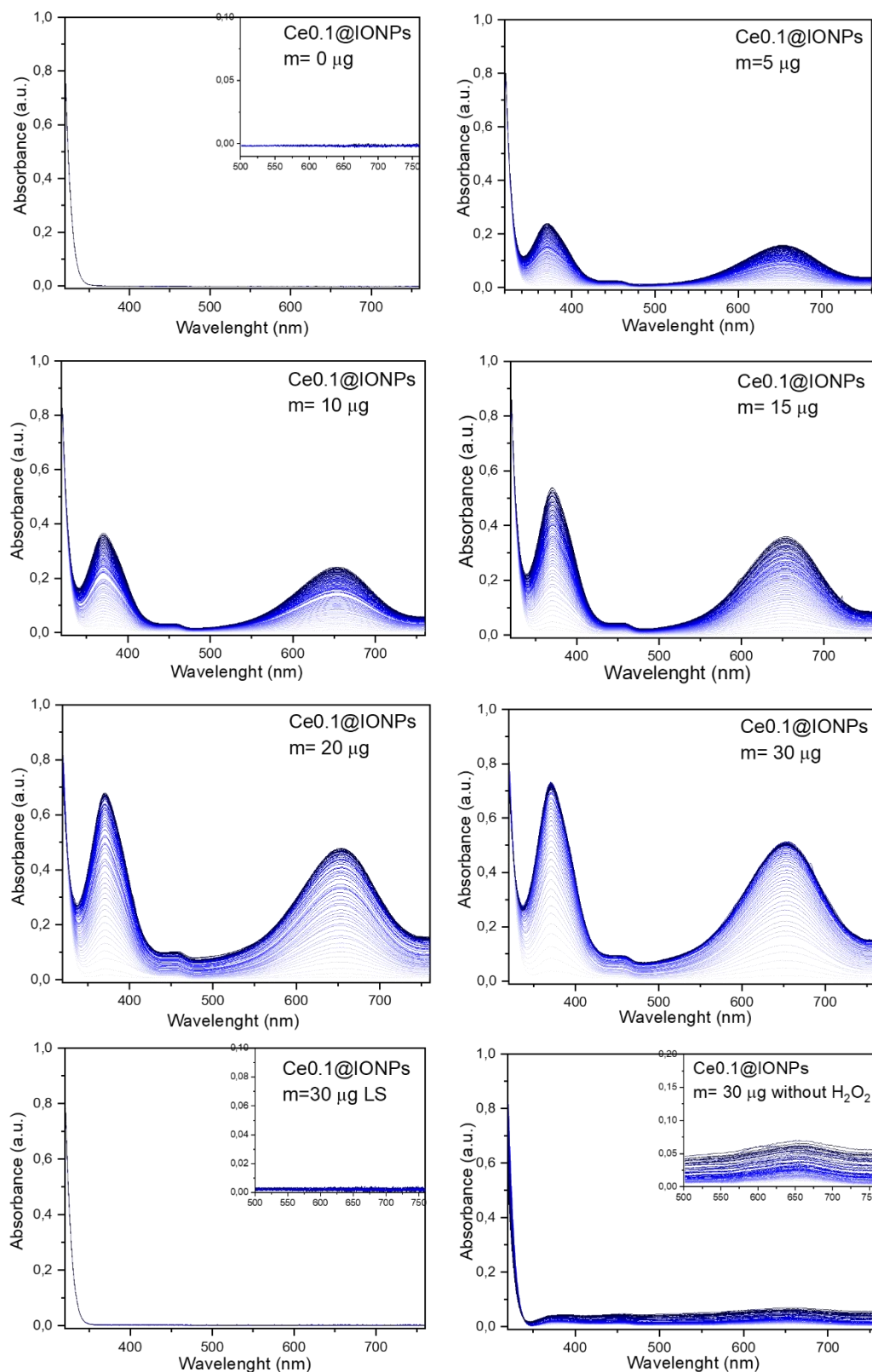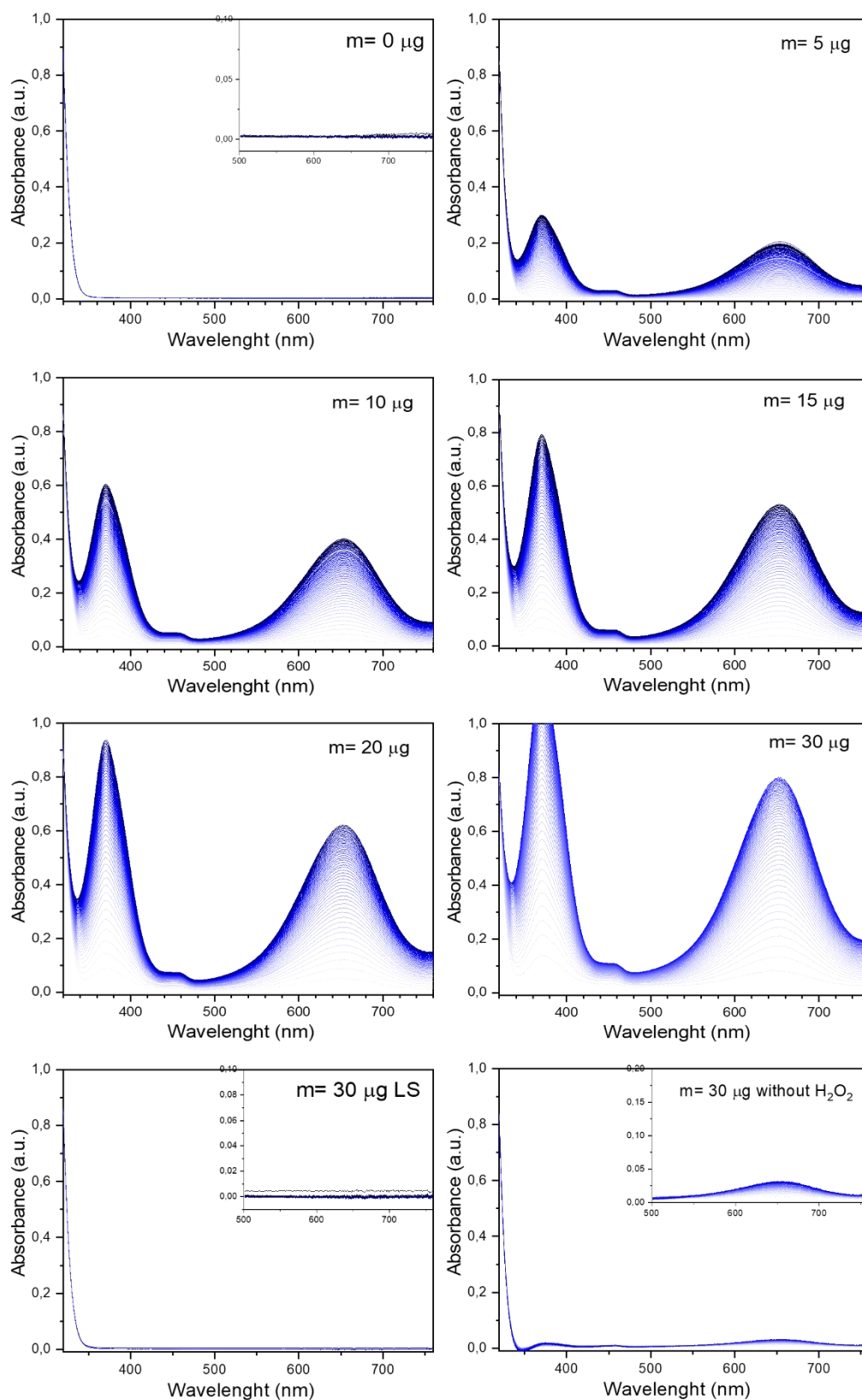
Figure C2. *UV-vis spectra of the reaction times curves of Ce0.25@IONPs for the catalytic oxidation of TMB (0.1 mg) by H₂O₂ (150 mM) by varying the NPs amount from 0 to 30 ug, ΔT=10s. 30 ug of NPs were used for blank and leaching solution experiments.*
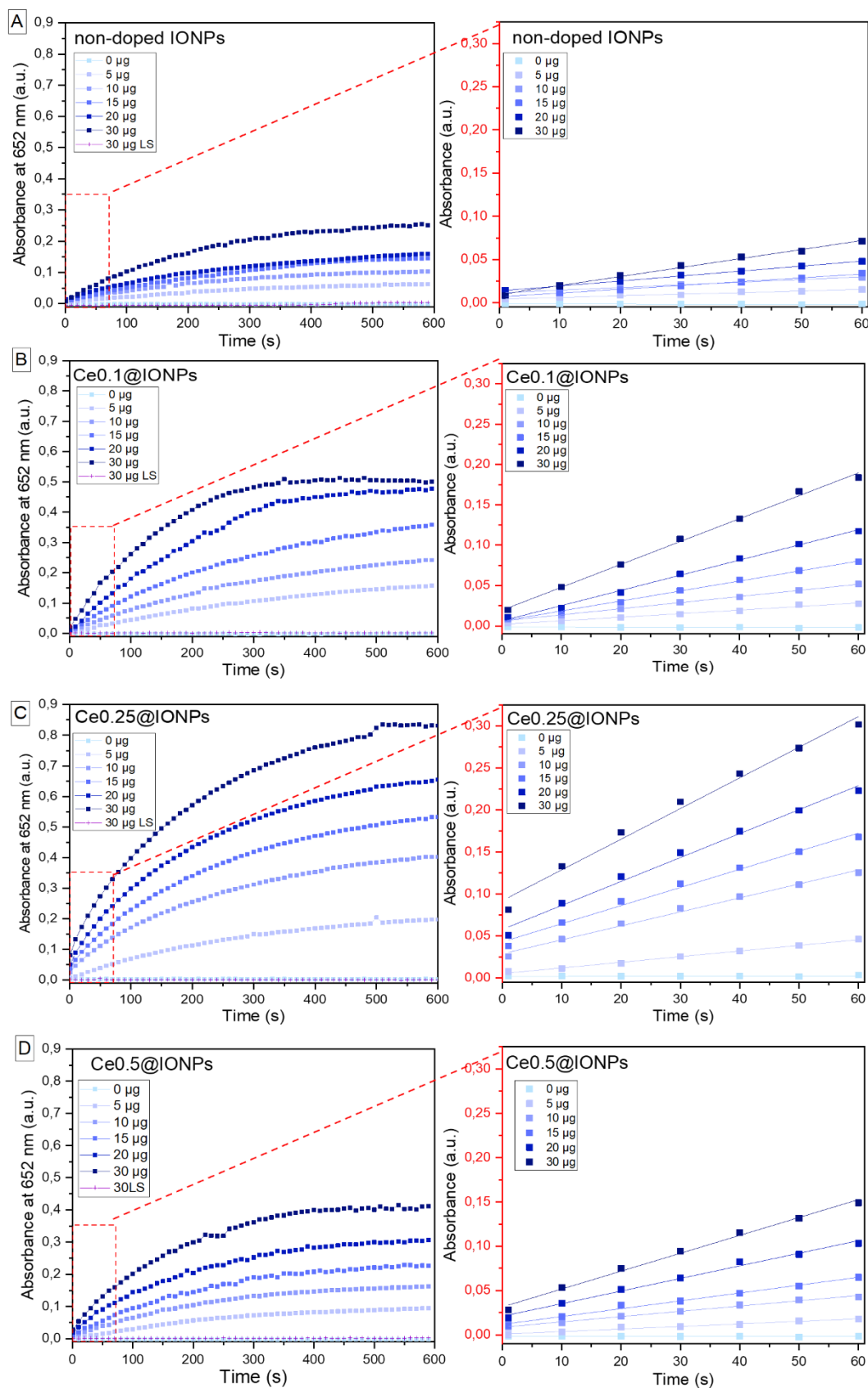
Figure C3. *Comparison of the reaction times curves at 645nm absorbance and magnification of the linearization until 60s reaction of TMB colorimetric reaction catalyzed by (A) IONPs, and Ce@IONPs at (B) Ce0.1, (C) Ce0.25, (D) Ce0.50, (E) Ce0.75, (F) Ce1.0, (G) Ce1.25, and (H) Ce2.0, as a function of their mass (µg).*
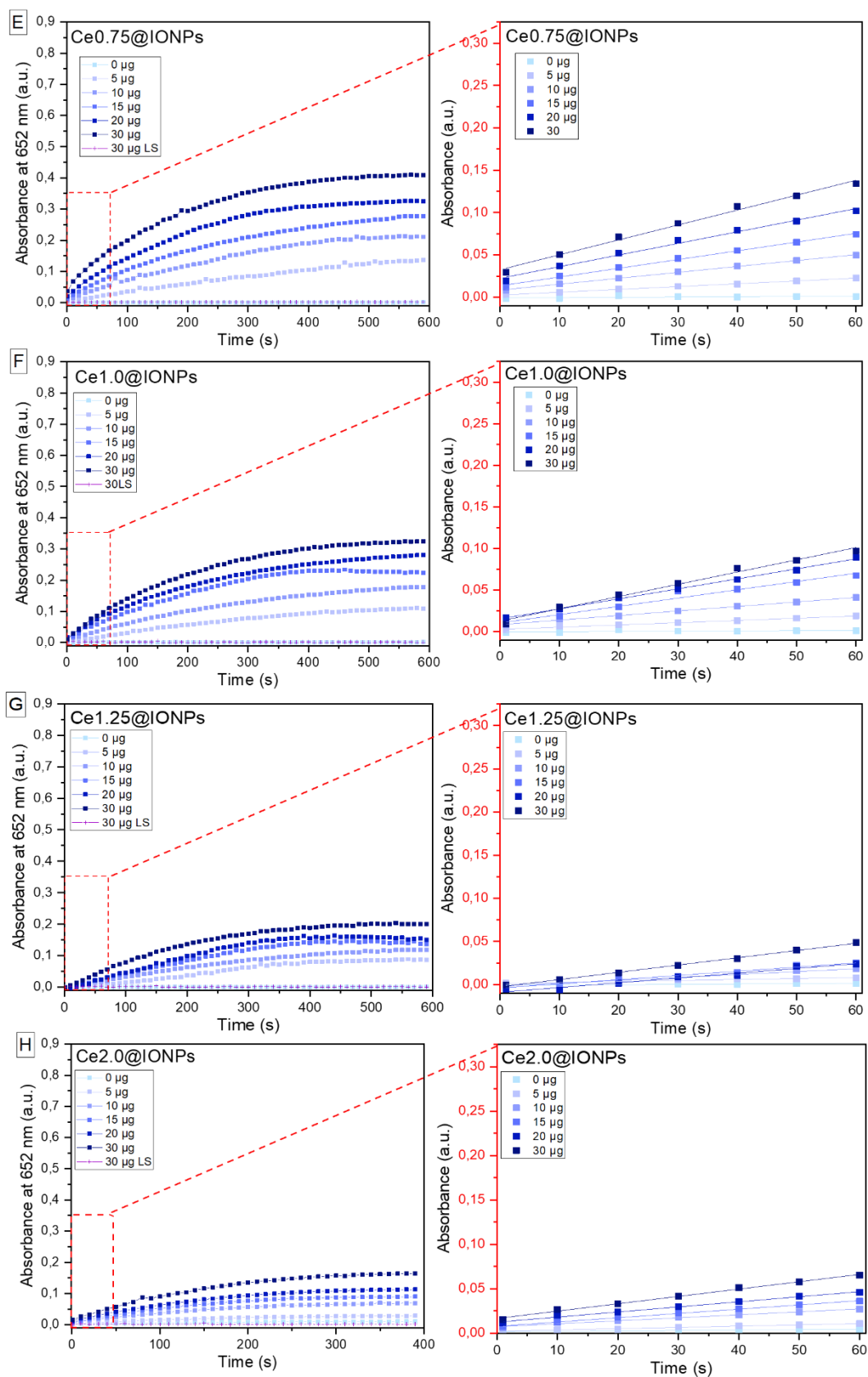
Figure C3. *Continued.*

Table C1. Summary of the physicochemical properties and catalytic activity of Ce@IONPs.

Sample[a] Ce@IONPs	Ce^{3+} precursor (mM)[b]	$X_{(Ce/Ce+Fe)}$ (%)[c]	D_{STEM} (nm)	NPs number/ mL	Total Surface Area (cm^2/mL)	SA by Mass (U/mg)	SA by Area x10^{-4} (U/cm^2)
Non doped	0.00	0.0	9.3 ± 3.4	~$6,7 \times 10^{12}$	18,26	0,0337	0,27
Ce0.10	0.10	1.2	13.4 ± 2.7	~$2,3 \times 10^{12}$	12,67	0,0956	1,10
Ce0.25	0.25	3.2	22.7 ± 3.8	~$4,7 \times 10^{11}$	7,51	0,1237	2,41
Ce0.50	0.50	1.7	26.7 ± 4.2	~$2,8 \times 10^{11}$	6,36	0,0690	1,59
Ce0.75	0.75	1.6	34.0 ± 5.9	~$1,4 \times 10^{11}$	5,00	0,0594	1,74
Ce1.00	1.00	1.5	42.3 ± 7.4	~$7,1 \times 10^{10}$	4,02	0,0509	1,86
Ce1.25	1.25	1.5	46.3 ± 7.2	~$5,5 \times 10^{10}$	3,67	0,0273	1,09
Ce2.00	2.00	1.8	90 ± 20[d]	~$7,4 \times 10^{9}$	1,89	0,0265	2,06

[a] All prepared in the presence of SC (4mM).
[b] Nominal concentration of Ce^{3+} put in the reaction.
[c] Acid digestion, ICP-OES determination.
[d] Rod width measurement.

Table C2. *Summary of the two-way ANOVA for the viability assay of Ce@IONPs (~23 nm) by varying their concentration, evaluated at 24 h and 72 h.*

Anova: Two-Factor With Replication

SUMMARY	24h	72h	Total
Control			
Count	4	4	8
Sum	361,27	357,44	718,71
Average	90,3175	89,36	89,83875
Variance	48,787292	7,4318	24,355841
0,13 mg/mL			
Count	4	4	8
Sum	336,72	359,45326	696,17326
Average	84,18	89,863314	87,021657
Variance	77,857467	12,359281	47,892908
0,2 mg/mL			
Count	4	4	8
Sum	367,3	341,02	708,32
Average	91,825	85,255	88,54
Variance	1,4758333	13,7151	18,843229
0,5 mg/mL			
Count	4	4	8
Sum	346,63	336,98	683,61
Average	86,6575	84,245	85,45125
Variance	18,584558	12,513967	14,990841
Total			
Count	16	16	
Sum	1411,92	1394,8933	
Average	88,245	87,180828	
Variance	38,98264	15,676675	

ANOVA						
Source of Variation	SS	df	MS	F	P-value	F crit
Sample	86,369682	3	28,789894	1,1950645	0,3327537	3,0087866
Columns	9,059688	1	9,059688	0,3760664	0,5454844	4,2596773
Interaction	155,34415	3	51,781384	2,149438	0,1203867	3,0087866
Within	578,17589	24	24,090662			
Total	828,94942	31				